A 3D hydro-mechanical discrete element model for hydraulic fracturing in naturally fractured rock

Efthymios Papachristos

Communauté UNIVERSITÉ Grenoble Alpes

THÈSE
Pour obtenir le grade de
DOCTEUR DE LA COMMUNAUTE UNIVERSITÉ GRENOBLE ALPES
Spécialite: **2MGE: Matériaux, Mécanique, Génie Civil, Electrochimie**
Arrêté ministériel: 25 mai 2016

Présentée par

EFTHYMIOS PAPACHRISTOS

Thèse dirigée par **Frédéric Victor DONZÉ** et
codirigée par **Luc SCHOLTÈS**

préparée au sein du **Laboratoire 3SR: Sols, Solides, Structures et Risques** dans **l'École Doctorale I-MEP²: Ingénierie - Matériaux, Mécanique Environnement Energétique Procédés Production**

A 3D hydro-mechanical discrete element model for hydraulic fracturing in naturally fractured rock

Thèse soutenue publiquement le **08.02.2017**,
devant le jury composé de:

Dr. Chloé ARSON
Associate professor, Georgia Tech, Membre invité
Prof. Pierre BÉREST
Directeur de Recherche, École Polytechnique, MINES ParisTech, Président
Dr. Bruno CHAREYRE
Maître de conférences, Grenoble-INP, Membre invité
Prof. Frédéric DONZÉ
Professeur, Université Joseph Fourier, Directeur de Thèse
Dr. Farhang RADJAÏ
Directeur de Recherche, CNRS, MIT, Rapporteur
Hamid POURPAK
Dipl-Ing., TOTAL S.A., Membre invité
Dr. Luc SCHOLTÈS
Maître de conférences, Université de Lorraine, Co-encadrant de thèse
Prof. Jean SULEM
Professeur, ENPC ParisTech, Rapporteur

Dedicated to my parents, my heroes.

Thanks

First of all, thanks to TOTAL S.A. for offering the grant for this work and more specifically to Hamid Pourpak, Adeline Garnier and Atef Onaisi for their support.

Thanks to the Lab-3SR for offering me a great place to work and for surrounding me with such nice people. I am really proud to have been part of this team.

Speaking of the lab-life, thanks to Shéhérazade and Carole for helping me out with the French bureaucracy and for putting up with my constant incompetence in this field... Also, thanks to Jerome and Remi for being such a helpful and trustworthy IT-team.

Thanks to all my office-mates for the nice working atmosphere, for sharing the nice moments and for being patient and supportive during the difficult ones.

Thanks to Stamos Mylonas, Vagelis Liarakos, Yannis Zevgolis, Zach Agioutantis, George Exadaktylos, Denis Caillerie, Cino Viggiani and various people from the ALERT community for lighting the spark of research in me.

I consider myself very lucky for meeting so many (I mean..MANY) wonderful people during this PhD! Unfortunately it is not possible to refer to each one of you individually in these lines.. I have no words to express how glad I am for having met every single one of you. For every amazing memory, for every unique moment: *Thank you! - Grazie! - Danke! - Hvala! - Gracias! - Blagodaria! - Merci*^{3}*! - Ευχαριστώ!* Really, from the heart.

Thanks to my family for.. well, for everything! For their 24/7 support, their understanding and their love, basic ingredients for letting me chasing my dreams. This thesis would have never been possible without you.

Thanks to Jérôme for helping me out with YADE and to Emanuele for introducing me to the PFV scheme during my "noob" days. Also thanks to Marcello for the nice collaboration.

Special thanks to Alessandro and Eddy for the numerous exciting discussions, for your suggestions (varying from coding to writting the document), for your ability to make everything look much easier and for teaching me a million new things and ways to tackle the different problems I faced throughout this PhD work.

Thanks to the jury for offering me the opportunity of a fruitful discussion and especially the two "rapporteurs", Dr. Farhang Radjaï and Prof. Jean Sulem, for dedicating some of their already overloaded time to review this thesis, for their valuable suggestions and for their very kind comments.

To my advisors:

Thanks Bruno, although not officially my advisor, you helped a lot in this work and I've learned a lot from you. Thanks for your help in developing the DFNFLOW Engine, for your solid answers to my questions and the constructive discussions.

Luc, thank you very much for introducing me to the world of DEM, for being always "there", ready and efficient each time I needed your help, for being an enthusiast for almost every new idea and for your patience. It was a great pleasure working with you!

Finally, a big, big thanks to the most positive and enthusiastic advisor anyone could have. So, thank you Frédéric, first of all for letting me be part of this PhD-journey. Thanks for your many and innovative ideas, for your continuous support, for the discussions, the laughs, and for all this positive energy you emit. Thank you so much..

Abstract in English

Hydraulic fracturing is at the core of a number of naturally occurring and induced phenomena and crucial for a sustainable development of energy resource production.
Given its crucial role this process has been given increasing attention in the last three decades from the academic world. Nonetheless a number of very significant aspects of this process have been systematically overlooked by the community. Two of the most notable ones are the inability of the vast majority of existing models to tackle at once the propagation of hydraulic fractures in realistic, fractured rocks-masses where hydraulic fracturing is a competing dipole mechanism between fracturing of the intact rock and re-activation of exiting fracture networks. Another essential aspect of this process is that it is intrinsically three-dimensional which is neglected by most models. To tackle this vital problem taking into account these pivotal aspects, a fully coupled hydro-mechanical model based on the discrete element method has been developed. The rock mass is here represented by a set of discrete elements interacting through elastic-brittle bonds that can break to form cracks inside the simulated medium. Theses cracks can coalesce to form fractures. A finite volume scheme is used to simulate the fluid flow in between these discrete elements. The flow is computed as a function of the pore space deformation in the intact medium and of the cracks' aperture in the fractures. Furthermore, the natural fractures are modelled explicitly and present mechanical and hydraulic properties different from the rock matrix. Employing this model in an intact numerical specimen, single fluid injection and multiple closely spaced sequential injections, enabled the description the full spatio-temporal evolution of HF propagation and its impact on quantitative indexes used in description of hydraulic fracturing treatments, such as fractured volume, fracture intensity and down-the-hole pressure for different control parameters and *in-situ* stress-fields. Moreover, injections from perforation slots which are not well aligned to the minimum stress plane showed possible creation of percolating non-planar hydraulic fractures of low connectivity, which can be troublesome for proppant placement. Also, strong interactions between closely spaced HF was highlighted by tracking the local principal stress rotation around the injection zones, emphasizing the importance of stress shadow effects. Optimization solutions are proposed for multiple treatments from an non-perfectly aligned wellbore. Finally, interaction between a single hydraulic fracture and a single natural fracture of varying properties and orientations was studied using the proposed model. The evolution of the hydraulic fracture and the global response of the specimen were recorded in a way comparable to existing experimental data to bridge the experimental and numerical findings. Persistent natural fractures appeared to be barriers for the hydraulic fracture if their conductance is high compared to the matrix conductivity or if their stiffness is significantly low compared to the rock matrix rigidity. Low stiffness in non-persistent defects might also cause a bifurcation of the main hydraulic fracture due to the local stress field perturbation around the defect and ahead of the hydraulic fracture tip. Furthermore, high approach angles and differential stresses seemed to favour crossing of the natural fracture while low angles enable shear slippage or dilation on the part of the plane which is not affected by the local stress perturbation.

Résumé en Français

La fracturation hydraulique est au cœur d'un certain nombre de phénomènes naturels et induits et est cruciale pour un développement durable de la production de ressources énergétiques.
Compte tenu de son rôle crucial, ce phénomène a été pris en compte au cours des trois dernières décennies par le monde académique. Néanmoins, un certain nombre d'aspects très importants de ce processus ont été systématiquement négligés par la communauté. Deux des plus remarquables sont l'incapacité de la grande majorité des modèles existants à aborder la propagation des fractures hydrauliques dans les massifs rocheux fracturés où l'injection de fluide peut à la fois conduire à la fracturation de la roche intacte et à la réactiviation de fractures pre-existantes. Un autre aspect essentiel de ce processus est qu'il est intrinsèquement tridimensionnel, ce qui est souvent négligé par les modèles actuellement disponibles. Pour aborder ce problème essentiel, un modèle hydro-mécanique couplé basé sur la méthode des éléments discrets a été développé. La masse rocheuse est ici représentée par un ensemble d'éléments discrets interagissant à travers des lois de contact cohésifs qui peuvent se casser pour former des fissures à l'intérieur du milieu simulé. Ces fissures peuvent se coalescer pour former des fractures. Une méthode de volume fini est utilisée pour simuler l'écoulement de fluide entre les éléments discrets. L'écoulement est calculé en fonction de la déformation de l'espace poreux dans le milieu intact et de l'ouverture des fissures dans les fractures. De plus, les fractures naturelles sont modélisées explicitement de sorte qu'elles peuvent presentées des comportements mécanique et hydraulique différents de ceux de la matrice rocheuse intacte. La simulation des processus de fracturation hydraulique dans un milieu initialement intact en considérant plusieurs points d'injection plus ou moins espacés a permis de mettre en évidence l'évolution spatio-temporelle des fractures hydrauliques et de quantifier l'impact des différentes stratégies d'injection sur des indices representatifs du volume fracturé, de l'intensité et de la densité des fractures ou encore sur la pression de fluide au niveau du puit. De plus, l'injection dans une fente de perforation non alignée sur le plan de contrainte minimum a génère des fractures hydrauliques non planaires percolantes si la connectivité est faible, ce qui peut être gênant pour la mise en place du proppant. En outre, des interactions fortes prennent place entre des fractures hydrauliques étroitement espacées ont ete mises en evidence grace au le suivi de la orientation de contrainte principale locale et ont révélé l'importance des effets d'ombre de contrainte. Des solutions sont proposées pour optimiser les traitements multiples à partir d'un puits de forage non parfaitement aligné. Enfin, l'interaction entre une seule fracture hydraulique et une seule fracture naturelle de propriétés et d'orientations variables a été étudiée à l'aide du modèle proposé. L'évolution de la fracture hydraulique et la réponse globale de l'échantillon ont été enregistrées d'une manière comparable aux données expérimentales existantes pour établir un pont entre les résultats expérimentaux et numériques. Les fractures naturelles persistantes semblent être des barrières pour la fracture hydraulique si leur conductance est élevée par apport a celle de la matrice ou si leur raideur est faible par rapport a la rigidite du milieu environnant. D'autre part, une faible rigidité dans les discontinuités non persistantes pourrait provoquer une bifurcation de la fracture hydraulique principale. De plus, des angles d'approche élevés et des contraintes differentielles fortes semblent favoriser le croisement de la fracture naturelle alors que des angles faibles engendrent plutot un glissement ou une dilatation par cisaillement de la partie du plan qui n'est pas affectée par la perturbation de la contrainte.

Contents

List of Figures

Nomenclature

Variables used throughout the document

F_n: Normal contact force
k_n: Normal contact stiffness
u_n: Normal displacement
F_s: Tangential contact force
k_s: Tangential contact stiffness
Δu_s: Incremental tangential displacement
E_{eq}: Parameter that relates to bulk modulus
δ: Dimensionless parameter that relates to Poisson's ratio
R_A,,R_B: Radii of interacting particles A and B
F_n^{max}: Maximum contact tensile force
$\mathcal{T}$: Interparticle tensile strength
F_t^{max}: Maximum contact tangential force
c: Interparticle cohesion
ϕ: Interparticle friction angle
s: Crack disk's size (area)
$\ddot{\vec{x}}$, $\dot{\vec{x}}$: Particle's translational acceleration and velocity respectively
$\dot{\vec{\omega}}$, $\vec{\omega}$: Particle's rotational acceleration and velocity respectively
$\vec{F}$: Resultant force applied on a discrete element
$\vec{M}$: Resultant torque applied on a discrete element
m: Discrete Element's mass
J: Discrete Element's moment of inertia
$\vec{g}$: Body forces applied on a discrete element
γ: Dimensionless parameter to control damping
n: Porosity
K: Contact density
Ω_i: Elementary pore unit
$\partial\Omega_i$: Interface between pore units Ω_i and Ω_j
$\dot{V}_{p,i}$: Time derivative of pore volume
E: Young's modulus
ν: Poisson's ratio
ρ_f: Fluid density
B_f: Fluid bulk modulus
$\vec{v}$: Fluid velocity
μ: Dynamic viscosity of the fluid
$\vec{n}$: Outwards pointing vector normal to the fluid domain $\partial\Omega_i$
$\vec{u}$: Velocity of the domain $\partial\Omega_i$
P_i: Pressure at pore i
k_{ij}: Local conductance of the throat between pores i and j
$V_{f,i}$: Volume of fluid contained in pore i
t: Time

α,β: Dimensionless local conductance factors
h: Mechanical crack aperture
h_i: Initial crack aperture
S_{ij}^f: Pore throat's cross-sectional area
S_{ij}: Surface of a facet between pore i and j
S_{ij}^s: Projected surface of DE on the facet
R_{ij}^h: Hydraulic radius of the pore
$\vec{F^f}$: Total force applied from the fluid on each discrete element
Γ: Surface domain occupied by a discrete element
$\partial\Gamma$: Wetted surface of the discrete element
$\vec{F^b}$: Buoyancy force
$\vec{F^P}$: Force due to losses of piezometric pressure from viscous flow
$\vec{F^v}$: Force due to viscous shear stress
L_w^k: Length of the interporal interface between a discrete element k and the fluid domain interface $\partial\Omega_{ij}$
κ: Macroscopic permeability
Q: Volumetric flow rate
A: Specimen's cross-section
L: Specimen's length (in permeameter tests)
D_{mean}, D_{min}, D_{max}: Mean, minimum and maximum diameter of discrete elements in a packing
h^{eff}: Macroscopic effective aperture of the fracture plane (in fracture permeameter test)
χ: Dimensionless number defined as the ratio between viscous-toughness transient and storage compressibility-toughness transient
t_{mk}: Characteristic time associated with viscous-toughness transient
t_{uk}: Characteristic time associated with storage compressibility-toughness transient
$K\prime$: Fracture toughness
U: Wellbore storage compressibility
$E\prime$: Plain strain Young's Modulus
L_{uk}: Characteristic lengthscale associated with storage compressibility-toughness transient
σ_v, σ_H, σ_h: Applied vertical, maximum horizontal and minimum horizontal stress respectively
ϵ_v, ϵ_H, ϵ_h: Vertical, maximum horizontal and minimum horizontal strain respectively
$P33$: Total fractured volume
$P32$: Fracture intensity
$V_{fracture}$: Total fracture volume
V_{total}: Specimen's volume
$A_{fracture}$: Total fracture area
N_c: Total number of cracks
θ_s: The angle between the slot's normal and the minimum horizontal stress axis
θ_w: The angle between the fictitious wellbore axis and the minimum horizontal stress axis
d: Distance between the injection slots

Description of Acronyms and Abbreviations

SIF - Stress Intensity Factor, described in the chapter detailing hydraulic fracturing.
DEM - Discrete Element Method, described in the chapter detailing the numerical model.
HF - Hydraulic Fracture, described in the chapter detailing the mechanics and physics of hydraulic fractures.
NF - Natural Fractures, described in the chapter detailing the simulations of pre-fractured rock.
BCs - Boundary Conditions, described in the chapters detailing the tests' setup.
SRV - Stimulated Rock Volume, described in the chapters detailing the historical hydraulic fracturing developments and natural fractures.
FEM - Finite Element Method, referred to in the chapter detailing several numerical methods.
FVM - Finite Volumes Method referred to in the chapter detailing several numerical methods.
FDM - Finite Differences Method referred to in the chapter detailing several numerical methods.
FEMDEM - The combined Finite Discrete Element method referred to in the chapter detailing several numerical methods.
CD - Continuous Damage apporaches referred to in the chapter detailing several numerical methods.
AE - Acoustic Emissions, reffered to in chapters describing comparisons between numerical simulations and experiments.

Chapter 1

Introduction

Hydraulic fracturing is the process of progressive crack growth in any medium undergoing pressurized fluid loading. This fundamental process is encountered in a plethora of natural and anthropogenic issues. For instance, it is known to be a triggering factor of earthquakes, whose lack of understanding and predictability makes them one of the most lethal natural hazards.

Analogously, hydraulic fracturing underlies several other natural phenomena such as magma intrusion through dikes, diagenetic fluid migration and ice sheet failure by water intrusion.

Furthering our understanding of hydraulic fracturing processes is also pivotal in a number of engineering applications, the most notable of which being perhaps rock stimulation for the extraction of fossil fuels or geothermal energy production. These engineering applications have gained particular attention in recent times for being at once crucial for solving the energetic crisis and controversial for the divergent perception some applications have risen.

Despite the aforementioned enormous impact, hydraulic fracturing is only partially understood and has received due attention from the scientific community only since the 80's. More specifically, while the underlying physics of both the host rock and the fluid have been thoroughly tackled by rock and fluid mechanics respectively, the understanding of the spatio-temporal evolution of hydraulic fractures in realistic geomaterials has lagged behind both disciplines. Furthermore, geological complexities, such as natural fracture networks, fault zones, inhomogeneities in stratigraphy and the interaction between competing hydraulic fractures form a complex and intrinsically three-dimensional problem.

This doctoral work aims at providing new insights into the understanding of hydraulic fracturing processes through the use of a coupled hydro-mechanical model specifically developed for that purpose. The proposed model is based on a three dimensional discrete element method coupled to a finite volume scheme and has been developed inside the open source platform YADE Open DEM.

Beside the range of possible applications explored in this dissertation, the aim of the developed code is to help the advancement of the scientific community at large, and was therefore developed within the framework of an open-source scheme.

Layout of this thesis

In order to fully appreciate the contribution of the proposed model to the existing approaches, this PhD dissertation is divided in three parts. In the first part the reader is first introduced to hydraulic fracturing as a process and as an application. The second part is an extensive description of the proposed methodology. Finally, part three is dedicated to the application of the method to different hydraulic fracturing scenarios.

The first part of the document consists of Chapter 2, Chapter 3 and Chapter 4 that introduce the reader to the subject of the PhD work and the motivation driving the need for the current research.

Chapter 2 begins with a historical note on the observations of hydraulic fracturing process and its use on shale gas extraction. Different techniques and innovations that have been used in the field and on the analysis are described. Then the mechanics and physics governing the hydraulic fracturing process are explained. Using some elements of well established theories, existing ways of predicting the initiation, propagation and interaction of hydraulic fractures are presented. Also, an example on scaling field-scale tests to lab-scale tests and *vice-versa* are described. Finally, several open problems concerning the modelling of hydraulic driven fractures in naturally fractured rock mass are listed in Section 2.3. Chapter 3 starts with the presentation of several mechanisms that can cause natural fracture genesis. The direct possible impact of natural fractures to the hydraulic properties of the rock-mass is then detailed. Finally, an introduction to the effect of natural fractures on HF propagation, as studied through different experiments, field work and numerical modelling, is given.

In Chapter 4, an overview of the different methods that have been used up to now to simulate rock failure, hydro-mechanical interaction of fluids and rocks and finally hydraulic fracturing is presented Each method has its own advantages, disadvantages and limitations. By the end of the chapter, the trending problems in HF modelling are listed.

The second part of this PhD dissertation (Chapters 5 and 6) aims at describing the developed numerical tool and it's capabilities. In Chapter 5, first, the scheme for modelling rock-related problems with the discrete element method is explained. Then, the strategy for the model calibration in terms of mechanical properties is presented. The scheme for modelling the fluid flow in both the rock matrix and the fracture and its coupling to the discrete element method is then detailed. Here again, the calibration procedure of the model in terms of hydraulic properties is explained. In Chapter 6, two benchmark tests are presented for validating the proposed coupled model. The first test deals with the elastic deformation under fluid pressurization of a penny shaped crack under constant pressure load. The second one deals with the hydraulic fracture propagation of a penny-shaped crack under constant flow rate injection in a zero-toughness medium. Finally, the model is compared to a laboratory experiment.

The third part of the manuscript, consisting of Chapter 7 and Chapter 8 is dedicated to the applications of the developed numerical model on different configurations. Chapter 7 presents the application of the model on an intact rock numerical specimen subjected to hydraulic fracturing. The influence of the medium's permeability and the contributions of the fluid compressibility, the flow rate and the stress state are investigated for a single injection treatment first. The curvature of the HF and the crack aperture distribution over its surface are analysed to assess the possibility for the proppant to propagate correctly inside the hydraulic fracture. Then, the results from multiple injection treatments are presented and the effect of the perforation clusters interval, the wellbore and the cluster orientations are discussed with regard to the evolution of the fracture volume and fracture intensity indices. The objective of Chapter 8 is to analyse HF propagation in a numerical specimen containing a pre-existing discontinuity. As mentioned in Chapter 3, rock-masses usually contain natural fractures. The interaction of a hydraulic fracture with natural fractures being not fully understood yet, an attempt is made hereafter to study the process. Two types of natural fractures will be studied: persistent and non-persistent. The non-persistent discontinuities correspond to the cases where the natural fractures are of size comparable to the size of the HF. On the other hand the persistent defects correspond to large horizontal and sub-horizontal structures such as large bedding planes, cemented zones or open corridors. The importance of the *in-situ* stress field, the control parameters (*i.e.*, injected fluid viscosity and imposed flow rate), along with the defect's properties (such as orientation, size, initial aperture and stiffness) on the hydraulic fracture propagation, on specimen's response and on the final patterns will be explained and justified. Moreover, by comparing the medium's response to the ones obtained by similar experimental campaigns, an attempt to grasp the gap between numerical modelling and experimental findings on dynamic evolution of hydraulic fracture is made. Finally, a discussion of hydraulic fracture growth after the intersection with

a natural fracture is provided and aims at giving indicators on the order of importance of each parameter on their interaction.

The thesis is closing with a conclusion chapter, summing up the thesis, and driving the main conclusions of this work. Finally, a detailed list of ongoing work and possible future work that can be done by the contribution of this PhD work is presented.

Part I

Literature Review

Chapter 2

Hydraulic fracturing

This chapter introduces the reader to hydraulic fracturing (HF). A lot of research has been carried out the last decades on this topic. Many important findings regarding HF as either a physical phenomenon or an applied technique have been reported.

Being a multidisciplinary problem, it shares concepts coming from different scientific domains. Thus, going through the mechanics and physics of HF is mandatory for better understanding the phenomenon. First, a short introduction to the basics of fracture mechanics will be presented to define the physical quantities and the concepts used in the description of HF. Then, the fully coupled problem of HF propagation will be discussed from a mechanical and energetic point of view. Finally, scaling laws that arise from the analysis and help in connecting field scale HF, lab-tests and numerical simulations will be presented.

Finally, as HF involves several complex mechanisms and phenomena, there are sides of the problem that are still unexplored or not well captured yet by models. The chapter ends with a sum up of the trending, open problems remaining while considering realistic modelling of HF.

Layout of chapter

The chapter begins with a historical note (Section 2.1) on the observations concerning the HF phenomenon and the use of HF on engineering applications such as rock stimulation. Different techniques and innovations that have been used in the field to optimize the process are described.

Then the mechanics and physics governing the HF phenomenon are explained in Section 2.2. Stress concentration at fracture tip, propagation regimes and dimensionless scaling of the HF propagation are analysed in terms of mechanics of materials, fracture mechanics and energy balance. Also, ways to scale field-scale applications to lab-scale tests and simulations are described.

Finally, several open problems concerning the modelling of the hydraulic driven fractures in naturally fractured rock mass are listed in Section 2.3. The listing of the open problems justifies the development of the model.

2.1 Historical note

Hydraulic fracturing involves the progressive failure of a material under fluid pressurization. The fluid pressure can cause opening (tensile) failure in the intact material, or opening and shearing failure - sliding along pre-existing fractures (also referred to as "hydroshear"). Fluid driven fractures can occur in many different contexts, originating from either natural or anthropogenic processes. It has been observed in nature under the form of diagenetic or maturation induced fluid migration (or primary migration) (Kobchenko *et al.*, 2011), magma intrusion through dikes (Lister and Kerr, 1991; Roper and Lister, 2005; Rubin, 1995; Spence *et al.*, 1987), ice-sheet failure due to water intrusion (Tsai and Rice, 2010), failure mechanism in dams (Lo and Kaniaru, 1990; Sherard, 1986), and reactivation mechanism in fault slippage (Leclère *et al.*, 2012). However,

apart from their natural occurrence, HF have been most commonly studied in the context of reservoir engineering as a technique for permeability enhancement of tight formations in order to exploit hydrocarbons or geothermal fluids (Administration and Kuuskraa, 2011; Arthur *et al.*, 2008; Davies *et al.*, 2012; Eshleman and Elmore, 2013; Fairhurst *et al.*, 2013; Lee *et al.*, 2011). Other examples of industrial applications is the use of HF for roof-control in coal mines in order to avoid rock-bursts (Fan *et al.*, 2012) and *in-situ* stress measurements (Zoback, 2010).

Regarding the industrial applications, the procedure lays within the following methodology (see Figure 2.1 for details). A wellbore is drilled until it reaches the reservoir. Then, the walls of the wellbore are stimulated by explosive charges, so as to create initial defects (perforation clusters) from which the HF will initiate to propagate. The wellbore segment at the stimulation point is then isolated by packers. Next, a fluid (usually referred to as "fracking fluid") is pumped between the packers until the fluid pressure reaches a certain level in the stimulated rock (Britt, 2012; Economides *et al.*, 2000; Yew and Weng, 2014). After this point a HF starts propagating outwards from the wellbore. The aim is to create a set of well shaped HF or to increase the connectivity of the pre-existing fracture network (Deo *et al.*, 2013; Grasselli *et al.*, 2015) and thus the permeability of the formation. In absence of pre-existing fractures, the HF initiation pressure depends on the in-situ stress as well as on the strength of the intact rock (Zoback, 2010). HFs are generally produced by pumping low viscous "slick water" fluids at high rates into the host formation (Arthur *et al.*, 2008; Gaurav *et al.*, 2012; Weng, 2015) because it seems to produce a more complex fracture network. The slick water composition includes a polyacrylamide which reduces the viscosity of the fluid and thus the friction of the water in the pipe as well.

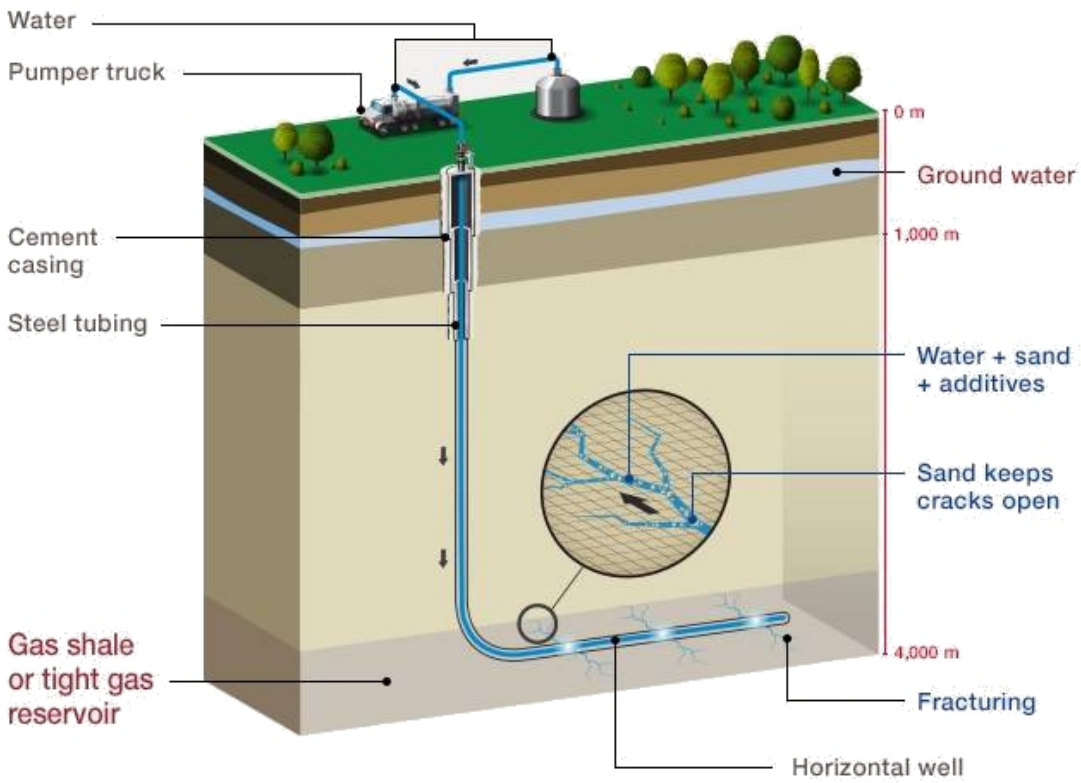

Figure 2.1: Illustration of hydraulic fracturing application (from TOTAL, n.d.).

With the advent of directional drilling techniques, the use of horizontal wells has drastically improved the resources recovery (Eshleman and Elmore, 2013; Lee *et al.*, 2011; Uzoh *et al.*, 2010). If no major geological structures (*e.g.*, faults) are present, the wells are generally oriented in the direction of the minimum in-situ stress to generate HF with an orientation perpendicular to this

direction (Economides *et al.*, 2000; Lecampion and Desroches, 2015; Uzoh *et al.*, 2010). This configuration promotes extension of long planar fractures (Soliman and Boonen, 2000) which are believed to create the largest stimulated reservoir volume (SRV) (Nobakht *et al.*, 2013). Coupling multistage fracture completions and multiple wells, higher level of drainage can be reached (Lecampion and Desroches, 2015; Nagel *et al.*, 2013; Yew and Weng, 2014). Moreover, decreasing the spacing between the different perforation clusters (see Figure 2.2) can potentially increase the level of interaction between HF and thus improve the size of the SRV, as long as stress shadow effects (*i.e.*, local non favourable perturbation of the state of stress caused by interaction of propagating HF) remain negligible (Bunger *et al.*, 2012; Nagel *et al.*, 2013; Yew and Weng, 2014). It is still not clear however if the creation of long planar HF represents the optimum SRV configuration. For example, it has been observed that in the case of a well not aligned with the minimum stress direction, the creation of sharp curving of the HF can create difficulties for the proppants to propagate inside the fracture and can thus drastically reduce its conductivity (Soliman *et al.*, 2012). To overcome this limitation, orientated injections can be used to promote the alignment of HF in the minimum stress direction what ever the orientation of the well (Burghardt *et al.*, 2015).

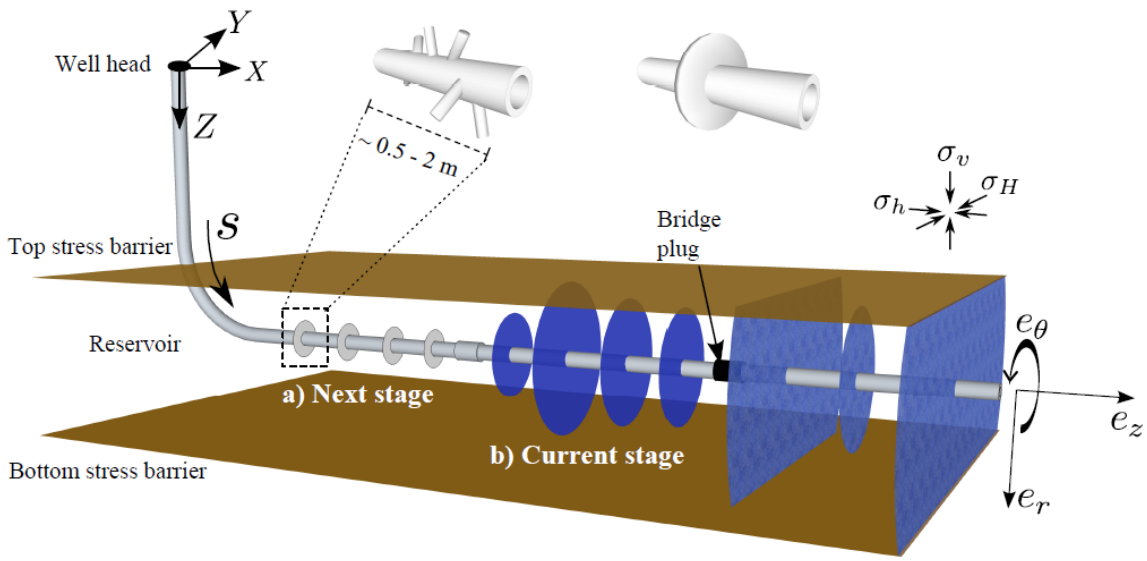

Figure 2.2: A sketch explaining multiple treatments along a well bore (from Lecampion and Desroches, 2015, modified).

The concept of SRV was initially proposed to provide a quantitative assessment of stimulation effectiveness based on the spatial distribution of microseismic events induced by hydraulic injections. However, such assessment provides little insight into critical parameters such as, for example, the hydraulic fracture conductivity (Cipolla, Wallace *et al.*, 2014) that can vary significantly depending on the rock properties, the local stress regime and the fracture treatment design. For example, the fracture conductivity can depend on the geometry of the fracture and on the degree of its shear displacement (Zhang *et al.*, 2015) which is directly related to the stress distribution in the vicinity of the HF (Rorato *et al.*, 2016). Moreover, microseismicity is often representative of shear dominated rupture mechanisms whereas fluid driven fractures propagate mainly due to tensile mechanisms (Maxwell, 2011). If so, the SRV concept may not be sufficient for completion evaluation and optimization of the recovery and complementary indices more representative of the HF properties have to be considered.

The effective HF propagation mode is mainly related to the in-situ state of stress and HF

align with the maximum stress direction, exhibiting maximum apertures which should lead to an optimal conductivity. A question nonetheless arises: could the conductivity of the stimulated volume be better represented in a model by the total volume of connected HF per unit volume (P33) (Dershowitz, 1984), rather than by the one deduced from the intensity of fracture, which can be related to the surface of the connected HF per unit volume (P32)? Using a coupled hydro-mechanical (HM) model, one of the objectives of the current PhD thesis objective is to investigate the optimum configuration for the HF conductivity by recording the evolution of the P33 and P32 indices during the simulations.

2.2 Mechanics and physics of hydraulic fracture

2.2.1 Elements of fracture mechanics

It is known that defects embedded in a solid body cause stress concentrations. In particular, when these defects are not smooth (*e.g.*, circular/ ellipsoidal) but rather edgy, the stress-field becomes singular on the edges (Inglis, 1913). Such defects with the edge angle approaching π are called fractures (or cracks). Another way for one to imagine this type of defects is to consider ellipses with diminishing length of their minor axis. Strictly speaking, a fracture, is defined as a thin discontinuity (of infinitesimal width) such that (a) the traction vanishes on it's surface and (b) the displacement field undergoes a discontinuity when crossing the two lips of the crack. Based on the direction of loading, there are 3 modes of fracture loading (Figure 2.3):

1. Opening mode or Mode-I
2. In plane sliding or Mode-II
3. Anti-plane sliding or Mode-III

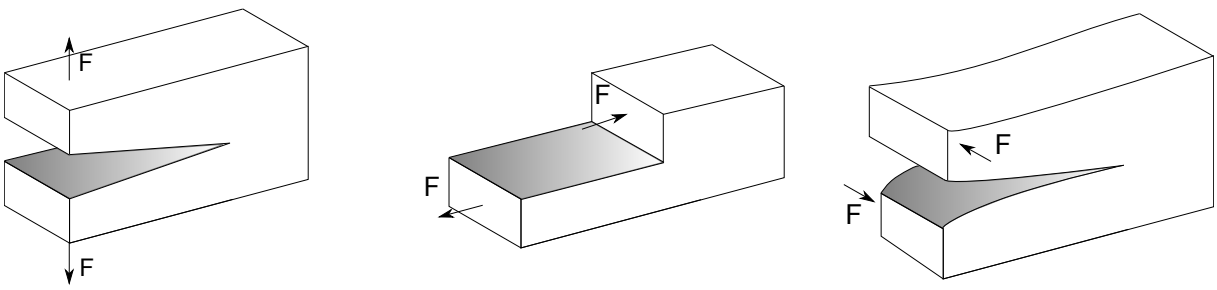

Figure 2.3: Modes of fracture loading. Left to right: Opening (Mode-I), In-plane sliding (Mode-II) and Anti-plane sliding (Mode-III).

One of the main hypothesis of fracture mechanics is that the stress field in the vicinity of the fracture tip governs the behaviour of the fracture and not the so called far-field stresses. In order to quantify the influence of this near-tip stress-field, (Barenblatt, 1962) introduced the stress intensity factor (SIF). There exists a SIF for each loading mode and they are usually noted as K_i, with i being $\mathrm{I}, \mathrm{II}, \mathrm{III}$. The SIFs depend on both the fracture geometry and the far-field stress field. The principal components of stress and displacement close to the fracture tip, for linear, isotropic, elastic solids can be given in terms of SIFs in the following form:

$$\sigma(r,\theta) = \sum_{i=\mathrm{I}}^{\mathrm{III}} \frac{K_i}{\sqrt{2\pi R}} f_i(\theta) \tag{2.1}$$

$$u(r,\theta) = \sum_{i=\mathrm{I}}^{\mathrm{III}} \frac{K_i}{\sqrt{2\pi R}} g_i(\theta) \tag{2.2}$$

σ being the stress, r the radial distance from the fracture tip, θ the angle around the fracture tip, $f_i(\theta)$ and $g_i(\theta)$ geometric parameters.

Moreover, for each material there is a specific limit for the K_i, above which the fracture starts to grow. This limit is called fracture toughness, noted as K_{iC} and it's a material parameter. Based on this, the fracture will initiate to propagate while:

$$K_i \geq K_{iC}, \quad \text{for } i = [\mathrm{I}, \mathrm{II}, \mathrm{III}] \tag{2.3}$$

An alternative idea on the fracture propagation comes from a second approach based on the energy concentration. The so-called Griffith-Irwin criterion of propagation (Irwin *et al.*, 1958) is based on the fact that fracture propagation associated to the creation of new fracture surface dA requires an energy release dW_F which causes a decrease of the total elastic potential of $2\gamma_F$ (specific fracture energy):

$$dW_F = 2\gamma_F dA \tag{2.4}$$

Considering a system defined by applied forces X and cracks of surface A, the total elastic potential Ψ is given by:

$$\Psi(X, A) = \Phi(X, A) + \Xi(X, A) \tag{2.5}$$

where Φ, Ξ are noting the elastic potential and the potential of external loads respectively.

For the creation of a new fracture surface of dA, the energy release dW_F will be positive when:

$$dW_F = -\frac{\partial \Psi(X, A)}{\partial A} dA > 0 \tag{2.6}$$

So, by noting the energy release rate as:

$$\mathcal{G} = -\frac{\partial \Psi(X, A)}{\partial A} \tag{2.7}$$

according to Griffith - Irwin criterion the fracture initiates to propagate while:

$$\mathcal{G} \geq 2\gamma_F \tag{2.8}$$

After the initiation, if G is positive (the energy released by the system increases as the fracture propagates), the fracture propagation is "unstable". If G is negative, the fracture propagation is "stable". Irwin's formula for energy release rate can be written as a function of K_i as:

$$\mathcal{G}_{\mathcal{I}} = \frac{(X+1)}{8\mu_l} K_{\mathrm{I}}^2 \quad \mathcal{G}_{\mathcal{II}} = \frac{(X+1)}{8\mu_l} K_{\mathrm{II}}^2 \quad \mathcal{G}_{\mathcal{III}} = \frac{K_{\mathrm{III}}}{2\mu_l} \tag{2.9}$$

Later, Rice introduced the so-called *J-integral* that relates the energy release to the crack deformation independently from the contour path Γ used for the calculation. The *J-integral* reads:

$$J = \int_{\Gamma} W n_1 - T \frac{\partial u}{\partial x_1} dS \tag{2.10}$$

and for the case of linear elasticity $J = G$. Both G and J have two principal forms:

1. One in which the closed contour follows the extend boundary of the body, which gives accessibility to the energy release in experiments.

2. One in which the contour follows closely the crack, which enables their relation to the SIFs.

Most of hydraulic fracturing theories explained on the following section are based on the aforementioned concepts and quantities.

2.2.2 Hydraulic fracture

The most common information that someone can obtain directly from a field or lab test is the pressure evolution in time at the wellbore, during the HF treatment. In Figure 2.4 a sketch of a typical recording is shown. The injected fluid causes a pressure raise under a constant pressurization rate. When the initiation pressure P_i [Pa] is reached, fracturing initiates from the wellbore walls and the pressurization rate changes. Then, an unstable fracture starts propagating (formation break-down) and causes a pressure drop since the fluid is injected at rate that is lower than the new fractured volume increase rate (Fjar *et al.*, 2008). The peak pressure causing the unstable fracture growth is called the breakdown pressure, P_b [Pa]. The difference between P_i and P_b can be explained either by the creation of a filter cake in the fracture which shields the tip (Morita *et al.*, 1996) or by possible fluid storage at the injection point caused by the fluid's and pumping system compressibility (Abbas and Lecampion, 2013). After the drop, the pressure at the injection point remains quasi-stable as the fracture switches to stable propagation. In some cases, there is no clear evidence of P_b or even P_i due to various possible parameters (Fjar *et al.*, 2008). Finally when the injection stops, at the so-called shut-in point, the pressure decays down to the pore-pressure of the medium.

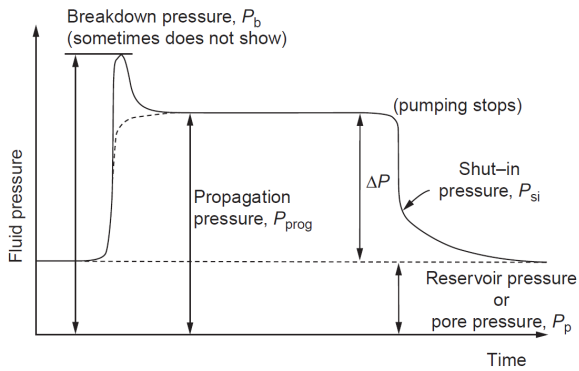

Figure 2.4: Idealized typical recording from HF treatment (from Yew and Weng, 2014).

Different ways have been proposed to deal with the prediction of the initiation of HF and their propagation. Considering for example fluid pressure applied in a circular defect (such as a borehole, in 2D) placed in an infinite medium subjected to far-field stresses σ_H and σ_h (see Figure 2.5), Kirsh elastic solution around a circular defect would give the failure criterion (and thus the fracture initiation) for an impermeable rock matrix in plane strain conditions as:

$$P_i = T + \sigma_H - 3\sigma_h \tag{2.11}$$

with P_i being the fracture initiation pressure and T the medium's tensile strength. An initial pore pressure P_0 can be added on the right hand side of Equation 2.11 if the matrix is saturated. The critical pressure value agrees with the findings of (Zoback *et al.*, 1977), who performed hydraulic fracturing laboratory experiments.

However, in some cases, where a perforation slot is used for the initiation of the HF, the aforementioned assumptions might cause an overestimation of P_i. The same problem can be solved using a fracture mechanics approach and the superposition principle of linear elasticity to take into account the initial fracture (perforation slot) at the wellbore (Rummel, 1987) as shown in Figure 2.5. Thus superimposing the the mode-I intensity factors caused by the far-field stresses, the pressure inside the circular defect and the pressure inside the initial fracture, K_{σ_H}, K_{σ_h}, K_P, K_{Pa} respectively, the initiation pressure can be obtained by:

$$P_i = \frac{K_{IC}}{f_o + f_a} + \sigma_H \frac{f_H}{f_o + f_a} - \sigma_h \frac{f_h}{f_o + f_a} \tag{2.12}$$

where f_i $(i = o, a, H, h)$ are dimensionless stress intensity functions.

The two solutions for determining P_i (circular defect and circular defect with perforation slot) converge for high fluid viscosity and high injection rate since the fluid doesn't enter the slot before the HF initiation. Thus, Equation 2.11 is seldom used due to it's simplicity.

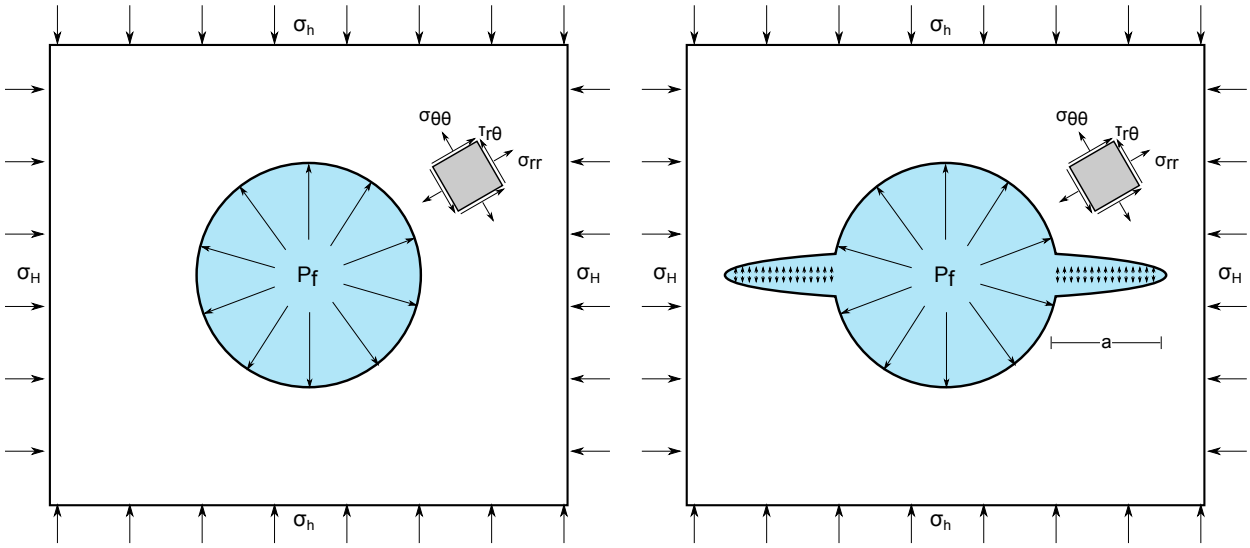

Figure 2.5: 2-Dimensional sketch of (a) Strength of materials idealized approach (b) LEFM idealized approach

.

Qualitative information can be obtained by experimental research using *post-mortem* tracking of the HF footprint. The fluid used, might contain colouring agents so that the total HF growth can be tracked by cutting the specimen and following the colour trace (see *e.g.*, Zoback and Byerlee, 1976). It is only recently that some experiments have proposed real-time recordings for tracing the HF evolution in 3D, using acoustic emissions (AE), combined with quantitative descriptors such as pressure evolution at the injection point and volumetric deformation of the specimen (see Stanchits *et al.*, 2013; Stanchits *et al.*, 2015).

In order to understand the whole evolution of the problem and get information such as HF length, spatial distribution of opening and pressure, fracturing rate, and fluid loss in the formation, actual final HF shape, the propagation of the HF has to be explained. HF propagation is found to be an evolution problem involving several competing physical phenomena, each one of them based on different time-scales and length-scales. For this reason the following approach was proposed by Detournay and co-workers based on energy balance, dimensional analysis and tip asymptotics to bridge the phenomena.

In Figure 2.6a, a 2D top-view representation of the different scales in a planar horizontal fracture are shown. Under the imposed injection rate Q, two different domains appear in the fracture. The domain $\mathcal{A}_f$ represents the fluid domain, and it's enclosed by the contour $\mathcal{C}_f$ which represents the fluid front. On the other hand, the domain $\mathcal{A}_c$ represents the total domain of fracture which is enclosed by the contour $\mathcal{C}_c$ that corresponds to the fracture tip. During the injection, the two fronts are moving on different velocities noted $\mathbf{V}_f$ and $\mathbf{V}_c$ respectively. The normal distance between $\mathcal{C}_f$ and $\mathcal{C}_c$ corresponds to the fluid lag λ. Finally, s is the distance from the fracture tip to the injection point. Based on this configuration, a travelling wave solution can be built for the propagation of the HF in time. Figure 2.6b, shows a sketch that sums up the variables and the phenomena involved in the propagation from a side view.

The way the non-linear equations describing the fracture growth are degrading close to the fracture tip during the propagation and the dominance of the different involved processes are crucial for the understanding of the evolution of the HF. These competing processes are (Detournay,

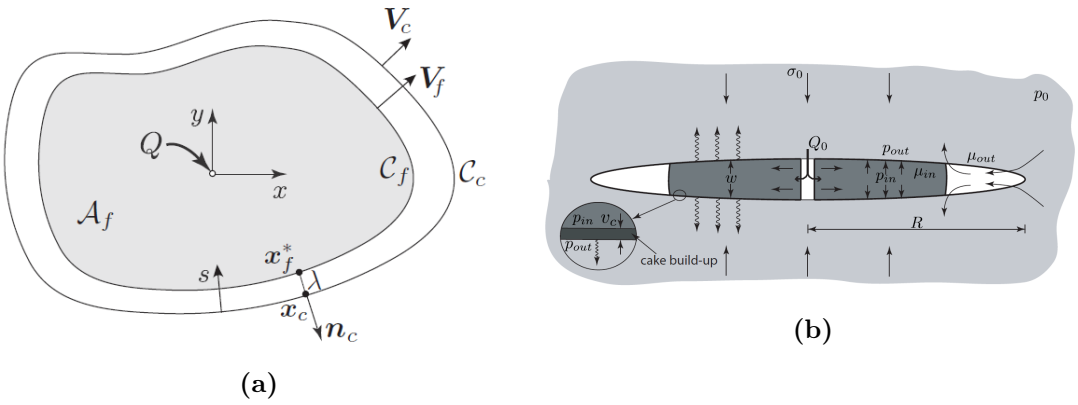

Figure 2.6: (a) 2-Dimensional sketch of the different scales involved in HF (after Detournay and Peirce, 2014). (b) 2-Dimensional sketch of the HF propagation problem (after Kovalyshen, 2010).

2016):

1. Creation of new fracture surfaces (fracturing).
2. Viscous flow of the injection fluid.
3. Elastic deformation of the rock.
4. Formation of a fluid lag behind the fracture tip.
5. Fluid leak-off from the fracture to the matrix.

The combination of these processes makes the HF propagate under different regimes regarding the energy dissipation (viscous fluid flow versus energy release from fracturing) and the way the fluid is affecting the problem (fluid stored in the HF or leaking off in the formation). Usually, the HF passes from early time storage-toughness regime of propagation, with the limit case (or vertex-solution) corresponding to a dry fracture with a traction force acting at fracture center, to the long time leak-off toughness solution (see Figure 2.7). For a given type of rock, control parameters that can be changed during the treatment are the flow rate Q and the fluid viscosity μ. The fluid viscosity can mainly affect the toughness - viscosity transition whereas the flow rate can affect the storage to leak-off transition (Sarris and Papanastasiou, 2015).

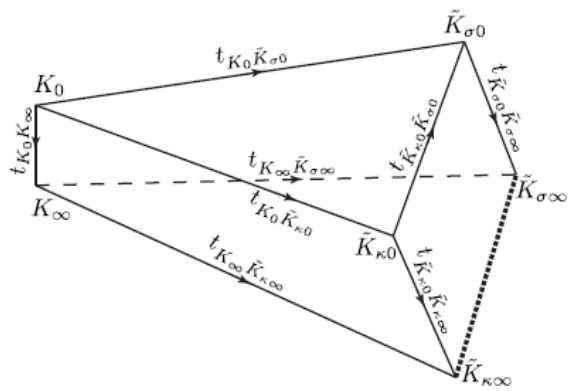

Figure 2.7: Parametric space of the HF propagation regimes (from Kovalyshen, 2010).

However, based on the parameters and the time of the treatment, the HF propagation can follow a trajectory that follows a combination of different transient regimes. The most appropriate regime for the HF propagation description is selected based on the characteristic times of

each transient compared to the time of the treatment and a dimensionless parameter such as the dimensionless viscosity $\mathcal{M}$ or the dimensionless toughness $\mathcal{K}$. In the case of *e.g.*, a penny-shaped crack propagation in the viscosity-toughness transient in absence of fluid leak-off, $\mathcal{M}$ and $\mathcal{K}$, are defined as (Savitski and Detournay, 2002):

$$\mathcal{M} = \mu' \left(\frac{Q^3 E'^{13}}{K'^{18} t^2} \right)^{1/5} \qquad \mathcal{K} = K' \left(\frac{t^2}{\mu'^5 Q^3 E'^{13}} \right)^{1/18} \tag{2.13}$$

with $\mu' = 12\mu$ [Pa.s] , $Q\,[\mathrm{m}^3.\mathrm{s}^{-1}]$ the imposed flow rate, $E' = E/(1-\nu^2)$ [Pa] the plain strain Young's modulus, $K' = 4(2/\pi)^{1/2} K_{IC}$ [Pa.m$^{1/2}$] and t [s] the time.

These analytical and semi-analytical solutions are very helpful in explaining and describing HF propagation in specific regimes and for simplified geometries. For more complex configurations numerical models must be used (see Chapter 4). Nevertheless, these solutions can be used as benchmarking tests for the numerical models in specific configurations (see Section 6.2).

In order to connect all the different time-scales and length-scales to relate lab tests to field cases and *vice-versa*, the following analysis was done in the work of (De Pater *et al.*, 1994). By deriving the field equations into dimensionless form, they created a complete set of dimensionless groups (considering Carter's leak-off model and elastic rock behaviour and assuming constant fluid density and no body forces and inertial effects) needed for the scaling:

$$N_t = \frac{tQ}{r_w^3} \quad : \quad \text{Time of treatment} \tag{2.14}$$

$$N_{E'} = \frac{E' r_w^3}{Q\mu'} \quad : \quad \text{Elastic deformation} \tag{2.15}$$

$$N_\Gamma = \frac{\Gamma}{E' r_w} \quad : \quad \text{Fracture growth} \tag{2.16}$$

$$N_{K_l} = K_l \sqrt{\frac{r_w}{Q}} \quad : \quad \text{Leak-off} \tag{2.17}$$

$$N_{\sigma_c} = \frac{\sigma_c}{E'} \quad : \quad \text{Confinement} \tag{2.18}$$

with r_w [m] the wellbore radius, Γ[N.m] the separation energy and σ_c [Pa] the confining pressure.

The total energy dissipation should be equal to three major components, namely:(1) Energy release rate from rock deformation due to HF opening and confining stress, $\dot{U}_e$, (2) Energy release rate from viscous fluid flow (friction), $\dot{U}_f$ (3) Energy release rate from fracture growth $\dot{U}_c$. Using the set of dimensionless groups and the dimensionless energy release rates, the following interpretation can be derived:

(i) The dimensionless group associated to the elastic response of the rock to the loading can be related to the ratio of the elastic energy dissipation rate to the viscous flow dissipation rate as:

$$N_E \sim \frac{\dot{U}_e}{\dot{U}_f} \tag{2.19}$$

(ii) On the other hand, the dimensionless group associated to the creation of new fracture surface can be related to the ratio of the energy release rate for new fracture surface creation to the elastic energy release rate as:

$$N_\Gamma \sim \frac{\dot{U}_c}{\dot{U}_e} \tag{2.20}$$

Comparing these ratios one can know in which regime of propagation the treatment is going to take place.

Furthermore, the characteristic time t^* for the scaled model can be given by a combination of the dimensionless groups N_t and $N_{\bar{E}}$ as:

$$t^* = \frac{t}{N_t N_E^{1/4}} = \left(\frac{r_w^3}{Q}\right)^{3/4} \left(\frac{\mu'}{E'}^{1/4}\right) \tag{2.21}$$

Assuming as known the dimensions of the test and the injection time, by comparing the dimensionless length of the fracture and the treatment time between the different cases, one can compute the scaling factor S_Q of the model compared to the reference case for the flow rate as:

$$S_Q = \frac{S_{r_w}^3}{S_t} \tag{2.22}$$

In a similar way, relating the toughness to length-scale, the toughness scaling factor $S_{K_{IC}}$ is computed by:

$$S_{K_{IC}} = S_{E'} \sqrt{S_{r_w}} \tag{2.23}$$

Then, by setting $N_{E'}$ to unity, the viscosity scale factor S'_μ can be obtained by:

$$S_{\mu'} = \frac{S_{E'} S_{r_w}^2}{S_Q} \tag{2.24}$$

Finally, using the leak-off dimensionless group we end up to the scale factor:

$$K_l = \sqrt{\frac{S_Q}{S_{r_w}}} \tag{2.25}$$

Using the above scaling procedure, it is possible to track and relate simulations (or experiments) of smaller spatial or time domains with real-scale *in-situ* treatments. This way, time or space restrictions can be bended while the HF propagates in the same regimes as in the reference case. Knowing the length and time-scales involved, the results can be extrapolated to *in-situ* conditions.

As mentioned in Section 2.1, in order to increase the stimulated volume, multiple HFs are initiated from the same or parallel wellbore segments. However, if the HFs are placed too close to each other they might decrease the efficiency of the treatment due to strong interactions among them usually referred to as stress-shadow (Yew and Weng, 2014). The stress created by neighbouring HFs increases the confinement on the propagating HF and thus reduces the maximum aperture (Roussel and Sharma, 2011). Furthermore the HF act as repellers to each other causing a curvature to the propagation (turning away from the closest neighbour HF). This is caused because the HFs are trying to propagate along the "easiest" path regarding the local stress field that is perturbed by the growth of the neighbouring HFs. Also, it is observed that during a treatment stage, inner HFs are considerably shorter than the ones located on the periphery of the treatment. (Bunger and Peirce, 2014; Bunger *et al.*, 2012; Peirce, Bunger *et al.*, 2015). Furthermore, it has been found that closely placed treatments are usually creating HF with no radial-axisymmetry (see Figure 2.8), which is a widely used assumption in modelling (Kear *et al.*, 2013). In case of sequential multistage HF though, if the neighbouring HFs are already closed (after flow-back), the neighbouring HFs might act as attractors (Bunger *et al.*, 2012).

Usually the plastic zones in HF propagation are neglected if their length is small compared to the HF length. However, in some cases, in weak porous formations, the recorded pressures can be much higher than the expected ones. By considering the rock matrix as poro-elastoplastic, (Sarris and Papanastasiou, 2015) found out that plastic zones ahead of the fracture tip could lead to an increase of the pressure of about 20%, whereas the final HF was found to be wider as the fracture tip is shielded. If the size of the plastic zones is not negligible compared to the HF

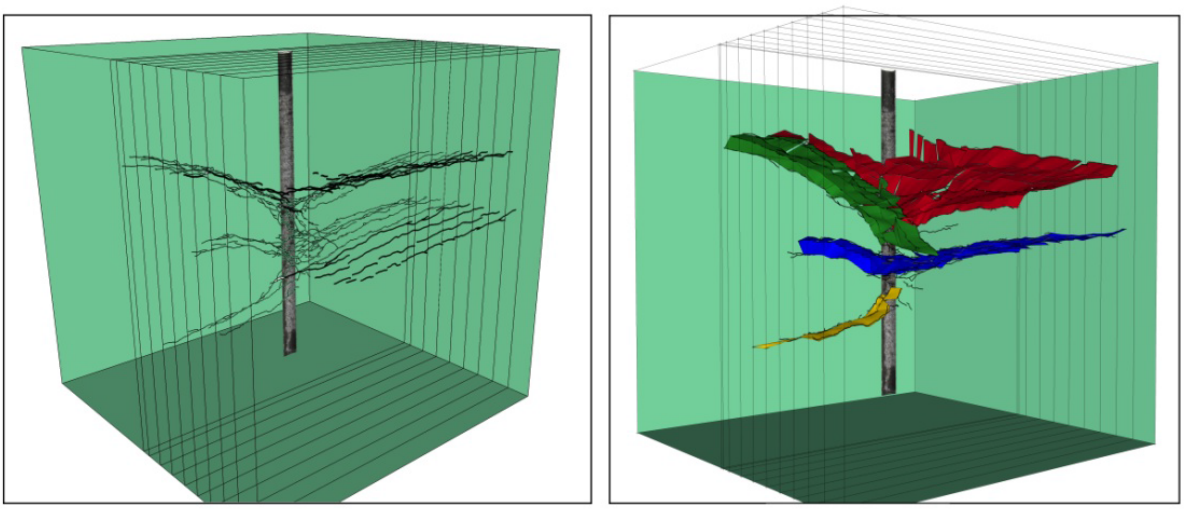

Figure 2.8: (Left) Demonstration of specimen's partition in thin sections to trace HF footprints. (Right) The 3D reconstruction of the equivalent fracture surfaces (from Kear *et al.*, 2013).

size, they might affect the brittleness/ductility of a formation which can be in some cases crucial for the treatment (Papanastasiou *et al.*, 2016).

2.3 Open problems

Although a lot of research has been done to model HF, several problems remain unsolved or unclear. Well established theories exist for the growth of a single 2D or axi-symmetric 3D HF in homogeneous media, however, in reality, the problem is much more complex due to existing heterogeneities in the host rock. Those heterogeneities can range from micro-structural defects such as micro-cracks, collapsing pores, or mineral composition and schistosity to large scale bedding planes, natural fracture networks, folds and faults. Some studies (*e.g.*, Warpinski and Teufel, 1987) tried to explain the way HF interacts with a single pre-existing fracture in 2D or pseudo-3D conditions. However, most of the experimental set-ups dealing with HF propagation are based on *post-mortem* tracing of the HF footprint (*e.g.*, Zhou *et al.*, 2008) while the various competing physical mechanisms have to be studied during the propagation (in order for example to examine which mechanism is dominant at each propagation step).

Moreover, when the problem includes multiple treatments from multiple wells, material anisotropy and multiple discrete fracture sets, changes in fluid rheology, proppant transport *etc.*, it becomes highly complex and of pure 4D (3D + time) nature. The prediction of HF propagation, interaction between HF and other pre-existing defects, final HF patterns and total stimulated volume requires the use of powerful 3D numerical models.

Several numerical techniques that have been used up to now for the modelling of HF propagation will be discussed in the following chapter.

Chapter highlights

- A lot of research has been carried out in HF propagation in homogeneous media and well-established theories have been built to describe it.
- HF propagation in naturally fractured rocks can be a very complex process. 4D information for its description is needed from both experimental and numerical studies.

Chapter 3

The role of natural fractures on hydraulic fracturing

Although in most of the applications HF takes place in tight, very low permeability, formations, considering the rock mass as homogeneous and impermeable might be a shortcoming. In reality, different kinds of discontinuities might exist in a reservoir. From single fractures or faults zones to networks of interconnected, or not, fractures or fractures corridors, every discontinuity can play a major role on HF propagation and thus on recovery optimization. Depending on their mechanical and hydraulic properties, orientation and chemical composition, natural fractures (NF) can enhance but also divert or even seal the propagation of the main HF.

Layout of chapter

The way NF are formed might be a good indicator of their importance on a HF treatment. Several mechanisms of NF genesis are explained in Subsection 3.1.1. The direct possible impact of NF on the hydraulic properties of rock-masses is detailed in Subsection 3.1.2. Finally, in Subsection 3.1.3, an introduction to the effect of natural fractures on HF propagation, as studied through different experiments, field work and numerical modelling, is presented.

3.1 Importance of natural fractures on hydraulic fracturing

Rocks, in large scales, are usually not intact but contain discontinuities. These discontinuities can be individual features but usually they form networks of fractures that can be either connected or not. Defects like these that exist before any man-induced loading are usually refered to as NF.

A NF can be open, closed, infilled, barren, rough or smooth. Generally, NF are characterized by a roughness. Roughness, depending on the type of the NF, can be the result of the asperities on each fracture lip following the rock fabric, or of bridges of cemented material or individual grains precipitated by fluids. It can modify drastically the fracture properties. Actually, roughness tends to increase the shear resistance of fractures as well as their compliance. On the other hand, the hydraulic aperture of rough fracture surfaces is lower than the one expected for a smooth fracture. Finally, it is due to roughness that even after extreme confinement, the aperture remains not null but reaches a limit value, the residual aperture.

3.1.1 Natural fracture genesis

In order to predict the NF's response under hydro-mechanical loading (such as the loading exerted by a propagating HF towards or close to a NF), the understanding of NF genesis is essential. NF may appear at many different scales due to several processes:

1. Physico-chemical process loading

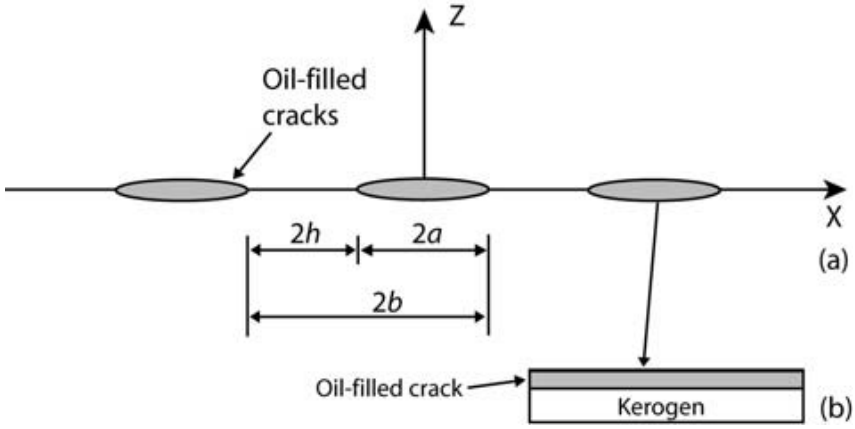

Figure 3.1: (a) Oil-filled microcracks, (b) micro-crack formation along the top edge of a kerogen lens (after Jin *et al.*, 2010).

Organic content maturation (hydrocarbon generation) has been a recognized factor for potential source of NF in source rocks (Comer and Hinch, 1987; Özkaya, 1988; Spencer, 1987; Swarbrick *et al.*, 2001; Vernik, 1994). In specific rocks, *e.g.*, shale, a large amount of organic content (kerogen) might be stored in lenses inside the low-permeability rock matrix. For a given set of conditions such as high temperature and sufficient time, the kerogen disolves and casts-off oil. Due to the low-permeability of the medium, oil creates pathways to migrate. These pathways are NF, formed by the coalescence of several micro-cracks. This is what (Kobchenko *et al.*, 2011) found while running an experimental campaign, using time resolved X-ray tomography, to investigate the mechanisms of fracture pattern development and fluid escape in a low permeability, organic rich shale under slow heating. Cracks start forming due to pressurization by the oil located in the lenses and coalesce to form a fracture network (see Figure 3.2) . According to the experiments, for very low permeability host rocks under low confinement, a fracture initiation criterion can be given as function of the kerogen lens:

$$\Delta P \left(\frac{2L_c}{h_k} - 1 \right) > \sigma_v \left(2 - k_0 \right) + T \tag{3.1}$$

L_c being the lens's characteristic length, h_k the lens's width, k_0 the lateral to vertical stress ratio and T the tensile strength of rock.

On the same line, (Fan *et al.*, 2014; Jin *et al.*, 2010) studied the problem of sub-critical fracture growth from kerogen maturation using finite difference models and showed how the temperature, phenomenon velocity and material properties affect the crack coalescence and the formation of macro-fractures. (Olson *et al.*, 2009) studied the sub-critical growth of NF in tight sandstones and (Kobchenko *et al.*, 2014) in elastic matrices, and found that propagation occurs even at very small extensional strains.

(Gale *et al.*, 2014) state that shales are generally diagenetically active (see illustration in Figure 3.3) and thus prone to seal fractures. However non-filled fractures of "possibly natural origin" have also been observed. In a recent study, (Alevizos *et al.*, 2016) claimed that at large depths and thus under large stress and temperature environments, there is a competition between two mechanisms. The viscoplastic deformation due to the in-situ stresses that tends to reduce the porosity of the formation, and a diagenetic fluid-release mechanism that tends to increase the porosity. In the case of very low porosity and large enough amount of diagenetic fluids - release, a periodical network of stress singularities

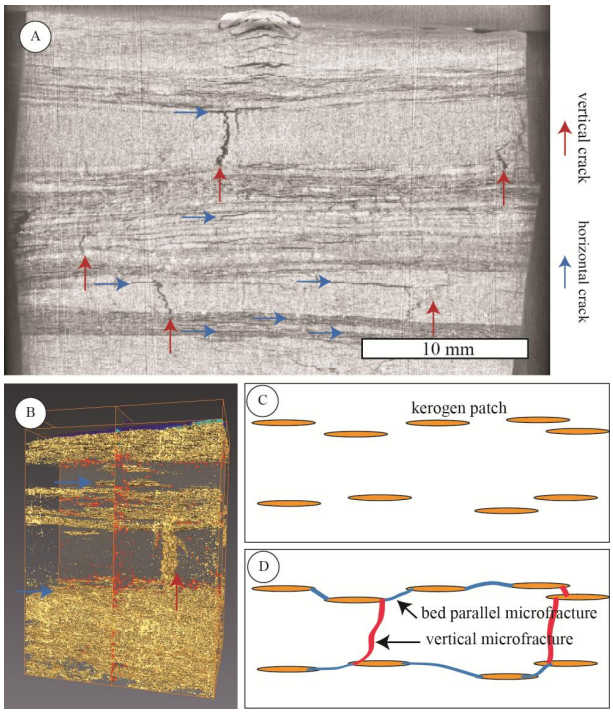

Figure 3.2: (a-b) Microtomography views of a shale sample after maturation at 390°C and differential stress for 24 hours in laboratory conditions. Bed parallel (blue arrows) and bed perpendicular microfractures (red arrows) for a 3D percolating network. (c-d) Conceptual diagram of the development of a 3D microfracture network and damage creation by the maturation of organic matter in shales (after Teixeira *et al.*, 2016).

lead to open cracks (channelling instabilities). The folowing critical condition for the onset of this structures as a function of the poromechanical properties was proposed:

$$\tilde{\lambda} = \frac{\dot{\epsilon}_n \mu}{\kappa p'_n} H^2 \geq \tilde{\lambda}_{cr} \tag{3.2}$$

$\tilde{\lambda}$ being the hydro-mechanical coefficient, $\dot{\epsilon}_n$ the loading strain rate, p'_n the volumetric mean stress, H the length of the reservoir in the compression direction.

In cases where the diagenetic fluid contains cement, or the $\tilde{\lambda}$ factor is low, the resulting fractures might be infilled (cementing) leading to compaction bands. In this case the composition of the filling material will play key role on the fracture plane strength. For example, (Gale *et al.*, 2014, 2008), have shown (for two different formations) that although calcite-filled fractures were sustaining half the strength of the rock matrix, on the other hand, quartz-filled fractures were stronger than the intact rock. So, based on their infilled material NF can be weakness planes of the formation or not.

2. Mechanical loading

   Changes of tectonic stress can cause large NF structures such as fault zones or folds. Fault zones result (in an idealistic configuration) from shearing relative displacement between two rock-blocks. Folds on the other hand are flexural deformations that may appear due to bending or buckling of a formation. (Murray Jr, 1968) reported NF networks in shales, as a consequence of shear bands close to faults or folds. En echelon NF patterns are commonly observed in fault's neighbourhood transverse to the fault plane. (Couples *et al.*, 2007; Wolfsberg, 1997) through numerical and physical modelling explained the formation of the observed vertical fractures at flexural opening in the syncline and anticline regions

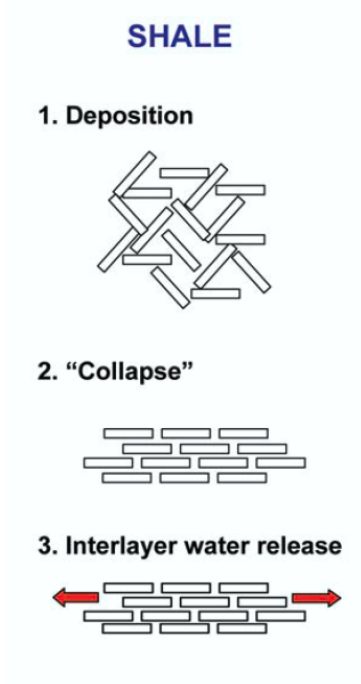

Figure 3.3: Effect of diagenesis in shale matrix (from Avseth *et al.*, 2003, modified).

of folds. Furthermore, in rocks that have been formed at large depths (*i.e.*, under high confinement), fractures might form when the rocks are uplifted, due to the stress release in the new, low-confined stress state (see Segall *et al.* (1990)). Subduction or uplift can lead to local pore collapse, or cause inhomogeneities to form fractures. Weak pores and other local imperfections are prone to propagate under local stress variation. These local imperfections can appear also at crystal level due to inclusions.

3. Thermal and fluid loading

   Thermal influx (or outflux) takes place due to formation submerge (or uplift), magma intrusion, during the creation of magmatic rocks or even because of the presence of radioactive materials. Under thermal loading, the grains or crystals undergo different volumetric deformations, based on their composition and structure, that might cause separation and thus micro-cracking (Browning *et al.*, 2016). Furthermore, trapped fluids in low permeability formations, or fluid-inclusions in minerals can initiate HF under pore-pressure raise or decrease of the confining stresses. Those HF or mini-HFs can form networks of NFs.

3.1.2 Hydro-mechanical effects

NF can play a significant role on flow in naturally fractured reservoirs (Bourbiaux *et al.*, 2005; Mäkel, 2007; Nelson, 2001; Ostad *et al.*, 2016; Sahimi, 2011; Stalgorova and Babadagli, 2012). From the study of different shale plays, it has been observed that most of the NF have apertures in the interval h=0.03 $\sim 7 \times 10^{-3}$ [m] (Figure 3.4). Considering flat fracture lips and Cubic law for unit width, that would mean that the minimum permeability of NF in shale is of the order of $\mathcal{O}\left(10^{-15}\right)$ [m^2]. Compared to a typical shale permeability of $\mathcal{O}\left(10^{-21}\right)$ [m^2], that would mean that the fractures show $\sim \mathcal{O}\left(10^{6}\right)$ times higher permeability than the matrix. Of course the comparison is only indicative and local since the length of the fractures varies from few centimetres to few meters (Gale *et al.*, 2014).

However, as mentioned before, the fracture walls are rarely smooth. In order to take into account the surface profile for the aperture calculation, the general idea (for a 2D configuration) is given by (Zimmerman and Main, 2004):

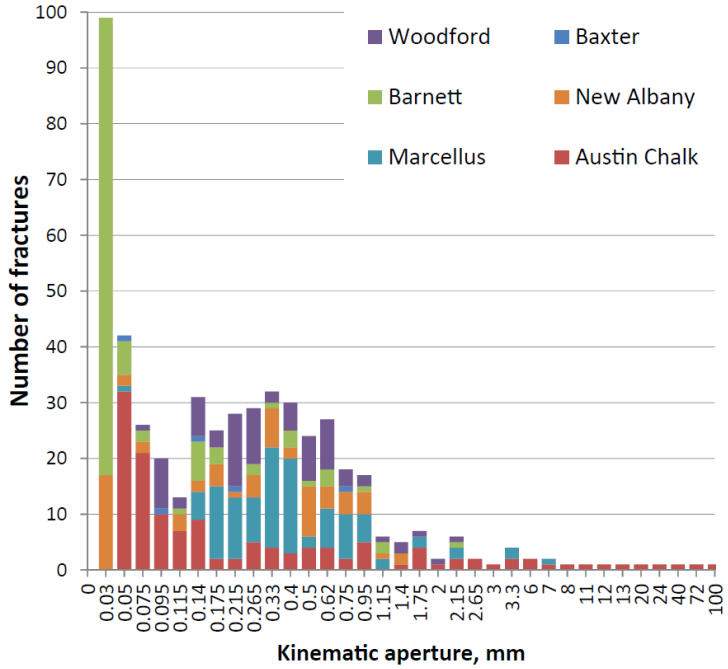

Figure 3.4: Distribution of apertures observed in gas shales (from Gale *et al.*, 2014, modified).

$$h_i(x, y) = h_0 - z_1(x, y) - z_2(x, y) \tag{3.3}$$

where, h_i is the initial (unloaded) fracture hydraulic aperture, h_0 is the equivalent aperture between the reference planes of a smooth fracture and z_1,z_2 two surface-height functions of the two fracture walls (see Figure 3.5). A lot of research has been done on defining these surface functions through homogeneous or self-affine statistical distributions (Adler and Thovert, 1999; Zimmerman and Bodvarsson, 1996; Zimmerman *et al.*, 1991).

Apart from the initial hydraulic aperture h_i, the coupled aperture of the fracture is controlled from the way the asperities and the cement-bridges and hard-grains inclusions affect the compliance of the fracture under loading (Tsang and Witherspoon, 1981). Several models have been proposed by to take into account fractures local geometry either statistically or conceptually in idealized situations (the reader is referred to the Chapter of Zimmerman and Main, 2004 for further information on hydromechanical behaviour of rock fractures.)

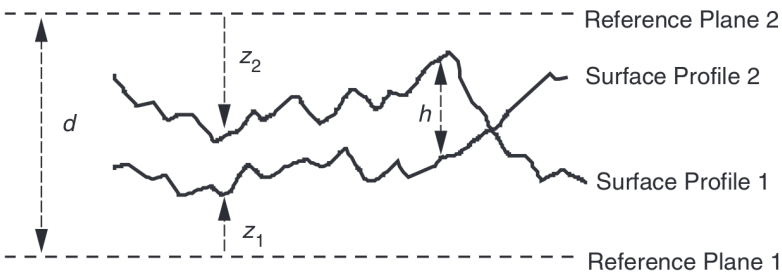

Figure 3.5: Aperture comparison between flat fracture walls and fracture walls with asperities (from Zimmerman and Main, 2004).

Connected NFs form networks which are, in most cases, the main path for flow in tight formations due to high permeability compared to the rock matrix, especially when the fractures

are open. Actually, a lot of research has been carried out on the representation of NF networks in the form of discrete fracture networks (DFN). DFNs can be generated stochastically or by assessing experimental data from loggings (Ostad *et al.*, 2016). Many researchers focused on percolation indexes, topology and their effect on permeability (Dreuzy *et al.*, 2010; Le Goc *et al.*, 2010). (Sarris and Paleologos, 2004) conducted Monte Carlo simulations to study the effect of stratification on permeability while (Lang *et al.*, 2014) used a FEM-DFN scheme to asses the permeability tensor in medium containing DFNs of various topologies. Apertures are usually following self-similar or self-affine distributions and locally they can result in conduits or bottlenecks (Dreuzy *et al.*, 2012). The effect of the aperture upscaling and also the way it is affected by the temporal stress field is believed to play an important role on the network's connectivity (Jiang and Younis, 2015; Klimczak *et al.*, 2010; Lei *et al.*, 2015)

Due to the high complexity of the networks, the vast amount of discontinuities, and variety of length-scales involed, the computational cost can be very high (Jiang and Younis, 2015) and in some cases prohibiting for extensive studies. At the same time, the interaction of HF with single NF is not completely understood and/or fully captured yet. It is thus essential to explain the key mechanisms controlling the frackability of a formation containing NFs. The next section aims at explaining the effect of a single NF on progressive failure due to HF propagation and on the overall response of the system.

3.1.3 Hydraulic fracturing and natural fractures

Since NF networks seem to be very important for the optimization and controllability of the stimulated volume, it is of primary importance to investigate first how single defects can affect HF propagation. It is more and more generally accepted that NF, even the sealed ones, affect HF propagation and the SRV (Fischer *et al.*, 2002; Gale *et al.*, 2014). Thus, the key mechanical and hydraulic parameters controlling the HF-NF interaction should be well identified and studied in order to enhance the SRV of a reservoir. For example, there have been cases where, NFs enhanced the productivity of the shale (Curtis, 2002) and cases where, due to their orientation, NF have sealed and stopped the HF or led to a segmented shorter HF than in the intact rock (Gale *et al.*, 2014, 2007). So, stress-field anisotropy and HF-NF angle (or, angle of approach) should be taken into account while studying HF-NF interactions

Also, open, persistent NFs in some cases capture the HF fluid and stopped the HF growth (*i.e.*, decrease of productivity). That would mean that high permeability - high storage capacity of the NF can be a barrier for the HF growth. Furthermore, although horizontal NFs are typically sealed and cannot provide permeability enhancement or storage (*e.g.*, in Vaca Muerta formation), if the cemented plane is thin, they can act as planes of weakness during treatment and arresting the HF growth in favour of horizontal reactivation. On the other hand, the cement layer is thick enough, it may stop the vertical growth of the HF (barrier) (Gale *et al.*, 2014). Thus, NF shear strength is an important parameter for the HF-NF interaction and so is the plane toughness. Another possible parameter could be the relative size of NF compared to HF according to (Bahorich *et al.*, 2012).

In order to quantify the effect these parameters on HF growth, several laboratory and numerical studies have been carried out. Most of them are based on the pioneering work of (Warpinski and Teufel, 1987). The typical classification for HF-NF interaction in this type of studies refers to "crossing", when the HF crosses the NF, "dilation" when the HF opens the NF and tends to re-initiate from the NF's tips and "arrested" when no re-initiation or crossing is observed until the end of the test (see Figure 3.6). Plane shear strength is believed to be a key parameter for shear reactivation of NF (Dahi-Taleghani, Olson *et al.*, 2011). (Zhou *et al.*, 2008) conducted lab experiments to investigate the influence of shear strength of NF on HF propagation behaviour for varying differential stresses (Set up sketch in Figure 3.7). The authors found that besides the influence of stress-anisotropy and angle of approach, shear strength of NF was influencing the propagation. NF with higher shear strength, are more prone to arrest. Crossing is mostly

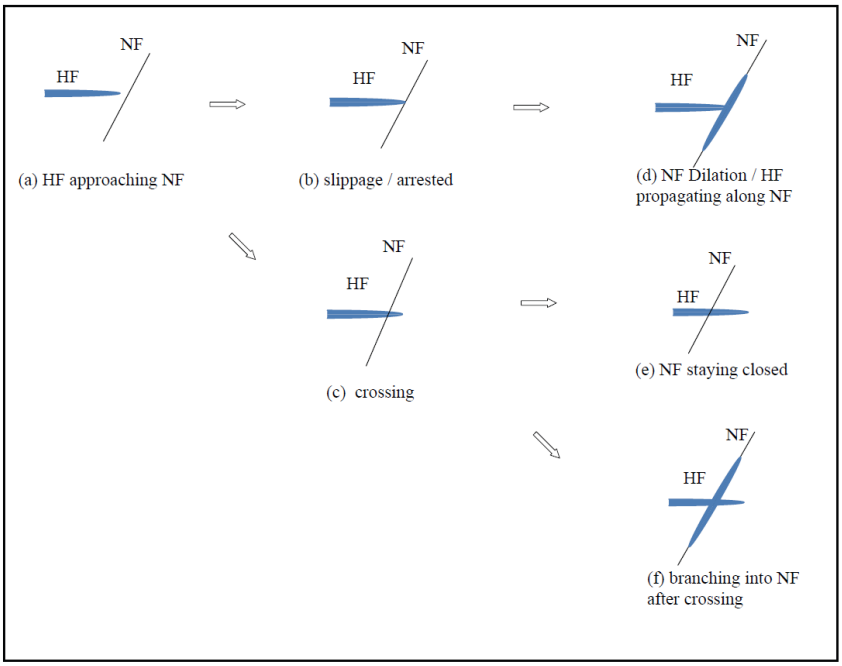

Figure 3.6: Classification of the different types of HF-NF interactions (from Gu *et al.*, 2012).

observed for low NF apertures, and dilation is more dominant behaviour for larger apertures. (Zhao and Paul Young, 2011) repeated the experiments numerically also for varying approach angles and obtained similar results. However, the third dimension of the problem could give interesting insights that are hidden in 2D models as suggested by (Damjanac and Cundall, 2015). (Guo *et al.*, 2015) in another numerical study, investigated the effect of the same parameters at a larger scale. They concluded that the smaller the approach angle and differential stress are, the easier it gets for NF to initiate and propagate. Several other criteria exist in the literature such as the one proposed by (Liu *et al.*, 2015, see Chapter 8).(Gu *et al.*, 2012) also found that a HF is more likely to diverge and propagate along a NF (instead of crossing it) when the approach angle is smaller than 90 degrees.

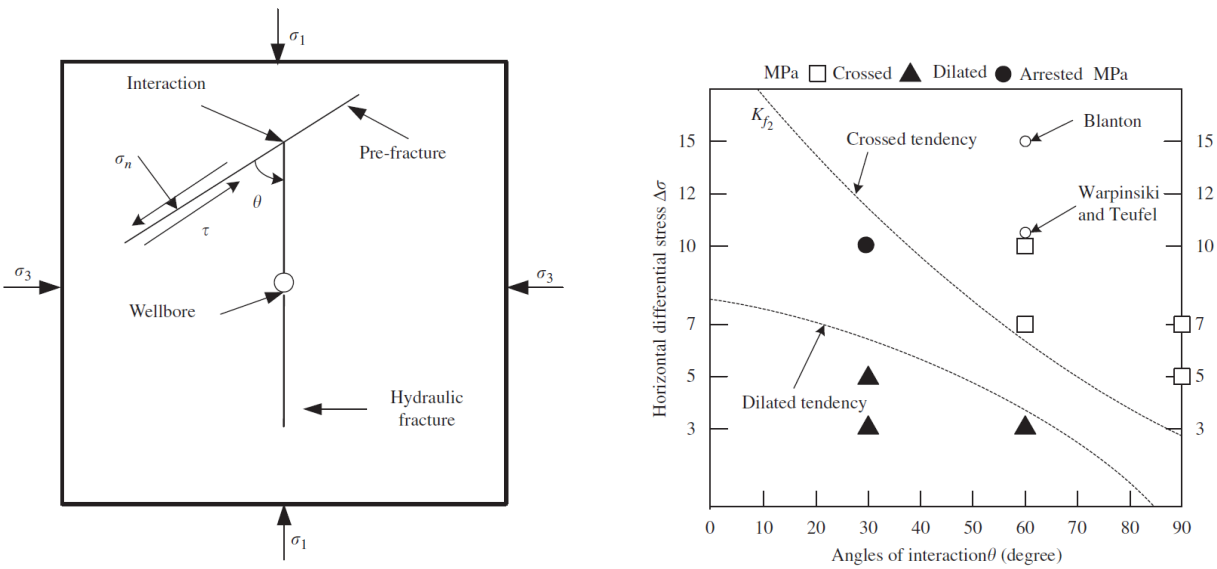

Figure 3.7: ((Left) Sketch of an experimental setup used to study HF-NF interaction for a single NF and (Right) results interpretation based on the type of interaction observed (from Zhou *et al.* (2008)).

Finally, (Chuprakov *et al.*, 2014)investigated the effects of the injection parameters, namely injection rate Q and fluid viscosity μ on the interaction. They observed that these parameters are of first order importance for the crossing. Their findings were in agreement with several experimental campaigns' results such as the ones by (Blanton *et al.*, 1982; Warpinski and Teufel, 1987).

Chapter highlights

- Reservoir rocks are seldom naturally fractured. The origin of these natural fractures scales from coalescence of diagenetic fluid created micro-cracks to large tectonic faults.
- The hydraulic properties of the natural fractures can vary depending on the type of the natural fracture (or the network), the origin, intensity, connectivity and the infilling material. They can be conduits for the fluid flow or barriers.
- The impact of the natural fractures on the HF growth and on the final stimulated volume is of high importance. Depending on their hydro-mechanical properties, connectivity, size distribution and orientation they can enhance the total SRV or decrease it. Their impact has to be explicitly taken into account in HF modelling.

Chapter 4

Existing tools for hydraulic fracture modelling

On Chapter 2 it was stated that the use of hydraulic fracturing as a stimulation technique dates several decades back. Also, it was shown that it is a 3D highly complex process with a large number of unknowns. Those facts led to the need for the development of efficient tools to model the problem of HF. In this chapter, an overview of the different methods that have been used up to now to simulate rock failure, hydro-mechanical coupling and finally hydraulic fracturing is presented to the reader. Each method has its own advantages, disadvantages and limitations. By the end of the chapter, the trending problems in HF modelling are listed.

Layout of chapter

This chapter is a state of the art on different models for the simulation of hydraulic fracturing that already exist. In order to get there, the chapter is divided in three sections presenting types of existing models and ends up with open problems that new models have to face.

On the first section, different models dealing with the simulation of progressive failure of rocks are presented. The differences are mainly laying on how the rock is treated *i.e.*, as a continuum or as a discrete medium and how the fractures propagation is modelled within it.

Then, different hydro-mechanical strategies are presented along with their pros and cons. The way different schemes are coupled can provide access to different phenomena taking place at different scales and under different regimes. Emphasis is also put on the computational effort of each method since multi-physic couplings can increase tremendously the calculation cost.

The last section details how, some of the aforementioned models and coupling schemes have been combined in order to deal with HF modelling and discuss their contribution to the field. The chapter ends with a list of ongoing open problems and possible approaches to solve them.

4.1 Progressive failure modelling

The logical first step in an attempt to reproduce a realistic HF process, would be the representation of progressive failure/breakdown of rocks and rock masses. Thus, the numerical approach should be capable of simulating adequately the deformation of rocks under mechanical loading and their progressive failure. Furthermore, realistic rock mass modelling should include pre-existing fractures or fracture networks as they are seldom found in nature (see Chapter 3). The combination of the rock's and pre-existing fracture's properties and the constitutive laws that govern their behaviour under a given loading path will predict whether the breakdown will be driven by sliding on the fractures or from fracturing of the intact part of the rock in between

them (also called a rock-bridge). Different loading paths can result in completely different final failure patterns.

The progressive failure in brittle or quasi-brittle rocks is usually driven by pre-existing defects at the micro-scale. The micro-cracks or the collapsed pores connect during the loading and they gradually form fractures that dictate the macroscopic behaviour of the rock. On the other hand, from a macroscopic point of view, the progressive failure in rocks can be seen as a non-linear behaviour generally associated to volumetric dilatancy (the reader is referred to Paterson and Wong, 2005 book for a detailed and complete description of brittle failure in rocks). In cases where the formations are weak, highly porous rocks, where the distinction between cracks and pores is hard, the model should adequately represent the formation of strain localization patterns (shear and compaction bands) rather than fracture patterns (see *e.g.*, Tengattini *et al.*, 2014).

There exist several approaches for modelling the progressive failure in rock-masses. Some of them are: analytical methods focusing on single defects, numerical continuum methods focusing on single defects, numerical continuum methods using damage laws and numerical discrete methods.

Analytical methods focus on single discontinuities such as existing micro-defects (*e.g.*, micro cracks), usually modelled for simplicity as lines, circles or ellipses in 2D or planes, spheres and penny-shaped ellipsoids in 3D. The stress and strain fields are computed around the defects by considering elasticity and Airy functions or conformal mapping (Exadaktylos and Stavropoulou, 2002; Muskhelishvili, 1966; Muskhelishvili and Radok, 2008). According to the stress concentration at the periphery of these defects, fractures can propagate under Mode-I,II or III based on the LEFM criteria. Mode I propagation causes a crack propagating parallel to the major principal stress while Mode-II causes sliding. The combination of the two modes creates subvertical curved wing cracks which can wrap around the defect in combination with an anti-plane Mode-III propagation (see Cannon *et al.*, 1990; Dyskin *et al.*, 1999; Wong and Einstein, 2009). As mentioned before, analytical solutions applied on single defects have a rather narrow domain of application in very idealized problems. Though they can give clear insights in some cases. For example the spalling effects on circular openings along with the transition from stable to unstable state was well captured in the framework of discrete fracture growth (Germanovich and Dyskin, 2000). Furthermore the solutions might be used in continuum numerical models that take into account microstructural defects (*e.g.*, Exadaktylos, 2010) and/or discrete large-scale defects.

In general, models focusing on single fractures seem to be adequate in pre-peak regime to predict non-linear behaviour of rocks, strain hardening behavior for the axial propagation of the wing cracks and strain softening behavior between cracks (Yuan and Harrison, 2006). On the other hand, when it comes close to the peak strength regime, analytical models for single defects cannot capture the localization phenomena. Even if the interaction between the existing cracks, intersecting or not, is described (Exadaktylos, 2010), coalescence of cracks and new cracks cannot be described by these models.

On the other hand numerical continuum damage methods (CD), instead of examining explicitly the predefined micro-cracks, deal with the progressive failure as an impact of the micro-cracking on the constitutive behaviour of the continuum. This impact is taken into account as an internal variable in the constitutive law. Different approaches have been implemented in CD method. Some of them are based on multi-scale mechanics, using the concept of representative elementary volume (REV). The damage evolution is analysed at the small-scale (micro or meso-scale) and using a homogenization (*e.g.*, periodical, self-consistent or numerical) technique, it is upscaled to the constitutive law in the macro-scale (Argilaga *et al.*, 2016; Maghous *et al.*, 2008; Pouya and Ghoreychi, 2001; Van den Eijnden *et al.*, 2016; Zhang *et al.*, 2012). Some approaches account for damage internal variable as calibration parameter to experimental data while others as a micro-mechanically justified state variable up-scaled in a thermodynamically consistent framework (Borst, 2002; Shao *et al.*, 2006; Swoboda *et al.*, 1998; Swoboda and Yang,

1999; Tengattini *et al.*, 2014; Zhao *et al.*, 2004). Numerical tools for incorporating these theories can be conventional FEM,FVM,FDM methods when the problem in the REV can be directly homogenized (Argilaga *et al.*, 2016) or more advanced numerical techniques such as FEMxFEM or FEM^2 (Van den Eijnden *et al.*, 2016), where the constitutive law needs to be homogenized numerically, material point method (MPM) for capturing large deformations (Tengattini *et al.*, 2014) or enhanced-FEM (EFEM) for taking into account fracturing in REV without the need of heavy meshing or re-meshing (Roubin *et al.*, 2015). Finally, phase-field methods such as (Nguyen *et al.*, 2016) are currently developed and seem to be promising in the topic of progressive failure.

To conclude, CD methods are able to reproduce adequately enough the macroscopic progressive failure of rocks, at least in a quantitative way (see Figure 4.1). There exist models like (Shao and Rudnicki, 2000) that can treat crack coalescence or (Bui, 2010; Kuhl *et al.*, 2000) that can describe post localization softening responses, using gradient enhanced damage formulation in order to keep the boundary problem well-posed after the bifurcation point. The main disadvantages of CD methods lay in the amount of unknown variables that have to be defined at the micro-scale (or meso-scale). Furthermore, some of the state-variables require very specialized experimental set-ups (*e.g.*, X-Ray Tomography) in order to be properly defined. Finally, some of the numerical, multi-scale techniques needed for capturing the correct large-scale response of rocks are still computationally expensive. In addition, introducing pre-existing fracture networks in these model, would significantly increase the computational effort due to heavier meshing needed or special discontinuity elements.

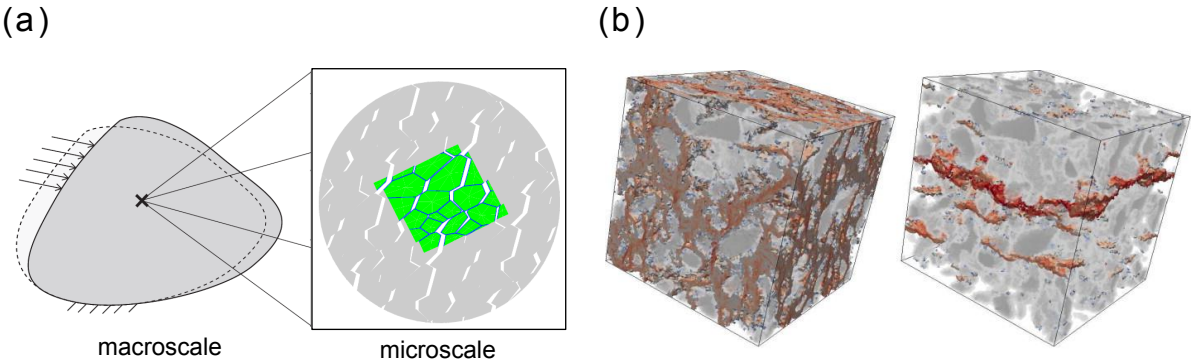

Figure 4.1: (a) Sketch of progressive failure concept starting from micro-cracking between grains in the REV using FEM^2 (from Van den Eijnden *et al.*, 2016, modified) and (b) crack propagation between aggregates of a single REV using EFEM (from Roubin *et al.*, 2015)

.

In recent years, numerical discrete models have been very popular for tackling rock-mass progressive failure problems. Several different discrete models are nowadays available which share very similar principles. The problem's domain is decomposed into discrete bodies such as blocks or polyhedra (Itasca, 2013) in the distinct element method, discrete triangular finite elements (Mahabadi *et al.*, 2012; Software, 2003) or in the combined FEMDEM method, spheres,disks or beams (D'addetta *et al.*, 2002; Itasca, 1999; Kozicki and Donzé, 2008, 2009; Potyondy and Cundall, 2004) in the discrete element method (DEM) and lattice element method (LEM) respectively. Each element is connected to its neighbouring ones through inter-particle bonds. The constitutive law is then defined locally, at the contact of the discrete bodies, to describe their interaction. If the local loading exceed a threshold which corresponds to the bond's strength, the bond breaks and a crack forms. The displacements of the crack lips is then governed from the relative movement of the neighbouring elements. In order to study the progressive failure of rocks (Hazzard *et al.*, 2000; Hazzard and Young, 2000) and later (Potyondy and Cundall, 2004) proposed the so-called bonded particle model (BPM). Although the BPM is able to reproduce

realistic macroscopic failure patterns the model's response can diverge from realistic rock like behaviors due to the use of spherical elements. As an attempt to enhance spherical DEM capability in terms of rock modelling, (Scholtès and Donzé, 2013) proposed a model that takes into account DE interlocking. The model gives similar failure patterns for different size distributions of DEs and also allows for non-linear failure envelops as well as high values of compressive to tensile strength ratio. Other approaches have proposed such as the combined FEMDEM (*e.g.*, Lisjak *et al.*, 2014; Mahabadi *et al.*, 2014) or the distinct element method (Chen *et al.*, 2016; Kazerani and Zhao, 2010). Whatever the approach (spherical or polyhedral elements, explicit or implicit formulation),the discrete numerical methods can describe progressive failure due to crack initiation and nucleation (see Figure 4.2) as well as crack opening and closure, without the need of special enhancement techniques.

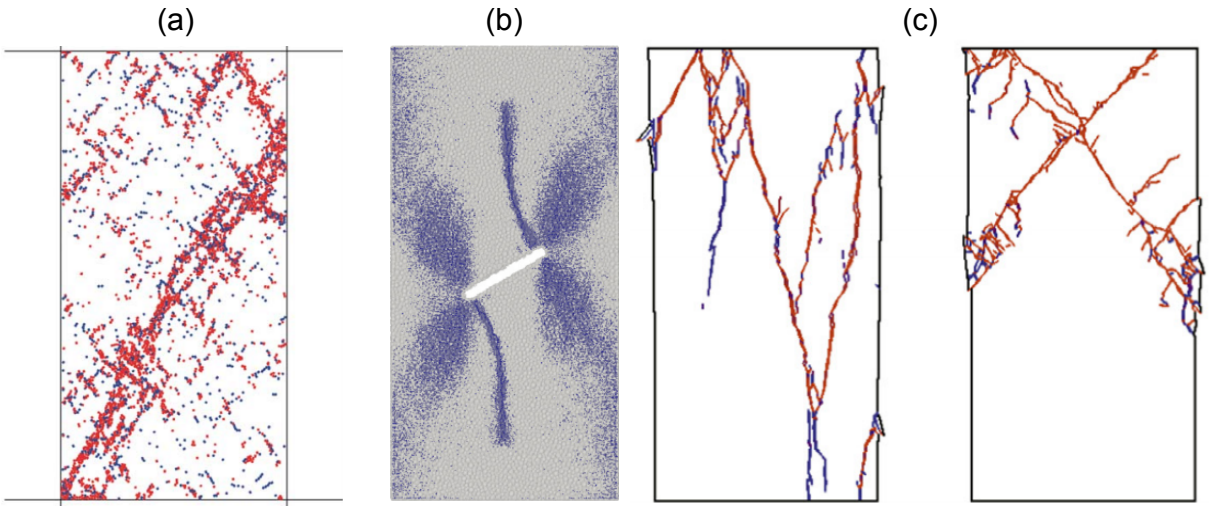

Figure 4.2: (a) BPM - rock specimen crack-localization pattern at failure (from Potyondy and Cundall, 2004) , (b) Wing crack propagation from an open flaw in a BPM rock specimen (from Duriez *et al.*, 2016 and (c) failure patterns for two cases of anisotropic FEMDEM rock (from Lisjak *et al.*, 2014).

Furthermore, energy released from crack events can be directly translated into micro-seimicity by clustering crack events happening at the same time (Hazzard and Young, 2000; Lisjak *et al.*, 2013). This is an important feature which can give a lot of information while comparing simulations to field-case data or lab-experiments.

Finally, adding a deterministic or a stochastic discrete fracture network (DFN) to discrete models is straightforward and enables to capture the break down of naturally fractured rocks-mass, including plane slipping and intact rock fracturing (Harthong *et al.*, 2012; Lisjak *et al.*, 2015; Mas Ivars *et al.*, 2011; Scholtès and Donzé, 2012). On the same basis (adding structural components to the models), discrete methods can reproduce anisotropy emerging from different scales, such as structural anisotropy and and larger scale natural fracture network (Carol *et al.*, 2004; Lisjak *et al.*, 2014).

Overall, discrete models seem to be able to describe progressive failure of rocks in a logical sense according to observations. In particular, DEM and FEMDEM methods can reproduce fracture propagation, creation of new fractures and fracture coalescence along with their interaction with existing fracture networks. They can describe localization initiation and post localization behaviour with no need for enhancement techniques in order to keep the macroscopic response well-posed. Furthermore, the macroscopic dilation and opening/closure of cracks is emerging as a physical response of the system without the need for the introduction of internal variables. Finally they can provide information about micro-seimiscity during the progressive failure.

On the other hand, the main drawback is the need of extensive calibration for setting up the correct local mechanical parameters that described a specific rock. The computational cost was high in the past years, especially for 3D models with non-spherical DEs. However, nowadays,

with the use of parallel and massive parallel computing (OpenMP,MPI,GPU) the modelling of dry rocks consisting of thousands or millions of particles is acceptable. On the contrary, due to the explicit numerical algorithms that are usually applied, the simulated (virtual) time is conjugated to the timestep and might be restrictive for very long term tests.

Considering the advantages and disadvantages of the different modelling techniques, the analytical methods focusing on single fracture propagation seem to be robust and not expensive in computational time, since they are based on closed form analytical or semi-analytical equations, and they can also reproduce macroscopic dilatancy. On the other hand, the existing techniques cannot reproduce the post localization behaviour, the creation of new cracks and the coalescence of pre-existing fractures due to propagation, features of great importance for what concerns hydraulic fracturing. CD models, can reproduce adequately the macroscopic behaviour of a rock-type medium, even in post localization regime, but the quantification of the internal damage parameters can be difficult or restrictive in most of the cases. Furthermore the numerical techniques needed to keep the problem well-posed or to account for single macroscopic defects or the damage description at the micro-scale can be prohibitively computationally costly.

On the other hand, the progressive failure mechanisms are naturally tackled by discrete numerical methods. They can reproduce both non-linear macroscopic behaviour of the medium, dilation, creation and coalescence of cracks and they are also able to take into account DFN without the need of special numerical treatment or enhancement. Also, they can provide information such as micro-kinematics or micro-seismicity that can be confronted to full-field lab experiments and field data. The computational cost of the method is it's main drawback due to the nature of the time-explicit schemes used. Also, the total number of elements has to be restricted in hundreds of thousands to few millions of elements (thus assumptions should be made in terms of rock's morphology for the large scale simulations). Finally, the calibration procedure can also be a disadvantage, since a number of preliminary tests should be run to ensure the desired macroscopic mechanical response of the medium.

4.2 Fluid coupling schemes

The need to model transient effects in the rock-mass, especially, the variation of pressure and fluid flow through existing voids and induced faults, has naturally led to the development of hydro-mechanically (HM) coupled models. Coupled HM models should be able to examine two main "sub-fields" of the hydraulic fracturing problem:

1. The influence of the pressure and viscosity of the fluid stored in the HF on the fracture propagation and thus on the progressive failure of rock.

2. The influence of a pre-existing set of fractures and of fracture propagation on the fluid leak-off and on the effective permeability of the medium.

Concerning the fluid flow in fractured media, semi-analytical solutions have been established for steady state fluid flow in saturated porous medium with a single fracture or a medium with a set of pre-existing curvilinear fractures (Exadaktylos, 2012; Liolios and Exadaktylos, 2006). Similar solutions could then be used through upscalling techniques (Pouya, 2012; Pouya and Ghabezloo, 2010) for the macroscopic description of flow in 3D isotropic or anisotropic infinite media containing cracks. Specific models for the transient flow in single propagating fractures in elastic or poroelastic solids have been established based on the fracture-tip asymptotics in the extensive work of (Desroches *et al.*, 1994; Detournay, 1999, 2004; Detournay and Cheng, 1991; Garagash and Detournay, 2000; Kovalyshen, 2010; Peirce and Detournay, 2008; Savitski and Detournay, 2002).

The main drawback of this kind of HM coupled models is due to the fact that they cannot capture fracture coalescence. Thus, the analytical or semi-analytical solutions that describe the

changes in fracture aperture (based on fracture growth and opening) and thus, the changes in fluid flow, are based on the assumption of constant crack density without taking into account the effect of crack coalescence (Yuan and Harrison, 2006).

Numerical continuum methods such as conventional HM-FEM models with additional nodes per element to deal with the flow problem seem to face difficulties even for a single fracture propagation. The need for re-meshing with heavy, coupled elements makes the problem computationally heavy.

On the other hand, HM-CD coupled models such as the ones proposed by (Souley *et al.*, 2001; Tang *et al.*, 2002), consider the effective permeability as an internal state variable which increases as damage increases. This holds true for low porosity rocks but might not be the case (especially in weak, porous rocks) when pre-existing fractures or micro-fractures close due to damage. In addition, HM-CD models lack in the representation of dilatancy and the effect of confining pressure on the failure patterns, both phenomena being related to permeability (Yuan and Harrison, 2006).

Regarding discrete numerical techniques, HM-DFN models have been widely used to study fluid flow in massively fractured systems in both at the macro scale (Maillot *et al.*, 2014) and at the REV scale (Alain and Vincent, 2004; Baghbanan and Jing, 2008; Lang *et al.*, 2014; Min *et al.*, 2004a; Ren *et al.*, 2015). However, HM-DFN models are restricted to flow in predefined paths and don't take rock-fracturing into account.

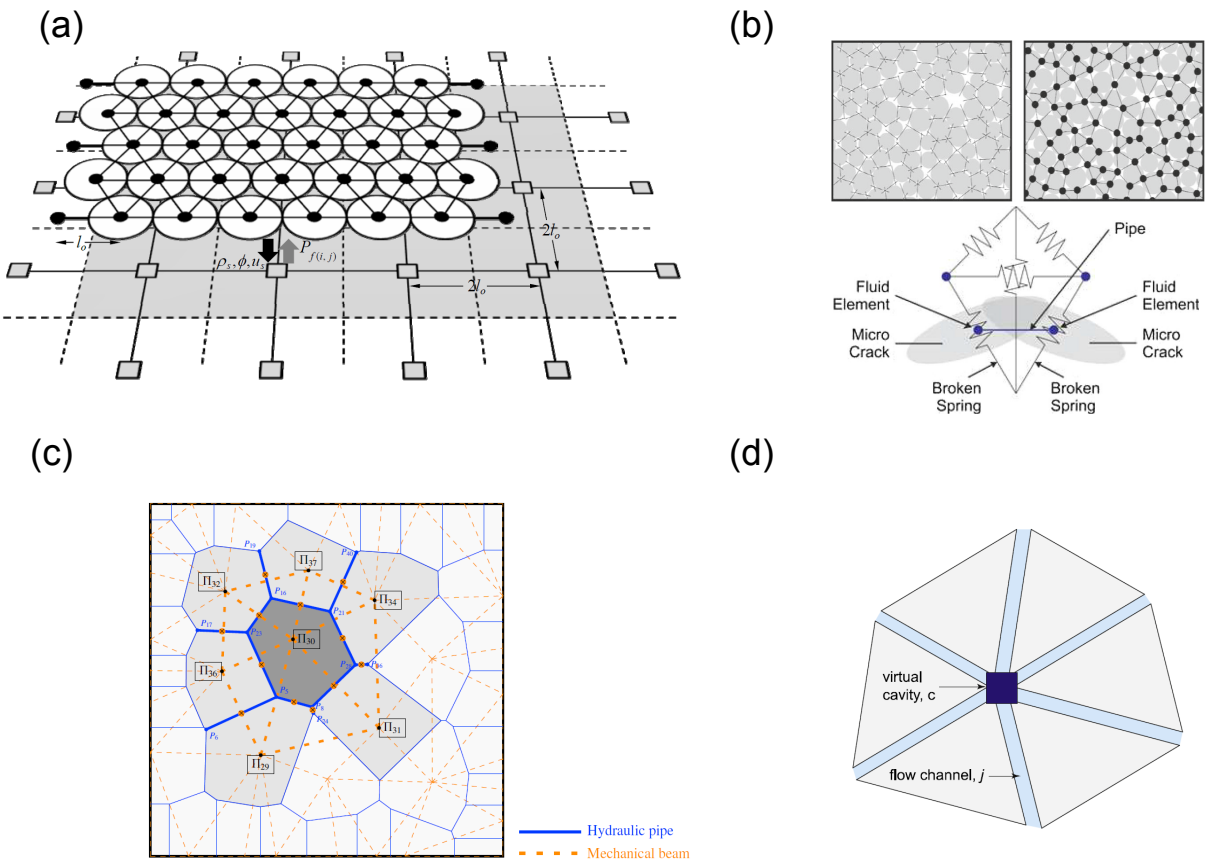

Figure 4.3: Examples of different discrete HF simulators' coupling: (a) Superimposition of the discrete elements on a continuous (LB) fluid domain (from Boutt *et al.*, 2007), (b) DEM with dual pipe network (from Damjanac and Cundall, 2015, (c) LEM with dual pipe network (from Grégoire *et al.*, 2016), (d) FEMDEM with dual pipe network (from Lisjak *et al.*, 2017)

.

For this reason, hybrid HM models are used more and more often. (Latham *et al.*, 2013) for example used the combined FEM-DEM method to model the influence of stress regime on

permeability, taking into account fracture network and fracture propagation. In their approach, cracks can be connected or they can coalesce during loading due to fracture propagation and changes in permeability can be observed due to fracture bending. However, the model presented works in 2D plane strain mode and doesn't take into account the poroelastic effects and the fluid pressure in the fracture. (Boutt *et al.*, 2007) used a hybrid Lattice-Boltzmann (LB) DEM approach (DEM for solving the solid mechanics problem and LB method to solve the fluid mechanics problem) to investigate the hydraulic fracturing process in 2D porous media. By means of the LB-DEM, the strong coupling of largely deforming materials was described without assumptions such as Darcy flow and effective stress.

Although several studies have shown that using Navier-Stokes equations (as for example in the case of LB method) is powerful and robust for fluid flow in coupled models, the computational cost makes it prohibiting for simulations of big number of particles and large contrast in scales. Another model, developed to deal with HM coupling in porous media, taking into account pore-scale effects and at the same time reducing the computational cost by considering Darcy flow, was presented by (Catalano *et al.*, 2014; Chareyre *et al.*, 2012). The model being based on a hybrid Pore-scale Finite Volume (PFV)-DEM (DEM for the simulation of the solid and PFV for the darcy flow of the pore fluid) has been verified against Navier-Stokes solutions for a given porous medium. The use of inter-element space as a fluid volume network discards the need for a second grid superimposition. Similar models can be found in more discrete-coupled models such as DEM with coupled flow-pipe network (Damjanac and Cundall, 2015), LEM with dual pipe network (Grégoire *et al.*, 2016), distinct-element method with finite difference grid for the fluid flow (Itasca, 2013), FEMDEM with dual pipe network (Lisjak *et al.*, 2017). Illustrative examples of the couplings are shown in Figure 4.3. Specifically for HF simulations, the use of the dual space between the elements (discrete, distinct, finite-discrete or lattice elements) for the fluid flow has two direct main advantages: (i) there is no need for additional meshing for the fluid coupling since all the geometrical quantities are described by the solid domain (ii) the HF evolution can be naturally captured without the need of remeshing (it will only be needed in the case of very large deformations).

4.3 Hydraulic fracture modelling

In the following, some of the most well-known models applied to hydraulic fracturing are presented and discussed. The most common methods used for HF modelling are based on the framework of LEFM criteria for fracture propagation. The KGD and PKN planar HF assumptions have become classical (Geertsma, De Klerk *et al.*, 1969; Perkins, Kern *et al.*, 1961) along with the penny-shaped crack solutions based on the radial pressurized crack problem (Green and Sneddon, 1950; Sneddon, 1946) shown in Figure 4.4.

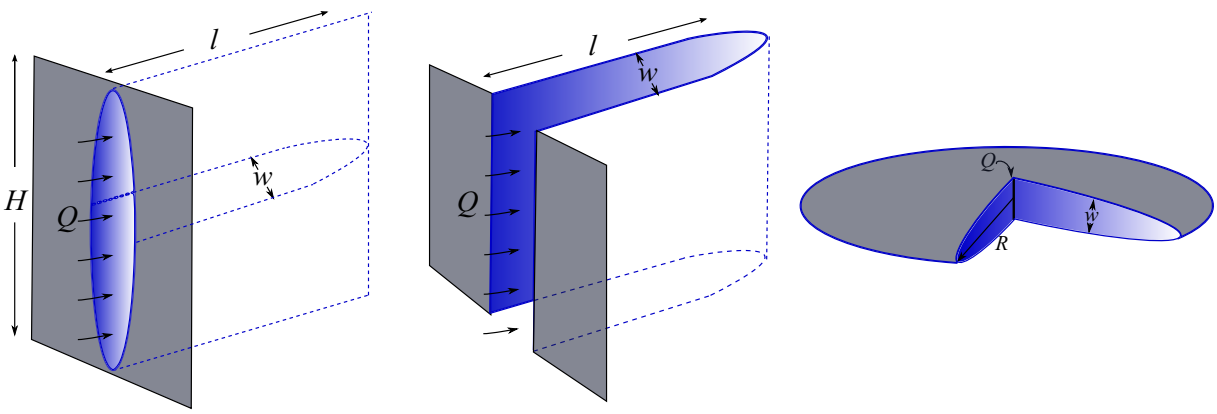

Figure 4.4: Sketches of PKN (Left), KGD (Centre) and Radial penny shaped HF concepts.

These models consider a single planar HF growing in a homogeneous elasto-brittle medium under a growing internal pressure. The opening of the HF is calculated through elasticity non-local integral solutions such as the one by Sneddon, 1946. The viscous fluid flow is usually described by Reynolds equation assuming a Poiseuille flow and taking into account the total mass balance. The leak-off from the fracture to the host rock is described traditionally by Carter's model. Finally, the propagation criteria are based on the fracture toughness of the medium and the SIFs. Different time-scales and length-scales can be introduced based on semi-analytical solutions (see *e.g.*, Bunger *et al.*, 2005; Detournay, 2004; Kovalyshen and Detournay, 2010; Savitski and Detournay, 2002) to deal with specific regimes of propagation. In order to track the HF front, specific techniques have to be considered (Peirce and Detournay, 2008).

However, although these models are robust and precise, the main restriction lays in the fact that they can describe very specific idealized scenarios, media with homogeneous elastic properties and perfectly elasto-brittle behaviours. However, due to their precision they are currently the best applicants for benchmarking tests for numerical models.

In an attempt to study the fully 3D problem, Pseudo-3D (see *e.g.*, Dontsov and Peirce, 2015) models and Planar 3D models that can take into account multiple horizontal layers of different elastic properties were also used (Advani *et al.*, 1990; Siebrits and Peirce, 2002). These models are not as computationally expensive as other methods (see below). However, they were still built under many important assumptions such as homogeneous elastic properties on each layer (see Figure 4.5).

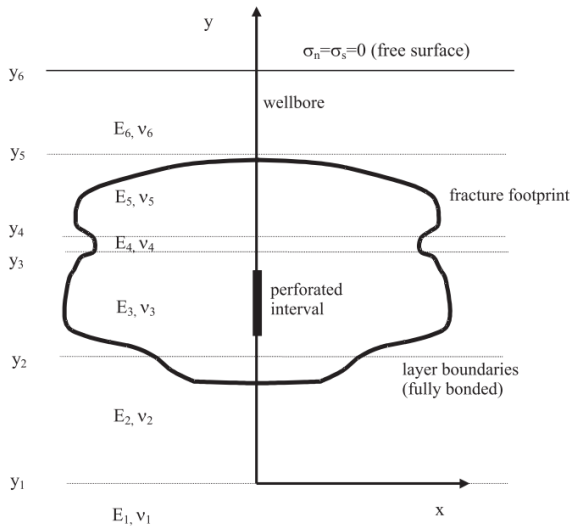

Figure 4.5: Example of a planar-3D model HF propagation in multiple horizontal layer of different elastic moduli (from Adachi *et al.*, 2007).

Other complications related to HF design within the LEFM framework might be (Adachi *et al.*, 2007):

1. The presence of different rock layers (usually not parallel to each other).
2. The existence of a natural fracture network in the reservoir.
3. The possibility for the HF to be non-planar and prone to branching effects.
4. Changes in magnitude/orientation of the in-situ confining stresses caused by surrounding wells or other poroelastic effects.
5. The relatively oversimplified models for the fracturing fluid rheology. The fluids are usually considered to behave as power-law fluids. The effects of shear and temperature on the

fracturing fluid rheology are not taken into account (viscoelasticity or yield stresses for actual fracturing fluids neglected).

6. The leak-off of the fracturing fluid into the surrounded rock.

7. The transport of suspended proppant particles.

8. The modelling of fracture recession and closure.

Adaption of the LEFM criteria in coupled FEM (Ouyang *et al.*, 1997), FDM / FVM (Zhou and Hou, 2013) and BEM (Hossain and Rahman, 2008) was a step forward in a more versatile modelling. The fluid coupling can be established either by special enhanced elements with extra nodes in which the fluid flow non-linear equations are solved or by using the superimposition of a second discretized domain of FDM or FVM. Being continuum methods, the existence of displacement discontinuities such as cracks is causing problems. For example either the path over which the HF will propagate has to be predefined and discretized by special discontinuity-elements (*e.g.*, Pouya, 2015) or the mesh has to be re-built each time the HF front is propagating. Being a computationally heavy operation, special adaptive-remeshing techniques have been developed to reduce the cost (Schrefler *et al.*, 2006; Secchi and Schrefler, 2012). A promising solution to this problem came by the development of the extended-FEM (XFEM) technique for fracture propagation (Zi and Belytschko, 2003) and the phase-field method (Miehe and Mauthe, 2016; Mikelić *et al.*, 2015). The techniques allows discontinuities to propagate through the finite elements without the need of re-meshing.

FEM modelling of HF revealed another problem. The classical models for the simulation of single HF propagation consider the framework of linear elastic fracture mechanics (LEFM) for the fracture growth. The net pressure (*i.e.*, the difference between the fracturing pressure and the far-field stress) these models predicted didn't coincide with the field observations of the down-hole pressure (Papanastasiou, 1999). An elasto-plastic analysis by the same author has shown that the plastic region in front of the crack tip produces a shielding to the tip (the yielded rock cannot support the same values of stresses as the elastic rock) and so, the effective fracture toughness increases by more than one order of magnitude. The phenomenon is also known as dilatancy hardening (Schmitt and Zoback, 1992; Schmitt and Zoback, 1993). Thus, the "cohesive zone" elements (see Figure 4.6) started playing an important role in the numerical models . The philosophy behind these elements lays on the fact that the process zone ahead of the HF tip has degraded mechanical properties and thus undergoes a softening behaviour (described by damage parameters).

The state of the art in continuum models consists of fully hydro-mechanically (HM) coupled XFEM models with cohesive zone elements (Faivre *et al.*, 2016; Salimzadeh and Khalili, 2015; Sarris and Papanastasiou, 2011; Settgast *et al.*, 2016; Wang *et al.*, 2015; Yao *et al.*, 2015). This technique allows for HF propagation without remeshing, since the HF can pass through the elements and thus there is no need for re-meshing, and also captures the plastic shielding of the fracture tip (see Figure 4.6). However, although the XFEM is more promising than previous FEM method, the technique is still computationally heavy (at least compared to usual FEM) and it cannot deal yet with fracture coalescence. Furthermore it doesn't take into account all the types of non-linear couplings (Pouya, 2015).

Other continuum models that were used recently to reduce the computational cost are CDM which don't consider a discrete HF propagation, or specific element for capturing the process zone but rather a damage mechanics constitutive law which takes the creation and coalescence of micro-cracks into account (Shojaei *et al.*, 2014). That would mean that all the computational effort of heavy XFEM techniques of re-meshing is avoided.

Since the effect of the fracture networks in hydraulic fracturing seems to play a very important role on the HF propagation and the total stimulated volume, some techniques that disregard the

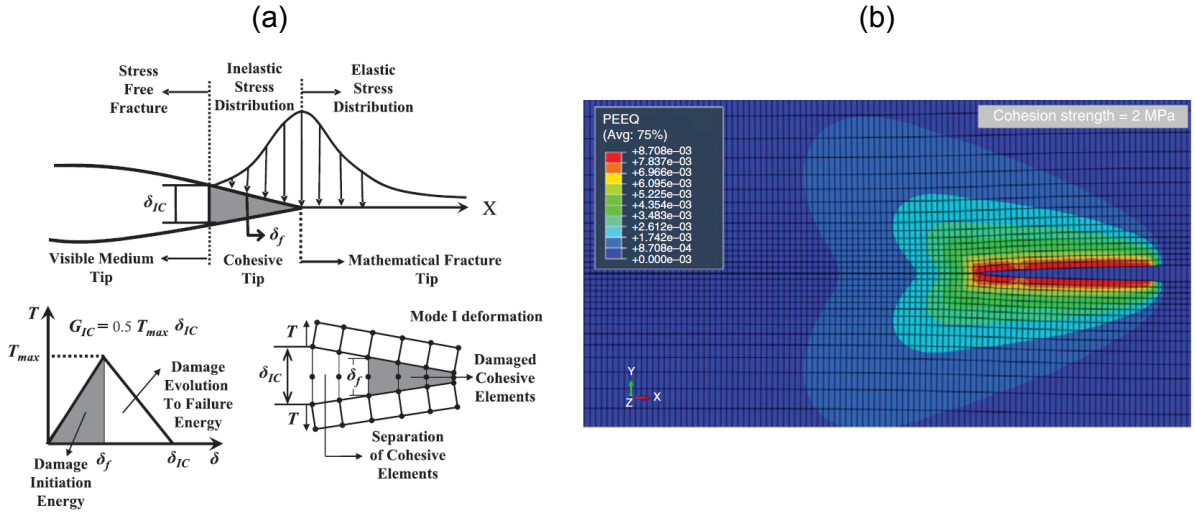

Figure 4.6: (a) Top: Sketch of the cohesize zone physical concept,Bottom-left: Traction-Separation relation and Bottom-right: sketch of cohesive zone element (from Sarris and Papanastasiou, 2015). (b) Plastic strains around HF which propagates in a pre-defined path using HM-XFEM with cohesive zone elements (from Wang *et al.*, 2015).

progressive failure of the rock matrix have been also applied (Ben *et al.*, 2012; Min *et al.*, 2004b; Riahi, Damjanac *et al.*, 2013a; Yaghoubi and Zoback, 2012; Zou *et al.*, 2016). The main idea in this case is that the HF propagation doesn't really affect the total stimulated area/volume but rather activates a hydraulic conduit throughout the fracture network (see Figure 4.7). Usually, these numerical tools are based on coupled (DFN) models, DEM or DDA models that consider fluid flow only in the DFN domain or in the both the rock matrix and the DFN domains, but the HF propagation is restricted only by the reactivation of the fracture network (the main conduit).

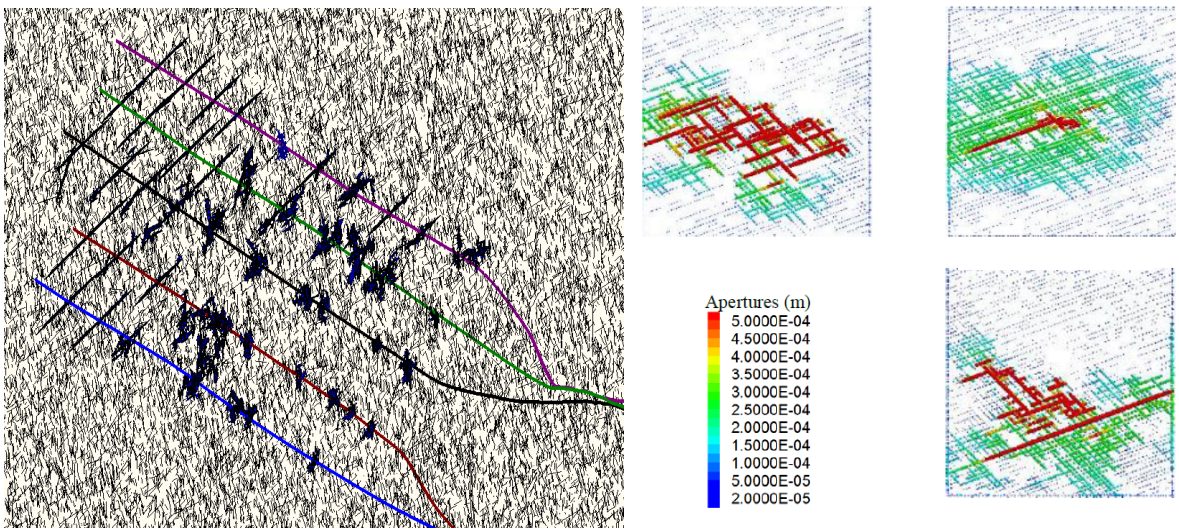

Figure 4.7: (Left) DFN flow model showing the reactivation of a natural fracture network in Barnett shale (from Yaghoubi and Zoback, 2012). (Right) Shear-activation of a natural fracture network modelled in DEM-DFN model (modified from Riahi, Damjanac *et al.*, 2013a).

Although these methods are efficient for modelling flow in dense fracture networks of higher permeability than the rock matrix, which is typically the case in the field, they don't account for HF propagation in the matrix. The interaction of a propagating HF with the fracture network plays a major role on the final stimulated surface/volume and pattern (see *e.g.*, Riahi, Damjanac

et al., 2013b). The introduction of a predefined HF path to study the interaction with the DFN is though possible in some of the methods as in the later mentioned case.

In an effort to extend of DFN-like models to account for HF propagation in the intact rock matrix, a lot of research has been carried out the last years on the use of discrete models such as DEM, LEM or FEMDEM. The reason is mainly the efficiency of the methods while dealing with fracturing and fracture networks. The solid is represented by DEM or FEMDEM respectively while the fluid flow can be described in various ways. The most usual one and less computationally expensive is the use of the dual-network in-between the elements as flow paths (see Figure 4.3). Other types of coupling involve a superimposition of a continuum grid for the flow (Boutt *et al.*, 2007; Fu *et al.*, 2011; Ghani *et al.*, 2013).

Furthermore, the discrete methods enable to relate the HF process with micro-seismic events (Zhao *et al.*, 2014; Zhao and Paul Young, 2011). This feature can be very helpful to relate numerical simulations with lab experiments or field tests since acoustic emissions is one of the primary tools used to follow the HF process. For instance, (Al-Busaidi *et al.*, 2005) investigated the influence of heterogeneity of rocks in hydraulic fracturing. The studies were based in 2D DEM numerical simulations of Acoustic Emissions (AE) test and verification with lab-scale AE tests.

Several phenomena can be explained by using these types of numerical models. For example (Shimizu *et al.*, 2011), based on the same methodology (comparing AE simulations to real AE experiments), have shown the formation of thin unstable HF growth by low viscosity fluid injection versus a stable thick HF by viscous fluid injection. The model has shown that in the first case the fluid diffuses easier in the matrix causing an effective stress reduction ahead of the HF tip. Apart from the academic interest, the discrete HF models can actually help in optimizing the efficiency of the treatment (Yoon *et al.*, 2014).

The presence of NF, flaws and faults, might be a primary agent that controls the treatment and the fracture propagation itself. For example, when a HF crosses a pre-existing fracture, it's direction of propagation might be driven by the fracture plane for a while and then continue on the direction defined by the stress regime or completely change its initial direction (see Chapter 3). Several discrete models have been recently built to deal with the interaction of a natural fracture network with propagating HFs. Most of them in 2D (Grasselli *et al.*, 2015; Grégoire *et al.*, 2016; Lisjak *et al.*, 2017) but few are functional in 3D (Damjanac *et al.*, 2016).

4.4 Discussion

Several numerical methods can be used to assess the performance of different stimulation strategies (Adachi *et al.*, 2007; Bunger and Peirce, 2013; Papanastasiou, 1999; Zhou and Hou, 2013). However, HF involves complex HM processes often difficult to tackle with continuous methods (Day-Lewis, 2008; Wheeler *et al.*, 2014; Yew and Weng, 2014). Some of them have been used to study HF in rock but only few of them can take into account the progressive failure mechanism taking place along non predefined fracture planes while being computationally efficient (Adachi *et al.*, 2007; GuoXin *et al.*, n.d.; Hossain and Rahman, 2008; Rutqvist *et al.*, 2000; Zhou and Hou, 2013). Moreover, due to the localization of the deformation along narrow fracture zones, the determination of a representative elementary volume to set up a homogenization procedure seems out of reach or applicable only in specific configurations for which a damage zone is large enough to be identified at the problem scale (Guangqing and Mian, 2009; Nagel *et al.*, 2013; Peng and Zhang, 2007; Vermylen, 2011). A reasonable approach would be therefore to explicitly represent the initiation and propagation of the HF inside the rock with a numerical method able to integrate a fully coupled HM formulation (Wang *et al.*, 2009; Zhang *et al.*, 2013). Among the different explicit formulations available, the DEM, has shown to bring valuable insights to improve our understanding on the progressive development of HF within porous media (Baghbanan and Jing, 2008; Al-Busaidi *et al.*, 2005; Damjanac and Cundall, 2015; Damjanac, Detournay

et al., 2013; Grasselli *et al.*, 2015; Grassl *et al.*, 2015; Riahi, Damjanac *et al.*, 2013a; Shimizu *et al.*, 2011; Yoon *et al.*, 2014; Zhao and Paul Young, 2011). It has thus been chosen for the present study.

In this thesis, an attempt will be made to build a coupled HM-DEM model able to deal with progressive failure of rock under fluid injection, coupled fracture behaviour to describe opening (during hydraulic loading), closure (during hydraulic unloading such as flow-back), as well as fracture creation, propagation, natural fracture network re-activation, crack coalescence and interaction between the HF and NF.

Chapter highlights

- Modelling HF in naturally fractured brittle and quasi-brittle formations require numerical models than can predict the progressive failure of the rock mass from slip in discontinuity planes as well as fracturing of the intact rock matrix (rock bridges).
- Description of the flow in both matrix and fractures is needed for the complete description of HF problem in complex permeable and fractured formations, along with the mechanical effect on it.
- A large variety of HF simulators exist based on different techniques and having different pros and cons. Very few of them can deal with 3D fully coupled HF induced progressive failure and natural fracture network re-activation in realistic complex geological scenarios.

Part II

Model and Verification

Chapter 5

The DEM-PFV scheme for fluid saturated rock-mass modelling

The proposed method is implemented in YADE Open DEM, an extensible open-source software based on the DEM (Kozicki and Donzé, 2008, 2009). The medium is represented as an assembly of bonded discrete elements (also referred to as "DE" or "particles") whose respective motion is ruled by Newton's second law such as proposed by (Scholtès and Donzé, 2013). The fluid flow is simulated using a finite volume (FV) method (Catalano *et al.*, 2014) specifically enhanced for modelling flow in fractured media. The DEM and FV methods are coupled in the sense that any deformation of the solid phase affects the fluid flow and, conversely, any variation in pore pressure induces deformation of the medium. The following sections give the basis of the model formulation and present its calibration to the properties of a generic soft rock that will be used afterwards as the host medium for HF simulation.

Layout of chapter

First, in Section 5.1, the scheme for modelling rock-related problems with the DEM is explained. Emphasis is given to the way the fracture networks are treated in the developed software almost any kind of fracture network can be explicitly represented in the proposed model. Then the model's mechanical response calibration to the reference material that will be used on the following tests in the thesis is presented.

In Section 5.2, the fluid modelling by the PFV scheme and the coupling strategy are detailed for intact rock matrix, cracks and natural fractures. After the scheme is explained, Then the model's hydraulic response calibration to the reference material that will be used on the following tests in the thesis is presented.

5.1 Rock modelling with DEM

5.1.1 Bonded particle model

Similarly to classical bonded particle models (BPM), the rock matrix is represented as a dense packing of bonded spherical particles (see for instance Potyondy and Cundall, 2004; Wang and Mora, 2008). The concept of such representation is illustrated in Figure 5.1. In order to overcome some limitations of classical BPM to accurately simulate rock behavior, YADE's formulation has been upgraded for rock modelling purpose (Scholtès and Donzé, 2013). Specifically, by introducing the possibility of near neighbour interactions, the average number of bonds per particles K can be controlled and enables to simulate adequate ratios of tensile to compressive stengths and non linear failure envelopes typical of competent rocks. As an alternative to the use of clumps (Cho *et al.*, 2007) or enhanced interaction laws (Ding and Zhang, 2014; Potyondy,

2012), the proposed solution provides an effective approach to improve BPM capabilities without degrading its computational efficiency.

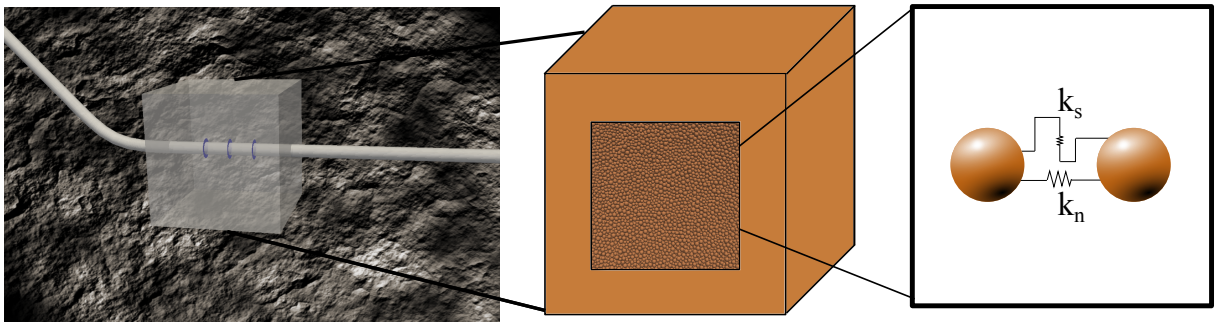

Figure 5.1: Illustration of the representation of a rock volume by DEM.

The behavior of the medium is determined through the normal and tangential contact forces acting between each pair (A,B) of interacting particles. The normal forces F_n are directly computed from the relative normal displacement u_n between the particles:

$$F_n = k_n u_n \tag{5.1}$$

whereas the tangential forces F_t are updated from the relative incremental tangential displacement Δu_t such as:

$$F_t = F_t^{t-\Delta t} + k_t \Delta u_t \tag{5.2}$$

with $F_t^{t-\Delta t}$ the tangential force at the previous timestep and k_n and k_t the contact stiffnesses defined as:

$$k_n = E_{eq} \frac{2R_A R_B}{R_A + R_B}, \quad k_t = \delta k_n \tag{5.3}$$

E_{eq} is a parameter that directly relates to the bulk modulus of the numerical assembly and δ is a dimensionless parameter that relates to its Poisson's ratio. R_A and R_B are the respective radius of the interacting particles.

In compression, the normal force is not restricted and can increase indefinitely (see Figure 5.2a). In tension, a maximum admissible force F_n^{max} is defined such that:

$$F_n^{max} = \pi \times min(R_A, R_B)^2 \times T \tag{5.4}$$

with T the interparticle tensile strength. Once F_n^{max} is reached, mode I (or tensile) rupture occurs.

In shear, a Mohr-Coulomb failure criterion is used (see Figures 5.2b, 5.2c) to define the maximum admissible tangential force F_t^{max} such that:

$$F_t^{max} = C \times \pi \times min\left(R_A, R_B\right)^2 + F_n tan\phi \tag{5.5}$$

with C the interparticle cohesion and ϕ the interparticle friction angle. Once F_t^{max} is reached, mode II (or shear) rupture occurs.

It has to be noted here that when the process-zone (internal) length in front of a fracture tip is comparable to few D_{mean}, the process zone can be described naturally by the model. On the other hand, in cases where the process-zone is emerging at a sub-particle scale, a law that considers softening before rupture can be used as described in (Scholtès and Donzé, 2013), to account for the effect of process zone on the fracture propagation. However, in order to reduce the parametric space of the problem at this step, only fully brittle fracture propagation is considered. Comparison with the quasi-brittle propagation is left for future work.

When a bond fails, either by mode I or mode II rupture, a crack is explicitly defined in the material by a circular disk whose size s is proportional to the sizes of the interacting particles

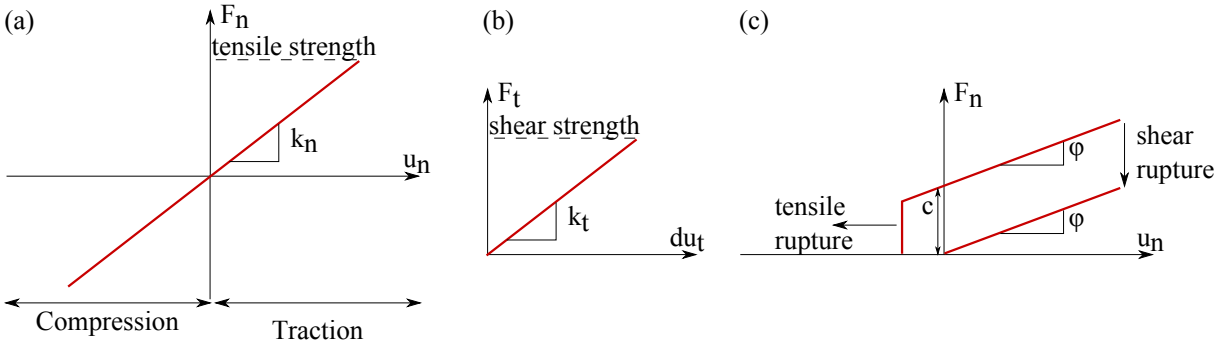

Figure 5.2: (a) Constitutive behaviour under normal loading, (b) constitutive behaviour under tangential loading and (c) failure surface.

($s = \pi \times mean(R_A, R_B)^2$) and with a normal vector collinear to the branch vector joining the two particles. The aperture of the crack can evolve during the deformation of the medium and corresponds to the normal relative displacement between the particles. If, for any reason, the particles come back into contact, the interaction forces are computed according to the same computational scheme without the cohesive components ($T = C = 0$).

In each computation cycle of duration Δt, Newton's 2nd law of motion is applied on each DE to obtain its translational $\ddot{\vec{x}}$ and angular $\dot{\vec{\omega}}$ accelerations whose k^{th} component ($k = 1, 2, 3$ in 3D) are thus calculated as,

$$\begin{aligned} \ddot{x_k} &= \frac{F_k}{m} \\ \dot{\omega_k} &= \frac{M_k}{J} \end{aligned} \tag{5.6}$$

with $\vec{F}$ and $\vec{M}$ the resultant force and torque applied on each DE and m and J their respective mass and moment of inertia.

The translational $\dot{\vec{x}}$ and angular $\vec{\omega}$ velocities are then evaluated at time $t + \Delta t/2$ using a second order centred difference scheme such that,

$$\begin{aligned} \dot{x_k}^{\left[t+\frac{\Delta t}{2}\right]} &= \dot{x_k}^{\left[t-\frac{\Delta t}{2}\right]} + \left(\ddot{x_k}^{[t]} + g_k\right)\Delta t \\ \omega_k^{\left[t+\frac{\Delta t}{2}\right]} &= \omega_k^{\left[t-\frac{\Delta t}{2}\right]} + \dot{\omega_k}^{[t]}\Delta t \end{aligned} \tag{5.7}$$

with $\vec{g}$ the body forces applied on the DE (*e.g.* gravity).

Finally, Eq. 5.7 is integrated over time and the final position of each particle at time $t + \Delta t$ is calculated as,

$$x_k^{[t+\Delta t]} = x_k^{[t]} + \dot{x_k}^{\left[t+\frac{\Delta t}{2}\right]}\Delta t \tag{5.8}$$

In addition, because of the dynamic formulation of the method (explicit time domain integration), a global non-viscous damping is used to dissipate kinetic energy and facilitate convergence towards quasi-static equilibrium. This damping directly acts on the forces (torques respectively) considered in the equations of motion so that the displacements are calculated from the damped force $\vec{F}^d$ whose components are computed such that:

$$F_k^d = F_k - \gamma\, sign\left(\dot{x}_k + \frac{\ddot{x}_k \Delta t}{2}\right)|F_k| \tag{5.9}$$

with γ a dimensionless parameter ranging from 0 to 1, $\gamma = 0$ corresponding to a totally undamped system and $\gamma = 1$ to a static one. γ had been previously presented as a parameter that would describe physical energy dissipation and that could thus be calibrated according to, *e.g.*, the seismic quality factor of the rock (Potyondy and Cundall, 2004). No clear evidence were given however concerning the relationship between the physical and the numerical quantities. Damping is thus considered here, as in most other studies, only as a convenient numerical tool to ensure the quasi-staticity of the simulations.

Finally, in order to follow the stress field under various loadings, and especially stress concentrations at the vicinity of fractures, stress is extracted locally from the "per-particle stress tensors". For the calculation of local-stresses, each particle is considered as a continuum and a per-particle stress tensor defined. The stress is then calculated from the contour integral of the applied load on the particle. At equilibrium:

$$\nabla \cdot \sigma_{ij} = 0 \tag{5.10}$$

Noting $x_i^{[C]}$ the vector containing the cartesian coordinates of a generic contact point, we can write the identity:

$$\sigma_{ij} = \sigma_{ij}\delta_{ij} = \sigma_{ij}\nabla x_i^{[C]} = \nabla \cdot x_i^{[C]}\sigma_{ij} - x_i^{[C]}\nabla \cdot \sigma_{ij} \tag{5.11}$$

and by applying divergence theorem, the average stress per particle can be given by:

$$\frac{1}{V}\int_V \sigma_{ij} dV = \frac{1}{V}\sum_k x_i^{[k,C]}\vec{F}^{c,k} \tag{5.12}$$

where $\vec{F}_c^k$ represents the contact force, and k the contact identity. Eq. (5.12) is implicitely based on the representation of external loads as Dirac distributions whose zeros are the so-called contact points (*i.e.*, 0-sized surfaces on which the contact forces are applied, located at $x_i^{[C]}$ in the deformed configuration Smilauer *et al.*, 2010).

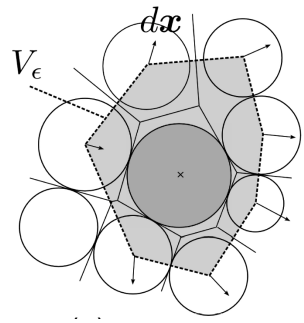

Figure 5.3: Domain V_ϵ assigned to each DE by the regular triangulation enclosing the volume of an equivalent continuum (from Catalano, 2012).

Using a similar logic, a per particle strain tensor can be defined. A domain V_ϵ is defined around each DE by the regular triangulation (see Figure 5.3). The displacement gradient of each neighbouring DE causes a deformation on the domain V_ϵ which encloses a volume of an equivalent continuum (Catalano, 2012).

$$\langle \nabla dx_i \rangle = \frac{1}{V_\epsilon}\int_{V_\epsilon} \nabla dx_j^{[k]} dv = \frac{1}{V_\epsilon}\int_{\partial V_\epsilon} dx_i^{[k]} n_j ds \tag{5.13}$$

the local strain tensor ϵ_{ij} can then be obtained from the symmetric part of the displacement gradient:

$$\epsilon_{ij} = \frac{1}{2}\left(\langle \nabla dx_i \rangle + \langle \nabla dx_i \rangle^T\right) \tag{5.14}$$

5.1.2 Mechanical properties calibration

As for any BPM, the local parameters of the interparticle bonds have to be determined so that the DE set has a mechanical behaviour equivalent to the one of the material under consideration. A particle growing technique was used here for the creation of the packings. A particular attention was paid to generate dense packings with similar geometrical and statistical properties in terms of particle size distribution ($R_{min}/R_{max} \approx 0.5$) and porosity ($n \approx 0.4$) in order to ensure a consistent mechanical behaviour whatever the scale and discretization considered. In addition, all samples present an isotropic contact fabric when free from any external loadings. The local, microscopic parameters were calibrated to the values of Table 5.1 in order to reproduce the behaviour of a generic low permeability soft rock with the mechanical properties summarised in Table 5.2.

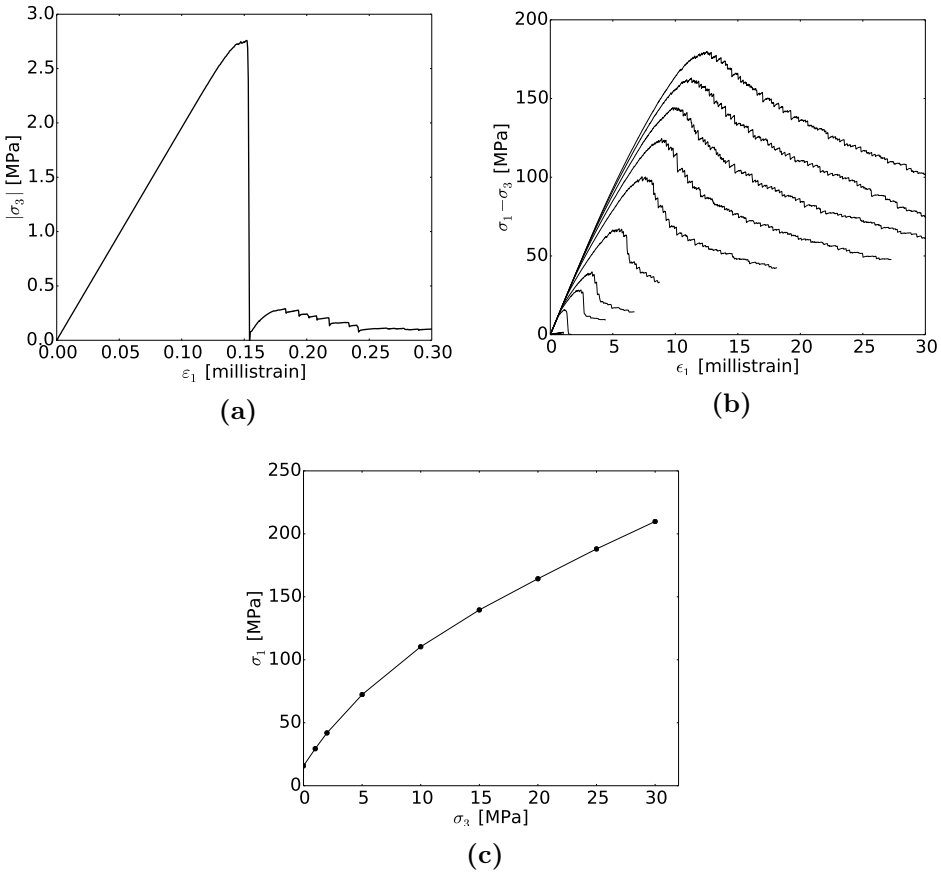

Figure 5.4: Stress-strain responses of the numerical sample under (a) uniaxial tensile loading and (b) compression under different confinements with (c) the resulting non-linear failure envelope.

Contact density K [-]	Elastic modulus E_{eq} [Pa]	Stiffness ratio δ [-]	Tensile strength T [Pa]	Cohesion C [Pa]	Friction angle ϕ [°]
10	30×10^9	0.2	40×10^5	40×10^6	18

Table 5.1: Micro-parameters used in the DEM.

5.1.3 Implementation of natural fractures

In order to account for NF in the numerical scheme, the following methodology is applied. First of all, the pre-existing discontinuity's (*e.g.*, NF or an injection slot) geometry is created as a meshed

Young's modulus E [Pa]	Poisson's ratio ν [-]	Compressive strength UCS [Pa]	Tensile strength UTS [Pa]
17.8×10^9	0.2	17×10^6	2.8×10^6

Table 5.2: Mechanical properties of the simulated rock.

surface which is then imported into the model. The interactions that lay in the discontinuity domain, *i.e.*, interactions between particles located on each side of the pre-existing fracture's wall, are identified as *e.g.*, "NF-interactions". Then, to avoid the effect of the local numerically induced roughness on the fracture walls, the smooth contact logic (SCL) is introduced for the NF-interactions (Mas Ivars *et al.*, 2011; Scholtès and Donzé, 2012). The SCL is a contact transformation (or, contact re-orientation) which allows the DE contacts to be projected on a local coordinate system, that uses the normal and tangential unit vectors of the discontinuity plane as references (see Figure 5.5). This allows friction and cohesion to be constitutive parameters, independent of packing and local geometry.

The numerical representation of a segment of a NF under pure shear loading is shown in Figure 5.5a. The DEs are coloured depending on which wall of the NF they correspond to. In Figure 5.5b, the expected velocities $\vec{v_i}$ and $\vec{v_j}$, for the DEs i and j respectively, are shown for classical DEM formulation, using the contact plane c. The associated trajectory of the DE i for the displacement u_i is shown in Figure 5.5d. It is clear that such a movement can be affected by the DE size. On the other hand, in Figure 5.5c, using the SCL, the velocities become parallel to the tangential plane of the NF as it would be expected for a smooth NF. The related DE trajectory is shown in Figure 5.5e. One can see that the DEs are moving along the tangential NF plane ($\vec{t}_{NF}$) without vertical displacements (along $\vec{n}_{NF}$). The indices $_{NF}$ refer to the NF reference system and $_c$ to the contact reference system. From the above, friction angle ϕ and dilation angle ψ turn out to be constitutive parameters, independent of the local packing tortuosity.

A set of six parameters defines the mechanical behaviour of the pre-existing fractures : $[k_n^{NF}, k_t^{NF}, c_{NF}, T_{NF}, \phi_{NF}, \psi]$. Regarding the constitutive equations for the NF-interactions, they may vary from the ones used for the intact rock matrix interactions. For the work presented here the same constitutive laws were used for intact matrix and pre-existing fractures, *i.e.*, a bi-linear Mohr-Coulomb type of interaction law is used for the particles on the walls of the NF which turns into purely frictional behaviour after tensile or shear failure. The formulation is similar to the one shown in Section 5.1.1. The NF constitutive properties are defined separately from the matrix and they can be different. Furthermore, dilation has been added to represent the normal displacement (opening) of the discontinuity during shearing (Mas Ivars *et al.*, 2011; Scholtès *et al.*, 2011). The effect of the dilation on the normal force is given by:

$$F_n = k_n \left(u_n + \delta u_s \tan(\psi)\right) \tag{5.15}$$

with ψ the dilation angle.

The NF's normal and tangential stiffness k_n^{NF} and k_s^{NF} in [Pa.m^{-1}], become size independent by defining them as:

$$k_n^{NF} = \frac{k_n}{A_{ij}} \tag{5.16}$$

$$k_s^{NF} = \frac{k_s}{A_{ij}} \tag{5.17}$$

A_{ij} being the contact area between the interacting DEs i and j, given by $A_{ij} = \pi R_{mean(ij)}^2$.

One should be careful as the normal stiffnesses k_n for the matrix and the NF k_n^{NF} have different dimensions ([Pa] and [Pa/m] respectively). More explicitly, the NF normal stiffness is given by Equation 5.16 while the matrix normal stiffness is defined as:

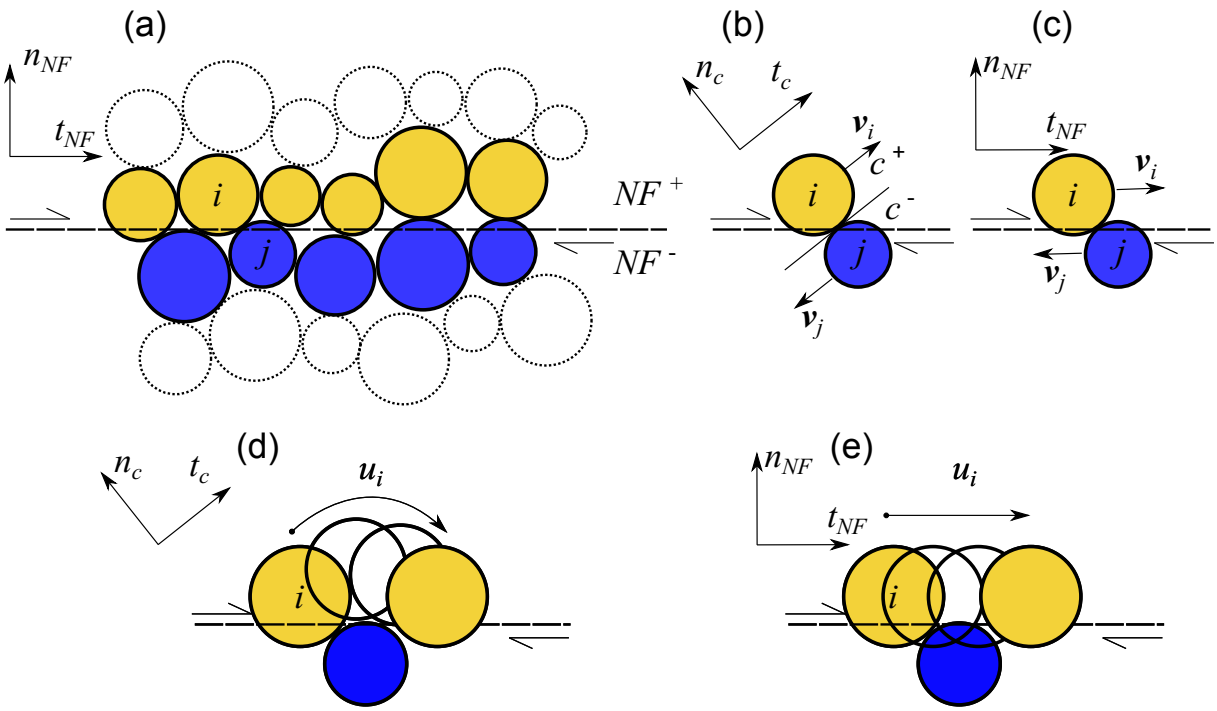

Figure 5.5: Schematic explanation of SCL in 2D for simplicity. (a) DEM represented by disks deposed on a NF during shear loading. The coloured DEM share joint type interactions. Yellow discs correspond to the upper wall of the discontinuity plane (NF^+) and blue disks to the lower wall (NF^-). (b) Velocities of elements i, j based on the contact orientation (global reference system). (c) Velocities of elements i, j based the NF orientation (local reference system). (d) Trajectory of element i without the contact re-orientation.(d)Trajectory of element j using contact re-orientation (SCL).

$$k_n = E \times R_{min} \tag{5.18}$$

where R_{min} here is the minimum radius of the two interacting spheres. Thus in order for, example to set similar normal stiffness for both matrix and NF, one should use:

$$k_n^{NF} = \frac{E}{\pi \times R_{min}} \tag{5.19}$$

It has been shown that the formulation leads to DE-size independent macroscopic behaviour and friction angle ϕ_{NF} and dilation angle ψ are thus material constants (constitutive parameters) that keep the same value on the at the contact or packing levels (Duriez *et al.*, 2016). The same study suggests that the proposed model for discontinuities can be macroscopically described by a perfect elasto-plastic equation with a constant yield surface $\tau = \sigma \tan(\phi_{NF})$ and a non-associated flow rule $\frac{du^p}{|d\gamma^p|} = -tan(\psi)$, with du^p and $|d\gamma^p|$ being the plastic normal and tangential displacement increments respectively.

The length-scales should be comparable between the DEs and the NF in the sense that the diameter of DE should be superior or equal to the fracture trace in order to obtain reasonable results.

Finally, it is to be noted here that only the fluid-coupling part (Section 5.2) is a new contribution while the mechanical part has been used in several studies. (Scholtès and Donzé, 2012) implemented a plug-in in YADE to deal with mechanical response of rock specimens containing single defects (flaws). Then, it was also used by (Duriez *et al.*, 2016; Harthong *et al.*, 2012; Scholtès and Donzé, 2012; Scholtès *et al.*, 2011) to study the effect of NF networks on rockmass strength. (Scholtès *et al.*, 2011) used a blocky type DFN to quantify scale-effects on mechanical

response of a coal sample. (Harthong *et al.*, 2012) performed a similar analysis to study the strength of rock masses containing stochastic networks of different topologies based on fractal powerlaws (Davy *et al.*, 2010). In the case of (Harthong *et al.*, 2012), stochastic networks of different topologies, based on fractal powerlaws (Davy *et al.*, 2010) have been used. DFN's spatial distribution, size and clustering impact on rock's strength were investigated. Other types of distributions can be relatively easily implemented as well.

5.2 Fluid modelling

In this section, the governing equations of the DEM-FV method are first summarized (an exhaustive presentation of the coupled scheme can be found in (Catalano *et al.*, 2014; Chareyre *et al.*, 2012; Scholtès *et al.*, 2015). The extension of the method to rock fracturing problems is presented and the calibration procedure of the model's hydraulic properties is finally illustrated.

5.2.1 Pore scale finite volumes scheme

Based on the DE set, the medium is discretized through a regular triangulation (Figure 5.6). In 3D, each triangle in Figure 5.6 corresponds to a tetrahedron as illustrated in Figure 5.7(c). The domain Ω_i limited by a tetrahedron and four discrete elements represents an elementary pore unit filled with fluid (the medium is considered as fully saturated here). At the scale of the DE assembly, an interconnected pore network is defined and a Stokes-flow can be established.

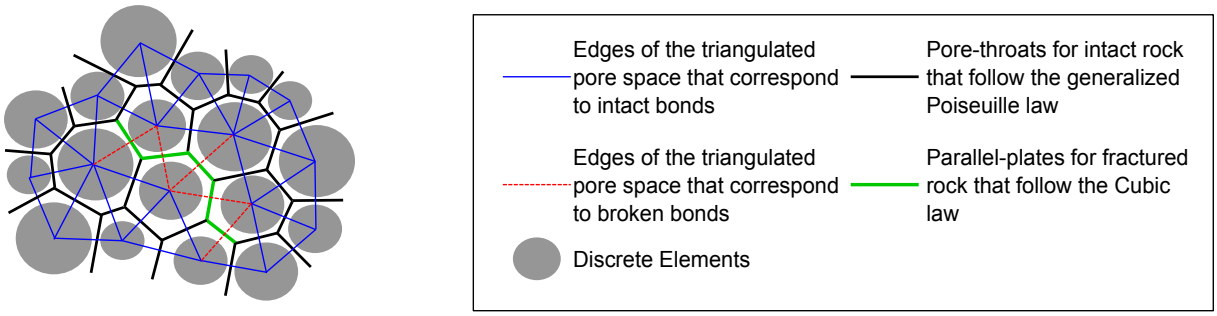

Figure 5.6: 2D representation of the numerical medium. Two types of flow paths are presented here: inside the intact rock matrix (black segments) where the DE are bonded together and inside the fractured medium (green segments) where the fluid flows inbetween unbonded DE.

For a compressible fluid, the integration of the continuity equation in the fluid domain Ω_i of pore i gives,

$$\int_{\Omega_i} \frac{\partial \rho_f}{\partial t}\, dV = -\int_{\Omega_i} \nabla \cdot (\rho_f \vec{v})\, dV \tag{5.20}$$

ρ_f being the fluid density and $\vec{v}$ the fluid velocity (Scholtès *et al.*, 2015).

The divergence theorem applied to Eq. 5.20 leads to,

$$\int_{\Omega_i} \frac{\partial \rho_f}{\partial t}\, dV = -\int_{\partial\Omega_i} \rho_f \vec{v} \cdot \vec{n}\, dS \tag{5.21}$$

with $\vec{n}$ the outwards pointing vector normal to the contour of the fluid domain $\partial\Omega_i$.

Since the vertices of the tetrahedron correspond to the centres of the DE, their displacements cause deformation of the pore at a rate that depends on the velocity of the DE. $\vec{u}$ being the velocity of $\partial\Omega_i$, Eq. 5.21 can then be written as,

$$\int_{\Omega_i} \frac{\partial \rho_f}{\partial t}\, dV = -\int_{\partial\Omega_i} \rho_f\, (\vec{v} - \vec{u}) \cdot \vec{n}\, dS - \int_{\partial\Omega_i} \rho_f \vec{u} \cdot \vec{n}\, dS \tag{5.22}$$

Considering the fluid to be compressible, the fluid bulk modulus K_f relates the density ρ_f and the derivative of pressure with respect to density such as,

$$K_f = \rho_f \frac{\partial P_i}{\partial \rho_f} \tag{5.23}$$

For small Mach number values, the continuity equation becomes,

$$\int_{\Omega_i} \frac{1}{K_f} \frac{\partial P_i}{\partial t} \, dV = -\sum_{j=1}^{4} \int_{\partial \Omega_{ij}} (\vec{v} - \vec{u}) \cdot \vec{n} \, dS - \dot{V}_{p,i} \tag{5.24}$$

where $\dot{V}_{p,i}$ is the time derivative of the pore volume and $\partial \Omega_{ij}$ is the interface between Ω_i and Ω_j (i has 4 neighbours and thus $\partial \Omega_i = \sum_{j=1}^{4} \partial \Omega_{ij}$).

Linking the flux integrals of the righthandside of Eq. 5.24 to the pressure jump between two pores i and j leads to,

$$\sum_{j=1}^{4} \int_{\partial \Omega_{ij}} (\vec{v} - \vec{u}) \cdot \vec{n} \, dS = \sum_{j=1}^{4} k_{ij} \left(P_i - P_j \right) \tag{5.25}$$

with k_{ij} the conductivity of the throat between i and j (see following section for its definition).

Finally, the time derivative of the pore pressure can be expressed as,

$$\dot{P}_i = -\frac{K_f}{V_{f,i}} \left[\dot{V}_{p,i} + \sum_{j=1}^{4} k_{ij} \left(P_i - P_j \right) \right] \tag{5.26}$$

with $V_{f,i}$ the volume of fluid contained in i.

The numerical solution of the hydraulic problem is computed using a backward-Euler finite difference discretization of Eq. (5.26) for the evaluation of $\dot{P}_i$ that reads:

$$\sum_{j=1}^{4} k_{ij} P_j^{[t]} - \left(\zeta_i + \sum_{j=1}^{4} k_{ij} \right) P_i^{[t]} = \dot{V}_{p,i}^{[t-\frac{\Delta t}{2}]} - \zeta_i P_i^{[t-\Delta t]}, \quad \text{with} \quad \zeta_i = \frac{V_{f,i}}{K_f \Delta_t} \tag{5.27}$$

where the time-centred evaluation of $\dot{V}_{p,i}^{[t-\frac{\Delta t}{2}]}$ is obtained from mid-step velocities of the particles evaluated at each time step in the DEM scheme (see previous section).

Considering Eq. 5.27 for each pore constituting the medium, a linear system can be set up relating the pressure field at time t as a function of the pressure field at time $t - \Delta t$.

While a Stokes flow is established in the medium, the total force $\vec{F}^f$ applied from the fluid on each DE is calculated from three components which are the three contour integrals of (a) the hydrostatic pressure, (b) the losses of piezometric pressure due to viscous flow P^* and (c) the viscous shear stress τ as follows:

$$\vec{F}^f = \int_{\partial \Gamma} \rho g z \vec{n} \, dS + \int_{\partial \Gamma} P^* \vec{n} \, dS + \int_{\partial \Gamma} \tau \vec{n} \, dS = \vec{F}^b + \vec{F}^P + \vec{F}^v \tag{5.28}$$

with $\partial \Gamma$ the wetted surface of the DE (Γ being the domain occupied by the DE).

The integrals give respectively, per element, the buoyancy force $\vec{F}^b$, the force due to losses of piezometric pressure induced by viscous flow $\vec{F}^P$ and the forces due to viscous shear stress $\vec{F}^v$.

Assuming constant pressure in each pore at the current timestep, $\vec{F}^P$ and $\vec{F}^v$ result from the contributions of the pressure jumps between all the pores containing the DE and can thus be derived at the scale of the interporal domain. Considering two neighbouring pores i and j and their common facet of surface S_{ij} (i.e. the triangular facet between the two tetrahedra) as

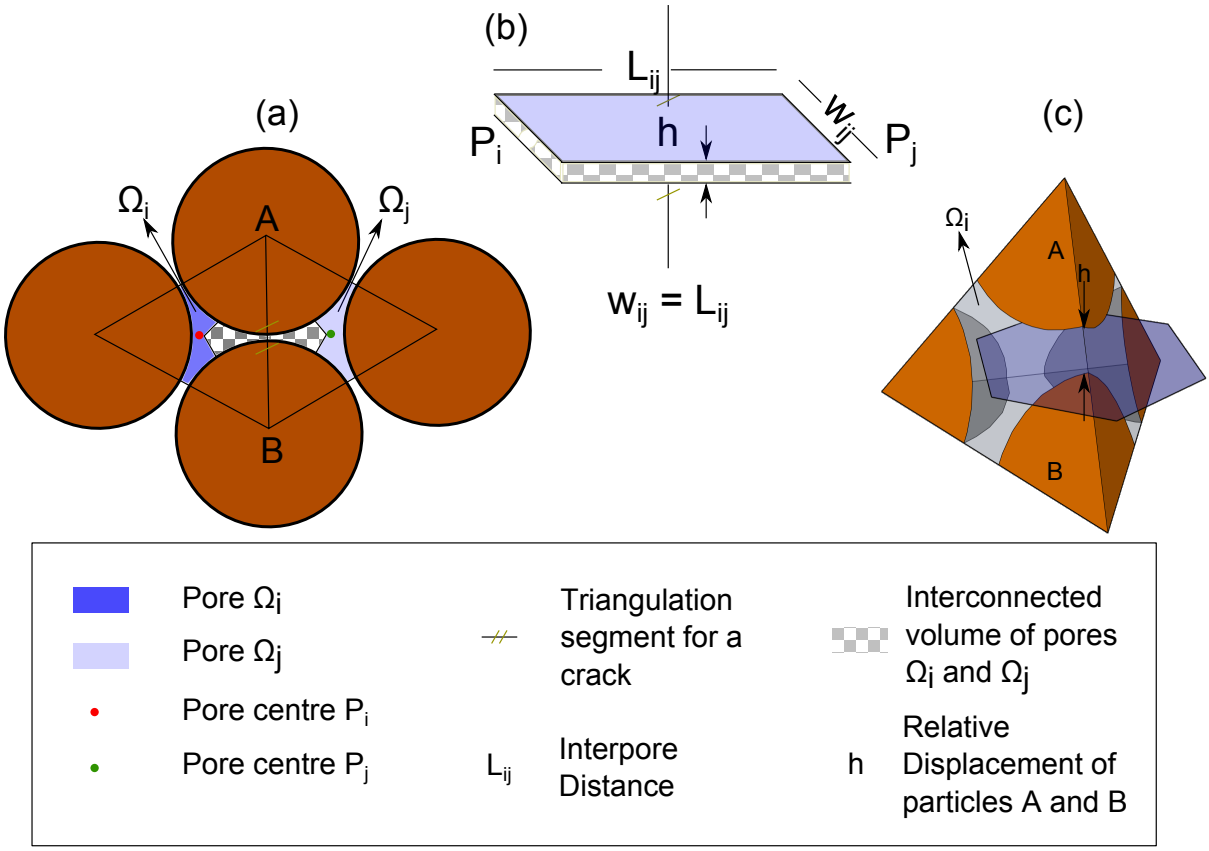

Figure 5.7: (a) 2D representation of the interporal volume with a crack between discrete elements A and B. (b) Geometric quantities in the fracture modelled as two parallel plates. (c) 3D representation of the crack in dark blue.

in Figure 5.8, the interporal pressure force $\vec{F}^P_{ij}$ is computed by distributing the pressure jump $(P_i - P_j)$ over each DE such that:

$$\vec{F}^P_{ij} = S^s_{ij}(P_i - P_j)\vec{n}_{ij} \tag{5.29}$$

where S^s_{ij} is the projected surface of the DE on the facet and $\vec{n}_{ij}$ the unit vector pointing from pore i to pore j.

Similarly, the interporal viscous force $\vec{F}^v_{ij}$ is computed by distributing the force $S^f_{ij}(P_i - P_j)$ over each DE such that:

$$\vec{F}^v_{ij} = \frac{L^k_w}{\sum_{k=1}^{3} L^k_w} S^f_{ij}(P_i - P_j)\vec{n}_{ij} \tag{5.30}$$

where L^k_w is the length of the interface between each DE k and the fluid domain interface $\partial\Omega_{ij}$.

The total force due to the fluid $\vec{F}^f$ on each DE is thus obtained by summing viscous and pressure forces from all incident facets with the buoyancy force such that:

$$\vec{F}^f = \sum_{(ij)incident} \left\{ \vec{F}^v_{ij} + \vec{F}^P_{ij} \right\} + \vec{F}^{b,k} \tag{5.31}$$

Finally, the coupling scheme involves two discrete equations to be solved, the continuity equation defined in Eq. 5.27 for all pores and the law of motion defined in Eq. 5.8 for all DE respectively. At this point, it is noteworthy that the mechanical scheme is fully explicit while the fluid scheme is implicit. The linear system built after Eq. 5.27 is solved to obtain the pressure field $P(t)$ at every time step t of the DEM. Then $P(t)$ is used to compute the fluid forces $\vec{F}^f$

which are added to the contact forces $\vec{F}$ in Eq. 5.6 before being time integrated to update the displacement $\vec{x}$ of each DE through Eq. 5.8.

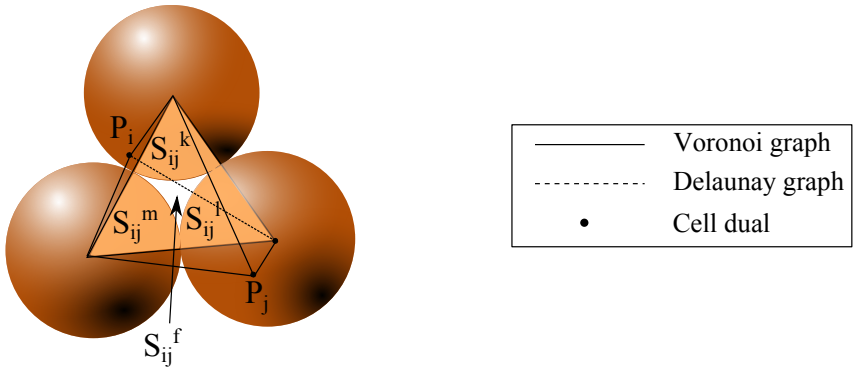

Figure 5.8: Volume decomposition: definition of facet-spheres intersections in 3 (from Chareyre *et al.*, 2012, modified).

Definition of local conductances

Although the DEM-PFV coupled scheme has been used and verified for studying granular materials saturated with both incompressible fluid (Catalano *et al.*, 2014; Chareyre *et al.*, 2012) and compressible fluid (Scholtès *et al.*, 2015), it has not been applied to rock-like material. Indeed, fractured rocks act as dual permeability media with fractures or cracks that might show up to 10,000 times higher permeability than the rock matrix. An enhancement was thus needed in the definition of the local conductance k_{ij} in order to capture the large permeability contrast between the fractures (pre-existing or induced) and the intact rock matrix. For instance, if the conductance of the throats located in the intact rock matrix can be computed as a function of the throat geometry as proposed in (Chareyre *et al.*, 2012), it cannot represent correctly the conductance of a crack. For that purpose, the broken interactions (or the ones belonging to a pre-existing fracture plane) are identified in the DEM code each time a crack occurs and the corresponding edges of the triangulated domain assigned a dedicated "cracked" state. The flow through all the facets related to the cracked edge is governed by the parallel plates model based on the cubic law (Figure 5.7) and the local interporal conductivity k_{ij} is thus computed as function of the crack's aperture which is updated at each time step of the simulation. Finally, this enhancement leads to a dual definition of k_{ij} that depends on whether the associated faced contains a crack or not such that:

$$k_{ij} = \begin{cases} \beta \dfrac{(h+h_i)^3}{12\mu} & \text{if the facet contains a crack} \\ \alpha \dfrac{S_{ij}^f (R_{ij}^h)^2}{\mu} & \text{if the facet is intact} \end{cases} \tag{5.32}$$

with α and β non-dimentional conductance factors that have to be calibrated (see Section 5.2.2), h the crack's aperture, which corresponds to the relative normal displacement between the unbonded particles, h_i the initial crack aperture which has to be defined a-priori as a material parameter (in the present study h_i is equal to 0 for the induced cracks), S_{ij}^f the pore-throat's cross-sectional area and R_{ij}^h the hydraulic radius of the pore (see (Chareyre *et al.*, 2012) for more details about these two latter parameters) and μ the dynamic viscosity of the fluid. The width of the plates has been considered here as equal to their length.

The numerical treatment of NF is similar to the ones for cracks. The difference lays in the fact that although the cracks have a null initial aperture $h_i = 0$ [m] when they form, a NF might have

an initial aperture $h_i \geq 0$ [m] at the given initial stress state (*e.g.*, *in-situ* conditions). Furthermore, the residual aperture h_r for NF and cracks can be different, *e.g.*, for the case of infilled NF.

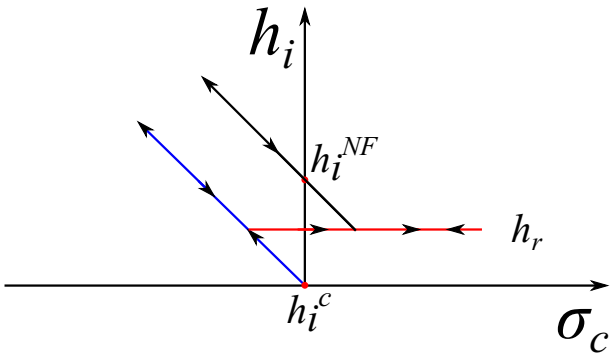

Figure 5.9: Aperture evolution during traction or compression of the discontinuity for a crack (blue line) and a NF (black line). The initial apertures h_i^c and h_i^{NF} of the crack and NF respectively are represented by red dots and the residual aperture h_r by a red line.

5.2.2 Hydraulic properties calibration

Similarly to the mechanical properties, the hydraulic properties of the numerical specimen must be calibrated and scaled to the ones of the material under consideration (Table 5.3). This is done by two permeability tests (one for the matrix and another one for the pre-existing fractures) performed on the complete discrete element model as the macroscopic permeability depends on the microstructure of the medium (*e.g.* the size distribution of the DE and the porosity of the assembly).

Permeability κ [m^2]	Fluid bulk modulus B_f [Pa]	Dynamic viscosity μ [Pa.s]	Fluid density ρ_f [kg.m^{-3}]
1×10^{-22}	2.2×10^9	1	1000

Table 5.3: Hydraulic properties of the rock and properties of the injection fluid.

For the matrix, a unidirectional flow of incompressible fluid is applied to the entire medium (Figure 5.10). The DE are fixed so that the medium is non deformable. A no-flux condition is imposed on the side-walls and a pressure difference ΔP is imposed along the vertical axis. Given that the volumetric flow rates at both extremities are equal at equilibrium, the macroscopic permeability of the specimen κ can be calculated using Darcy's law such as:

$$\kappa = \frac{Q}{A}\mu\frac{L}{\Delta P} \tag{5.33}$$

with A the cross-section of the sample, L its length and Q the volumetric flow rate at equilibrium.

In order to scale the permeability, the value of the dimensionless parameter α in Eq. (5.32) needs to be determined. For example, for modeling a rock with a permeability $\kappa = 1 \times 10^{-22}$ [m^2] using a DE packing of 10,000 DE with $D_{mean} = 0.048$ [m], $D_{min}/D_{max} = 0.55$ and a porosity $n = 0.374$, α is equal to 4.15×10^{-14}.

For pre-existing fractures, another test needs to be carried out to scale their permeability. In this case, a discontinuity plane is defined as in Section 5.1.3 (Figure 5.11). Outside this fracture plane, the sample is impermeable. Here again, the medium is non-deformable so as to keep the aperture constant during the simulation and a pressure difference ΔP is applied to generate a

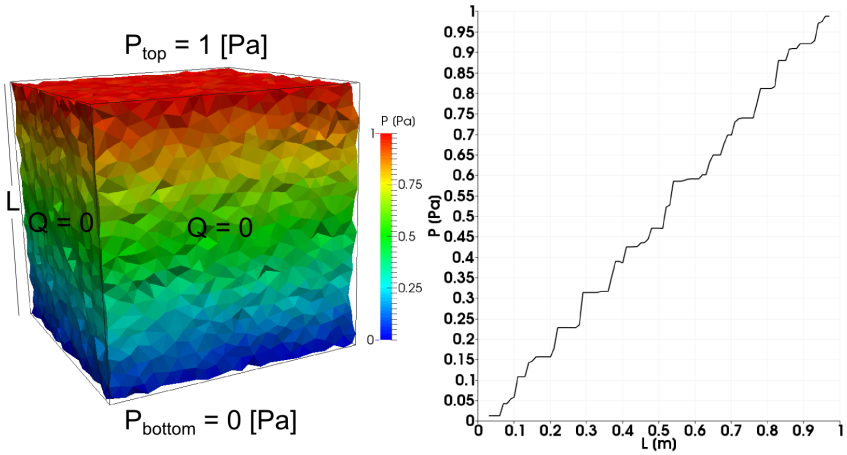

Figure 5.10: On the left, pore pressure distribution inside the rock matrix resulting from a permeability calibration test. On the right, the corrersponding vertical distribution of pore pressure inside the medium along its central column heigth.

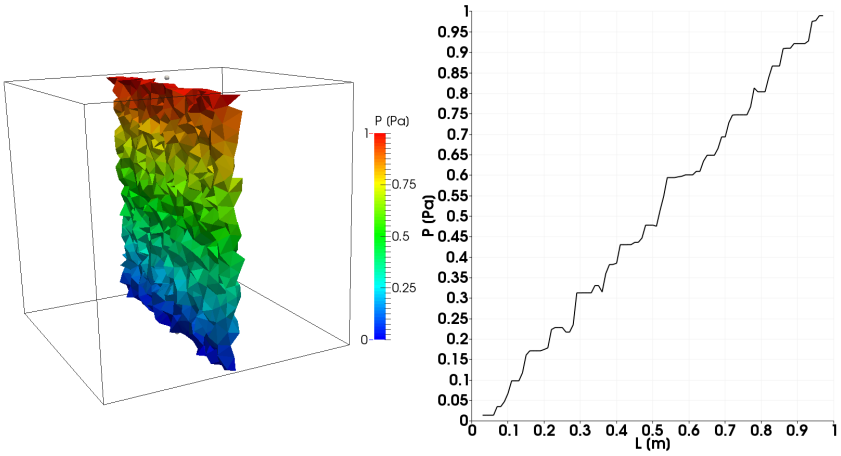

Figure 5.11: On the left, pore pressure distribution inside the persistent fracture plane resulting from a permeability calibration test.On the right, the corresponding vertical distribution of pore pressure along the vertical fracture.

flow along the fracture. Using the parallel plates model, the effective aperture h^{eff} of the fracture plane can then be calculated from the simulated flow rate Q such as:

$$h^{eff} = \left(12\mu\frac{Q}{\Delta P}\right)^{1/3} \tag{5.34}$$

Due to the tortuosity of the flow path through the fracture plane (resulting from the inter-particle cracks that constitute the fracture), a discrepancy can be observed between h^{eff} and the aperture defined at the particle scale h_i. As for the matrix, h^{eff} (*i.e.* the fracture permeability) can be adjusted by controlling the dimensionless factor β in Eq. (5.32). For example, for modeling a fracture with an aperture $h^{eff} = 1 \times 10^{-3}$ [m], with a packing of 10,000 DE with $D_{mean} = 0.048$ [m], $D_{min}/D_{max} = 0.55$ and a porosity $n = 0.374$, β has to be set to 1.4.

Chapter highlights

- A DEM model able to describe the progressive failure in rocks is used. The model can deal with rocks of different brittleness, non-linear failure envelopes and at the same time the macro-scopic behaviour of the material is DE size independent.
- The DEM model is coupled to a dual-finite volumes network to describe the fluid flow in the rock matrix and enhanced to deal with induced cracks and existing natural fractures.
- The calibration procedure for the mechanical and hydraulic properties is presented.

Chapter 6

Model verification

The following chapter presents a couple of typical benchmarking tests for HF models along with a comparison with experimental data from literature. Since the model is newly developed, the results of the benchmark tests are important for evaluating the model's precision but also to make clear possible limitations and weak points that will need further research. The comparison with the experimental work of (Stanchits *et al.*, 2013) highlights the novelties of the proposed numerical approach.

Layout of chapter

First, in Section 6.1 the model is verified against an analytical solution for the elastic opening of a fluid pressurized fracture in an impermeable elastic medium.

In Section 6.2, the numerical model's description of HF propagation is compared to the semi-analytical solution for the propagation of penny-shaped crack in an impermeable medium under constant fluid injection rate in a zero-toughness propagation regime.

Finally, the numerical model is compared to experimental findings coming from a laboratory HF experiment, in Section 6.3. The comparison concerns spatio-temporal evolution of crack events and injection-point pressure evolution.

6.1 Pressurized penny shaped crack opening

In order to test the validity of the numerical scheme, its predictions were verified against a well studied problem, often used as a basic benchmark test for HF models: the opening of a homogeneously pressurized penny shaped crack contained in an impermeable medium.

A circular fracture of radius $R = 0.1\,[\mathrm{m}]$ is introduced at the centre of an impermeable cubic block with a side length of 1 m (the fracture is small enough compared to the specimen's dimensions so as to avoid any boundary effects) and presenting the mechanical properties given in Table 5.2. The boundaries are stress-free so that $\sigma_h = 0$, $\sigma_H = 0$ and $\sigma_v = 0$, and a pressure $P = 1\,[\mathrm{MPa}]$ is applied inside the fracture by an incompressible fluid. Under this particular loading, the fracture does not propagate and the deformation corresponds to its elastic opening. The results can thus be compared to the analytical solution proposed by (Sneddon, 1946) which defines the opening u along the fracture as a function of the radial distance from the fracture centre r such that:

$$u(r) = \frac{2\,(1-\nu)\,PR}{\pi G}\sqrt{1-\left(\frac{r}{R}\right)^2} \tag{6.1}$$

with G the shear elastic modulus of the host medium and ν its Poisson's ratio.

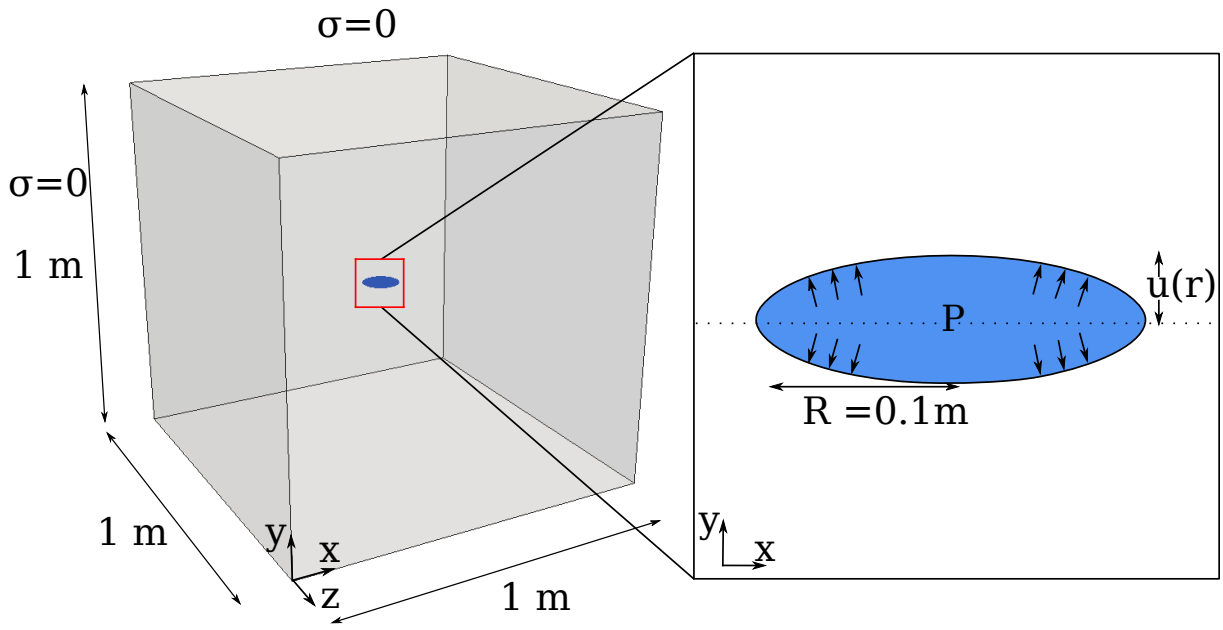

Figure 6.1: Illustration of the numerical set-up (BCs and geometry) for the problem of the elastic opening of a pressurized crack contained in an impermeable medium under constant imposed pressure.

The absolute values of the vertical displacement u of the DE located on each side of the fracture plane are plotted in Figure 6.2a together with the analytical solution obtained for $R = 0.1\,[\mathrm{m}]$. One can note that there is an offset of the measured values compared to the analytical solution. This is due to the numerical representation of the fracture which depends on the resolution of the model. Basically, the effective radius R_{eff} of the fracture is equal to $R_{eff} \simeq R + R_{DE}$, R_{DE} corresponding to the mean radius of the DE. Comparing the opening of the fracture with an effective radius $R_{eff} = R + R_{DE}$ to the numerical prediction confirms the accuracy of the coupled scheme in both terms of amplitude and distribution despite the scattering due to the discrete nature of the numerical model. The analysis shows good agreement between the analytical and numerical solutions and therefore validate the proposed scheme. To further illustrate the results, the displacement field obtained numerically is shown in Figure 6.2b.

6.2 Penny-shaped crack growth - zero toughness case

In most of the cases, the HF propagation during the treatment takes place close to the M-vertex regime (see Section 2.2). A verification example is thus set up for the limit case solution of a penny-shaped fracture propagating into an impermeable medium in absence of any toughness in the medium. That would mean that all the energy released during the propagation is dissipated by the viscous flow of the stored (in the fracture) fluid. The simulation is an attempt to mimic the idealized problem explained in the work of (Savitski and Detournay, 2002). Using the following scaling in order to turn all the involved variables in a dimensional form,

$$w(r,t) = \tilde{\epsilon}(t)L(t)\Omega(\tilde{\rho},\mathcal{P}(t)) \quad p(r,t) = \tilde{\epsilon}(t)E'\Pi(\tilde{\rho},\mathcal{P}(t)) \quad R(t) = L(t)\gamma(\mathcal{P}(t)) \quad \tilde{\rho} = \frac{r}{R(t)} \tag{6.2}$$

with $w(r,t)$ being the opening of fracture, $\tilde{\epsilon} = (\mu'/E't)^{1/3}$ a small number, $L(t) = \left(E'Q^3t^4/\mu'\right)^{1/6}$ the characteristic length, $\Omega(\tilde{\rho},\mathcal{P}(t))$ the dimensionless fracture opening, $p(r,t)$ the net pressure inside the fracture, E' the plane-strain Young's modulus, $\Pi(\tilde{\rho},\mathcal{P}(t))$ the dimensionless pressure

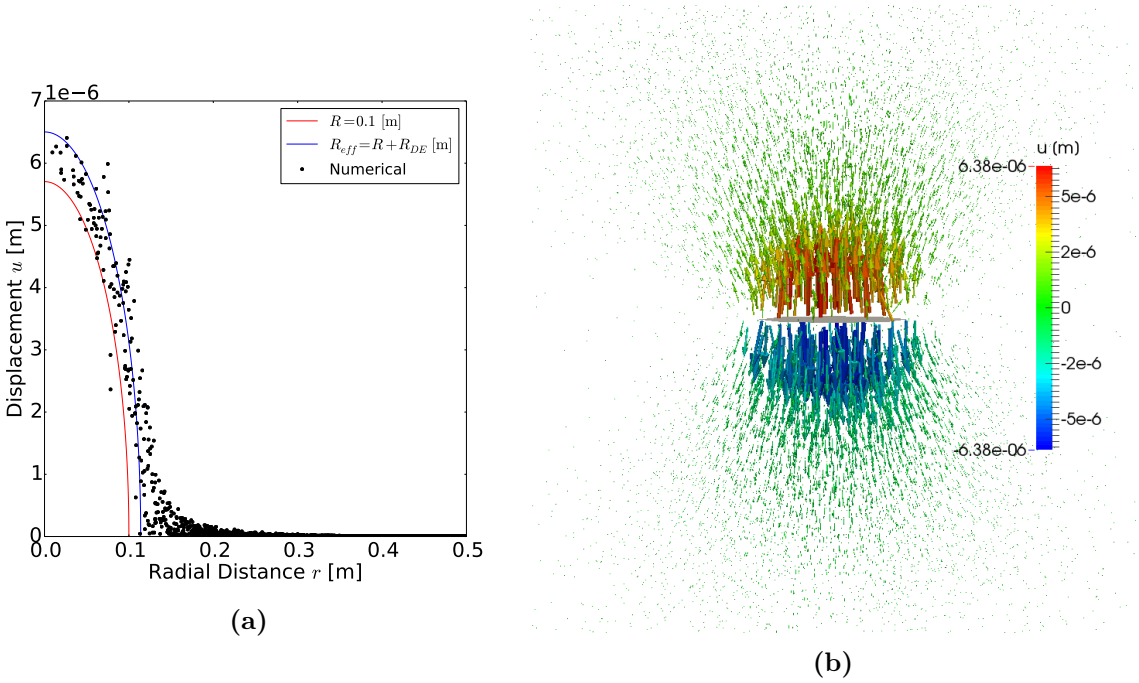

(a) **(b)**

Figure 6.2: (a) Opening of a pressurized penny-shaped crack of radius R embedded in an impermeable elastic medium: (a) comparison between the analytical solution proposed by (Sneddon, 1946) and the numerical prediction, (b) displacement field around the crack (the color bar corresponds to the normal displacement u [m]).

inside the fracture, $\tilde{\rho}$ the dimensionless radial coordinate, R(t) the fracture radius, γ the dimensionless fracture radius and $\mathcal{P}(t)$ a dimensionless parameter (*e.g.*, dimensionless toughness $\mathcal{K}$),

Specifically for the case of zero-toughness, the authors obtained a semi-analytical, self-similar solution for the dimensionless fracture aperture Ω_{m0} and fluid pressure Π_{m0} which reads:

$$\Omega_{m0} \simeq (C_1 + C_2\tilde{\rho})\,(1-\tilde{\rho})^{2/3} + B_1\left[\left(1-\tilde{\rho}^2\right)^{1/2} - \tilde{\rho}\arccos(\tilde{\rho})\right] \tag{6.3}$$

$$\Pi_{m0} \simeq A_1\left[\omega_1 - \frac{2}{3\,(1-\tilde{\rho})^{1/3}}\right] - B_2\left(ln\frac{\tilde{\rho}}{2}+1\right) \tag{6.4}$$

where $A_1 \simeq 0.3581$, $B_1 \simeq 0.1642$, $B_2 \simeq 0.09269$ $C1 \simeq 1.034$, $C_2 \simeq 0.6378$ and $\omega_1 \simeq 2.479$ are constants obtained at the fourth order polynomial solution.

An impermeable cubic specimen of 50×10^3 DEs of dimensions $50 \times 50 \times 50$ [m] containing a penny-shaped fracture at its center is considered. In order to represent a zero-toughness HF propagation, the tensile strength of the fracture's interactions is set to zero (and thus the fracture toughness drops to zero as well). Consequently, all the energy dissipation is caused by the viscous fluid flow and the elastic deformation of the medium. The cube's boundaries are stress-free since the far field stress doesn't affect the specific problem discussed here. The elastic constants of the material are given in the Table 6.1 along with the control parameters. A fluid with dynamic viscosity $\mu = 1 \times 10^{-3}$ [Pa.s] is injected at the centre of the fracture, whose initial aperture is $h_i = 1 \times 10^{-5}$ [m], at a constant flow-rate of $Q = 1 \times 10^{-2}$ [m^3.s^{-1}].

Young's Modulus E [Pa]	Poisson's Ratio ν [-]	Fluid Bulk modulus B_f [Pa]	Flow Rate Q [m^3.s^{-1}]	Fluid Viscosity μ [Pa.s]
20×10^9	0.12	2.2×10^9	1×10^{-2}	1×10^{-3}

Table 6.1: Mechanical properties and control parameters used in the verification test.

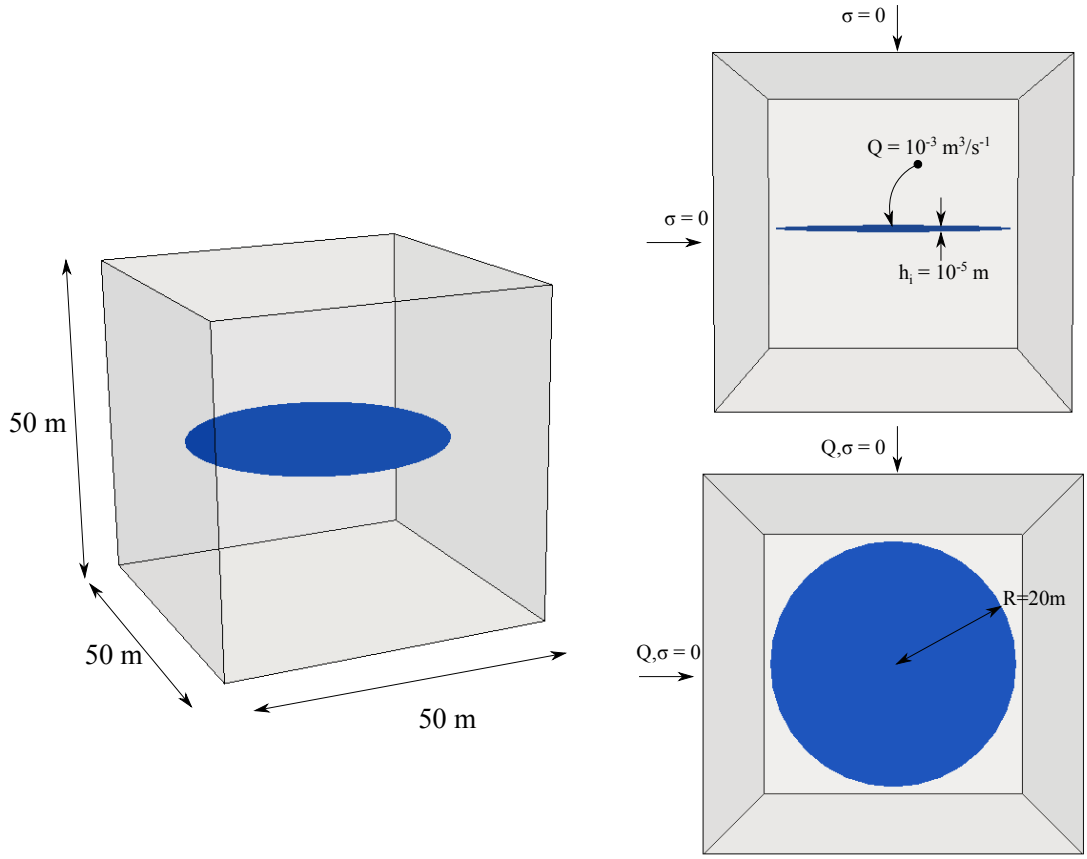

Figure 6.3: 3D, side and top views illustration of the numerical set-up (geometry and BCs) used for the zero-toughness HF propagation test.

The simulated aperture and pressure fields along the pre-existing fracture surface after $t = 5$ [s] of injection are presented in Figure 6.4. The comparison of the numerical *vs* semi-analytical solution of the distributions of aperture (Figure 6.5a) and pressure (Figure 6.5b) inside the fracture for $t = 5$ [s] are shown on Figure 6.5. The solid lines corresponds to the semi-analytical solution of Eq. 6.3 and Eq. 6.4 and the dot-symbols to the numerical values obtained by the local apertures h and pressure recorded on several cells along the fracture plane respectively.

By the time $t = 5$ [s] the HF has reached a half-length of 7 [m]. The distribution of the numerical values follow the distribution of the semi-analytical solutions. However, the numerical results show that the aperture ahead of the HF tip is not null as the semi-analytical solution suggests, which causes a discrepancy on the pressure distribution as well. The discrepancy is probably related to the existence of a remaining fluid lag during the injection. It is noted here that there is no enforced $h = 0$ condition at the tip related to zero fluid-lag as in the semi-analytical solutions (Lisjak *et al.*, 2017). Further research is currently being carried out on the specific issue.

6.3 Comparison with experimental data

In order to further validate the model, its predictions were compared to an experiment carried out by Stanchits and his co-workers on a block of Colton sandstone (Stanchits *et al.*, 2013). The rock block of dimensions $279.4 \times 279.4 \times 381$ [mm] was initially triaxially loaded in order to reproduce a representative in-situ state of stress. In the experiment, the major principal stress σ_v was applied vertically (Z-direction) and was set to $4,000$ [psi] (27.6 [MPa]). The intermediate

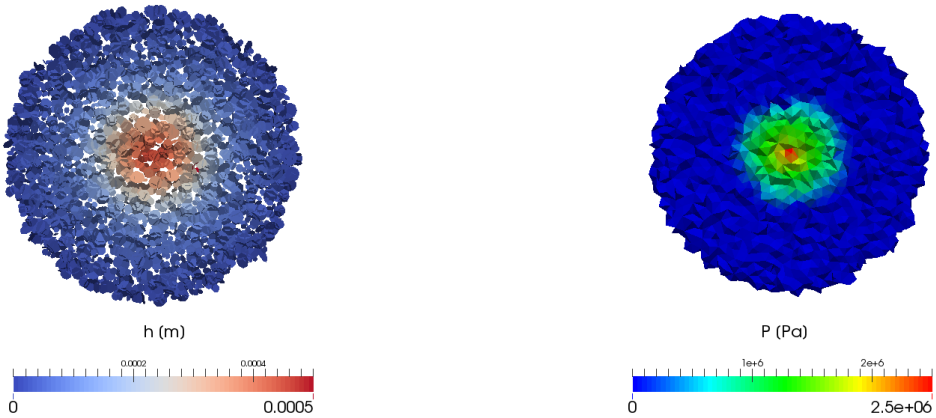

Figure 6.4: Top-views of: (Left) aperture and (Right) pressure field after $t = 5$ [s] of injection.

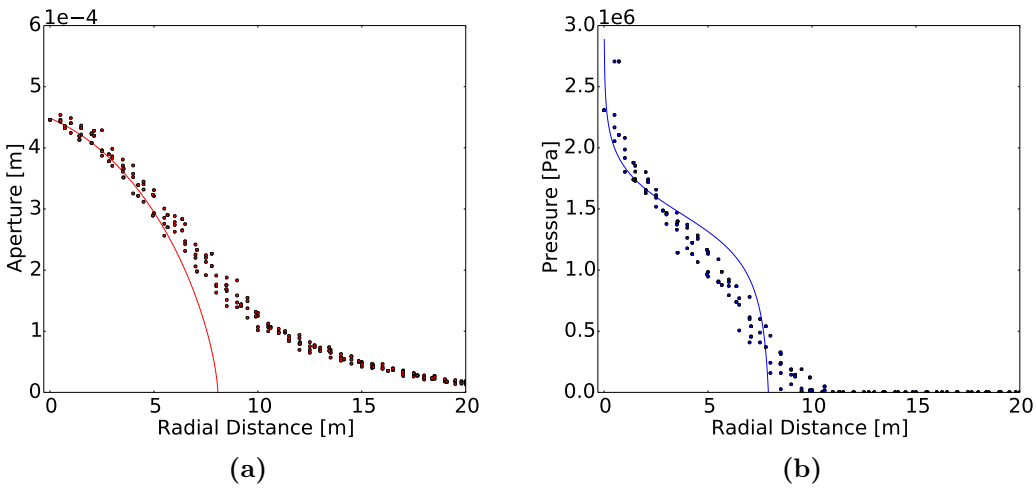

Figure 6.5: (a) Compariston to the analytical solution for the aperture distribution by (Savitski and Detournay, 2002) for t=5 [s]. (b) Compariston to the analytical solution for pressure distribution by (Savitski and Detournay, 2002) for t=5 [s].

principal stress σ_H was applied horizontally along the Y-direction and was set to $2,000$ [psi] (13.8 [MPa]). The minor principal stress σ_h was applied horizontally in the X-direction and was set to $1,000$ [psi] (6.9 [MPa]). The stress state was maintained during the experiment. The fracture was hydraulically induced by injecting a highly viscous fluid (2.5 [kPa.s]) at a flow rate of 0.83×10^{-7} [m^3.s^{-1}] in a borehole located at the center of the block. The experimental results of the injection test in terms of borehole pressure, volume of injected fluid, lateral deformation and AE measurements are shown in Figure 6.7a. The injection induced an increase of the fluid pressure up to the breakdown, reached for a pressure of about $4,700$ [psi] (32.4 [MPa]). The injection was then interrupted few seconds after the breakdown, resulting in high pressure decay. Post-mortem observations showed that, as expected, the vertical HF propagated in the direction perpendicularly to σ_h and presented a pancake like shape. A major finding of this study is that hydraulic fracturing actually initiated before the pressure breakdown as emphasized by the acoustic events recorded during the pressure increase, emphasizing therefore the progressive

nature of the associated failure processes. This experiment was thus simulated numerically in order to verify the ability of the model to reproduce the fracture path, injection pressure and progressive failure mechanisms. The simulations were run by injecting a compressible fluid with a viscosity significantly lower than in the experiments (25 [Pa.s]) since the flow rate was increased to $Q = 8.33 \times 10^{-6}$ [m/s]. Besides this lower fluid viscosity, the difference to the experiment lies in the fact that the injection was done in a pre-existing penny shaped crack of 50 [mm] diameter placed at the center of the numerical specimen.

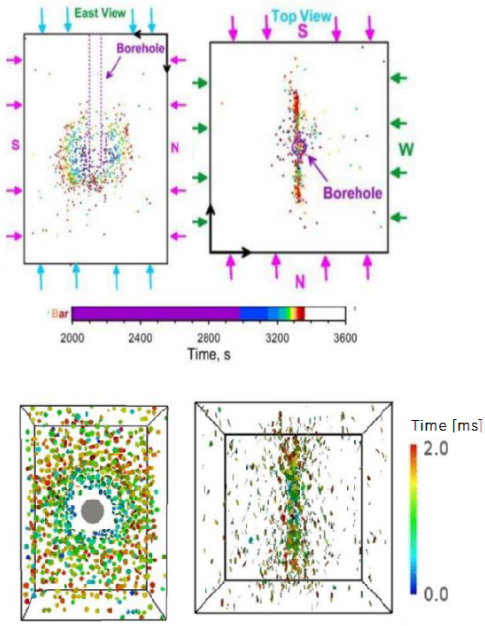

Figure 6.6: (Top) Acoustic emissions recorded during the experiment by (Stanchits *et al.*, 2013). (Bottom) Crack events recorded during the numerical test. In both cases the colour map is moving from cold colours to warm colours.

In addition, injection was not interrupted after the breakdown conversely to what was done in the experiment. The spatio-temporal distribution of the micro-crack events recorded during the simulation are shown in Figure 6.6 together with the AE hypocenters recorded during the experiment. Finally, in order to reduce the simulation time, the fluid compressibility was decreased, thus the same volume of fluid has been injected in shorter time.

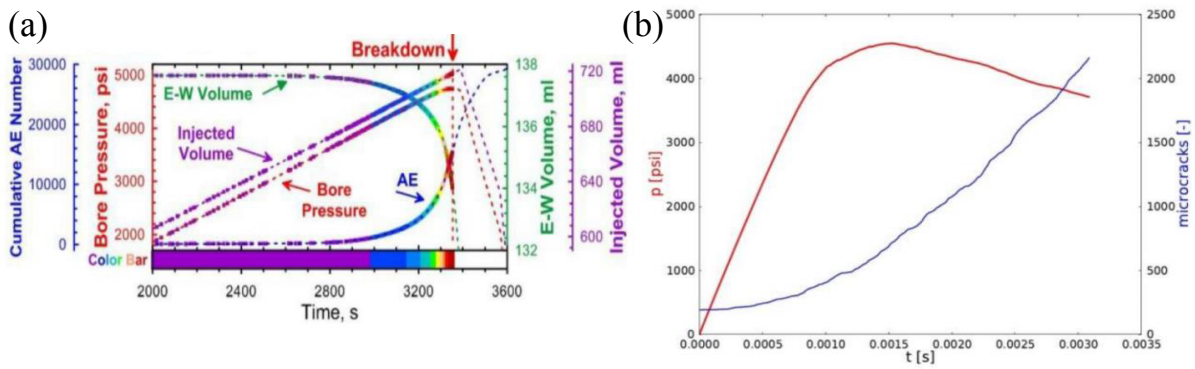

Figure 6.7: (a) Recorded evolution of the HF experiment untill breakdown (from Stanchits *et al.*, 2013). (b) Pressure response and cummulated crack events recorded during the simulation.

As observed experimentally, the hydraulically induced micro-cracks coalesced to form a ver-

tical HF which propagated from the center of the specimen towards its boundaries perpendicularly to the minor principal stress direction. Moreover, the localization and the time evolution of the micro-cracks are in reasonably good agreement with the AE events. However, one has to be careful when comparing micro-cracking and AE events as, even though correlated, several micro-cracks can be part of a unique acoustic event. With regards to that, the evolution of the micro-cracking over time is slightly different from the AE measurements and their spatial distribution is more diffuse. Research is currently carried out to relate micro-cracking to acoustic events. The evolution of the injection point pressure along with the micro-cracking evolution are presented in Figure 6.7b.

Despite the assumptions made in the simulation, the pressure breakdown value is comparable to the one obtained experimentally as presented in Figure 6.7). The overall evolutions of both the pressure and the micro-cracking events matches fairly well the laboratory data up to the breakdown. Moreover, similarly to the AE, micro-cracking occurs during the entire injection phase and continues after the breakdown However, the pressure increase exhibits an earlier and more pronounced departure from linearity in the simulation compared to the experiment. This discrepancy could be due to the nature of the fluid and requires further study to reach to a solid conclusion. Nevertheless, the proposed approach seems well adapted for simulating hydraulic fracturing processes in rocks.

Chapter highlights

- The model was verified against the elastic solution for pressurized penny-shaped crack contained in an elastic impermeable rock matrix. The compared property was the fracture aperture under constant pressure.
- The model was verified against the self-similar vertex solution of zero-toughness propagation into a homogeneous impermeable medium. The compared variables were aperture and pressure distributions at a given time.
- The model was qualitatively compared to a lab experiment. Important similarities arose from the comparison of pressure-evolution and cumulative cracks evolution.

Part III

Applications

Chapter 7

Injection in intact rock

This chapter presents the application of the PFV-DEM scheme to the study of hydraulic fracturing in intact rock. Regarding the facts listed in Section 2.1, the influence on the HF progression of the medium permeability and the contributions of the fluid compressibility, the flow rate and the stress state configuration are investigated for a single injection treatment first. In the case of non-favorable stress state orientation, the curvature of the HF and the crack aperture distribution over its surface are analysed to assess the possibility for the proppant to propagate correctly inside the fracture. Then, the results from multiple injection treatments are presented and the effect of the perforation clusters interval, the wellbore and the cluster orientations are discussed with regard to the evolution of the fractured volume and fracture intensity indexes. The way the simulation is set-up is presented extensively. The control parameters and fluid properties of the reference case are scaled to represent a case comparable to lab experiments such as (Stanchits *et al.*, 2013).

Layout of chapter

The analysis starts with single injection tests in an intact specimen in Section 7.1. The model set-up along with its geometry and boundary conditions is first presented. Then a reference case is shown, introducing the main properties that will be followed throughout the analysis namely the pressure at the injection point, the fractured volume and fracture intensity. A parametric study is following, studying the sensitivity of the results on parameters such as stress field, rock-matrix permeability, flow rate, fluid compressibility and model's resolution.

In Section 7.2, multiple sequential injection studies are presented. First, the robustness of the model is studied in terms of boundary effects and packing-fabric effect on the resulting fractured volume. Then, the way the HFs affect each-other, due to local re-orientation of the stress field, in terms of final HF patterns and the related impact on fractured volume and fracture intensity is studied. The parametric space includes spacing between the injection sources, well-bore deviation from the σ_3 axis, and injection slot orientation.

7.1 Single injection in intact specimen

The propagation of a single HF within a synthetic homogeneous rock is first studied so as to investigate the effects of the state of stress, permeability, fluid compressibility and injection flow rate on the overall process.

7.1.1 Geometry and boundary conditions

A numerical specimen with dimensions $1 \times 1 \times 1\,[\mathrm{m}]$ is considered here. Its hydro-mechanical properties were calibrated to the ones presented in Table 5.2 and Table 5.3. For all the studied

cases, the specimen is first subjected to a drained triaxial compression in order to reach a predefined "in-situ" state of stress. The injection is initiated once the desired boundary stresses are reached and the system is at equilibrium. The excess pore pressure is considered null when the injection starts.

The well is not explicitly represented in the simulations. Instead, the fluid is injected in a circular pre-existing fracture that represents a perforation slot (or a perforation cluster). The slot is simulated by a disk-shaped discontinuity that follows same logic as the NFs. An autonomous h_i and mechanical properties can be defined for it. The slot is located at the centre of the specimen and can be preferentially oriented with respect to the stress state. A fluid with the properties defined in Table 5.3 is injected at the centre of the slot under a constant imposed flow rate Q_{in}. Permeable boundaries have been assigned by an imposed zero pore-pressure condition.The material properties and control parameters for the simulation were selected after the dimensional analysis by (De Pater *et al.*, 1994) as shown in Section 2.2 and represent a set-up close to the ones used in (Stanchits *et al.*, 2013). The synopsis of the model is shown on Figure 7.1.

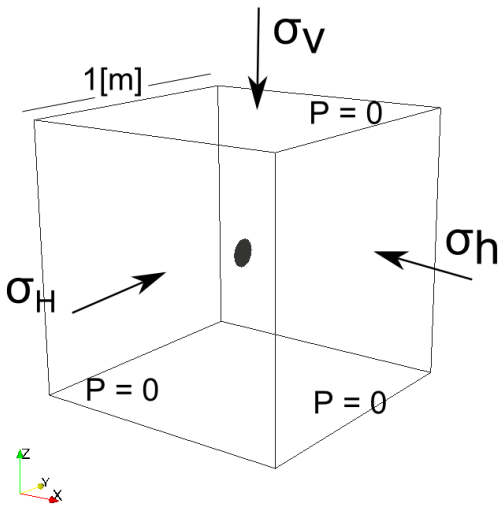

Figure 7.1: Model geometry and hydromechanical boundary conditions.

During the test, in addition to the stresses, strains and pore pressure distribution inside the sample, every crack event is recorded along with its failure mode, orientation, aperture and time of occurrence so as to provide a spatio-temporal overview of the coupled problem.

7.1.2 Reference test

The response of the numerical specimen obtained for an injection performed under the conditions defined in Table 7.1 is shown in Figure 7.2 in terms of borehole pressure and global deformation.

Parameter	Symbol	Value	Unit
Vertical stress	σ_V	10×10^6	[Pa]
Maximum horizontal stress	σ_H	13×10^6	[Pa]
Minimum horizontal stress	σ_h	6×10^6	[Pa]
Boundary pore pressure	$P_{boundary}$	0	[Pa]
Flow rate	Q_{in}	0.83×10^{-5}	[$m^3.s^{-1}$]

Table 7.1: Imposed loading conditions for the reference test.

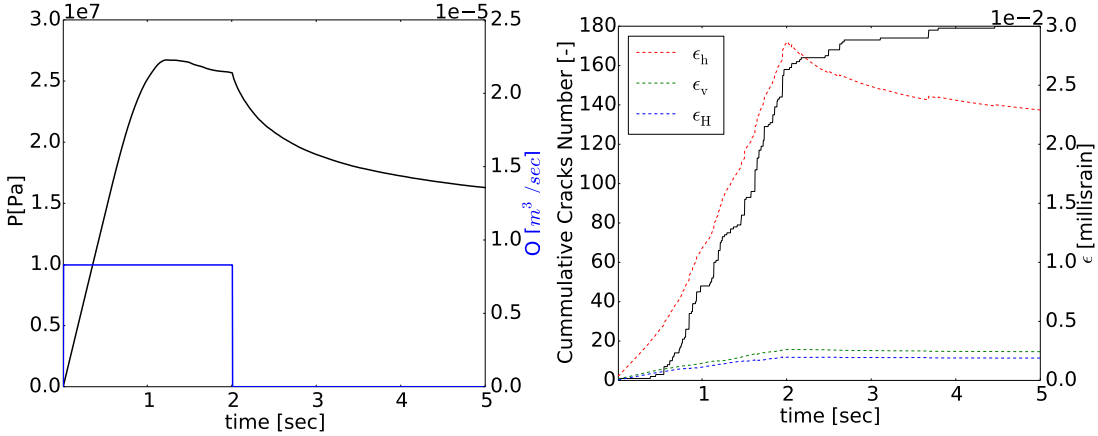

Figure 7.2: Evolutions of (a) pressure (in black) and flow rate (in blue) at the injection point and (b) deformation of the sample along each of its principal direction with the cumulative number of induced cracks (in black).

The injection produces a volumetric increase of the sample along the σ_h axis as shown by the rise of ϵ_h from the beginning of the injection till the shut-in ($t = 2$ [s]), since the HF develops perpendicular to the σ_h axis (x plane, see Figure 7.3). Afterwards, in accordance with the borehole pressure, ϵ_h decreases asymptotically up to reach an equilibrium state. It is noteworthy that since the permeability of the matrix is very low, at the test's time-scale there is no fluid diffusion observed into the matrix.

The HF results from the coalescence of the cracks induced at the DE scale as illustrated on Figure 7.3a. These cracks occurred here all along the pressurization of the slot as well as after the shut in, emphasizing the progressive nature of the process which is not uniquely reduced to the phase of the pressure breakdown as it has been observed experimentally by (Stanchits *et al.*, 2013). During the experiment the authors have shown that acoustic emissions were recorded right after the injection started, long before breakdown and also that they kept appearing for some time after the shut-in.

The crack events are represented in Figure 7.3 as disks coloured according to their time of occurrence and to their current aperture. Similarly, to the aforementioned experimental findings, the HF first localized around the injection slot before extending further away on the same plane, perpendicularly to the minimum principal stress σ_h.

In order to characterize the HF during its propagation, the total fracture volume $P33$ and the associated fracture intensity $P32$ were recorded. The $P33$ and $P32$ indices are calculated as:

$$P33 = \frac{V_{HF}}{V_{total}}\,[-], \quad P32 = \frac{A_{HF}}{V_{total}}\,[m^{-1}] \tag{7.1}$$

with V_{total} the overall volume of the specimen, A_{HF} the total fracture surface area and V_{HF} the total fracture volume.

A_{HF} is computed by:

$$A_{HF} = \sum_{c=1}^{N_c} A_{ij}^c \tag{7.2}$$

whereas V_{HF} is computed as:

$$V_{HF} = \sum_{c=1}^{N_c} \left(A_{ij}^c \times h_{ij}\right) \tag{7.3}$$

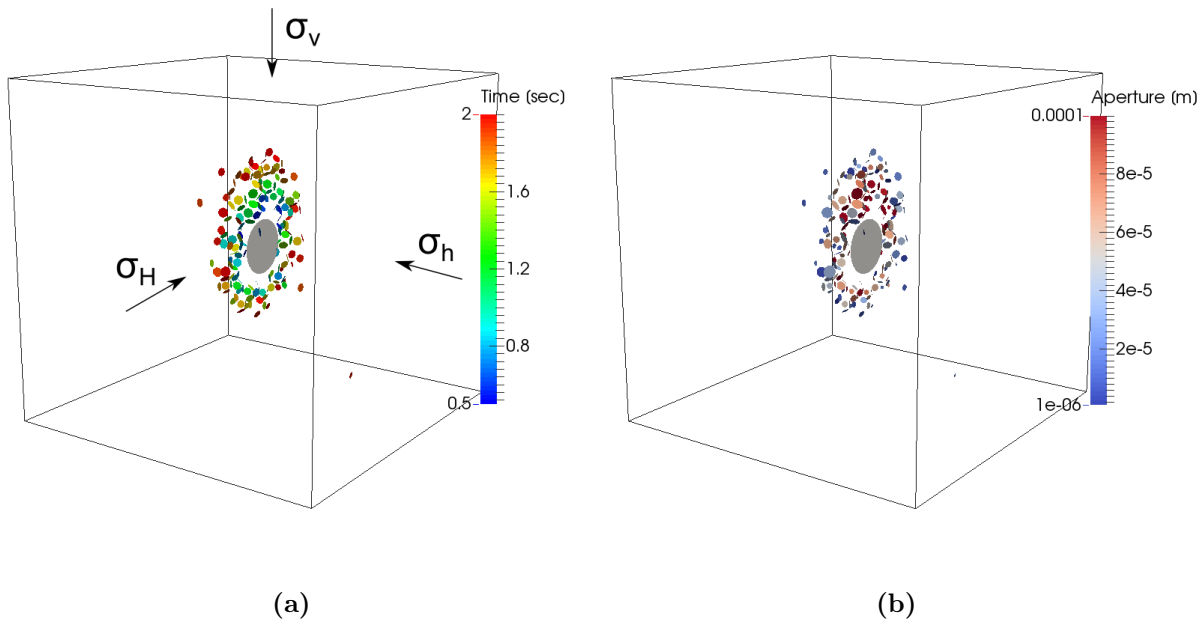

Figure 7.3: Crack events taking place within the block during the injection: (a) colored as a function of time occurrence and (b) colored as a function of their aperture.

with h_{ij} the aperture of the crack that formed between DEs i and j and that evolves during the simulation and A^c_{ij} the surface of the crack between DEs i and j.

The evolutions of $P33$ and $P32$ are presented in Figure 7.4. One can note that the fracture volume $P33$ is strongly related to the deformation ϵ_h of the sample along the minimum principal stress direction (Figure 7.2b), since the cracks open as the fluid propagates inside the HF. On the other hand, the fracture intensity $P32$ is directly related to the number of cracks (Figure 7.2b) taking place inside the medium, since they all have similar sizes ($A^c_{ij} \propto D^2_{mean}$).

7.1.3 Sensitivity analysis

Several tests were performed considering different properties for the rock and the injected fluid as well as different states of stress and injection flow rates in order to assess the impact of each control parameter on the response of the medium. The results of these tests are presented and discussed in the following subsections.

Permeability

Depending on the characteristic injection time with respect to the medium's permeability, leak-off phenomena can take place from the fracture to the matrix. In order to investigate up to which extent this assumption is valid, injection tests were performed on three different mediums representing rock materials with different matrix permeabilities:

- a permeable rock with $\kappa = 1 \times 10^{-16}\,[\mathrm{m}^2]$ which would correspond to, *e.g.*, a sandstone,
- a low permeability rock with $\kappa = 1 \times 10^{-22}\,[\mathrm{m}^2]$, which would correspond to a very tight formation, *e.g.*, a clayey rock and
- a fully impermeable rock where the fluid flows only inside the fracture and the induced cracks.

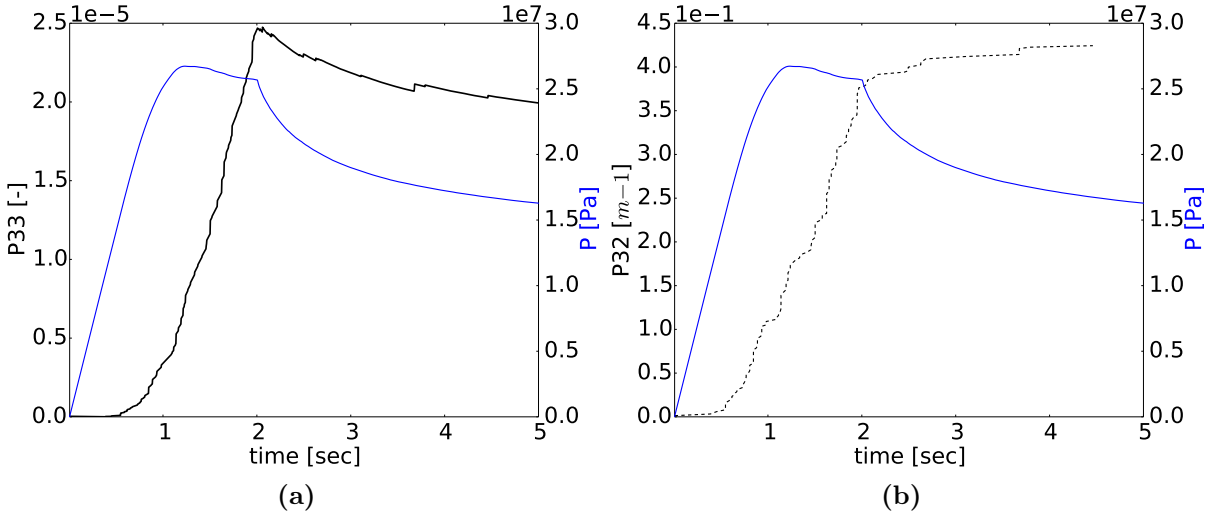

Figure 7.4: Evolutions of (a) fracture volume $P33$ and (b) fracture intensity $P32$ during the injection. The pressure evolution at the injection point is also represented for both cases (blue lines).

As illustrated in Figure 7.5, for the given injection time and flow rate, the low permeability and the impermeable rocks show a very similar response to the injection in terms of pressure at the injection point and total fracture volume evolutions. On the other hand, the more permeable rock presents a lower break-down pressure value due to the fluid diffusing behind the fracture front which tends to reduce the effective stress applied at the crack tip. Also the $P33$ value remains lower with the permeable rock (Figure 7.5a) because fewer cracks are generated (Figure 7.5b) and thus less fluid flows inside the HF.

Since we were interested here in simulating HF propagation in low permeability rocks, considering the given flow rate, the choice was made to run all the simulations with a fully impermeable rock medium as this solution enables a consequent reduction of the computational cost because the fluid domain is restricted to the network of cracks.

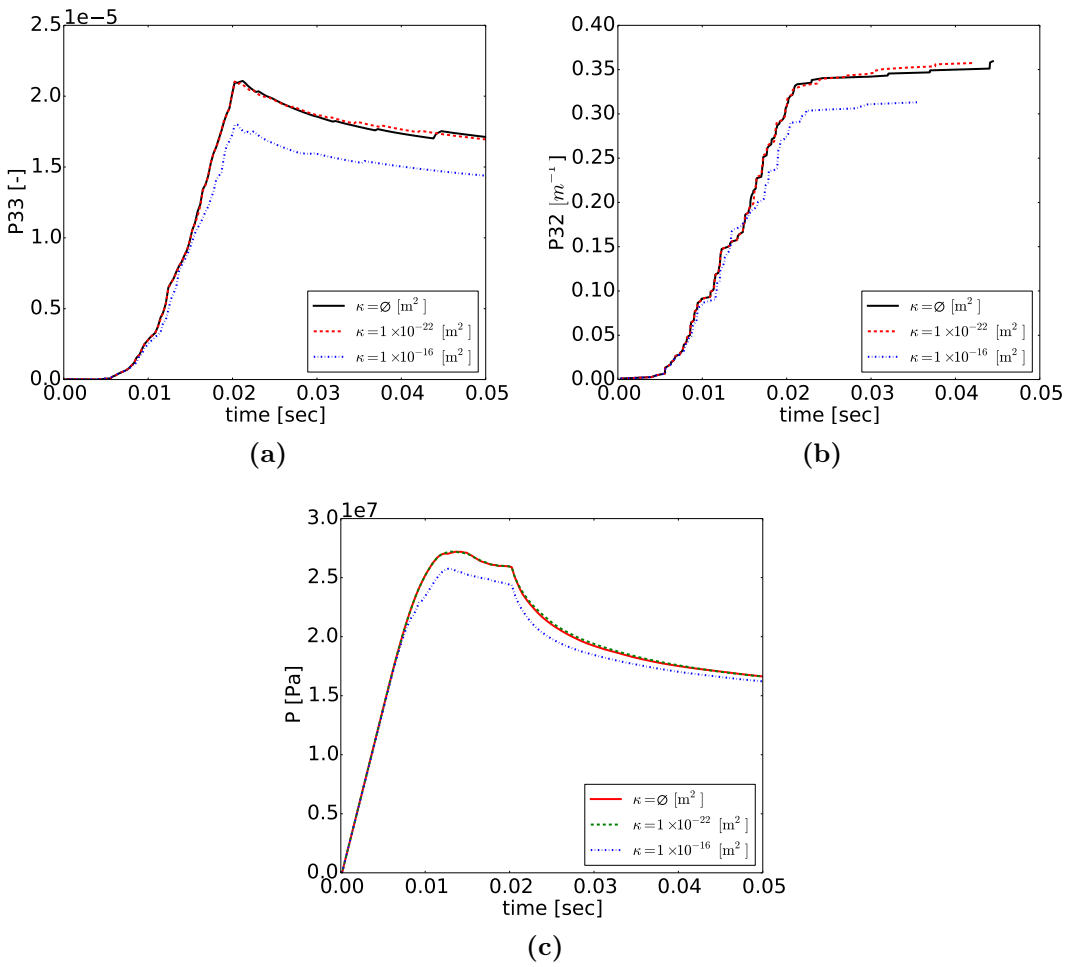

Figure 7.5: Evolutions of (a) fracture volume $P33$, (b) fracture intensity and (c) pressure P for 3 different matrix permeabilities κ.

Fluid compressibility

The evolution of both the pressure and $P33$ obtained for three simulations run with different fluid bulk moduli B_f equal respectively to 2.2×10^9 [Pa], 2.2×10^{10} [Pa] and 2.2×10^{11} [Pa] is presented in Figure 7.6.

On one hand, the three cases show very similar responses in both terms of pressure (*e.g.*, break down pressure and post-shut in pressure) and total fractured volume. Hence, the fluid bulk modulus does not thus influence the model's predictions. On the other hand, using fluids with high B_f enables to decrease the needed time domain to cover a similar hydro-mechanical response of the model. In particular, less time is needed to obtain the same HF length. Thus, the selection of a low compressible fluid seems an acceptable assumption that enables to speed up the calculations without affecting the model predictions.

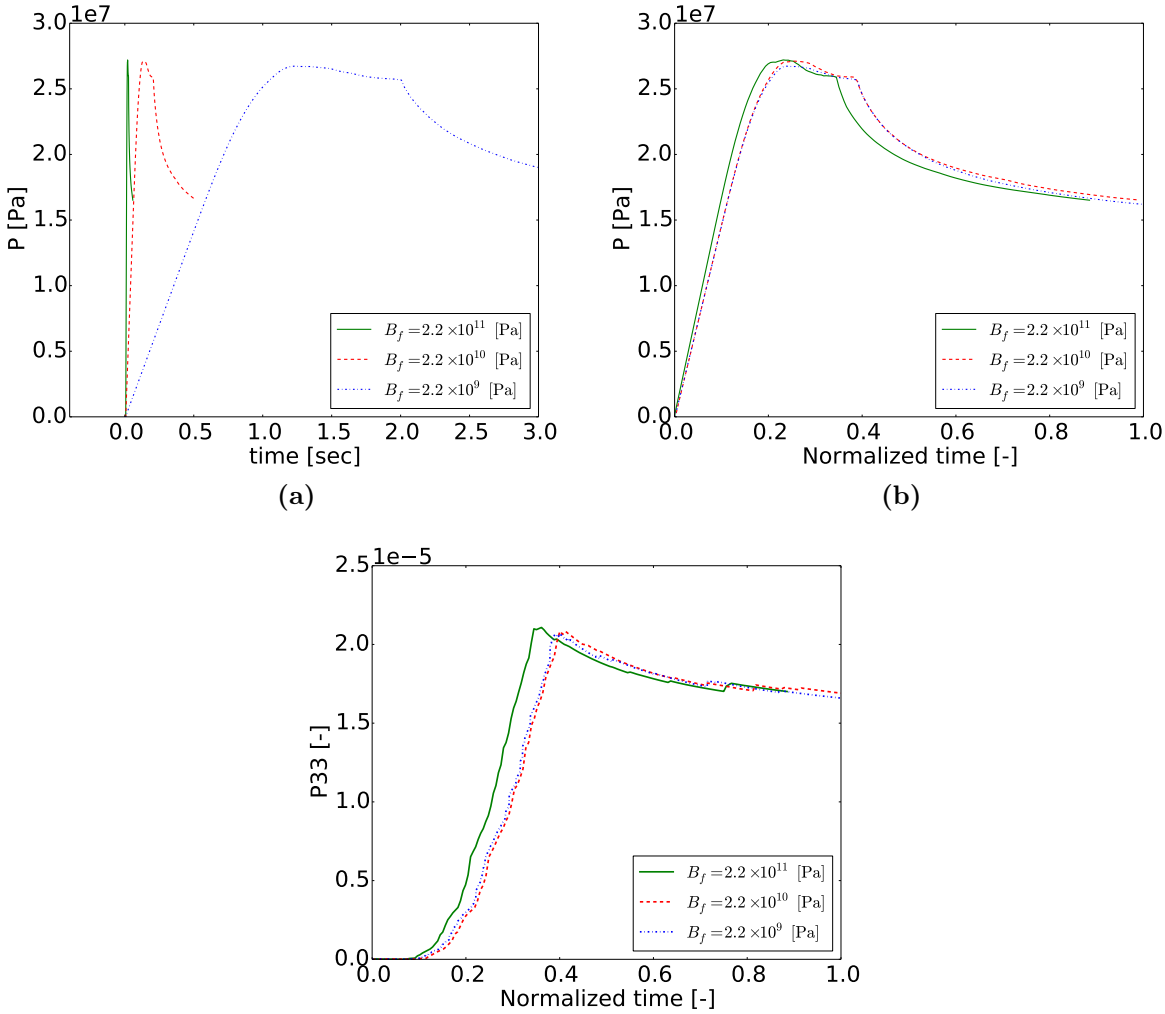

Figure 7.6: Evolutions of (a) pressure P over time, (b) same pressure P over normalized time and (c) the total fracture volume $P33$ for the three different fluid bulk moduli B_f.

State of stress

One of the main concerns while simulating hydraulic fracturing relates to the direction of propagation with regards to the stress field. Considering θ_s as the angle between the slot's normal and the direction of the minimum horizontal stress σ_h, four different configurations were tested to assess the efficiency of the proposed approach to capture the effect of stress field on HF propagation:

- a reference case corresponding to $\theta_s = 0°$, *i.e.* with the perforation slot aligned with the maximum horizontal stress σ_H,
- a case with the perforation slot rotated by $\theta_s = 90°$ around the vertical axis and thus aligned with the minimum horizontal stress σ_h and
- two intermediate cases with the slot rotated respectively by $\theta_s = 40°$ and $\theta_s = 60°$ around the vertical axis.

The HF patterns obtained in the two extreme cases ($\theta_s = 0°$ and $\theta_s = 90°$) for the same total injected volume are presented in Figure 7.7. In the reference case ($\theta_s = 0°$), the HF initiates as a localization of cracks around the injection slot and then keeps propagating on the same plane, *i.e.*, perpendicular to σ_h. On the other hand, for $\theta_s = 90°$, the HF is more diffused near the

injection slot before reorientating into the plane perpendicular to σ_h. The crack's orientation distribution diagrams plotted on the same figure shows that, even locally, the stress field fully controls the crack orientation and a complex distribution can be expected before the global re-orientation of the HF as observed for $\theta_s = 90°$.

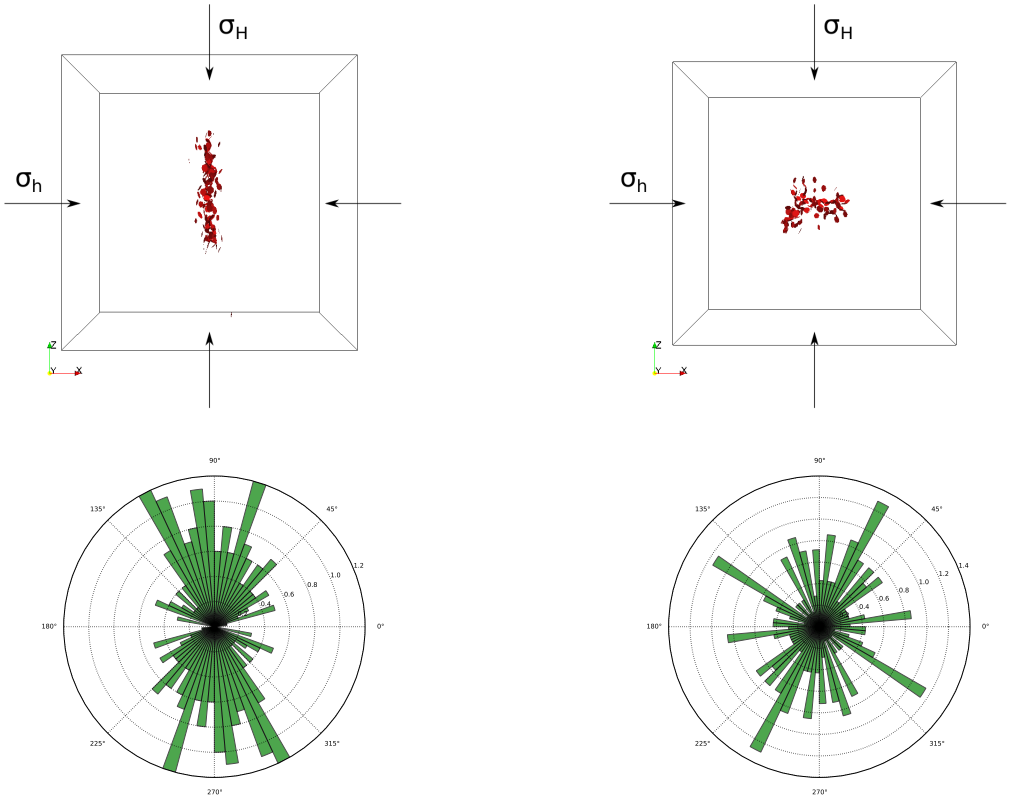

Figure 7.7: Specimen from top view with the HF represented as a set of cracks. On the left, the reference case $\theta_s = 0°$ with the corresponding orientation distribution of the cracks. On the right, the case for which the slot was rotated by $\theta_s = 90°$ around the vertical axis.

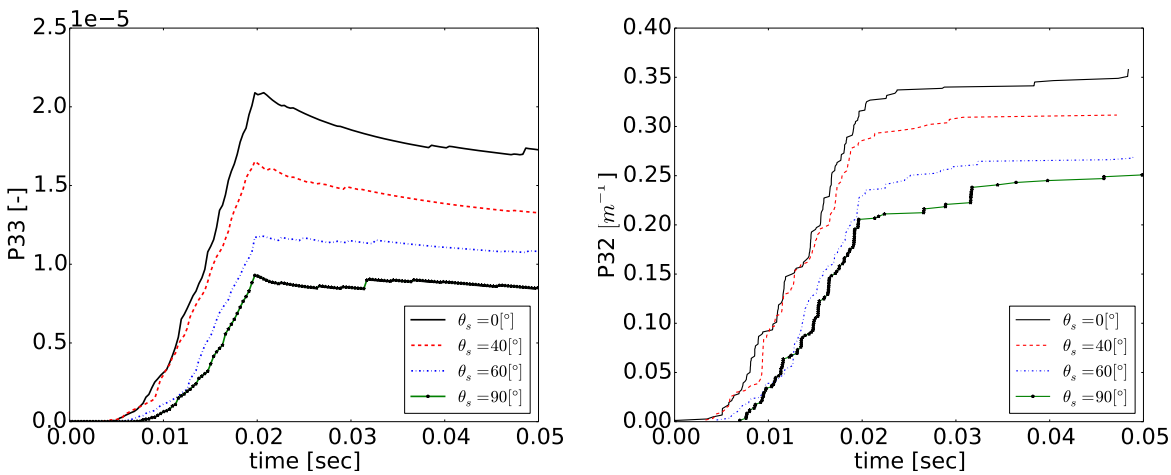

(a) **(b)**

Figure 7.8: Evolutions of (a) fracture volume $P33$ and (b) fracture intensity $P32$ for four different orientations θ_s of the injection slot with respect to the vertical axis.

The evolutions of $P33$ and $P32$ obtained for all four cases are compared on Figure 7.8. Here again, one can see that the relative orientation of the injection slots with respect to the the stress-field plays an important role on the stimulated volume. For instance, the alignment of the injection slot with σ_H promotes not only a planar HF but also eases the aperture of the cracks that leads to higher $P33$ values. On the contrary, $P33$ and $P32$ tend to decrease when θ_s increases from 0° to 90° due to the tendency for the HF to re-orientate toward the σ_H direction that leads to an increase of its curvature with θ_s. This tendency might have some consequences on the choices made in the completion design of HF with regards to the proppant. Indeed, curved profiles may reduce the possibility to inject proppant in all areas of the HF. In order to investigate this latter point, the aperture distribution of the simulated HF were studied for three different orientations of the injection slot ($\theta_s = 0°, 40°, 90°$). The results of this study are summarized in Figure 7.9. For illustrating the potential of the HF to be propped, a threshold aperture 1×10^{-4} [m] was considered as a reference value below which the proppant could not enter the HF (Figure 7.9, middle). One can see that, as the slot orientation becomes less favorable to generate a planar fracture, more and more cracks exhibit an aperture below this reference value. Consequently, proppant will experience more difficulties to be transported inside the HF (Figure 7.9, bottom). For example, for the case where $\theta_s = 0°$, 15.56% of the induced cracks have an aperture above this threshold value while the value is reduced to 6.61% for the case where $\theta_s = 90°$.

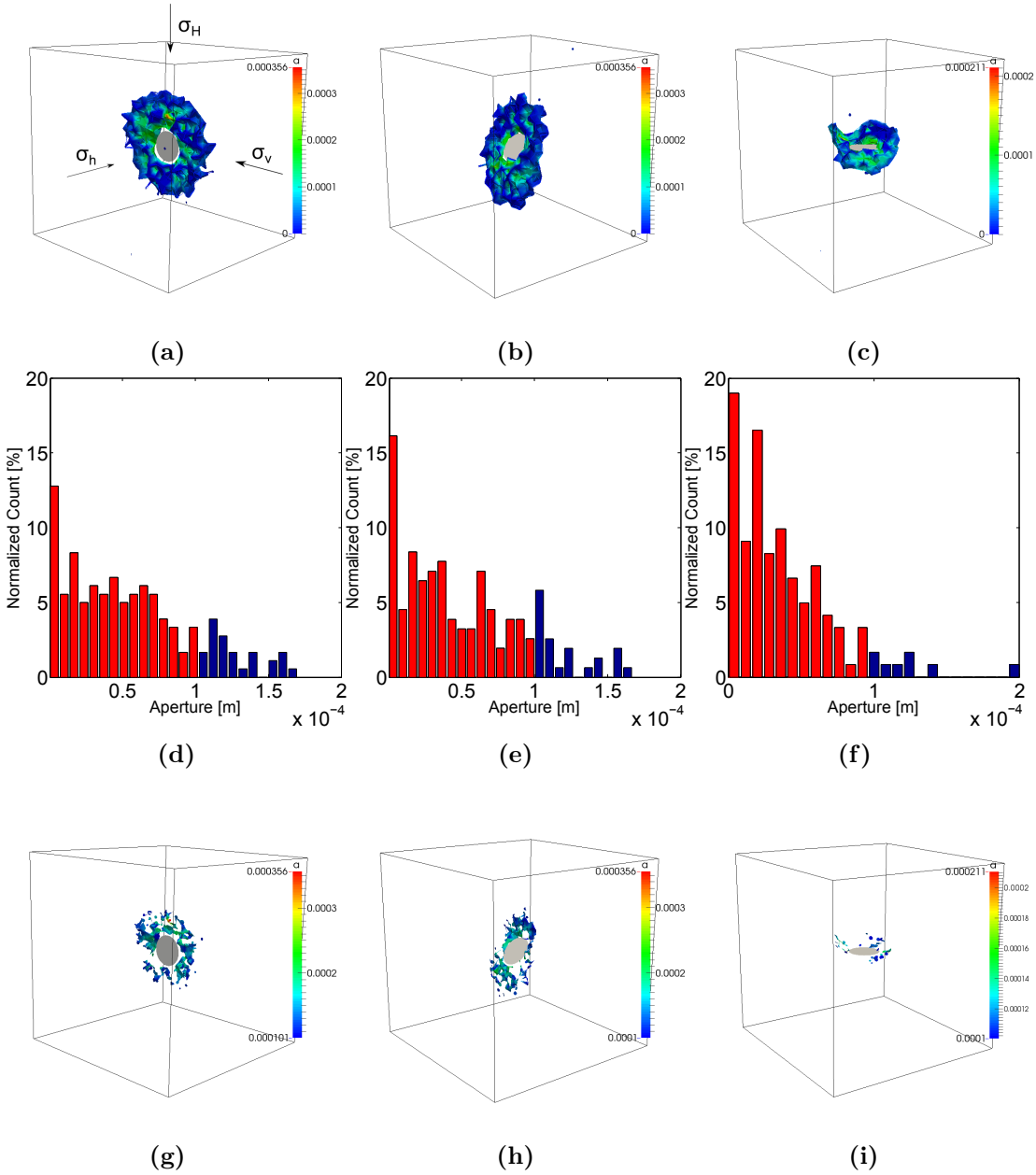

Figure 7.9: Comparison between three different configurations corresponding to three different orientations of the injection slot around the vertical axis: (left) reference case $\theta_s = 0°$, (middle) $\theta_s = 40°$ and (right) $\theta_s = 90°$. Top : HF surfaces coloured as a function of their local apertures (scale in $[m]$). Middle : apertures distribution histograms with the apertures higher than $1 \times 10^{-4}\,[m]$ in blue. Bottom: HF surface that can be propped (cracks with an aperture higher than $1 \times 10^{-4}\,[m]$, scale in $[m]$).

Imposed flow rate

Flow rate is a control parameter which might affect the pressure response and the fracture pattern of HF. The same HF treatment was here performed with three flow rates Q_{in} equal respectively to $0.83 \times 10^{-5}\,[\mathrm{m}^3.\mathrm{s}^{-1}]$, $1.66 \times 10^{-5}\,[\mathrm{m}^3.\mathrm{s}^{-1}]$ and $4.15 \times 10^{-5}\,[\mathrm{m}^3.\mathrm{s}^{-1}]$. One can observe in Figure 7.10 that, besides the fact that the break down pressure is reached more rapidly when the flow rate increases, its value tends to increase drastically as well with the flow rate. This result is in agreement with previous theoretical and experimental works (Zoback *et al.*, 1977) as well as with the dimensionless analysis provided by (Abbas and Lecampion, 2013). Notably, the influence of the flow rate on the $P33$ and $P32$ is small, these two values having a tendency to

increase linearly with Q_{in}.

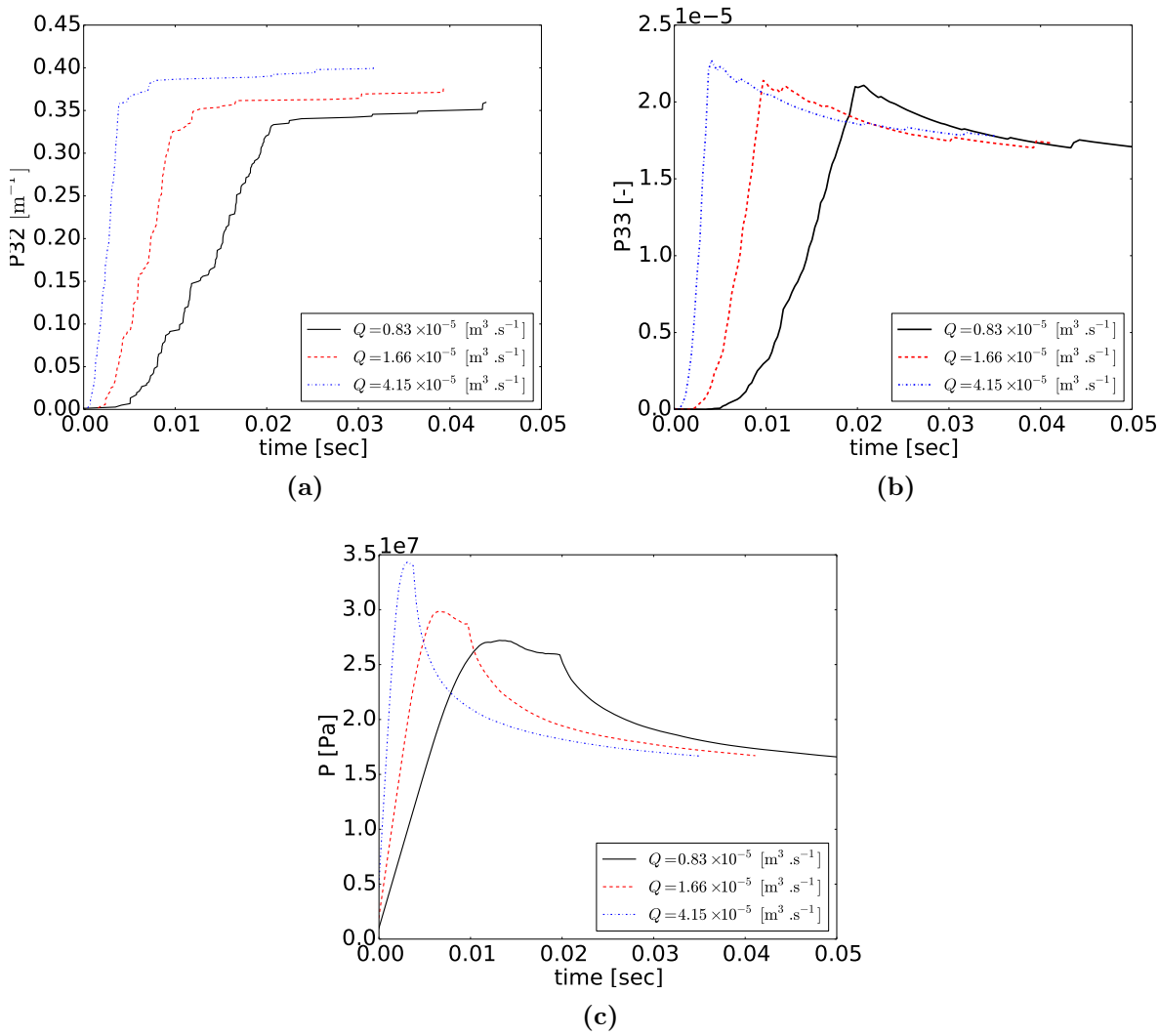

Figure 7.10: Evolution of (a) fracture intensity $P32$ (b) fracture volume $P33$ and (c) pressure P during the injection for different injection flow rates Q_{in}.

Model's resolution

Finally, because it is an important aspect of the model, the effect of its resolution was investigated. Specimens with 25×10^3, 50×10^3 and 100×10^3 of DE were thus generated and used in the simulations and the results compared to the reference case of 10×10^3 DE. Of course, the hydro-mechanical properties of the different specimens were carefully calibrated so as to represent the same material (Table 5.3).

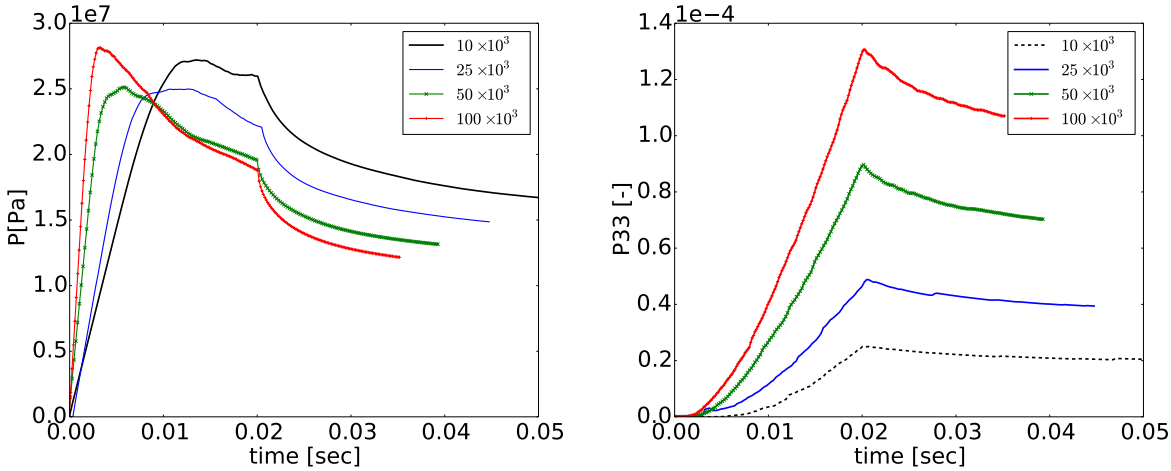

Figure 7.11: Effect of the discretization of the model on its response to hydraulic injection (N_{DE} corresponds to the number of DE constituting the numerical specimen).

For all cases the observed simulated breakdown pressure is similar with, however, a difference in the pressure drop which tends to be steeper for the finer discretization cases than for the coarser ones (see Figure 7.11). In terms of the associated final HFs, the total length and thus the $P33$ increases when the resolution increases (see Figure 7.13). So, although the breakdown pressure is independent of the particle size, the unstable crack growth after the breakdown leads to different HF final length for different resolutions (the total fracture length ratio between the 100,000 and 10,000 DEs packings is $\simeq 2/1$).

A possible explanation is given in (Duriez *et al.*, 2016) based on the crack surface creation dA_c $[m^2]$ during fracturing (see Figure 7.12). Considering the newly created surface after a propagation step to be of the order $\mathcal{O}(D^2_{mean})$, the critical surface energy will be $\mathcal{G}_{IC} = dW_F/dA_c$ (for mode I loading). Defining the energy release from a single bond breakage as $dW_F = (F_n^{max})^2/2k_n$ the critical surface energy is thus proportional to the particle size such as $\mathcal{G}_{IC} \propto D_{mean}$. That being said, the maximum load at breakdown seems not to be affected by the DE size, however, during all tests the same slot was used under the same control parameters, thus the energy surplus of at the breakdown keeps the HF propagation unstable for longer time for finer resolutions.

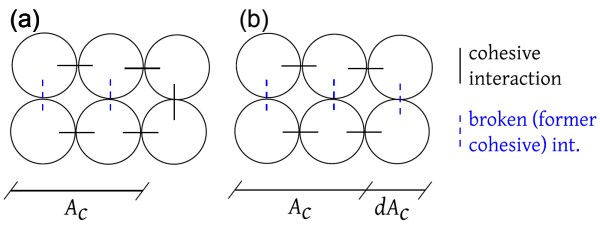

Figure 7.12: 2D sketch of the fracture tip on a regular DEM packing (a) before the propagation and (b) after the propagation (from Duriez *et al.*, 2016).

Another explanation could be related to a possible increase of stiffness for finer resolutions since the pressurization rate is higher for this cases. A possible increase of the total rigidity could affect the post-peak unstable fracturing.

Keeping this in mind, one should thus be careful to compare results emerging from similar resolutions when investigating the influence of physical quantities. The orientation and overall shape of the HF is nevertheless not affected by the resolution although being certainly more clearly defined for the finer models. Thus, if a sensitivity analysis is to be run, it will be robust if it is performed using the same resolution. Further research will be done on ensuring that a DE-size independent fracture growth.

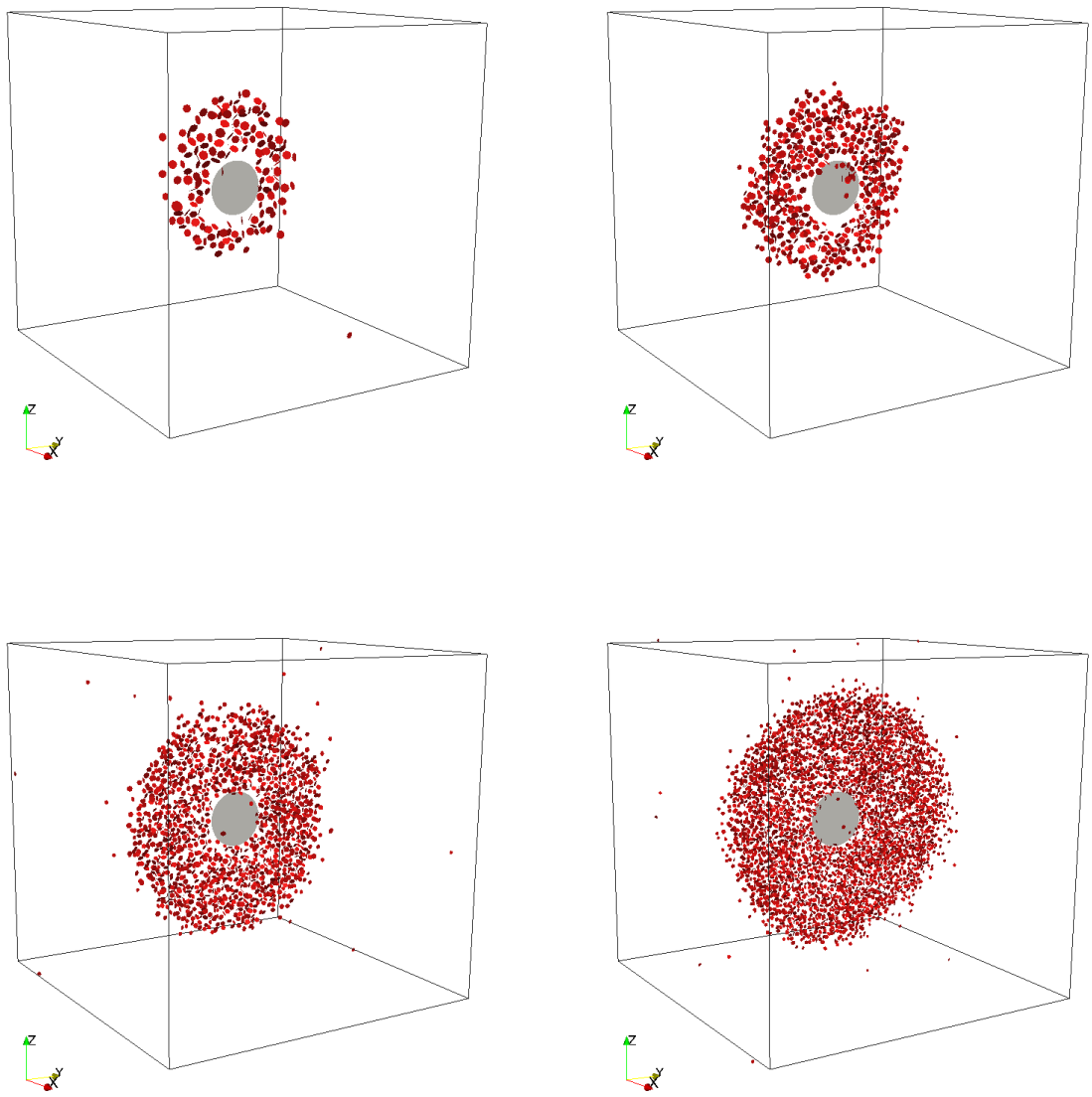

Figure 7.13: Final HF patterns for different resolutions of the model (a) 10×10^3, (b) 25×10^3, (c) 50×10^3 and (d) 100×10^3 constitutive DE.

7.2 Multiple injections along a well segment

Although single injection is common practice in laboratory and gives important information on HF propagation, in-situ completion designs usually utilize multiple perforation slots along each well to optimize the recovery. This multiple slots configuration can increase locally the intensity of the generated HF but can also cause strong interactions between them due to stress shadow effects. The aim of this section is to investigate the effects of the distance between the different perforation slots and of the wellbore-deviation from the minimum stress axis on the propagation of multiple HF and on the associated effective fractured volumes.

The host medium has the same properties as the one used in the previous section (see Table 5.2) and the loading procedure is similar. The specimen is first subjected to an in-situ stress field and then the fluid is injected at the slot centre under constant flow rate. This time, three

aligned injection slots (S1,S2 and S3) are placed inside the medium as described on Figure 7.14a. The injection is set up in a sequential way: a source is activated once the previous treatment has finished and the injection is stopped (Figure 7.14b). The order of injections is S1, then S2 and finally S3.

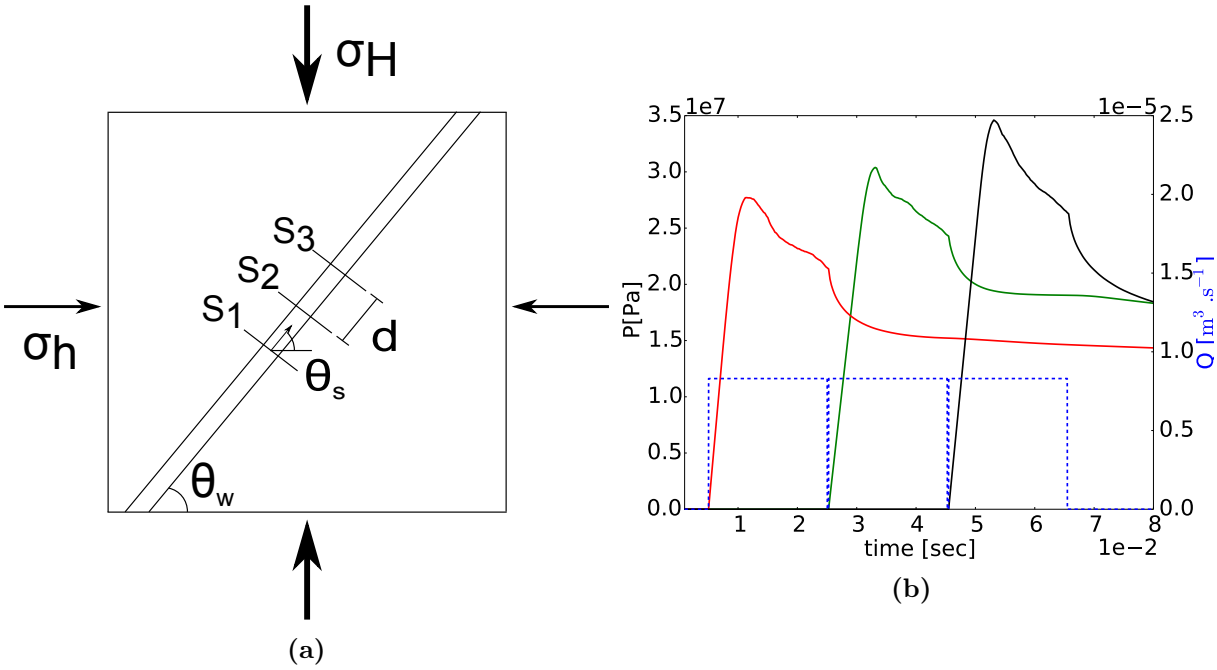

Figure 7.14: (a) Generic configuration of the multiple injections treatment. θ_w and θ_s correspond respectively to the deviation of the wellbore axis (*i.e.*, alignment direction of the slots) and of the perforation slot's normal from the σ_h direction. d is the distance between the perforation slots. (b) Pressure-responses resulting from a multiple injections treatment (case T1) and their corresponding hydraulic source activation (injection flow rate).

Test	Wellbore orientation θw [°]	Perforation slot orientation θs [°]	Perforation slot interval d [m]
T1	0	0	0.15
T2	0	0	0.25
T3	0	0	0.35
T4	40	40	0.25
T5	60	60	0.25
T6	40	0	0.25
T7	60	0	0.25

Table 7.2: Summary of the setup for each case.

7.2.1 Boundary and fabric effect on P33

In order to quantify the effect of the boundaries and of specimen's fabric on P33, the following tests have been done before the comparative multi-injection study.

First, single injection tests as described in Section 7.1.2 were carried out but this time the fluid is injected in different location each time *i.e.*, only on S1, then only on S2 and only on S3 (see Figure 7.14a) for $d = 0$, $\theta_s = 0$ and $\theta_w = 0$. From Figure 7.15 it can be seen a variation in $P33$ of -2,+12% between the injections closer to the boundaries (S1,S3) towards the injection in the center (S2).

Then, the same single injection tests were done on two more specimens of the same resolution (25,000 DEs) and with the same material properties. The resulting variability on the results is shown on Figure 7.16.

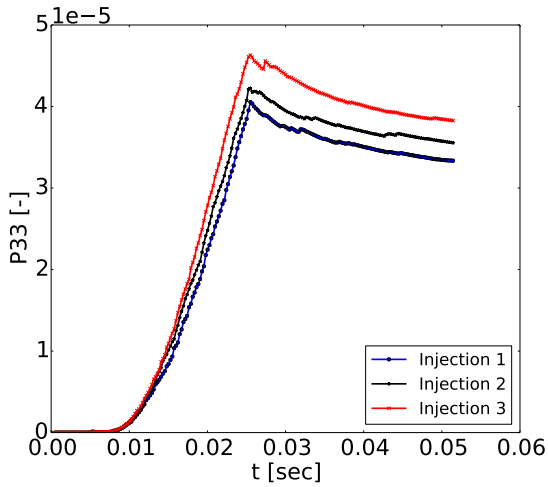

Figure 7.15: P33 variability between central injection S1 and the ones closer to the boundaries (S2,S3)for $d = 0$, $\theta_s = 0$ and $\theta_w = 0$.

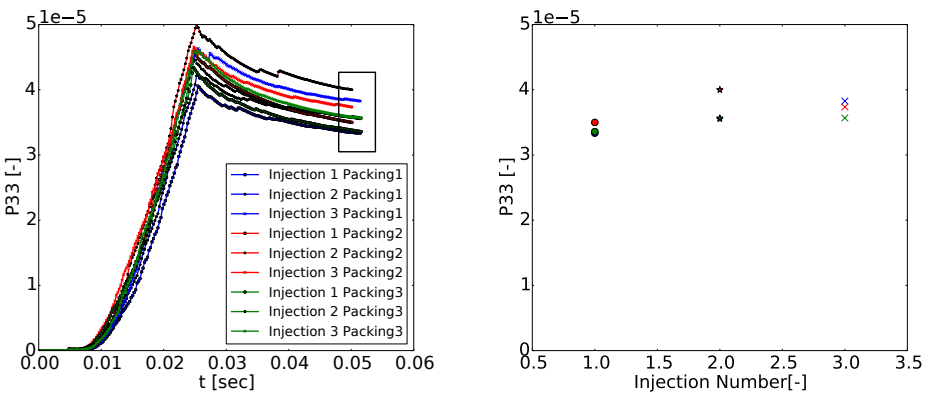

(a) **(b)**

Figure 7.16: Evolution and final values of the P33 for injection in 3 different points inside the sample and for different specimens of the same properties.

The same test was then done for $d = 0$, $\theta_s = 40$ and $\theta_w = 40$. By running single injection tests for each injection point the final variation found is of the order of $\pm$ 4%

Finally in order to see which order of variability should be expected for this resolution regarding the slot orientation around the σ_h axis, the same test as in Section 7.1.3 was performed on the 25,000DEs packing. The results are shown in Figure 7.18. As one can see, the change in total $P33$ can reach a value of 52% depending on the orientation of the initial slot with respect to the direction of the maximum horizontal stress.

7.2.2 Effect of the distance between the perforation-slots

One could expect that the closer the injection slots are, the greater the stimulated volume is. However, very closely spaced perforation slots could affect the response of the stimulated medium and thus minimize the performance of the treatment. Therefore, an optimum distance between the injection points needs to be selected in order to provide a good compromise between efficiency and cost. We try here to get an insight on how the $P33$ and $P32$ indices evolve as the injection slots distance varies.

The tests T1, T2, T3 presented in Table 7.2 were performed on the generic configuration shown in Figure 7.14a with $\theta_s = 0$ and $\theta_w = 0$. This configuration corresponds to a fictitious

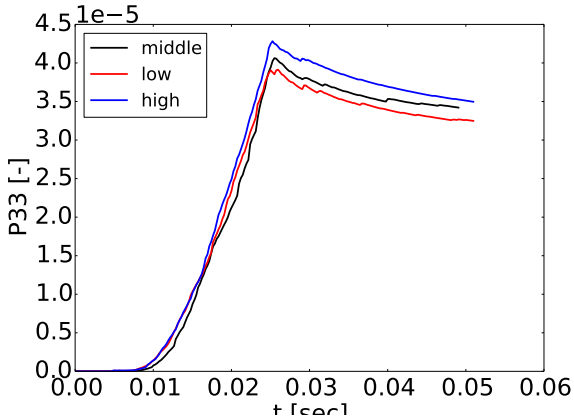

Figure 7.17: P33 variability between central injection S1 and the ones closer to the boundaries (S2,S3) for $d = 0$, $\theta_s = 40$ and $\theta_w = 40$.

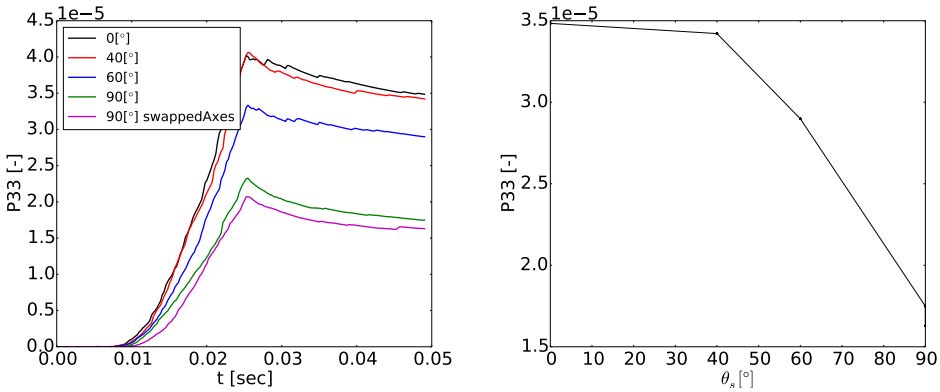

(a) **(b)**

Figure 7.18: Evolution and final values of the P33 for different slot orientations for the 25,000DEs packing.

well segment perfectly aligned with σ_h with the injection slots oriented perpendicularly to σ_h.

The final HF patterns obtained from the three tests are presented in Figure 7.19. A top view of the specimen is shown along with the hydraulically driven cracks forming the HF, the applied stress field and the direction of the wellbore. In the T1 case, with the shortest distance between the injection slots, the induced HF are not exactly symmetrical and slightly deviate from the maximum stress σ_H direction. During the simulation, we could see that, as a HF gets longer in one direction, its neighbor could stop to propagate and initiate a bifurcation process as mentioned by (Muhlhaus *et al.*, 1996). On the other hand, the T2 and T3 cases with larger intervals between the slots produce fully symmetrical HF all well aligned with σ_H. Actually, the bifurcation process observed in the T1 case can be explained by the local perturbation of the stress field around the pressurized HF as mentioned by (Chau and Wang, 2001). To illustrate this point, the direction of the maximum component of the local stress tensor are plotted in Figure 7.20 at the end of each injection performed during case T1. One can see that, after the first injection in S1, the surrounding local stress field experiences a rotation along the HF due to the pressurization of the fracture (Figure 7.20, left). Due to the dilation of the HF, the maximum compressive stress component is locally oriented along the minimum stress σ_H direction. This stress redistribution clearly affects the propagation of the second HF produced by the injection in S2, which is shorter at the end of the injection (Figure 7.20 center). The consequence on the propagation of the third HF is even more noteworthy with an asymmetrical growth with

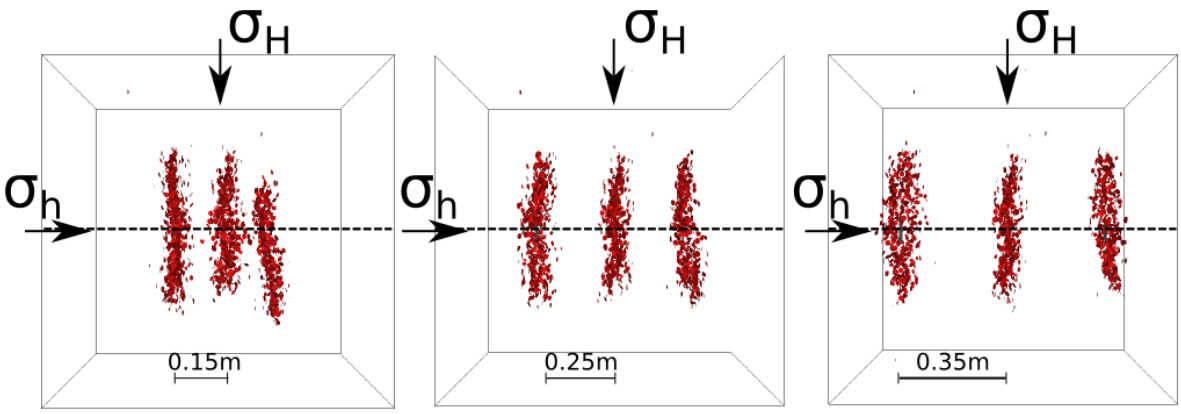

Figure 7.19: Final HF patterns obtained for the cases (from left to right) T1, T2 and T3 (see Table 7.2).

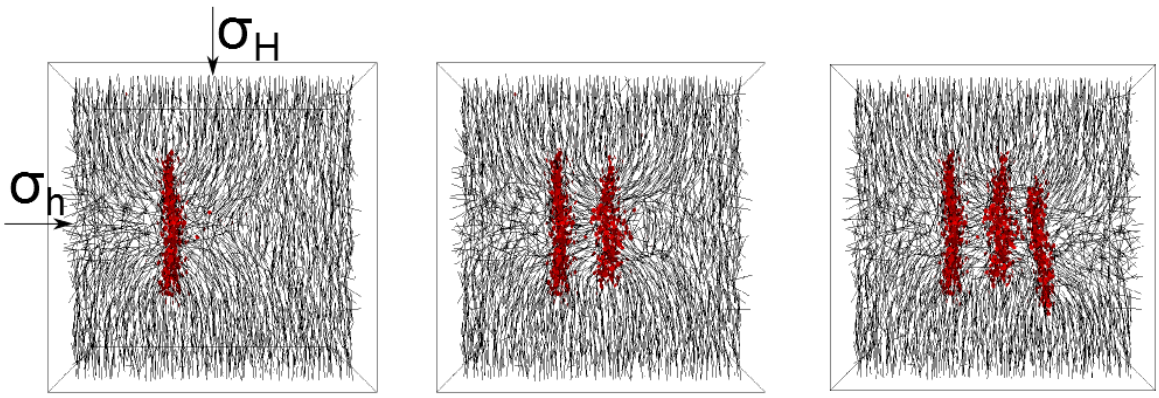

Figure 7.20: Stress field obtained at the end of each injection sequence for case T1. The black segments correspond to the direction of the maximum component of the per particle stress-tensor.

respect to the axis of the well and an overall non planar shape. Actually, the perturbation of the stress field resulting from the previous HF tends to limit its progression on one side of the well and also tends to deviate its growth from σ_H (Figure 7.20, right). Furthermore, the local stress perturbation due to the unpumped and remaining fluid in the cracks causes an increase of the breakdown pressures of the next injections as observed in laboratory experiments ran by (Kear *et al.*, 2013) (see Figure 7.14b).

Comparing the evolutions of both the $P33$ and $P32$ indices for all tested cases (Figure 7.21), one can note that the $P33$ decreases and the $P32$ increases while the interval between the sources decreases. In other words, when the sources are placed closer to each other, more cracks are created (the fracture surface is higher) but they are however less open (the fracture volume is smaller).

In order to conclude on the ability of these configurations to ease the propagation of proppant inside the HF, the local aperture distributions of the cracks forming the HF were compared to a minimum proppant diameter which was taken here equal to 1×10^{-4} [m] (Table 7.3). Note that the simulations were run on three different packings for this study in order to assess the variability of the results.

Taking into account this minimum aperture threshold, it is clear that even a large fractured area will not contribute significantly to the production if the aperture values are smaller than the threshold value, because the HF cannot be propped. Nonetheless, these results confirm the

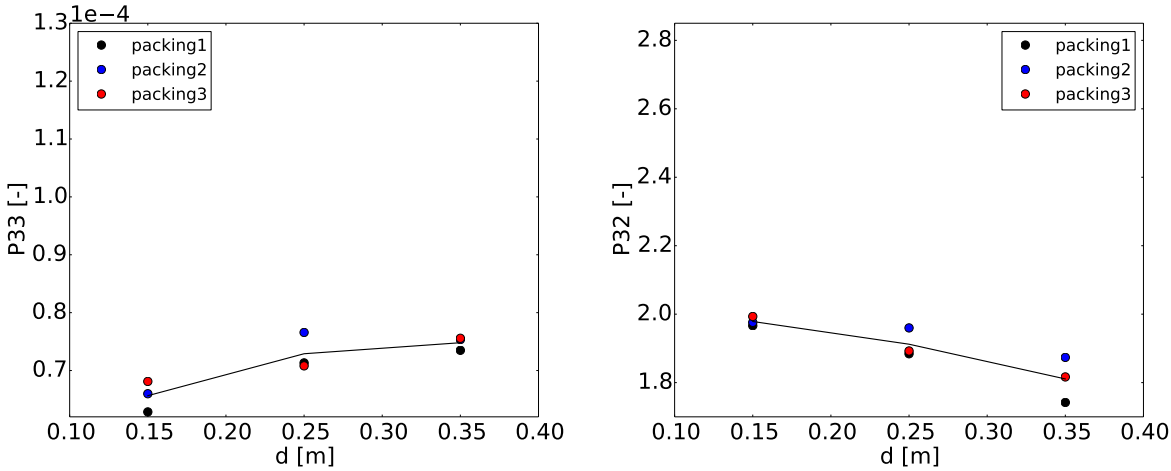

Figure 7.21: Effect of the distance d between the injections slots for three configurations where the well is aligned with σ_h ($\theta_w = 0°$) and the slots are aligned with σ_V ($\theta_s = 0°$). On the left, the total fracture volume $P33$ and, on the right, the intensity of cracks $P32$.

previous conclusions in the sense that the capacity for the fractures to be propped is reduced when they are close enough to interact one with another. One can thus conclude that, although shorter intervals produce larger fractured area inside the host medium, this might not be the optimum configuration in terms of productivity (at least for the intact medium considered here).

Test	Distance d [m]	Percentage of propped cracks [%]
T1	0.15	[8.38-9.94]
T2	0.25	[12.71-14.56]
T3	0.35	[13.71-16.82]

Table 7.3: Percentage of propped cracks versus the interval distance d between the injection slots.

7.2.3 Effect of deviation of the minimum stress axis

As discussed in section 7.1.3, the orientation of the injection slots with regards to the stress field can have a drastic influence on the HF properties. In fact, in the field, the wells might not be drilled perfectly aligned with the σ_h direction due to practical reasons or, more generally, due to the complexity of the subsurface (the stress field can be locally strongly perturbed by the presence of geological structures). Three configurations were thus tested, namely T2, T4 and T5, in order to investigate how multiple HF propagate when the well is deviated from σ_h (Table 7.2). The deviation is characterized by θ_w, the angle between the well axis and σ_h. For all the cases tested here, the perforation slots were considered perpendicular to the "fictitious" wellbore's axis, *i.e.* $\theta_s = \theta_w$ and the slots interval d was kept constant and equal to 0.25 to limit the induced HF to interact (see previous section). Configuration T2 corresponds to the previously described favourable case where the well is perfectly aligned with the σ_h direction, *i.e.* $\theta_w = 0°$. T4 refers to the scenario where the well is deviated from the σ_h direction with an angle $\theta_w = 40°$. T5 corresponds to the case where $\theta_w = 60°$. The final HF patterns obtained for the three configurations are presented on Figure 7.22.

One can see that, when $\theta_w > 0°$, the HF present a curved shaped pattern due to the tendency for the fracture to re-orientate along the σ_H direction. The apertures distribution analysis giving the percentage of fractures with an aperture higher than 1×10^{-4} [m] is summarized in Table 7.4. The maximum values of the $P32$ and $P33$ indices are plotted on Figure 7.23. Here again, the simulations were run on three different packings to assess the variability of the results.

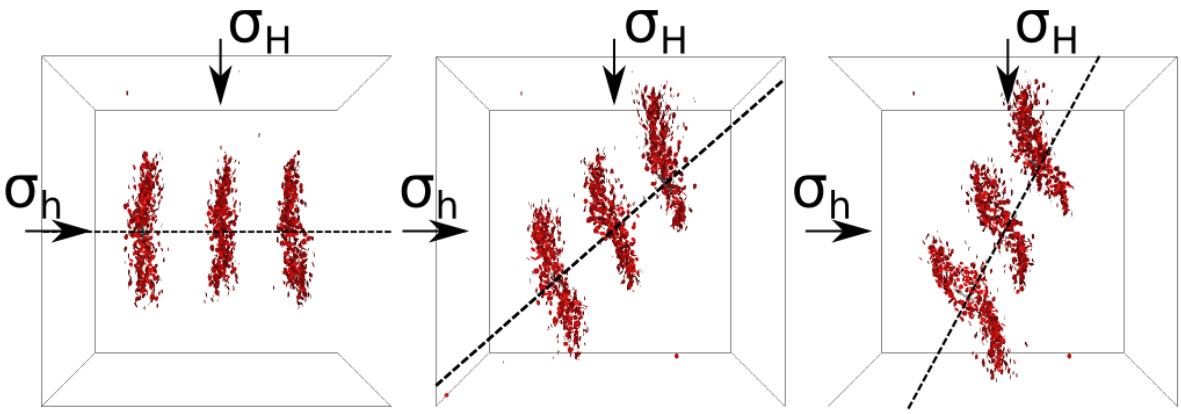

Figure 7.22: HF patterns obtained for three injections performed under different deviations θ_w of the wellbore (dashed line) with respect to σ_h. The injection slots are oriented perpendicularly to the wellbore for all cases ($\theta_s = \theta_w$). From left to right, results for test T2 ($\theta_w = 0°$), test T4 ($\theta_w = 40°$) and test T5 ($\theta_w = 60°$).

Test	Angle θ_w [°]	Percentage of propped cracks [%]
T2	0	[12.71-14.56]
T4	40	[16.27-18.16]
T5	60	[14.51-16.27]

Table 7.4: Percentage of propped cracks versus the deviation of the well axis θ_w from σ_h.

For the range of deviation tested here, there is no clear trends on how the amount of small cracks around the wellbore can affect the progression of the proppant. The small variations of the $P32$ and $P33$ values suggests however a possible combined effects due to the stress field disturbance and to the possible interaction between the fractures.

A way to overcome this deviated-well induced complex geometries could consist in orienting the injection slots perpendicularly to σ_h as proposed, for example, by (Burghardt *et al.*, 2015). Two other cases were thus tested, namely T6, T7 in Table 7.2, corresponding to cases where $\theta_w = 40°$ and $\theta_w = 60°$ respectively but with the injection slots always oriented in the σ_H direction ($\theta_s = 0°$). One can see that what ever the orientation of the well, the shape of the resulting HF are now planar (Figure 7.24). From the apertures distribution analysis, the percentages of induced cracks with an aperture higher than 1×10^{-4} [m] are given in Table 7.5 for cases T2,T6 and T7. The amount of open cracks tends to slightly increase when using such preferential orientation for the slots. Comparing the values of the $P32$ and $P33$ indices obtained for these tests (Figure7.25) to the ones obtained previously with (Figure7.23), one can clearly see an increase of both the volume and the intensity of the HF.

Test	Angle θ_s [°]	Percentage of propped cracks [%]
T2	0	[12.71-14.56]
T6	40	[15.48-17.93]
T7	60	[16.27-18.16]

Table 7.5: Propped cracks percentage versus deviation θ_s from σ_h axis.

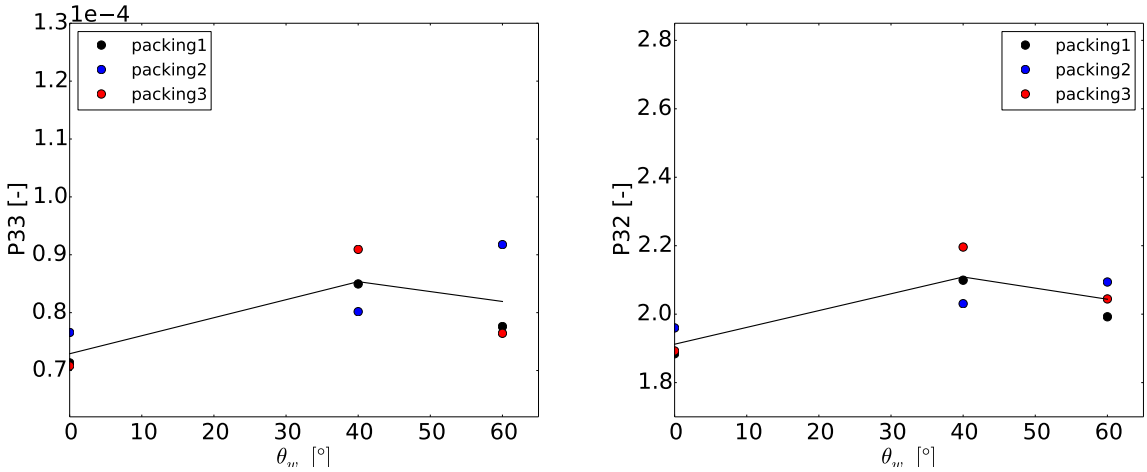

Figure 7.23: Effect of the fictitious well orientation θ_w for three configurations where the slot interval d is equal to 0.25 [m] and the slots are oriented perpendicularly to the well ($\theta_s = \theta_w$). On the left, the total fracture volume $P33$ and, on the right, the intensity of cracks $P32$.

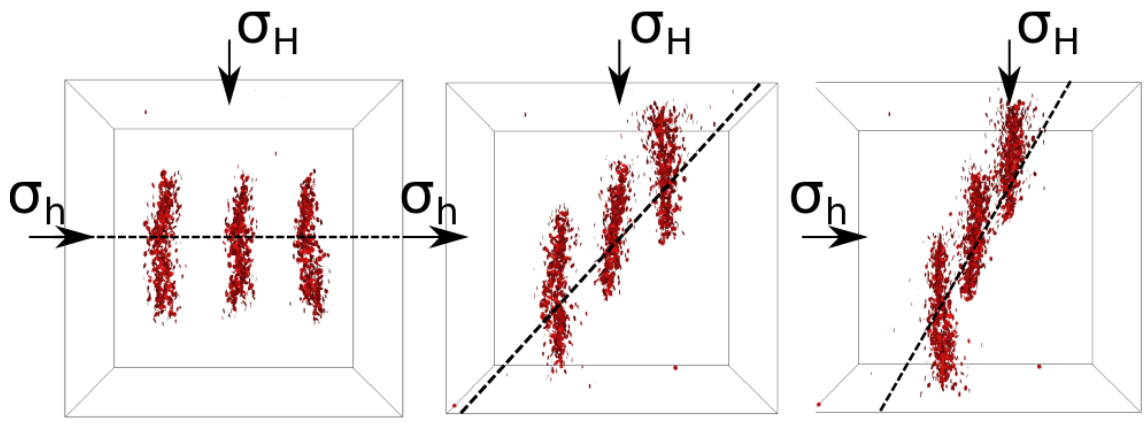

Figure 7.24: HF patterns obtained for three injections performed for different alignment angles of the wellbore θ_w with respect to σ_h. The injection slots are oriented in the direction of the maximum stress σ_H for all configurations. From left to right, results from test T2 ($\theta_w = 0°$), test T6 ($\theta_w = 40°$) and test T7 ($\theta_w = 60°$).

Conclusions

A reference simulation was built up to validate the proposed scheme. A parametric study was then performed to investigate the model's prediction regarding the different parameters controlling hydraulic fracture propagation. In particular, the results are discussed and compared in terms of breakdown pressure, fractured volume $P33$ and fracture intensity $P32$. Through this analysis, and for the set of parameters chosen here, the computationally favourable use of an impermeable numerical medium has been justified, since identical results were obtained for the low permeability formation the impermeable one, and thus it was adopted for the tests.

Also, by comparing the results obtained for different fluid bulk moduli, very small discrepancies were found in terms of deformation and rupture processes, break down pressure and values of either $P33$ or $P32$, giving thus the possibility to increase the computational efficiency by considering low compressibility fluids in the simulations.

Among all the different physical parameters tested here, it has been confirmed that the state of stress applied to the medium has a first order influence on the propagation of hydraulically driven fractures. Specifically, the deviation of the injection slot from the direction of the principal

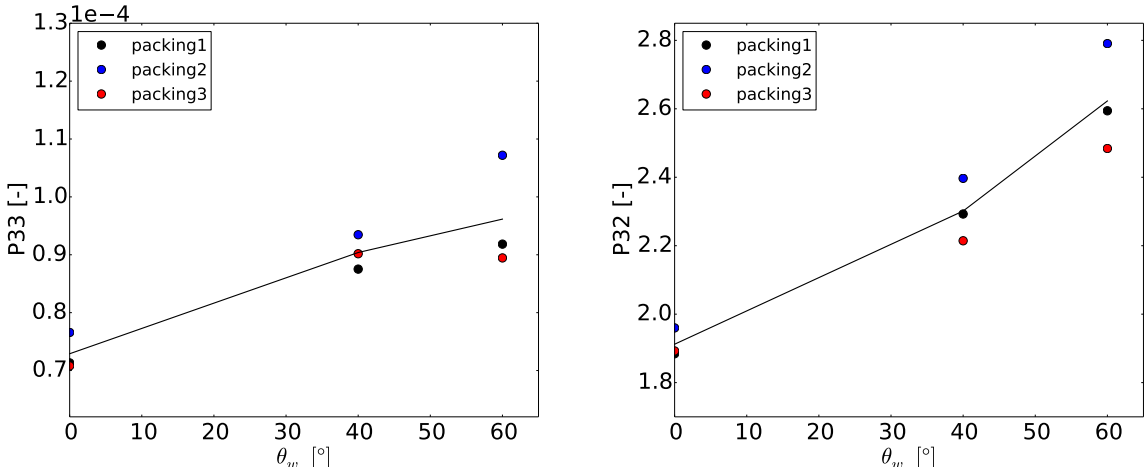

Figure 7.25: Effect of the fictitious well orientation θ_w for three configurations where the slot interval d is equal to 0.25 [m] and the slots are kept perpendicular to σ_h ($\theta_s = 0°$). On the left, the total fracture volume $P33$ and, on the right, the intensity of cracks $P32$.

horizontal stress direction induced hydraulic fractures with lower values of the $P33$ and $P32$ resulting from the tendency for the induced cracks to keep closed in the near-well bore region, the consequence of which would be to limit the transport of proppant away from the point of injection. For instance, for a configuration where the slots are aligned with the minimum horizontal stress direction, the induced HF showed a curved shape caused by its tendency to re-orientate along the direction of the maximum horizontal stress. Besides, the results also confirm that the injection flow rate is a controlling parameter that has to be considered in HF treatment design. For instance, the values of the $P33$ and $P32$ values were shown to increase proportionally to the injected flow rate.

The model was finally used to simulate multiple-injections treatments along a wellbore segment containing three injection slots. This configuration provided information on the effect of the distance between the slots, the well deviation from the minimum horizontal stress direction as well as the orientation of the injection slots with respect to the well axis on the fracturing pattern, fractured volume and fracture intensity. The results shows that the possibility of aligning the slots along the maximum horizontal stress direction tends to increase the dilation of the HF and would thus tend to optimize the transport of proppant inside the fracture.

Chapter highlights

- A simple case of single injection in a soft rock was simulated. The model enables to describe the full spatio-temporal evolution of HF during propagation and to quantify its properties through the computation of the $P32$ and $P33$ indexes.
- The impact of the different control parameters and the *in-situ* stress field on the pressure, $P33$ and $P32$ evolution was shown. The deviation of the slot's normal from the σ_h direction causes a large decrease on the P33 and P32 indexes, low propped volume and creates non planar, percolating HF.
- Multiple HF interaction was studied along a well segment. Due to stress-shadow effects, closely spaced HF tend to reduce the final stimulated volume ($P33$) but might increase the fracture intensity ($P32$).
- Keeping the perforation slot perpendicular to σ_h in multiple HFs in a non-favourably oriented well segment can decrease the stress-shadow effect on $P32$ and $P33$.

Chapter 8

Interaction between hydraulic fracture and natural fracture

The objective of this chapter is to analyse HF propagation in specimens containing a pre-existing defect as a continuation of the study for intact specimens presented in Chapter 7. As mentioned in Chapter 3, rock-masses contain natural fractures (NF). Thus, an attempt is made hereafter to study the HF-NF interaction.

Two types of NF will be considered, persistent and non persistent. The non-persistent case corresponds to cases where NFs have a size comparable to the length of the HF. On the other hand the persistent case corresponds to long horizontal and sub-horizontal structures such as large bedding planes, cemented zones or open corridors. The importance of the in-situ stress field, the control parameters (*e.g.*, injected fluid viscosity), along with the defect's properties (such as orientation, size, initial aperture and stiffness) on the HF propagation, will be emphasized. The different mechanical and hydraulic properties of the NF used in the study could be correlated to different degrees of cementation, asperities ratio, NF origin as previously described in Chapter 3.

Moreover, by comparing the medium's response to the ones obtained by similar experimental campaigns, an attempt to grasp the gap between numerical modelling and experimental findings on the evolution of HF will be made. Depending on the case, the qualitative comparison lays on data such as AE recordings, fracturing rate, pressure and volumetric deformation or final HF patterns. Finally, a discussion on HF-NF interaction based on the tested scenarios is provided, aiming at giving indicators on the order of importance of each parameter.

Layout of chapter

This chapter starts with the description of the numerical set-up which includes a persistent NF. Then, a reference case is presented with special emphasis put on comparing the numerical responses to the ones that have been previously studied experimentally by Stanchits and co-workers. Based on the results of the reference case, a series of tests is carried out to study the effect of different parameters on the response and their respective significance.

Then, a non-persistent type of NF is considered in Section 8.2. As in Section 8.1, a reference case is built. A sensitivity analysis is then performed to study how the control parameters of the injection and/or the material parameters of the non-persistent NF control the evolution and the final HF pattern.

Finally, the chapter closes with a discussion and summary of the principal findings in Section 8.3. The discussion is mainly oriented towards the identification of the key parameters controlling the crossing of the pre-existing NF. Also it emphasises the differences between persistent and non-persistent NF intersection with HF.

8.1 Persistent pre-existing fracture

A persistent fracture could represent a bedding plane of finite thickness, a long fracture present in the damaged zone of a fault or any other NF whose size is much larger than the HF. Due to their size, as mentioned in Chapter 3, this type of NFs might be the main reactivation path for driving the HF but might also stop the HF-growth as a result of large storage and/or massive fluid leak-off through it, or by causing an arrest of the HF as a result of its high toughness (*e.g.*, while infilled with hard cemented material). In the followings, the main mechanism affecting the HF growth in the presence of this kind of defects is investigated.

8.1.1 Geometry and boundary conditions

A cubic specimen of $1 \times 1 \times 1$[m] is used (see top view along with BCs in Figure 8.1). The specimen is made of $25,000$ DEs and its properties are calibrated, as in previous sections, to the properties of a soft impermeable rock (Table 5.2). An injection slot is placed at the centre of the numerical specimen. A pre-existing, cemented NF (see Table 8.1) is placed 0.20 [m] away from the specimen's centre (distance between specimen's centre to NF centre). The specimen is subjected first to a triaxial stress controlled compression to $\{\sigma_1, \sigma_2, \sigma_3\} = \{11, 10, 6\}$ [MPa]. All the walls surrounding the specimen are permeable (by imposing a $P = 0$ [Pa] condition). The model parameters are selected as in Chapter 7 in order for the simulation to be representative of the work by (Stanchits *et al.*, 2013; Stanchits *et al.*, 2015). The injection rate is set to $Q = 8.3 \times 10^{-6}$ [m.s^{-1}]. Based on this rate, an injection of total time $t = 4.5 \times 10^{-2}$ [s] was fixed to ensure that the injected fluid volume is sufficient to drive the HF up to the specimen's boundaries. The injection phase is followed by a shut-in and a relaxation phase in each test.

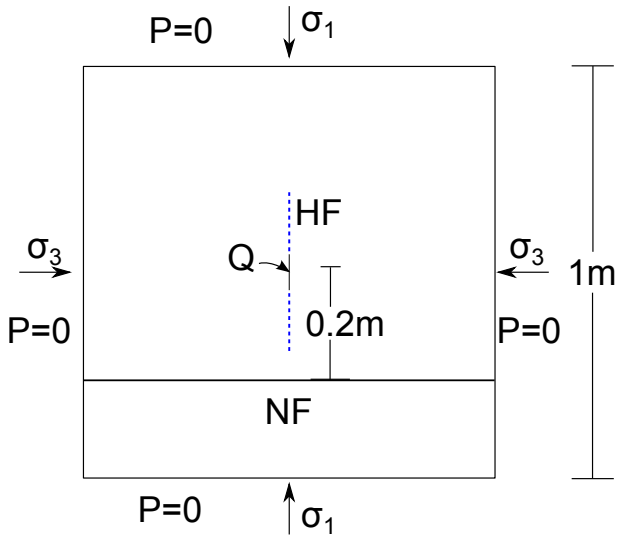

Figure 8.1: Top-view of the test's geometry and applied BCs.

8.1.2 Reference case results

The set of parameters used here are summarized in Table 8.1. This test will be first analysed in detail as a reference case before moving on in exploring the effect of individual parameters on the response of the sample later on in this chapter. The results obtained are analysed in a similar way to the analysis by (Stanchits *et al.*, 2011; Stanchits *et al.*, 2015) to bridge the experimental and numerical tests.

In Figure 8.2 the response of the numerical specimen during the injection is shown. The response can be subdivided into three stages:

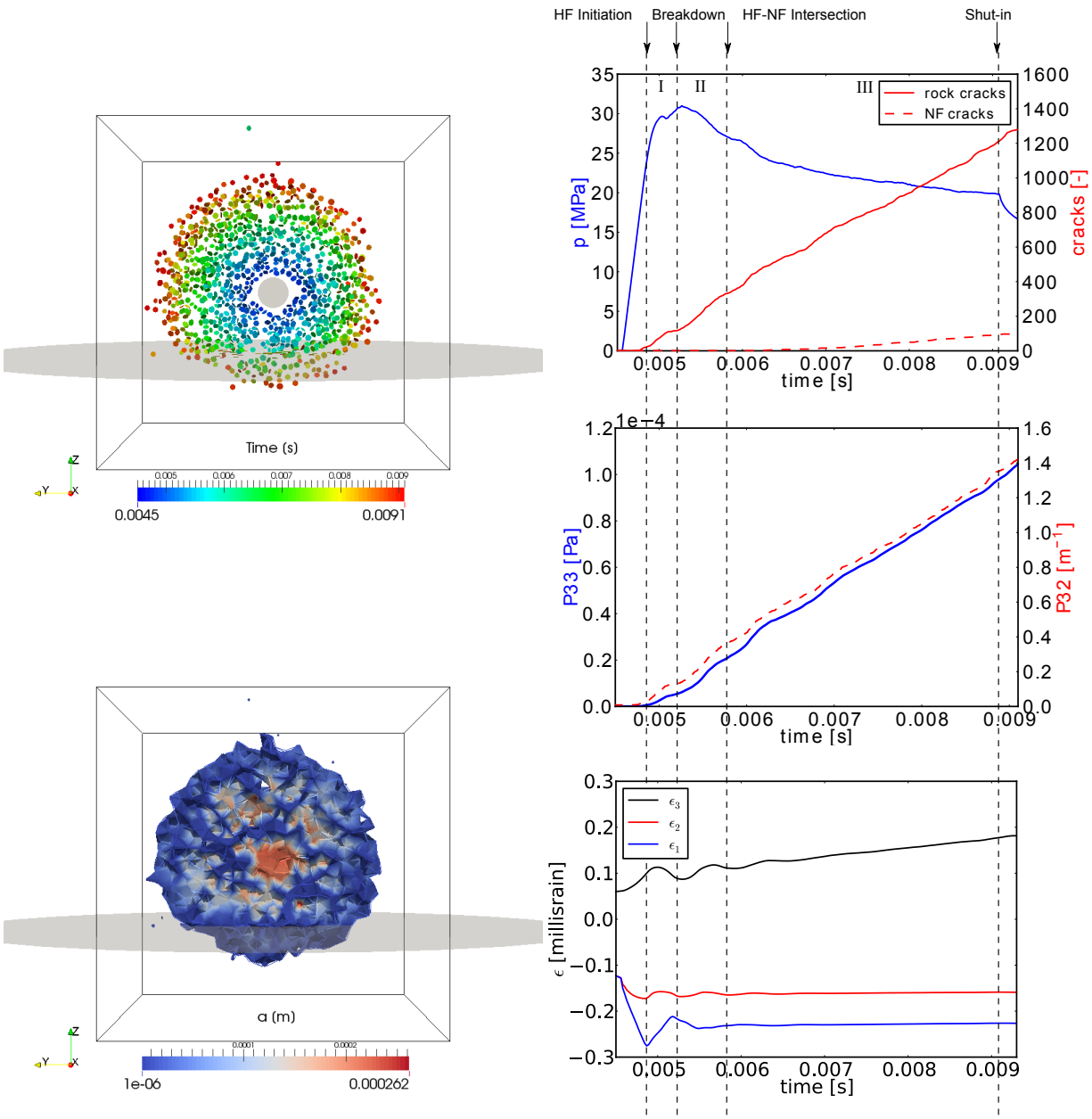

Figure 8.2: Case, TPNF1 with initial aperture $h_{init} = 1^{-4}$ [m]. On the left are shown two side views of the specimen on the $\sigma_1 - \sigma_2$ plane at the shut-in (stage III), (Top) crack events with the colour code representing the time of occurrence and (Bottom) aperture map at the shut-in. On the right side are shown (top to bottom): Evolution of pressure at injection point and cumulative crack events,, P33 and P32 indexes and volumetric deformation of the sample. The vertical dashed lines mark the initiation time, the breakdown time and the shut-in time respectively.

Flow Rate	Viscosity	NF to rock Stiffness ratio	NF stiffness ratio	Tensile strength	Cohesion	Friction angle	Initial aperture
Q [m/sec]	μ [Pa.sec]	$\frac{K_n^{NF}}{K_n^{rock}}$ [-]	$\frac{K_s^{NF}}{K_n^{NF}}$ [-]	t_{NF} [Pa]	c_{NF} [Pa]	ϕ [°]	h_i [m]
8.3×10^{-6}	1.00	1	0.2	1×10^6	1×10^6	30	1×10^{-4}

Table 8.1: Control parameters and joint material properties for persistent NF.

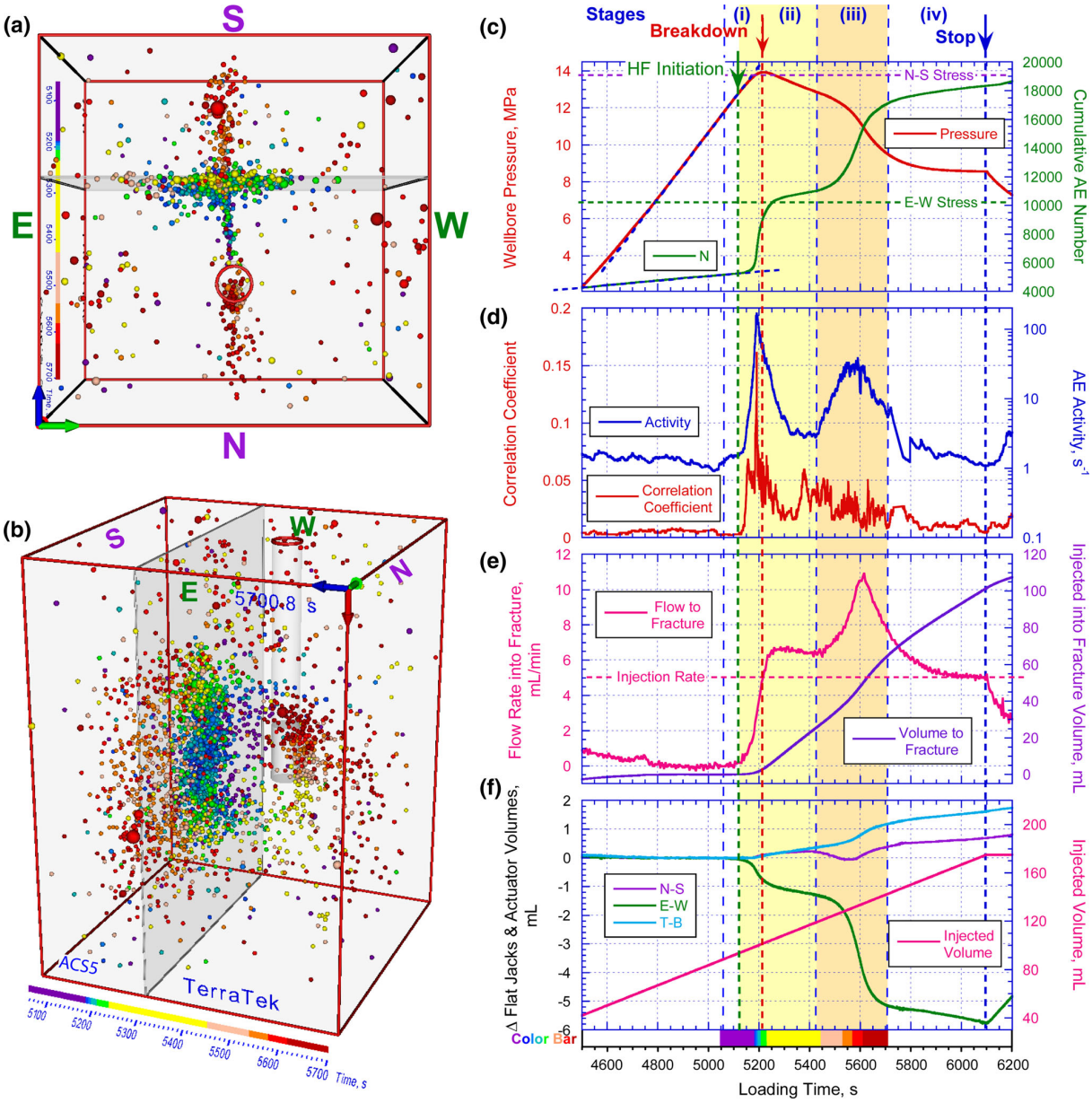

Figure 8.3: (a) Top and side (b) views of the specimen with the main AE events represented by spheres. The color-map represents time at which an event occured. On the right, the specimens response is described by (c) the wellbore pressure and cumulative AE events, (d) AE activity, (e) volume injected in the fracture and flow rate and (f) volumetric deformation of the sample in each direction. Experimental data from (Stanchits *et al.*, 2015).

(I) HF initiation till breakdown.

(II) Post-breakdown till HF/NF interaction.

(III) HF evolution after interaction with NF.

Stage (I) corresponds to the initiation phase of the HF. The pressure evolution (Figure 8.2) starts becoming non-linear at $t = 0.0047$ [s] which corresponds to the time at which the first cracks start to appear close to the injection slot. The opening of the HF causes an increase in strain ϵ_3, which corresponds to a dilative behaviour of the specimen along the minimum principal stress direction, and also a shrinkage along the other two axes ϵ_1 and ϵ_2. The HF opening also reflects on the P33 and P32 values that start raising. An acceleration on crack events is observed

till a breakdown that takes place around $t = 0.0050$ [s]. Since the fluid is filling the new fractured volume the pressure remains constant. At the same time a drop in the crack events activity and a "plateau" on the cumulative crack events curve are recorded. Once the pressure builds up again, it leads to a major breakdown at $t = 0.0053$ [s].

After the breakdown (II), the HF keeps propagating until $t = 0.0060$ [s] where the HF meets the NF. Then a series of crack events occurring along with leak-off through the NF cause another pressure drop followed by a decrease of the crack activity. With the initial aperture of the NF being small and the NF stiffness not small enough to allow for NF opening and thus important leak-off, the pressure drop is not large enough to cause an important delay or to stop the HF propagation. On the contrary the HF crosses the NF and propagates towards the boundaries.

These findings are comparable to what has been experimentally observed by (Stanchits *et al.*, 2011; Stanchits *et al.*, 2015) who investigated HF growth in Colton Sandstone specimens containing a persistent artificial fracture plane. In Figure 8.3 an example of their experimental analysis dataset is shown for comparison. It has to be noted that the numerical set-up was selected to be representative of the experiment but not meant to reproduce the experiments. Thus, a one to one comparison could be miss-leading at this point. However, it can help to explain qualitatively the underlying physics of the obtained response. The numerical results show crack events mainly along the σ_3 plane and few cracks on the NF plane just before crossing (Figure 8.2). This is in agreement with the response shown in the experiment. In that case, the AE events start clustering around the injection slot and then towards the NF. Then, after some stick-slip events on the pre-existing fracture plane, the AE events show that the HF crosses the NF (Figure 8.3(a) and Figure 8.3(b)). In terms of pressurization and cumulative AE events the experimental response shows also a linear pressurization up to the moment of fracture initiation. After the fracture initiation, the number of AE increases also rapidly. The pressurization rate becomes then non-linear and increases up to the breakdown point followed by a plateau in the AE events. The plateau is associated with the filling of both the new fractured volume and the pre-existing fracture. Finally a second breakdown occurs once the HF crosses the pre-fractured plane. The related dilation of the sample is given in Figure 8.3(f). This overall response agrees with the simulation's results even though the second breakdown is less pronounced in the numerical experiments.

In order to have a complete idea about the evolution of the HF in time, the pressure field and stress field were recorded in the numerical specimen. In Figure 8.4 three snapshots of the pressure field and of the minimum local principle stress component field are shown. The snapshots are taken respectively just before the HF-NF intersection, just after the intersection and at the shut-it. Regarding the colour maps, a binary map is used for the pressure field, to locate the fluid front $C_f(t)$ while the stress field map allows to highlight the regions under tensile loading (in red). In fact, these tensile regions indicate where the fracture front $C_c(t)$ will evolve. One can see that in this test, the effect of the NF on the HF propagation is almost negligible until the end of the injection (the shut-in). Thus, the last point is supported also by the results shown in Figure 8.5 where the binary pressure field and the minimum local stress component directions and magnitudes are shown. It is clear that the $C_c(t)$ follows the path prescribed by local tensile stresses perpendicular to the fracture tip. Although there is a small delay in the HF growth (compared to an intact scenario) coming from a pressure drop at the intersection and followed by a minimum leak-off in the NF, in the end, the HF follows the path that would be expected for the given boundary stresses.

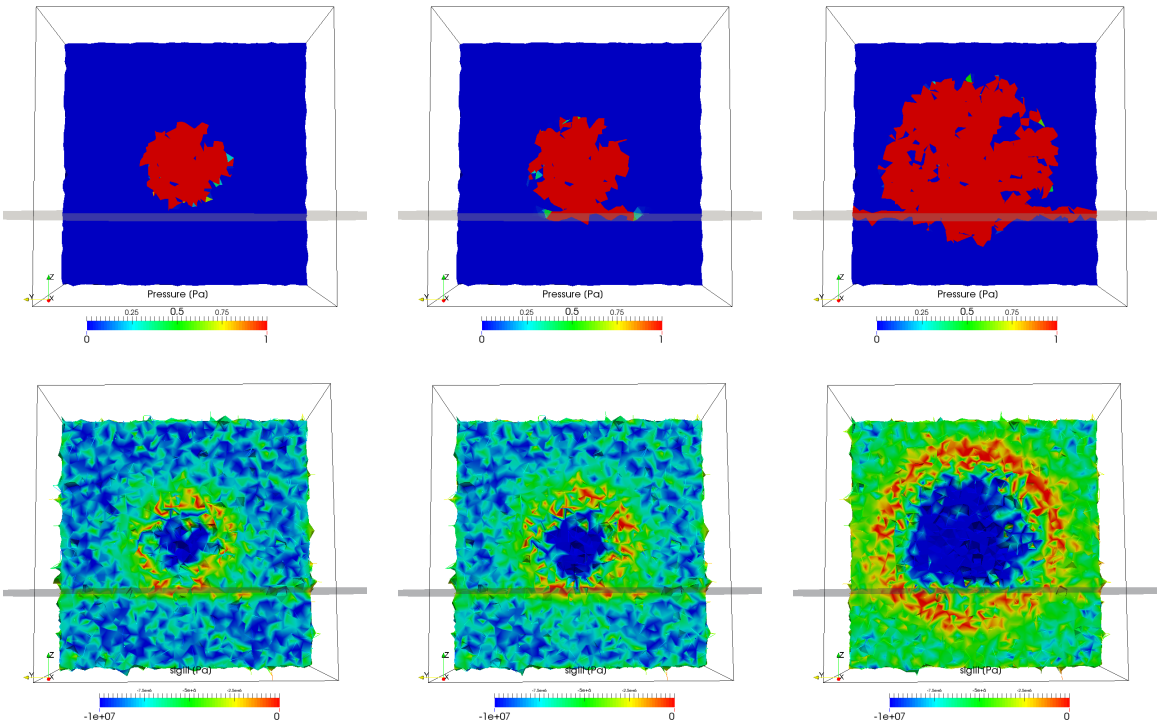

Figure 8.4: Case TPNF1, (Top) Binary pressure field showing the fluid distribution inside the specimen (red color) and (Bottom) local σ_3 magnitude (negative values correspond to compressive stresses) on the HF plane. From left to right: just before the HF/NF intersection, just after the intersection and at the shut-in.

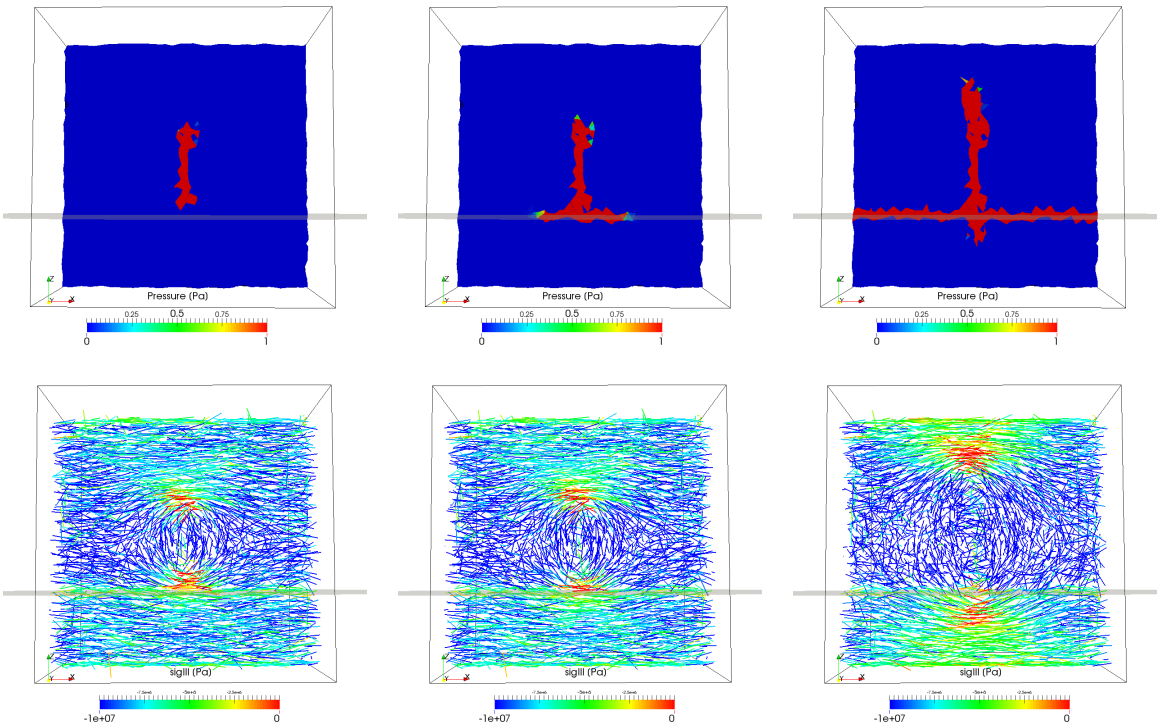

Figure 8.5: Case TPNF1, (Top) Binary pressure field showing the fluid distribution inside the specimen(red color) and (Bottom) local σ_3 direction vectors and magnitude perpendicular to the HF plane. From left to right: just before the HF/NF intersection, just after the intersection and at the shut-in.

8.1.3 Sensitivity analysis

This section investigates the respective effect of NF initial aperture h_i, NF stiffness, fluid viscosity μ and angle of approach θ_{NF}, on HF-NF interaction with respect to the behaviour of the reference sample. The following sensitivity analysis was carried out to determine how the different material or injection control parameters affect the HF propagation during and after the intersection with the NF plane.

The different tests are described in Table 8.2. On the same table, the observed interaction between HF and NF are presented. The results are distinguished to cases where the HF crosses the NF (marked as "crossed") and cases where the HF propagation stops when the HF meets the NF (marked as "arrested).

Test	Viscosity μ [Pa.s]	Initial aperture h_i [m]	NF Stiffness $[K_n^{NF}, K_s^{NF}]$ [Pa]	Approach angle θ_{NF} [°]	HF-NF interaction [-]
TPNF1	1	10^{-4}	$[K_n^{rock}, K_s^{rock}]$	90	Crossed
TPNF2	1	10^{-5}	$[K_n^{rock}, K_s^{rock}]$	90	Crossed
TPNF3	1	10^{-3}	$[K_n^{rock}, K_s^{rock}]$	90	Arrested
TPNF4	1	10^{-4}	$[K_n^{rock}/10, K_s^{rock}/10]$	90	Arrested
TPNF5	0.05	10^{-4}	$[K_n^{rock}, K_s^{rock}]$	90	Arrested
TPNF6	0.001	10^{-4}	$[K_n^{rock}, K_s^{rock}]$	90	Crossed
TPNF7	1	10^{-4}	$[K_n^{rock}, K_s^{rock}]$	70	Crossed
TPNF8	1	10^{-4}	$[K_n^{rock}, K_s^{rock}]$	60	Arrested
TPNF9	1	10^{-4}	$[K_n^{rock}, K_s^{rock}]$	50	Arrested
TPNF10	1	10^{-4}	$[K_n^{rock}, K_s^{rock}]$	30	Arrested

Table 8.2: Tests on rock specimens containing a persistent NF.

Aperture

In this subsection, two tests TPNF2 and TPNF3 are considered and compared to the reference case TPNF1. The aim here is to study the effect of the initial NF aperture h_i on the HF growth and HF-NF interaction.

In test TPNF2, the initial aperture of the NF is set to $h_i = 1 \times 10^{-5}$[m], *i.e.*, 10 times lower than the reference case. As for the TPNF1 test, the pressure curve at stage (I) starts becoming non-linear at $t = 0.0047$ [s], followed by the dilation of the specimen along the minimum principal stress direction (Figure 8.6). The opening also reflects on the P33 and P32 values that start raising. An acceleration on crack events is observed till a breakdown that takes place around $t = 0.0050$ [s]. Since the fluid is filling the new fractured volume the pressure remains constant. At the same time a drop in the crack events activity resulting in a "plateau" on the cumulative crack events curve is recorded. Once the pressure builds up again, it leads to a major breakdown at $t = 0.0053$ [s].

On stage (II), the decrease on the crack events is very small when the HF meets the NF at ($t = 0.0065$ [s]). The reason is that the initial aperture is too low to allow for leak off.

After this small decrease of the fracturing rate the HF starts propagating again entering stage (III). The HF is almost not affected by the NF and propagates until it reaches the boundaries of the numerical specimen. The crack events then keep increasing until the total breakdown of the sample. Actually, even after the shut-in, the number of crack events continues to increase as a result of highly viscous fluid and no leak-off from the NF (Figure 8.6). As a consequence the P33 and P32 indexes increase rapidly too. Also, the average aperture value is higher than in the reference case.

For test TPNF3, the initial aperture was set to $h_i = 1 \times 10^{-3}$ [m], *i.e.*, 10 times larger than in case TPNF1. According to the recorded reponse in Figure 8.9, stage (I) is similar to TPNF1 and TPNF2 as expected since the NF hydraulic properties don't affect the HF yet.

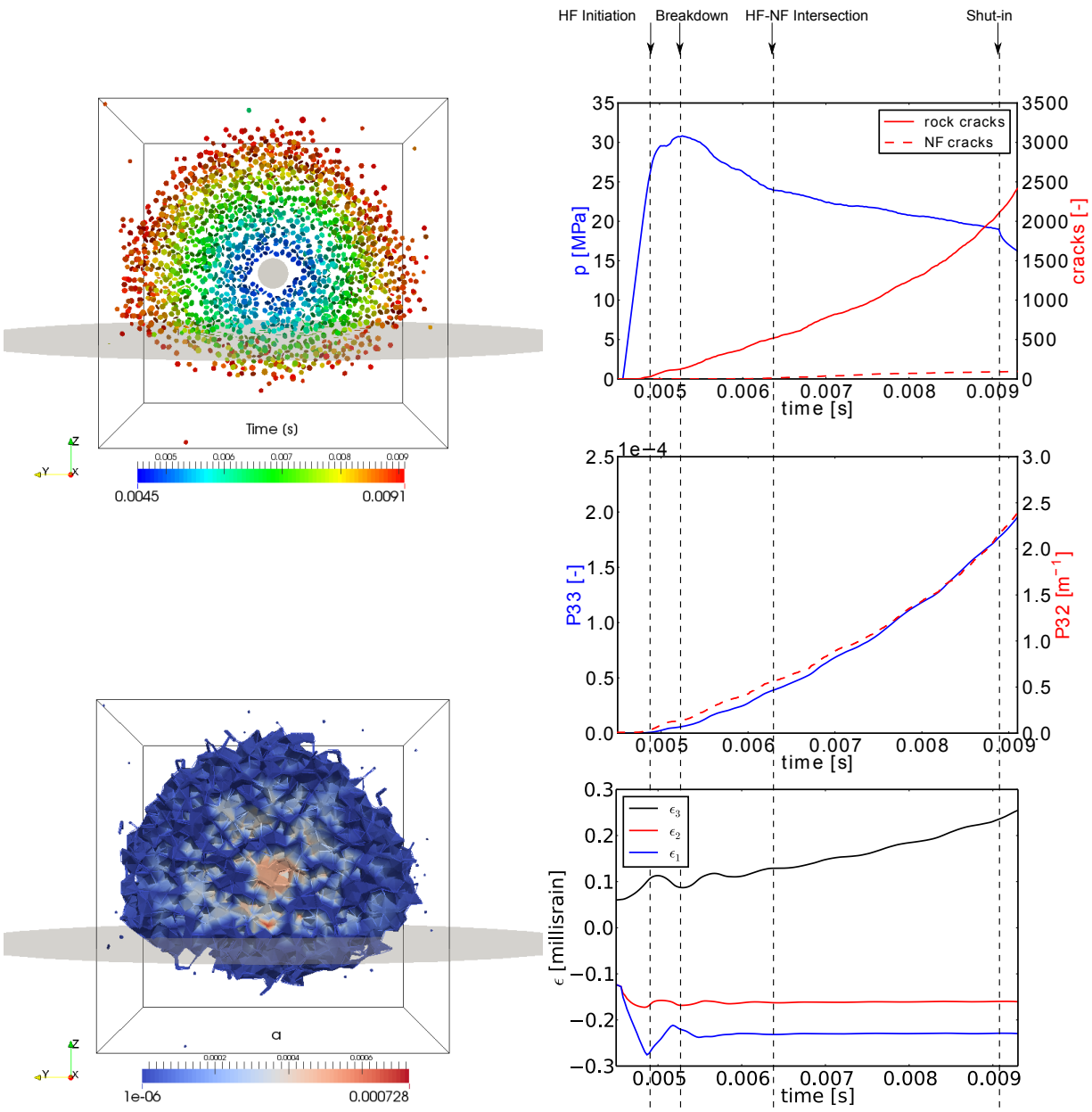

Figure 8.6: Case TPNF2 with initial aperture $h_{init} = 1^{-5}$ [m]. On the left are shown two side views of the specimen on the $\sigma_1 - \sigma_2$ plane at the shut-in (stage III), (Top) crack events with the colour code representing the time of occurrence and (Bottom) aperture map at the shut-in. On the right side are shown (top to bottom): Evolution of pressure at injection point and cumulative crack events,, P33 and P32 indexes and volumetric deformation of the sample. The vertical dashed lines mark the initiation time, the breakdown time and the shut-in time respectively.

On the contrary, after breakdown, on stage (II), the relatively large initial aperture causes an excessive leak-off and slows down the fracturing rate (see Figures 8.8).

The fluid pressure is dropping along the NF and the HF propagation stops temporarily. At the same time the HF is propagating on every other direction except for the one blocked by the NF.

Comparing the cases TPNF1,TPNF2 and TPNF3, it is clear that for the same volume of injected fluid, the intensity of the cracks and the total fractured volume decrease as the initial aperture of the NF increase (Figure 8.10). This is due to the increase of leak-off through the NF.

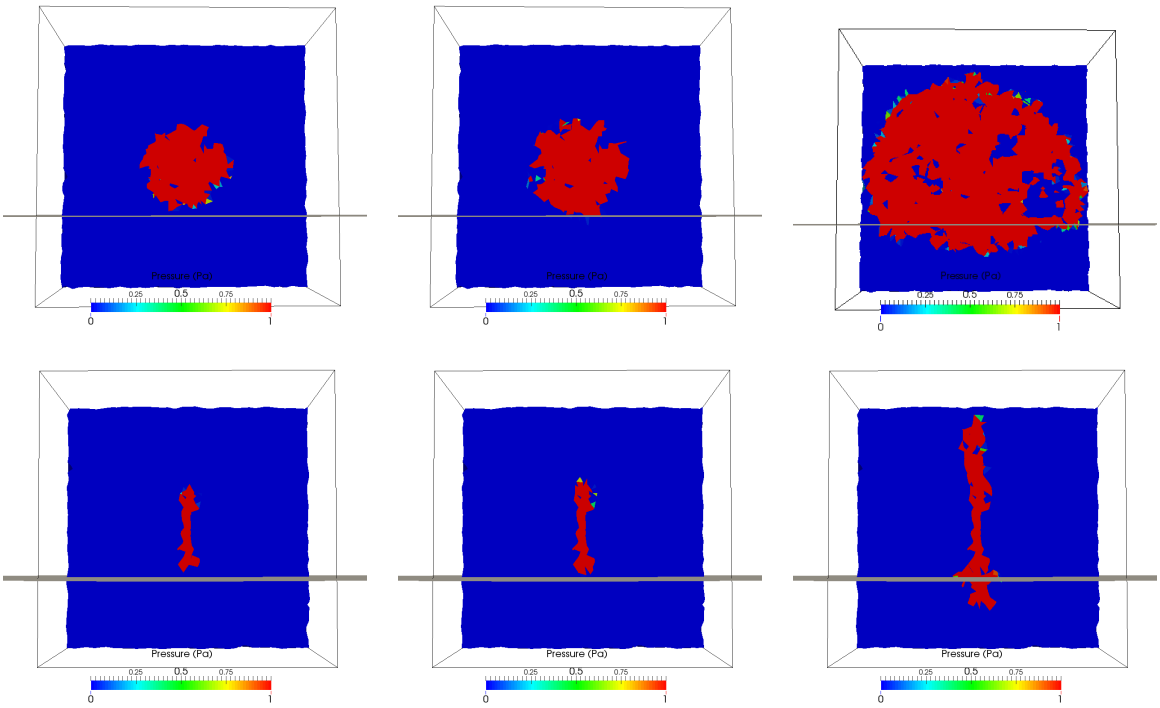

Figure 8.7: Case TPNF2:(Top) Binary pressure field showing the fluid distribution inside the specimen (red color) on the HF plane and (Bottom) perpendicular to the HF plane. From left to right: just before the HF/NF intersection, just after the intersection and at the shut-in.

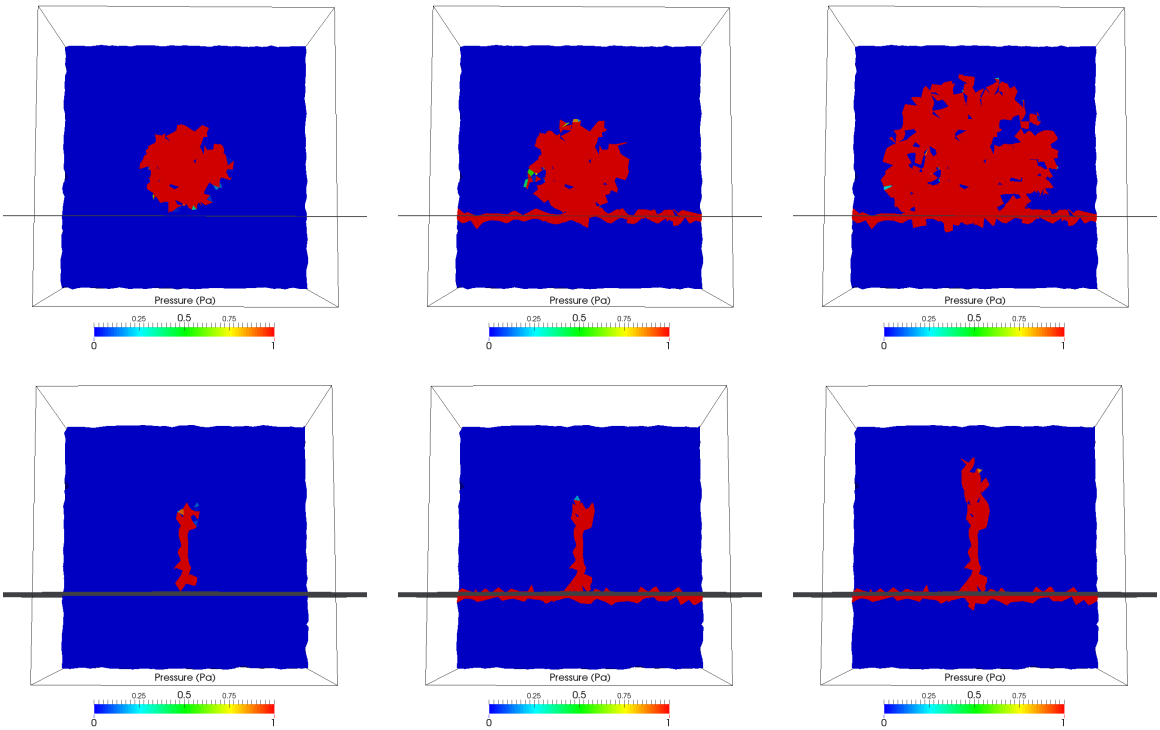

Figure 8.8: Case TPNF3:(Top) Binary pressure field showing the fluid distribution inside the specimen (red color) on the HF plane and (Bottom) perpendicular to the HF plane. From left to right: just before the HF/NF intersection, just after the intersection and at the shut-in.

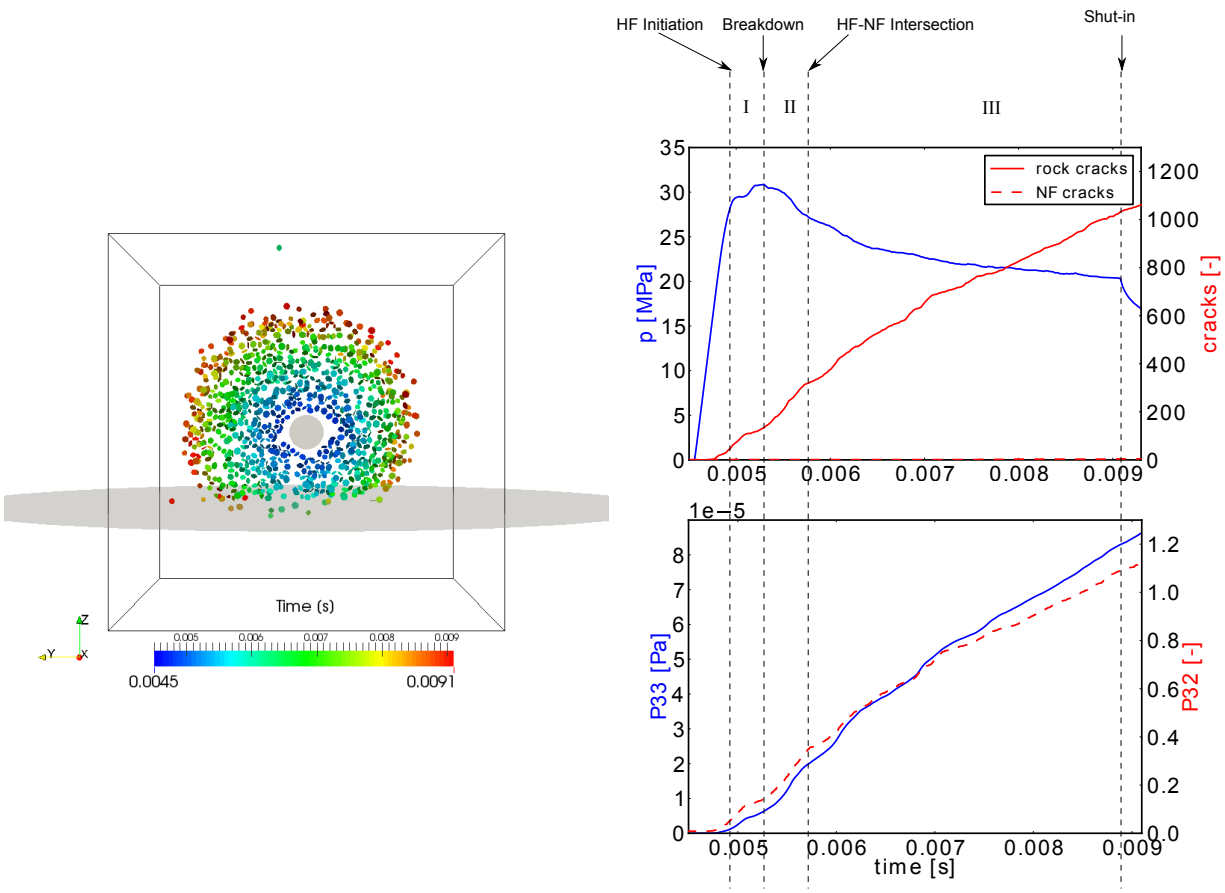

Figure 8.9: Case TPNF3 with initial aperture $h_{init} = 1^{-3}$ [m]. On the left is shown a side-view of the specimen on the $\sigma_1 - \sigma_2$ plane at the shut-in (stage III), with the crack events coloured according the time of occurrence. On the right side are shown (top to bottom): Evolution of pressure at injection point, cumulative crack events and P33 - P32 indexes. The vertical dashed lines mark the initiation time, the breakdown time and the shut-in time respectively.

Finally, regarding the shape of the HF, it can be observed that while the HF crosses the discontinuity for cases TPNF1 and TPNF2, it doesn't in case TPNF3 (see cracks distribution in Figure 8.2, Figure 8.6 and Figure 8.9). The conductance of the NF is high enough to turn it into a leak-off path preventing any pressure build-up close to the interaction point.

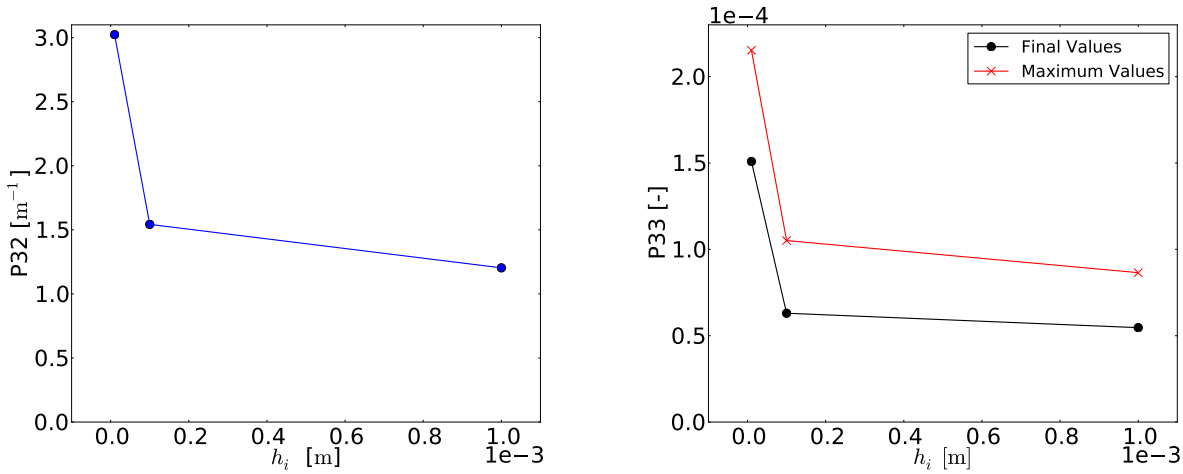

Figure 8.10: (a) $P32$ index for different initial apertures h_i of the NF. (b) $P33$ index final and peak values for different initial apertures of the NF. The results correspond to the cases TPNF1,TPNF2 and TPNF3.

Stiffness

Let us consider now a case for which the NF is more compliant than the matrix (*e.g.*, containing a sparse distribution of individual stiff grains such as quartzite grains or a fault infilled with a soft cohesive gauge material). For the test TPNF4, the control parameters remain the same as in the reference case except for the stiffness ratio between the rock matrix and the NF which we assume to be reduced to 1/10.

From the cracks' spatial and temporal distribution shown in Figure 8.11 one can observe that the NF becomes a barrier for the propagation of the HF. The low stiffness NF seems to act as a damper which reduces the stress concentration ahead of the HF and blocks the HF propagation through it (see Figure 8.12 and Figure 8.13).

From Figure 8.11, Figure 8.12 and Figure 8.13, it can be observed that although the fluid is entering and leaking-off through the NF plane, the fluid is not causing any damage inside the NF but instead, it is fracturing the rock matrix on the upper part of the specimen.

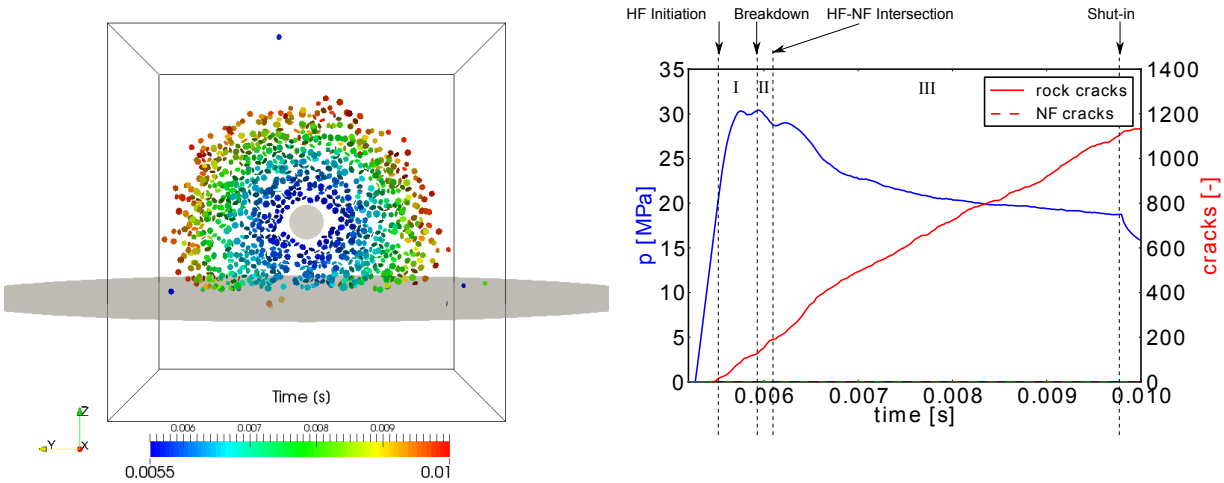

Figure 8.11: Case TPNF4 with K^{NF}/K^{rock} ratio 0.1. On the left is shown a side-view of the specimen on the $\sigma_1 - \sigma_2$ plane at the shut-in (stage III), with the crack events coloured according the time of occurrence. On the right side are shown the evolution of pressure at injection point and cumulative crack events. The vertical dashed lines mark the initiation time, the breakdown time and the shut-in time respectively.

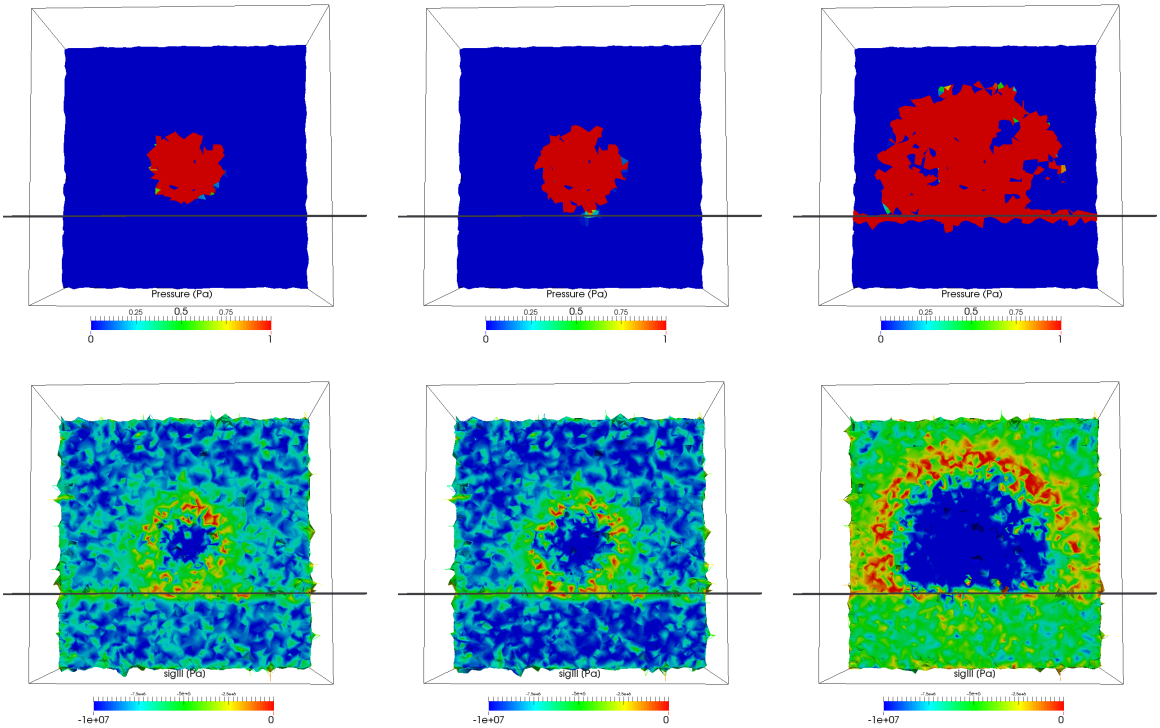

Figure 8.12: Case TPNF4,(Top) Binary pressure field showing the fluid distribution inside the specimen (red color) and (Bottom) local σ_3 magnitude (negative values correspond to compressive stresses) on the HF plane. From left to right: just before the HF/NF intersection, just after the intersection and at the shut-in.

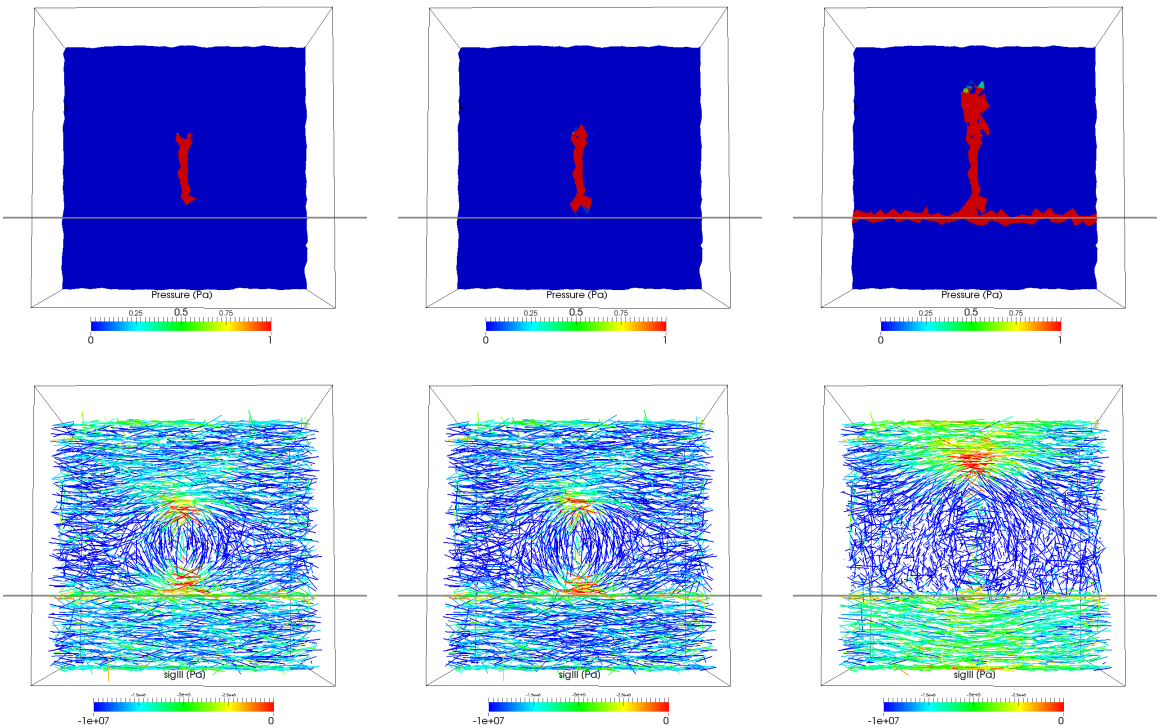

Figure 8.13: Case TPNF4,(Top) Binary pressure field showing the fluid distribution inside the specimen(red color) and (Bottom) local σ_3 direction vectors and magnitude perpendicular to the HF plane. From left to right: just before the HF/NF intersection, just after the intersection and at the shut-in.

Viscosity

This paragraph deals with the effect of fluid viscosity on the intersection of HF-NF.

In the case TPNF6, the fluid viscosity is set to $\mu = 0.05$ [Pa.s] (*i.e.*, 20 times lower than the one used in the reference case). The test response is shown in Figure 8.14.

At stage (i), although the initiation pressure is the same as in case TPNF1, the difference between initiation pressure at time $t = 0.0047$ [s] and breakdown pressure at time $t = 0.005$ [s] is smaller than in the reference case as it was expected according to the analysis by (Abbas and Lecampion, 2013). A second pressurization and breakdown phase followed by an important pressure drop is observed right after the first breakdown. After the second breakdown the HF meets the NF, and thus in stage (ii). The leak off in this test is more important given the lower fluid viscosity. This causes a deceleration in the fracturing rate described by the change of the curve of cumulative cracks number in Figure 8.14. At stage (iii), since the fluid is leaking out through the persistent NF, the pressure cannot raise at the intersection point and thus no crossing is observed. However, the pressure at the fluid front away from the NF is still built up and thus the propagation continues in this region. It should be noted than in this test, much smaller volumetric deformation takes place on the sample. On the other hand, fracture intensity is of the same order of magnitude.

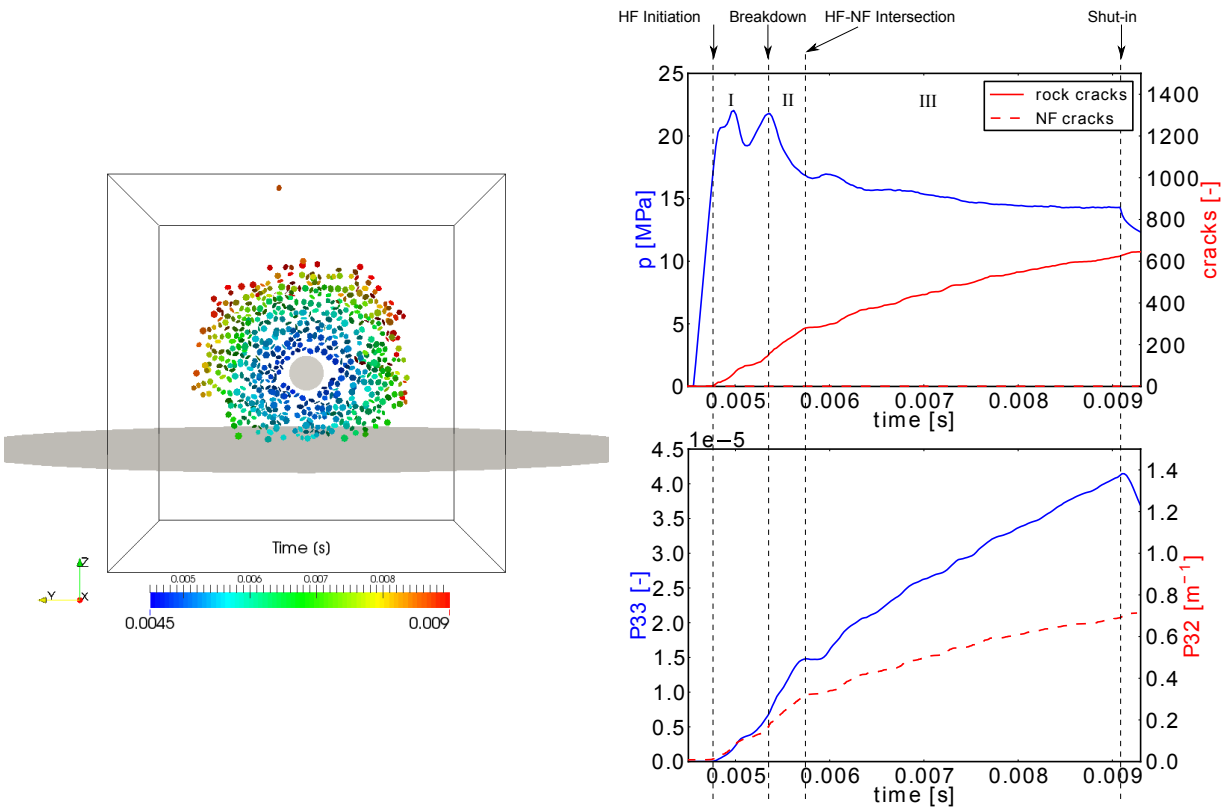

Figure 8.14: Case TPNF6 with viscosity $\mu = 5 \times 10^{-2}$ [Pa.s]. On the left is shown a side-view of the specimen on the $\sigma_1 - \sigma_2$ plane at the shut-in (stage III), with the crack events coloured according the time of occurrence. On the right side are shown (top to bottom): Evolution of pressure at injection point, cumulative crack events and P33 - P32 indexes. The vertical dashed lines mark the initiation time, the breakdown time and the shut-in time respectively.

In the case TPNF7, the viscosity is set to $\mu = 0.001$ [Pa.s] *i.e.*, 1000 times lower than in TPNF1. As it can be observed from Figure 8.15, the HF initiation pressure value p_i is very close in time to the breakdown pressure p_b.

The crack events for this case are few, clustered in time and not homogeneously distributed in space. These two facts are consequences of the toughness-driven HF. The HF is evolving through

the weakest path inside the medium. Then, after reaching the NF, due to the large leak-off, the HF propagation stops. No crossing, sliding of NF or propagation towards the other directions (intact rock) is observed (Figure 8.16 and Figure 8.17).

The fracture aperture, is very small compared to the other tests, since the HF is using a short path before meeting the NF, and the leak-off is high. These two processes limit the pressure build-up in the HF. Also the volumetric deformation is minimum and this is also reflected by the P33 index which is about $\simeq$ two orders of magnitude smaller than in the reference case TPNF1.

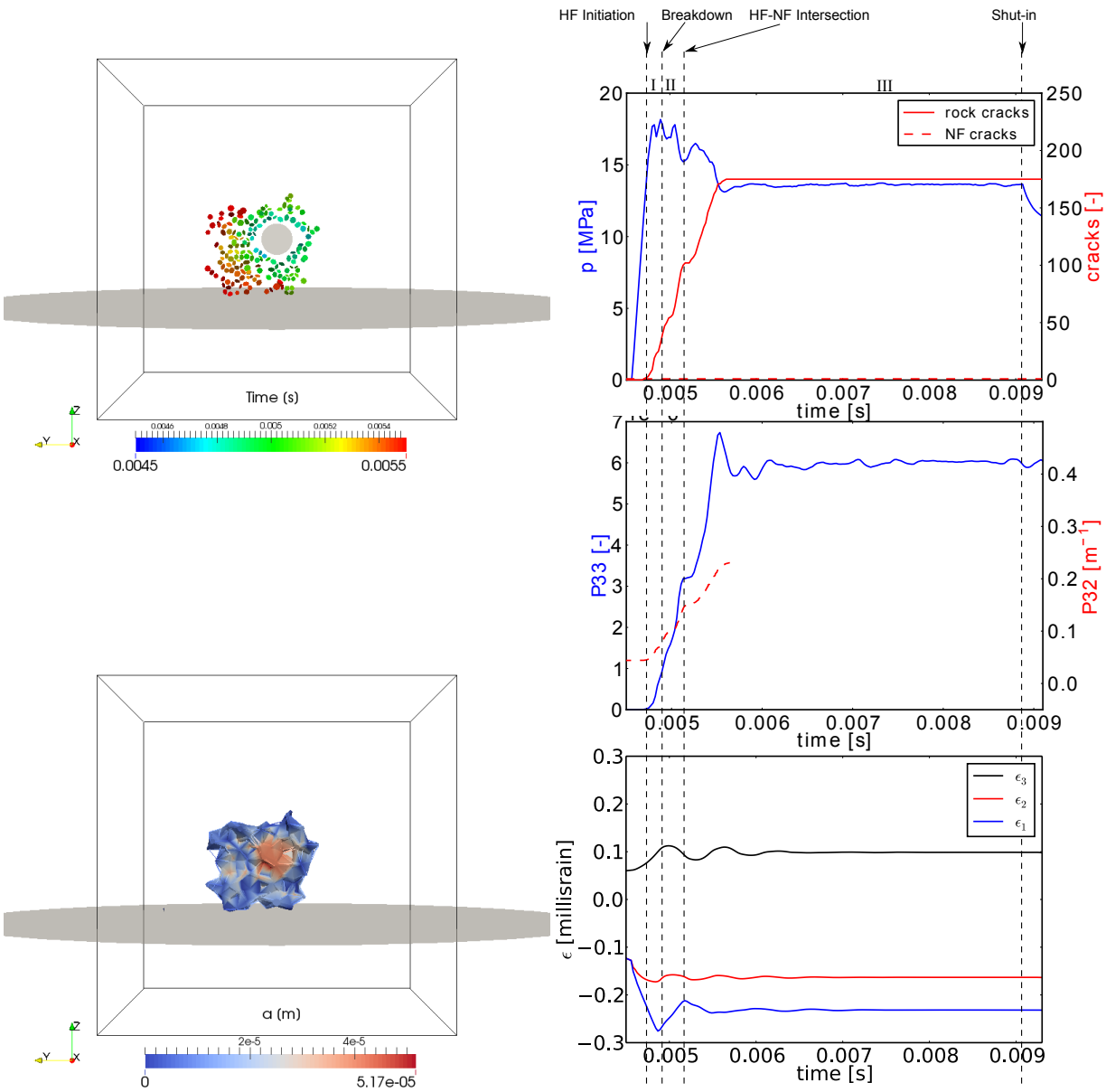

Figure 8.15: Case TPNF7 with fluid viscosity $\mu = 1 \times 10^{-3}$ [Pa.s]. On the left are shown two side views of the specimen on the $\sigma_1 - \sigma_2$ plane at the shut-in (stage III), (Top) crack events with the colour code representing the time of occurrence and (Bottom) aperture map at the shut-in. On the right side are shown (top to bottom): Evolution of pressure at injection point and cumulative crack events,, P33 and P32 indexes and volumetric deformation of the sample. The vertical dashed lines mark the initiation time, the breakdown time and the shut-in time respectively.

Comparing tests TPNF1,TPNF6 and TPNF7, (Figure 8.18) one can observe that the $P32$

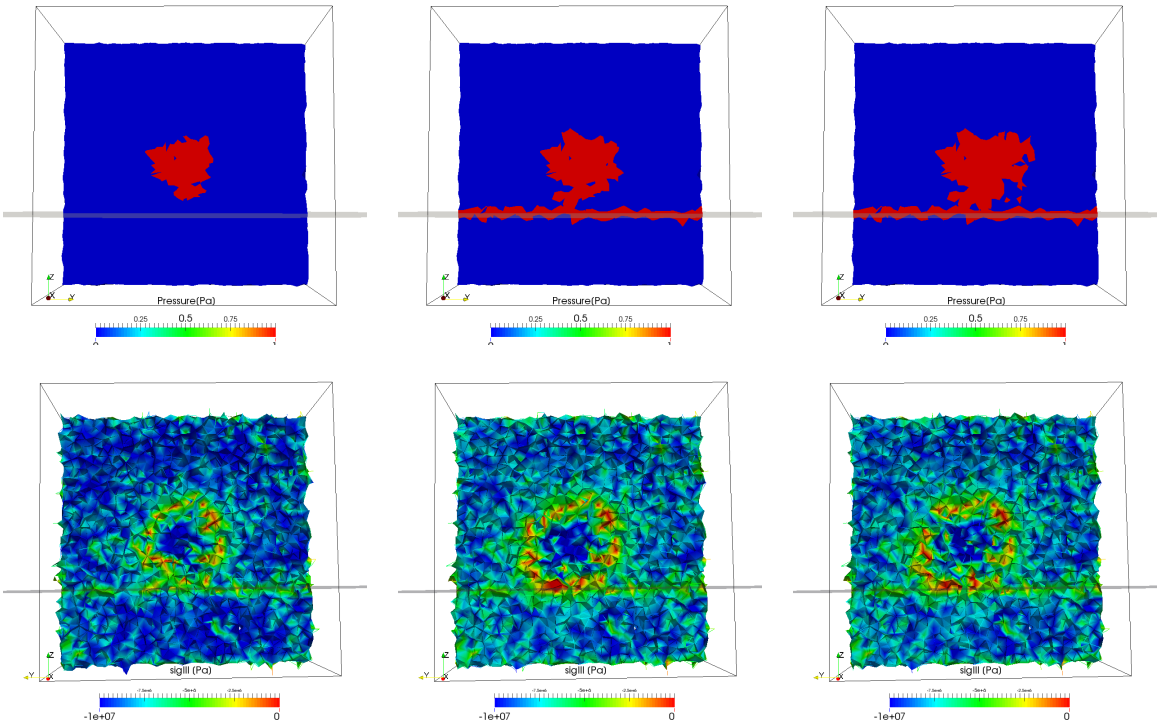

Figure 8.16: Case TPNF7, (Top) Binary pressure field showing the fluid distribution inside the specimen (red color) and (Bottom) local σ_3 magnitude (negative values correspond to compressive stresses) on the HF plane. From left to right: just before the HF/NF intersection, just after the intersection and at the shut-in.

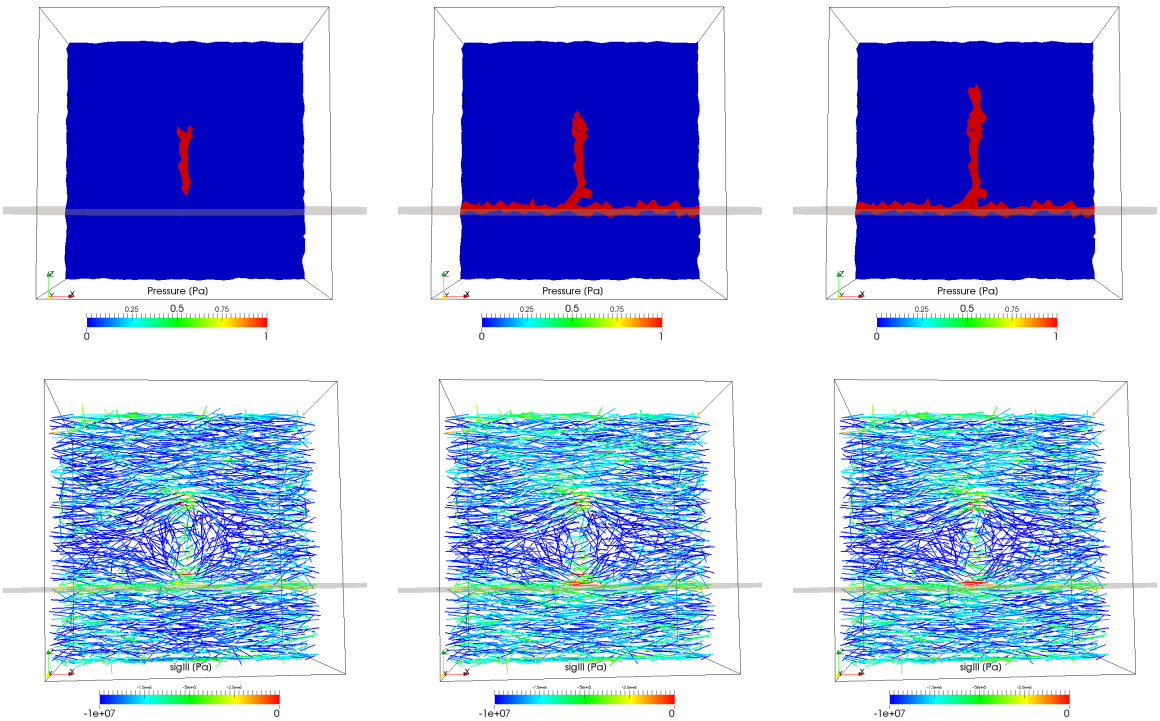

Figure 8.17: Case TPNF7, (Top) Binary pressure field showing the fluid distribution inside the specimen(red color) and (Bottom) local σ_3 direction vectors and magnitude perpendicular to the HF plane. From left to right: just before the HF/NF intersection, just after the intersection and at the shut-in.

and $P33$ indexes are directly related to the viscosity of the fluid. In fact, this is expected not only from the progressive failure of the rock block but also from the leak-off through the NF. Low viscosity fluids flow out of the sample once the HF meets the NF. On the other hand, as the viscosity increases, the fluid causes more and thicker cracks in the matrix and in the NF instead of leaking-off massively. Finally, comparing the HF propagation velocities $\vec{V}_c$ for the tests TPNF1 and TPNF7, one can observe that $\vec{V}_c$ is much higher.

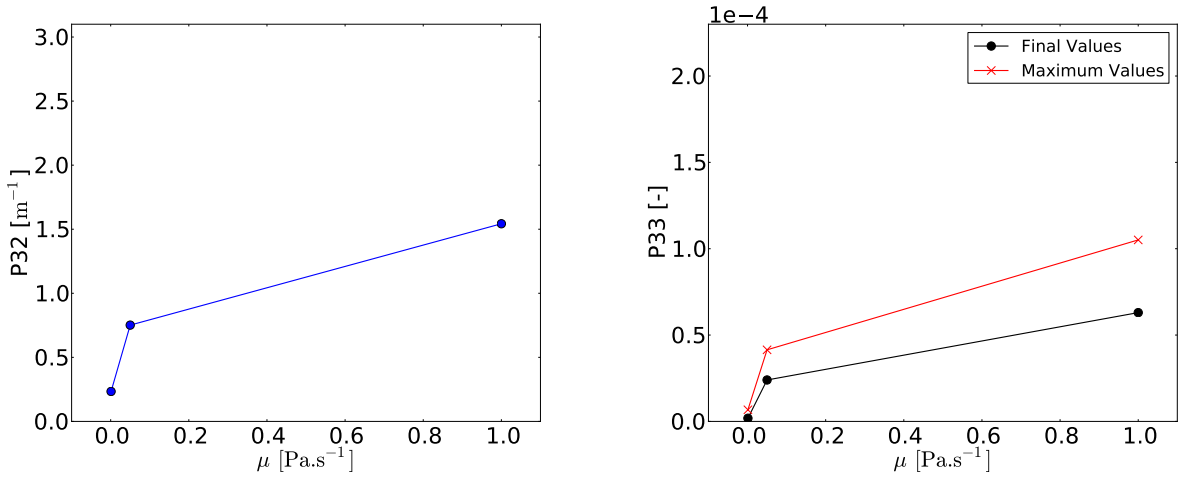

Figure 8.18: (a) $P32$ index evolution and (b) final and peak values of $P33$ evolution for different fluid viscosities μ.

Angle of approach

Finally, the effect of the angle of approach was investigated, keeping the set of parameters used for TPNF1. The angle of approach θ_{NF} was set to 90°, 70°, 60°, 50°, 30° for tests TPNF1, TPNF8, TPNF9, TPNF10, TPNF11 respectively.

The final fracture patterns are shown in Figure 8.19 for every test. From the analysis, it turned out that the HF crossed the NF plane only in cases TPNF1 and TPNF8. In addition, as the angle of approach is decreasing, the footprint (estimated from the cracks on the NF-plane) of the HF on the NF plane becomes more important.

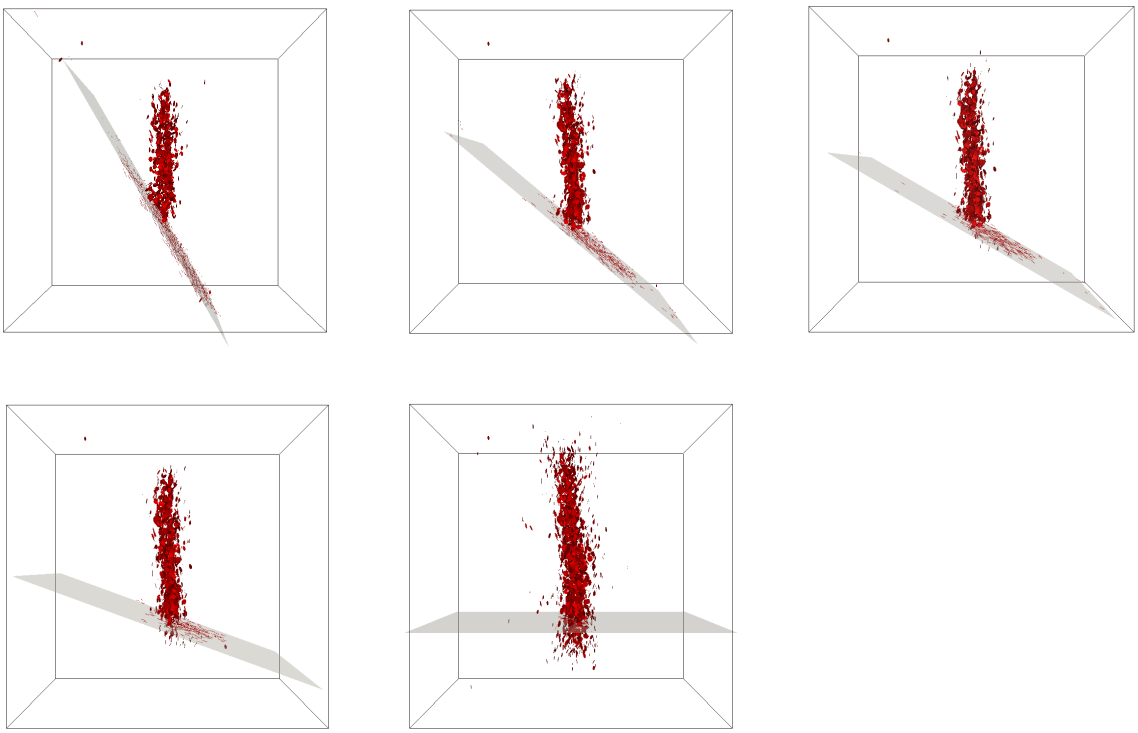

Figure 8.19: Top-view of the final fracture patterns, at the shut in (stage III), for increasing angle of approach θ_{NF} (30°,50°,60°,70°,90° for tests TPNF11,TPNF10,TPNF9,TPNF8,TPNF1 respectively).

It is also worth noting that in all cases where $\theta_{NF} < 90°$, only the segment of the NF which forms an obtuse angle with the HF is activated (*i.e.*, dilating or failing in shear) after the HF-NF intersection. This result agrees with large scale simulations of HF-NF interactions done by (Tsopela *et al.*, 2016a) for different approach angles where only the lead-segment (obtuse angle with the HF) was activated. Following the local stress field reorientation caused by the dilation of the HF, one can observe that the upper part of the NF plane is confined in the vicinity of the intersection point (Figure 8.20). Figure 8.21 shows the volumetric strain (computed as $\epsilon_{vol} = tr(\boldsymbol{\epsilon})$) at the intersection and at the shut-in phases of the test. It is clear that the upper part of the NF plane is compacted, and thus not activated, while the lower part is prone to dilation or shearing (depending on the angle of approach and on the *in-situ* state of stress). This is also in agreement with the observations made by (Jaber Taheri-Shakib, 2016) who found that the segment that draws an acute angle with the HF is confined by the stress field perturbation induced by the HF.

The results can also be compared to the analysis done in the pioneering work of (Warpinski and Teufel, 1987) and later in *e.g.*, (Liu *et al.*, 2015; Zhou *et al.*, 2010) where, HF-NF interactions are categorized into 3 types based on the main mechanism of failure:

(i) Dilation: the pressure inside the NF is higher than the confining stress and enough to open

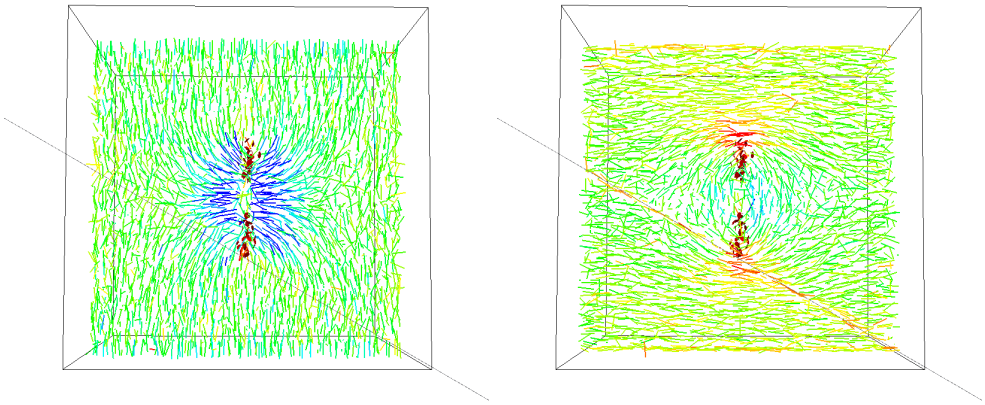

Figure 8.20: Direction and magnitude of local σ_1 (a) and σ_3 (b) principal component of stress tensor. The line is showing the direction and the colourmap is showing the magnitude set to cold colours for higher compressive stress and warm colours for lower compressive or tensile stress.

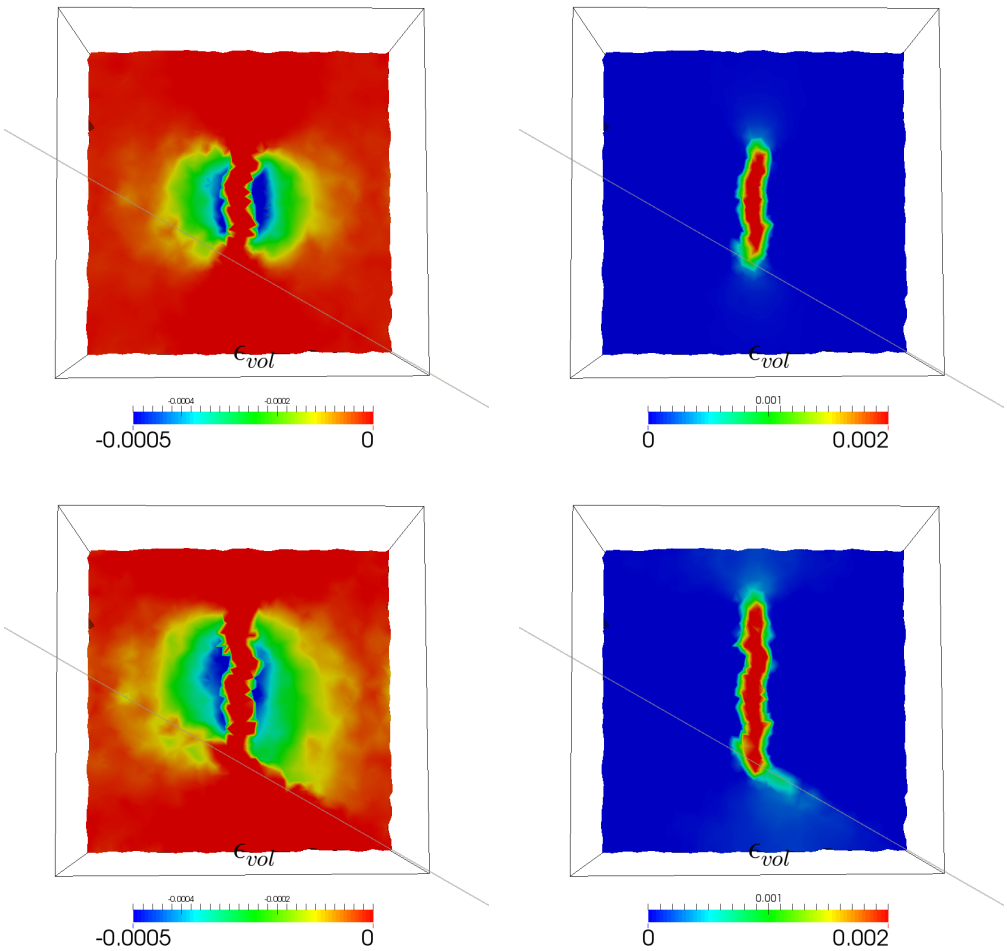

Figure 8.21: Side view on σ_2 plane showing compaction (Left) and dilation (Right) of the sample caused by the fluid injection for the TPNF9 test.

the fracture. This would mean that the fluid can enter the NF and eventually initiate a second HF from the NF tips.

(ii) Shear slippage: the local stress state leads to a shear stress along the NF that is higher than its shear strength. The shear re-activation might increase the flow in the NF and thus lead to a temporary arrest the HF.

(iii) Crossing: the pore pressure at the intersection point is sufficient to keep the HF propagating across the NF. Crossing can also be observed with a jog from the intersection point after shear slippage has occurred.

From the projection of the stresses on the NF plane, the normal stress component acting on the NF plane is given by:

$$\sigma_n = \frac{\sigma_1 + \sigma_3}{2} + \frac{\sigma_1 - \sigma_3}{2} \cos 2(90 - \theta_{NF}) \tag{8.1}$$

while the shear component is given by:

$$\tau = \frac{\sigma_1 - \sigma 3}{2} \sin 2(90 - \theta_{NF}) \tag{8.2}$$

In the recent work of (Liu *et al.*, 2015), the authors propose a criterion to predict the type of HF-NF interaction that can occur with respect to the differential stress applied. The criterion used is based on the pressure at the intersection point.

More explicitly, by considering a Mohr-Coulomb criterion for the NF and accounting for the effective stresses, the pressure p^τ needed to activate shear slippage along the NF is defined as:

$$p^\tau = \sigma_n - \frac{|\tau| - c_{NF}}{f} \tag{8.3}$$

f being the coefficient of friction of the NF and c_{NF} the cohesion.

On the other hand, the pressure needed to open the NF should be equivalent to the normal stress applied on the NF plane plus the tensile strength of the NF. It can be expressed as:

$$p^d = \sigma_n + t_{NF} \tag{8.4}$$

t_{NF} being the tensile strength of the NF.

Finally, the pressure needed to initiate a HF on the NF walls (thus, allowing the NF to cross the discontinuity) should be equivalent to the minimum principal stress plus the tensile strength of the matrix, expressed as:

$$p^c = \sigma_3 + t_m \tag{8.5}$$

t_m being the tensile strength of the rock matrix (UTS).

Based on the above failure-pressures, a factor $\mathcal{N}$ can be used to discriminate the failure processes, such as:

$$\mathcal{N} = \frac{p^c}{\min(p^d, p^\tau)} \tag{8.6}$$

In Figure 8.22 the differential stress $\Delta\sigma$, defined as $\Delta\sigma = \sigma 1 - \sigma 3$, which is needed for failure is plotted as a function of the approach angle, showing also three domains which hold for the three interaction cases[1]. For $\mathcal{N} \in (0, 1)$, the corresponding interaction is "crossing" while for higher values, the interaction leads to dilation or shear slippage failure. Thus, the red curve corresponds to the limit case $\mathcal{N} = 1$ and every point located above this line corresponds to crossing failure. Similarly, the black curve corresponds to the limit case for dilation and all points below this line correspond to dilation of the NF. The points between the two limit cases correspond to shear slippage failure.

[1]In the analysis, the pressure at the HF tip is considered to be $p = t_m$ at the intersection step.

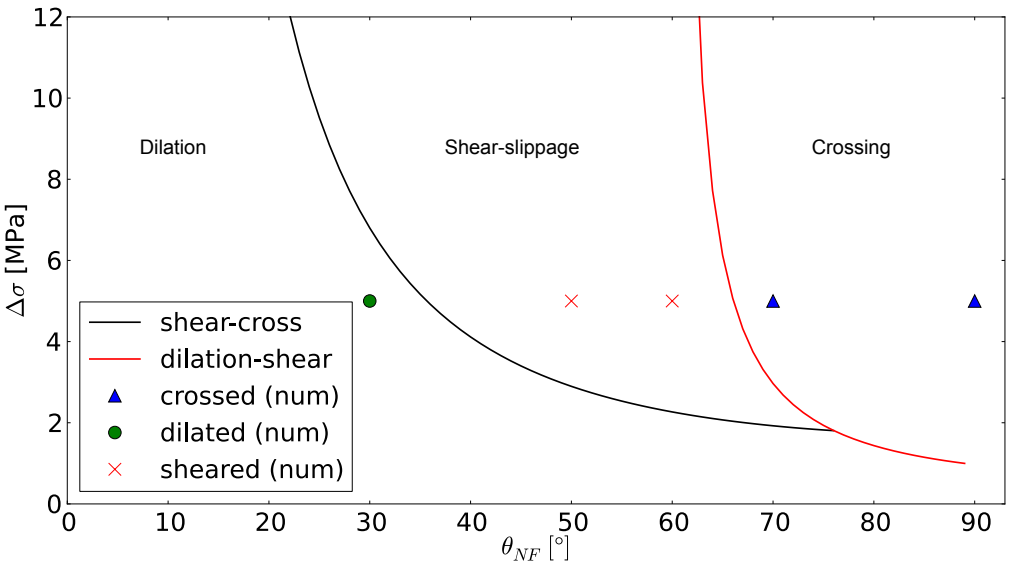

Figure 8.22: Numerical results of tests [TPNF11,TPNF10,TPNF9,TPNF8,TPNF1] regarding HF-NF interaction for different approach angles compared to the analysis proposed by (Liu *et al.*, 2015).

Regarding the numerical results, if the interaction was not of crossing type, the maximum shear and normal displacements on the NF plane were compared in order to characterize the type of failure. For the applied stress state ($\Delta\sigma = 5$ [MPa]), the NF was expected to dilate for the case where $\theta_{NF} = 30°$. The case where the simulation showed dilation along NF is plotted with a green dot in Figure 8.22. Similarly, for $\theta_{NF} = 50°$ and $\theta_{NF} = 60°$ the NF is expected to slip under the shear stress applied on the NF plane and the reduced effective normal stress. The simulated cases are plotted with red "x" signs on the same figure. Finally, for $\theta_{NF} = 70°$ and $\theta_{NF} = 90°$, the HF should theoretically cross the NF plane. This crossing can be seen in Figure 8.19. The results for the last case are plotted as blue triangles in Figure 8.22. Overall, it can be concluded that the simulations for persistent NF planes are in a good agreement with the proposed theory.

8.2 Non-persistent pre-existing fracture

As seen in Chapter 3, due to several physico-chemical processes or certain modifications in stress state from various hydro-thermo-chemo-mechanical loadings, a network of short, thin NFs might appear in the rock formation. These NFs are of varying lengths compared to the HF at different moments of the injection. The NFs can be cemented or not, presenting therefore different apertures, strength and stiffness. Also, their orientation might vary with respect to the present *in-situ* stress-field and thus, the HF growth direction. In this Section, an attempt is made to quantify the influence of each one of these parameters (approach angle, *in-situ* stress-field, aperture, matrix to NF stiffness ratio) and of the fluid viscosity on the HF fracture growth.

8.2.1 Geometry and boundary conditions

For these tests the specimen is similar to the one used in Subsection 8.1.1, with the properties presented in Table 5.2 and contains an injection slot placed at the centre. A pre-existing, non-persistent cemented "natural fracture" (NF) of radius $R_{NF} = 0.12$ [m] (unless stated differently) is placed at a distance $d = 0.15$ [m] away from the specimen's centre (distance between specimen's centre to NF centre). The configuration is similar to the one presented in subection 3.1.3 (Figure 3.7) the difference being that the NF is non persitent.

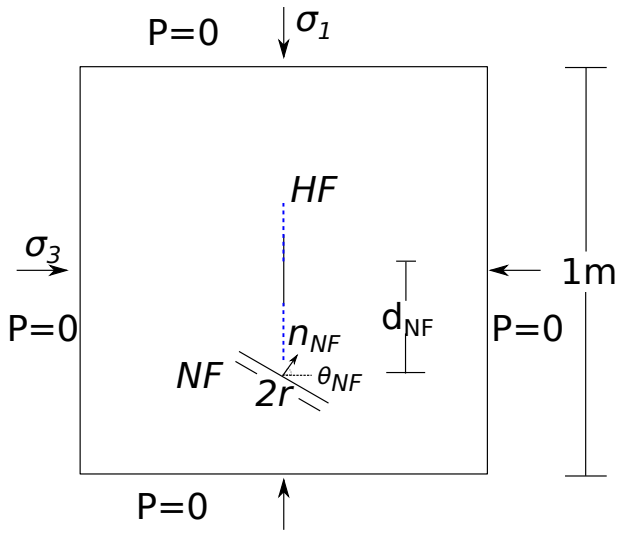

Figure 8.23: Top-view of the test's geometry and applied BCs.

The specimen is subjected to a triaxial loading before the injection starts. Both σ_2 (perpendicular to plane shown in Figure 8.23) and σ_3 are fixed to 6 and 10 [MPa] in all tests shown. On the other hand, σ_1 varies from 7 to 16 [MPa] providing a differential stress $\Delta\sigma$ ranging from 1 to 16 [MPa].

8.2.2 Sensitivity analysis

A series of tests was carried out to investigate three main points regarding the HF-NF interaction:

(i) The effect of the stress on the NF, by changing the applied boundary stresses difference, $\Delta\sigma$ and the orientation of the NF.

(ii) The effect of the NF conductivity, by controlling the initial NF aperture h_i and the fluid viscosity μ.

(iii) The effect of the NF compliance by controlling the stiffness ratio between the rock matrix and the NF, the distance from injection point d and the size of NF R_{NF}.

The different cases are compared in terms of final HF pattern, types of interaction and local deformation. The cases tested and the associated parameters are shown in Table 8.3.

Test -	Approach angle θ_{NF} [°]	Differential Stress $\Delta\sigma$ [Pa]	Viscosity μ [Pa.s]	Initial aperture h_i [m]	NF stiffness $[K_n^{NF}, K_s^{NF}]$ [Pa]	Interaction
TNF1	30	1	1.	1×10^{-4}	$[K_n^{rock}, K_s^{rock}]$	dilated
TNF2	30	7	1.	1×10^{-4}	$[K_n^{rock}, K_s^{rock}]$	shear slip
TNF3	30	10	1.	1×10^{-4}	$[K_n^{rock}, K_s^{rock}]$	shear slip
TNF4	30	7	1.	1×10^{-3}	$[K_n^{rock}, K_s^{rock}]$	shear slip
TNF5	30	7	1.	1×10^{-5}	$[K_n^{rock}, K_s^{rock}]$	dilated
TNF6	60	1	1.	1×10^{-4}	$[K_n^{rock}, K_s^{rock}]$	dilated
TNF7	60	7	1.	1×10^{-4}	$[K_n^{rock}, K_s^{rock}]$	shear slip
TNF8	60	10	1.	1×10^{-4}	$[K_n^{rock}, K_s^{rock}]$	shear slip
TNF9	60	7	1.	1×10^{-3}	$[K_n^{rock}, K_s^{rock}]$	shear slip
TNF10	60	7	1.	1×10^{-5}	$[K_n^{rock}, K_s^{rock}]$	crossed
TNF11	90	1	1.	1×10^{-4}	$[K_n^{rock}, K_s^{rock}]$	dilated
TNF12	90	7	1.	1×10^{-4}	$[K_n^{rock}, K_s^{rock}]$	crossed
TNF13	90	10	1.	1×10^{-4}	$[K_n^{rock}, K_s^{rock}]$	crossed
TNF14	90	7	1.	1×10^{-3}	$[K_n^{rock}, K_s^{rock}]$	dilated
TNF15	90	7	1.	1×10^{-5}	$[K_n^{rock}, K_s^{rock}]$	crossed
TNF16	90	7	0.05	1×10^{-3}	$[K_n^{rock}, K_s^{rock}]$	dilated
TNF17	90	7	0.05	1×10^{-4}	$[K_n^{rock}, K_s^{rock}]$	dilated
TNF18	90	7	0.05	1×10^{-5}	$[K_n^{rock}, K_s^{rock}]$	crossed
TNF19	90	7	0.001	1×10^{-3}	$[K_n^{rock}, K_s^{rock}]$	dilated
TNF20	90	7	0.001	1×10^{-4}	$[K_n^{rock}, K_s^{rock}]$	dilated
TNF21	90	7	0.001	1×10^{-5}	$[K_n^{rock}, K_s^{rock}]$	crossed
TNF22	60	7	1.	1×10^{-4}	$[\frac{K_n^{rock}}{1000}, \frac{K_s^{rock}}{1000}]$	dilated
TNF23[1]	60	7	1.	1×10^{-4}	$[\frac{K_n^{rock}}{1000}, \frac{K_s^{rock}}{1000}]$	dilated

Table 8.3: Numerical tests performed to study HF-NF interaction in the case of a non-persistent NF.

State of stress on NF

In most of the tests available in the literature, the studies generally focus on HF growth while intersecting a NF under different approach angles (and thus, different loading applied to the NF). Most of the studies deal with *post-mortem* analysis of the HF propagation in specimens containing pre-existing defects, as, for example, in (Zhou *et al.*, 2010). In this paragraph, the effect of approach angle and of *in-situ* stress on HF growth is investigated in 3D. Nine tests are compared, corresponding respectively to three different stress fields applied on a NF inclined by an angle of 30, 60 and 90° respectively with respect to the HF. Tests [TNF1,TNF2,TNF3] (see Table 8.3) deal with a NF place at an angle of approach $\theta_{NF} = 30°$, tests [TNF6,TNF7,TNF8] correspond to $\theta_{NF} = 60°$ and tests [TNF11,TNF12,TNF13] to $\theta_{NF} = 90°$.

[1] $d = 0.25$ [m] for this test

$\Delta\sigma$ [MPa] / θ_{NF} [°]	1	7	10
30	TNF1 - dilated	TNF2 - shear slippage	TNF3 - shear slippage
60	TNF6 - dilated	TNF7 - shear slippage	TNF8 - shear slippage
90	TNF11 - dilated	TNF12 - crossing	TNF13 - crossing

Table 8.4: Numerical results regarding the HF-NF intersection for different angles of approach θ_{NF} and values of differential stress $\Delta\sigma$.

By measuring the displacements after the HF-NF intersection, different types of responses are observed. For low differential stress ($\Delta\sigma = 1$ [MPa]), the NF was dilated in all cases. For higher differential stresses ($\Delta\sigma = 10$ [MPa]) the NF was activated in shear-slippage for lower angles ($\theta_{NF} = 30°$ and $\theta_{NF} = 60°$) while crossing was observed for $\theta_{NF} = 90°$. The test results are summed up in Table 8.4 and then plotted with respect to θ_{NF} in Figure 8.24, along with the limit-case lines from the analysis of (Liu *et al.*, 2015). There, again, as for the persistent NF cases, the comparison shows good agreement between the theoretical domains and the numerical results.

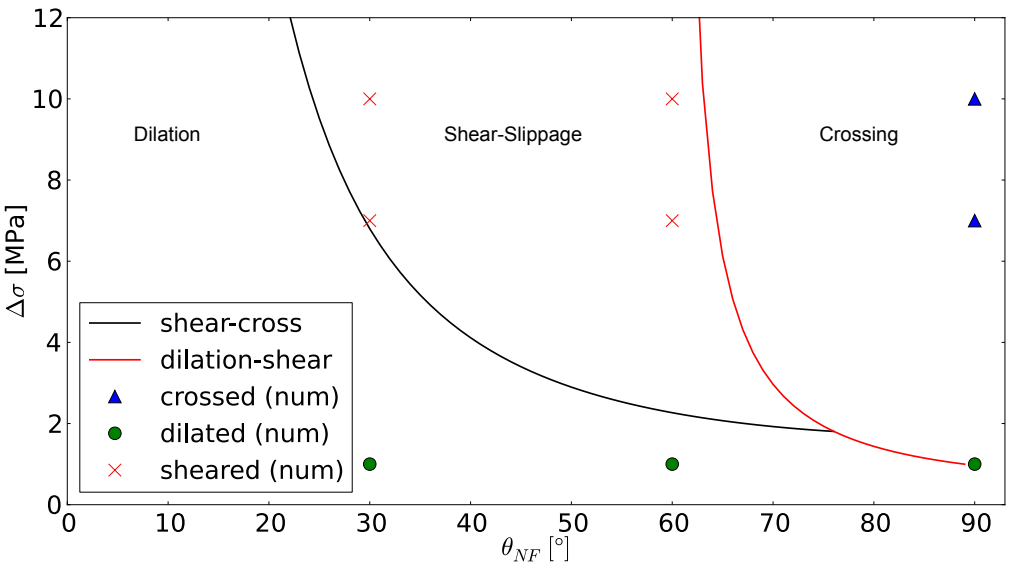

Figure 8.24: HF-NF interaction types compared to (Liu *et al.*, 2015) criteria for the cases [TNF1-3, TNF6-8, TNF11-13].

Focusing on the final patterns of [TNF2, TNF7, TNF12] shown in Figure 8.25, one can observe that the HF crosses the NF for $\theta_{NF} = 90°$ while it re-activates the NF and initiates the propagation from the lower tip following the direction of σ_1 when $\theta_{NF} = 30°$ or $60°$. The lateral development of HF is shown on the $\sigma 1 - \sigma_2$ plane (or HF plane).

In cases of shear-slippage or dilation of non persistent NF, the HF will re-initiate with a time delay. However the lateral extent of the HF during the arrest on the NF plane could be crucial for the HF evolution. Especially in formations with dense NF networks the HF could diverge from the expected plane or re-activate a completely different set of NFs. Full 3D analysis and is thus necessary in these cases to deal with the HF evolution since for different types of interactions, even for the same approach angle, the lateral growth of the HF can vary significantly.

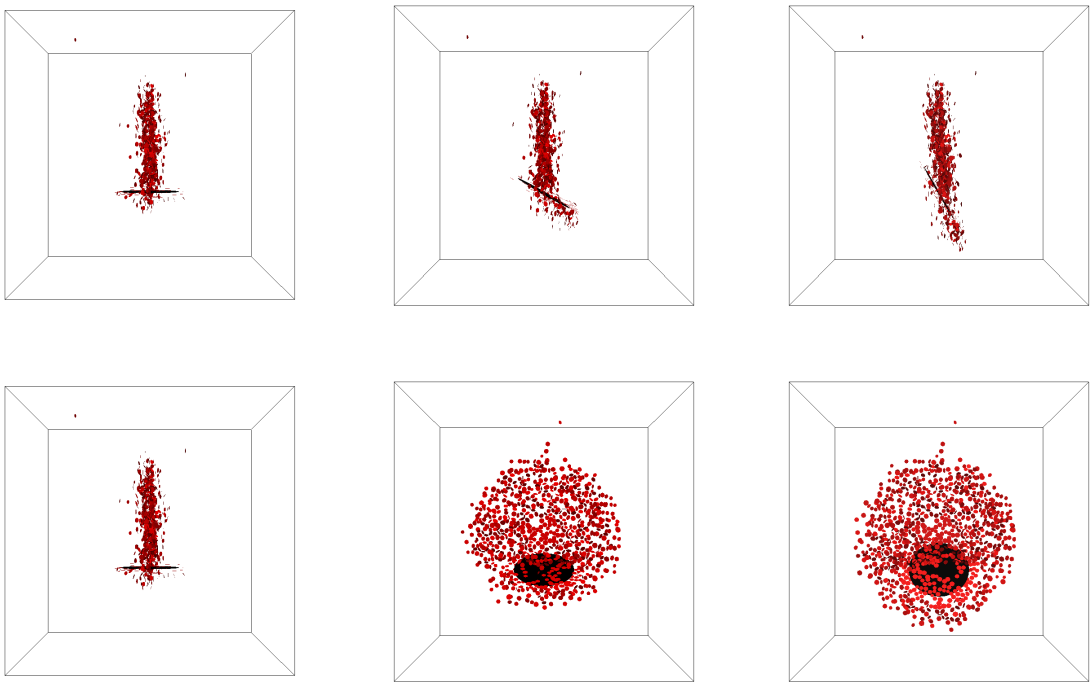

Figure 8.25: (Top) HF pattern on the plane $\sigma_1 - \sigma_3$ and (Bottom) HF pattern on the plane $\sigma_1 - \sigma_2$. From left to right TNF12, TNF7 and TNF2 for $\theta_{NF} = 90°$, $60°$ and $30°$.

Aperture of NF and fluid viscosity

Another parameter which deserves to be directly studied, is the hydraulic aperture of the NF. As shown in Chapter 3, the NF apertures for different shale plays is found ranging between $\mathcal{O}(10^{-5})$ and $\mathcal{O}(10^{-3})$ [m]. The NF aperture, in combination with the fluid viscosity, controls the conductivity of the NF. For a given constant flow rate, conductivity can play an important role on HF-NF interaction. For example, one should expect that low conductivity NF can easily lead to a crossing HF while higher conductivity NF favours dilation. The reason for crossing type of interaction is the resulting pressure-increase at the intersection point for low conductivity and thus low leak-off (inside the NF). On, the other hand, higher conductivity allows for pore-pressure increase along the NF which decreases the normal stress applied on it. That could result in shear slippage or opening of the NF (depending on the confining stress on it).

In this paragraph, the effect of the NF conductivity on HF growth is investigated for NFs with varying angles of approach and apertures, and then for varying apertures and fluid viscosity for a given approach angle of $\theta_{NF} = 90°$. First, nine tests are compared, considering 3 different initial apertures $h_i = [1 \times 10^{-5}, 1 \times 10^{-4}, 1 \times 10^{-4}]$ [m] for each approach angle. The tests [TNF2, TNF4, TNF5] refer to $\theta_{NF} = 30°$ case, the tests [TNF7, TNF9, TNF10] to $\theta_{NF} = 60°$ and tests [TNF12, TNF14, TNF15] to $\theta = 90°$ as shown in Table 8.3. Then, three different values of fluid viscosity are used $\mu = [1., 0.05, 0.001]$ [Pa.s] on three NFs with different initial apertures of $h_i = [1 \times 10^{-5}, 1 \times 10^{-4}, 1 \times 10^{-4}]$ [m] for $\theta_{NF} = 90°$ [TNF12, TNF14-TNF21].

In Figure 8.26, the fluid distribution is shown for the nine cases with different angles and apertures. For low values of θ_{NF} (*i.e.*, 30°), the NF is dilating even when the aperture is small. The NF still acts as a flow corridor for the HF. For $\theta_{NF} = 60°$, the HF crosses the NF for low apertures. Then, for increasing aperture, the NF is activated in shear and finally a new HF propagates close to the NF tip following the direction of σ_1. Further increase of h_i leads to a dilated NF that initiates a HF propagation directly at the NF tip. Finally, for $\theta_{NF} = 90°$, for $h_i = 10^{-5}$ [m], HF crosses the NF without penetrating into it significantly. For $h_i = 10^{-4}$ [m],

the HF also crosses the NF its HF length after crossing is smaller. Finally, for $h_i = 10^{-3}$ [m], the NF is dilated and the new HFs initiate from the NF tips. The intersection results are summed up in table 8.5.

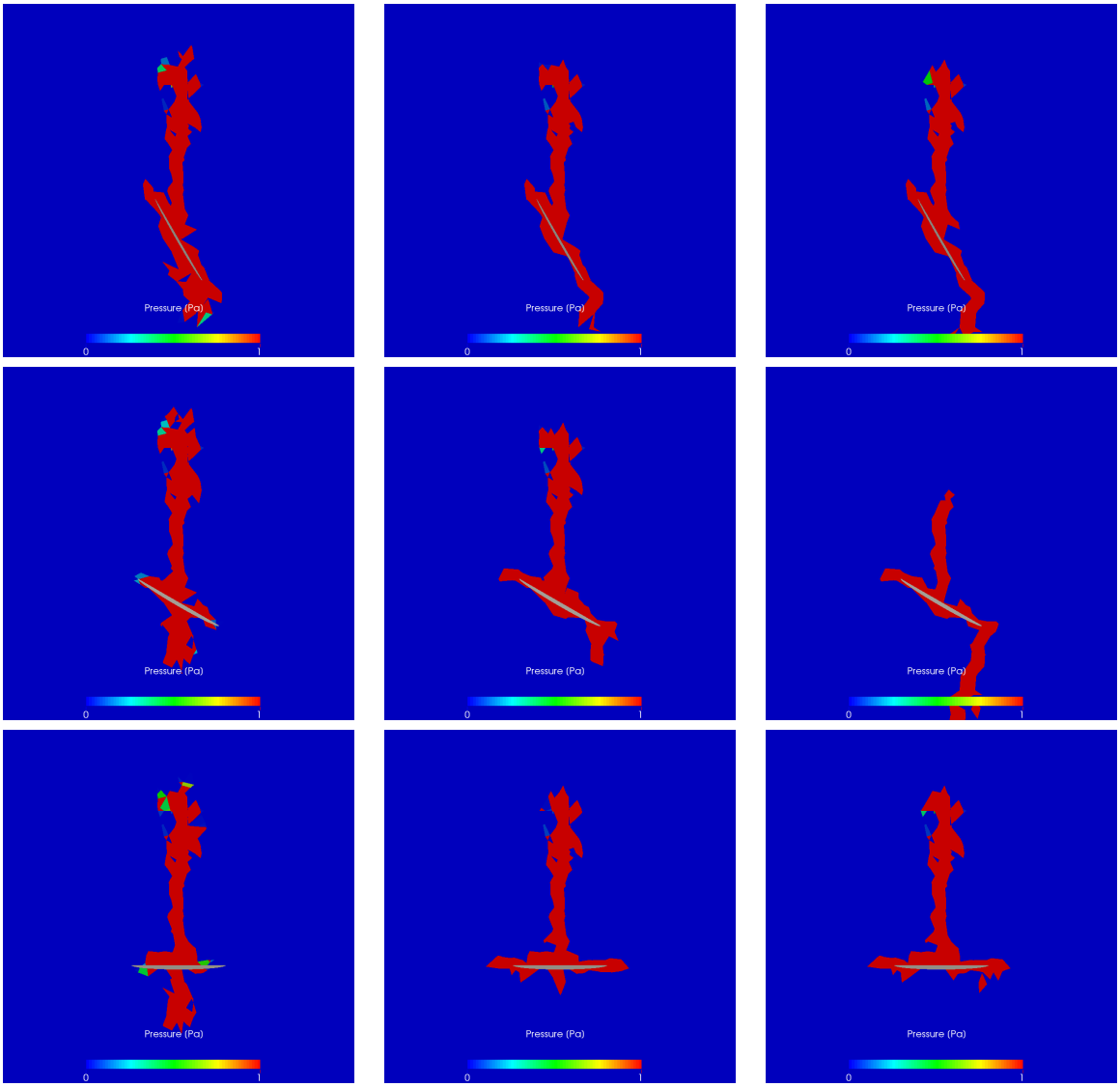

Figure 8.26: Binary pressure field showing the final HF patterns for different apertures, from left to right $h_i = 10^{-5}$, 10^{-4} 10^{-3} [m]. Results for cases corresponding to (Top) $\theta = 30°$ [TNF5,TNF2, TNF4], (Centre) $\theta = 60°$ [TNF10,TNF7 TNF9]and (Bottom) for $\theta = 90°$ [TNF15, TNF12, TNF14].

h_i [m] / θ_{NF} [°]	1×10^{-5}	1×10^{-4}	1×10^{-3}
30	TNF2 - dilated	TNF4 - dilated	TNF5 - dilated
60	TNF7 - crossing	TNF9 - shear slippage	TNF10- dilated
90	TNF12 - crossing	TNF14 - crossing	TNF15 - dilated

Table 8.5: Numerical results regarding the HF-NF intersection for different angles of approach θ_{NF} and apertures h_i.

From the tests on a single angle of approach, it was found that for an increasing conductivity the interaction evolves from crossing (even for very low viscosity) to dilating tendency (even for

higher viscosity). The results are summed up in Table 8.6.

h_i [m] / μ [Pa.s]	1×10^{-5}	1×10^{-4}	1×10^{-3}
0.001	TNF12 - crossing	TNF14 - dilated	TNF15 - dilated
0.05	TNF16 - crossing	TNF17 - dilated	TNF18 - dilated
1.	TNF19 - crossing	TNF20 - crossing	TNF21 - dilated

Table 8.6: Numerical results regarding the HF-NF intersection for different angles of approach θ_{NF} and values of differential stress $\Delta\sigma$.

Thus, the above results obtained in this paragraph confirm that lower conductivities enhance the crossing tendency during HF-NF interaction.

In terms of response, the pressure measured at the injection point and the cumulative crack events for the tests TNF7,TNF9 and TNF10 are shown in Figure 8.27. After the breakdown, the HF meets the NF and the pressure curve shows a local plateau (see Figure 8.27a around $t = 0.006$ [s]). One can notice however that due to the lack of leak-off in the NF, the fracturing rate is less affected when $h_i = 10^{-5}$ than in the other cases. This results in a much higher number of total crack events and consequently in larger HF length.

Stiffness of NF

In this paragraph the effect of stiffness ratio between the NF and the intact rock on HF growth is investigated for the case where $\theta_{NF} = 60\,[°]$. The tests under comparison are [TNF12, TNF22, TNF23] in Table 8.3 and correspond to stiffness ratio $\frac{K^{NF}}{K^{rock}} = 1$, $\frac{1}{1000}$, and $\frac{1}{1000}$ respectively while the distance between the injection point and the NF is $d = 0.15$ [m] for TNF12 and TNF22 and $d = 0.25$ [m] for TNF23. The tests where the stiffness is much lower than the one of the intact rock could correspond to cases where the NF walls are characterized by high aspect ratio asperities or where the NF is filled with a soft (clayey) material.

In presence of soft NFs, the system's behaviour is characterized by a compaction of the NF under the load imposed by the HF, that prevents the HF from crossing it. Instead, the crack events are localized behind the NF as if the NF works like a cushion (damping effect mentioned in Section 8.1.3 for the persistent NF) which tends to arrest the propagation in this direction. It is thus becoming a barrier for the HF. When fluid reaches the boundaries of the NF, the propagation is arrested or, favoured by the stress-field developed at the NF tip, and the HF starts propagating along direction of σ_1.

In Figure 8.28 the pressure field, volumetric strain field, local σ_1 field and crack events are shown on a slice perpendicular to the HF plane for case TNF22. One can observe by following the pressure field that the HF is diverged from the initial HF direction even in the early steps of the injection. Then, a relatively large fractured volume is created behind the NF. Finally the HF re-initiates from the lower tip of the NF. Studying the the local strain field can explain the HF-NF interaction here. It can be seen that the HF causes a compaction (cold colours in figure) along the NF which prevents the HF from entering it. When the fluid finally meets the NF on the lower part, it causes local dilation (the upper part of the NF is still compacted) which lets a HF to initiate at the lower tip. Also, the local σ_1 direction field can give complementary insights in this behaviour. The compliant defect causes a local stress redistribution in its vicinity initially. Multiple crack events are observed as the HF approaches the NF, since the HF is "trapped" behind the NF. Further injection lets the fluid enter the NF plane and make the stress field more homogeneous around the NF. Finally, the crack events occur at the lower fracture tip forming a new HF initiating at this point.

Compliant NFs induce a perturbation (local decrease) to the stress field in its vicinity. It is

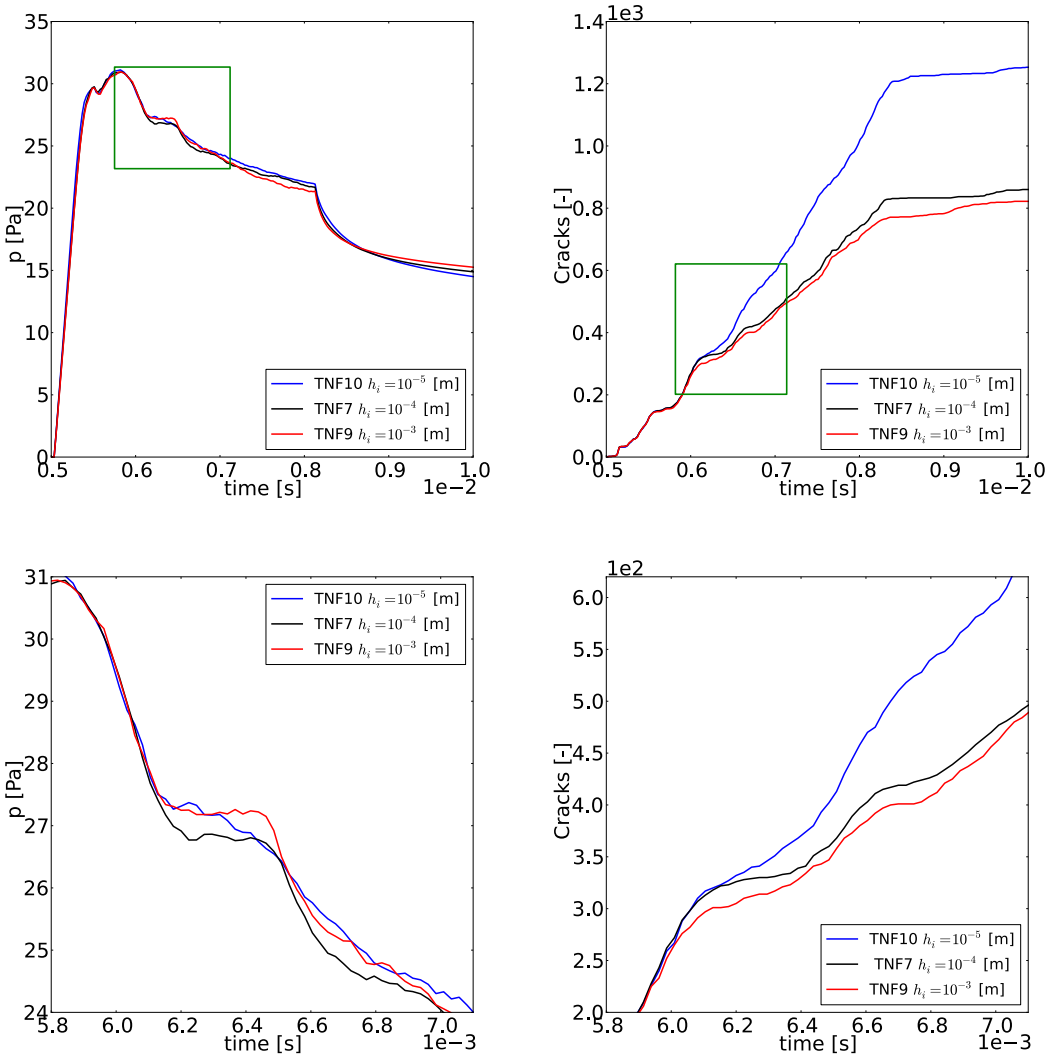

(a) **(b)**

Figure 8.27: Evolution during (Top) injection and (Bottom) HF-NF intersection of: (a) Pressure at injection point and (b) Cumulative crack events for $\theta_{NF} = 60°$, tests TNF7,TNF9 and TNF10.

interesting to note that in some cases, when the NF is placed further away from the injection point, the stress field perturbation, leads the HF to diverge and bypass the NF. This is more prone to happen when the NF is further away from the injection point because the HF initiates outside the perturbed stress region and follows the trajectory of the local σ_1 direction. In most of these cases, a HF-bifurcation is observed. The loss of pressure at the fluid front due to leak-off in the NF (if the HF meets the NF at the NF tip), causes the HF to arrest. At the same time, a second branch of HF initiates from the injection point towards the other side of the NF.

In order to emphasise this HF-bifurcation effect, another test (TNF23) was considered. The distance between the injection point and the NF is this time larger. As it can be seen in Figure 8.29, the HF is initially propagating vertically following the applied σ_1 direction. Then, when the HF approaches the NF, it diverges and propagates around the NF. A second branch of the HF developed from the injection point towards the other side of the NF with the micro-cracks following the local σ_1. This HF bifuraction is causing a compacted region between the two branches that arrests temporally the propagation.

Such an effect might be less evident in field-scale treatments due to the fact that size of the

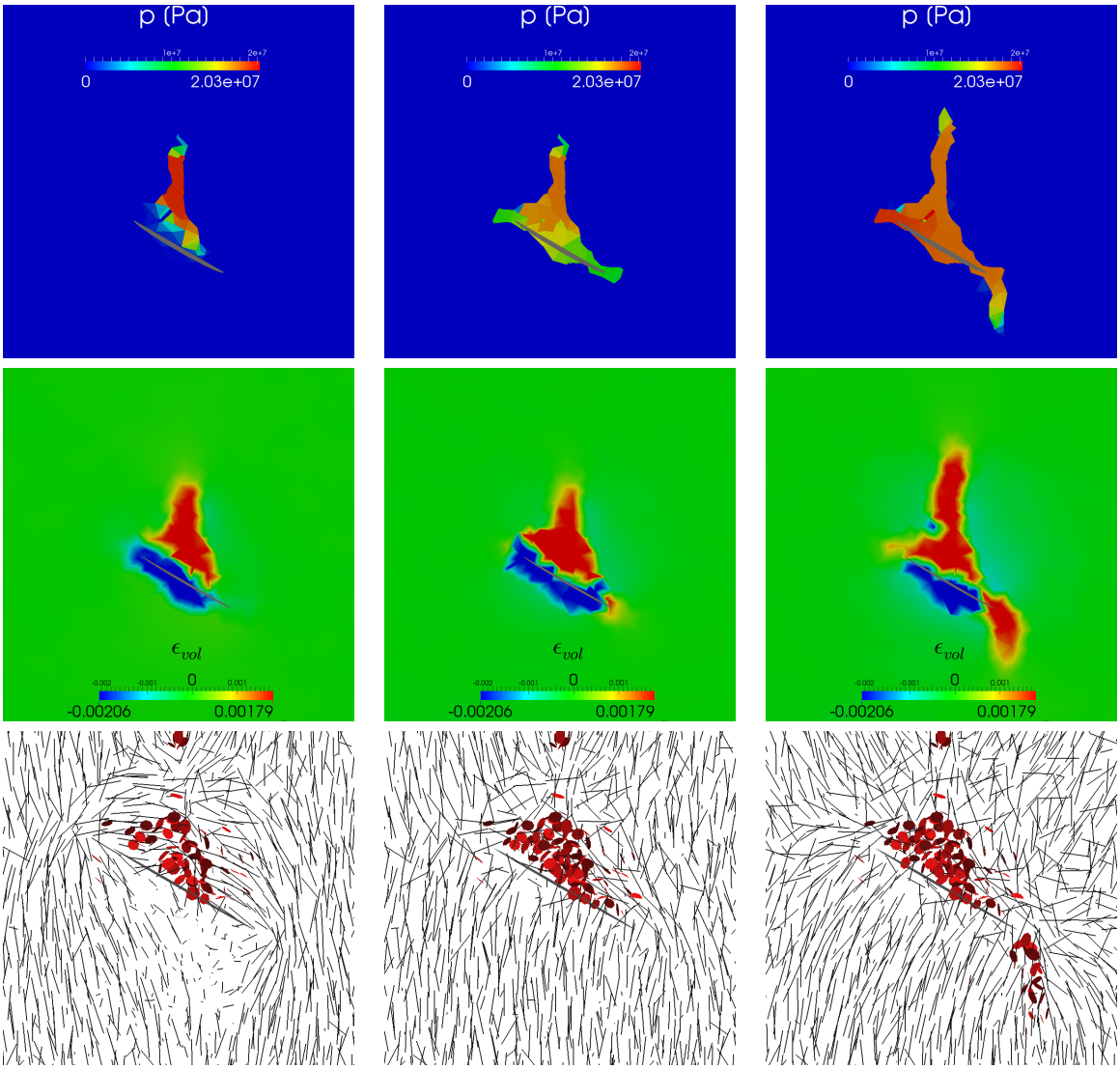

Figure 8.28: Case TNF22 (Top) Pressure field, (Middle) Volumetric strain field ϵ_v where $\epsilon_v > 0$ indicates dilation and $\epsilon_v < 0$ compaction, (Bottom) Local σ_1 direction and crack events. The values are shown for a slice perpendicular to the HF plane for three different stages of the injection.

perturbed area is a function of NF's size. According to Chapter 3 the length of a typical NF is ranging from $\mathcal{O}(10^{-2})$ to $\mathcal{O}(10^{0})$ [m], thus much smaller than the HF size ($\mathcal{O}(10^{1})$ to $\mathcal{O}(10^{2})$). However, the accumulation of stress perturbations in dens, compliant NF networks could affect the HF propagation especially in its early stages (after the main break down), where the HF size is still comparable to the NF sizes.

Regarding the tests' reponses, the evolutions of the pressures at the injection point and of the cumulative crack events are shown in Figure 8.30. Although TNF12 and TNF23 show similar behaviour up to break down, in the case of TNF22, the stress perturbation around the NF causes a massive breakdown with a more pronounced pressure drop. This pressure drop is accompanied by a large amount of cracks. The new fractured volume has caused a large pressure drop which needs a new pressure build up before fracturing can start again (around 0.007[s]). Comparing TNF12 and TNF23 one can observe that the behaviour is very similar up to the moment when the HF meets the NF for the test TNF12 (around 0.006[s]). The pressure drop is slightly higher for TNF12 and is followed by a plateau in the crack recordings as the injection fluid is just filling the discontinuity. On the other hand, when the HF is approaching the NF in TNF23, there is no plateau but rather an increase of the fracturing rate because of the intense fracturing in the

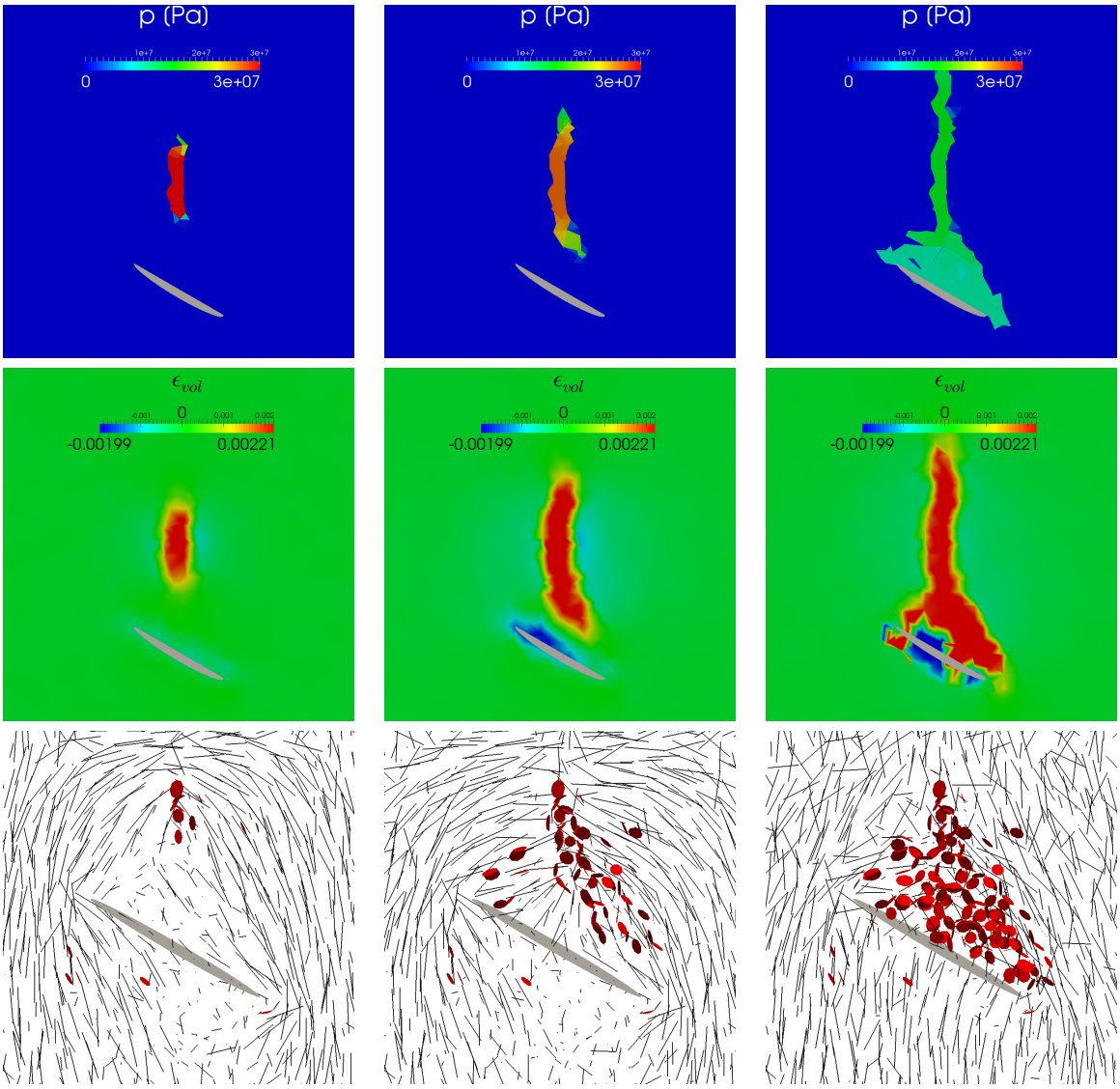

Figure 8.29: Case TNF23 (Top) Pressure field, (Middle) Volumetric strain field ϵ_v where $\epsilon_v > 0$ indicates dilation and $\epsilon_v < 0$ compaction, (Bottom) Local σ_1 direction and crack events. The values are shown for a slice perpendicular to the HF plane for three different stages of the injection.

compacted region.

8.3 Discussion

3D injections in triaxially loaded specimens containing persistent and non-persistent defects were studied to determine the impact of several material properties and control parameters on the HF-NF interaction.

For the set of parameters used and the cases of persistent NF studied, it turned out that the ratio of NF to rock matrix stiffnesses is of primary importance for the development of HF in fractured media. In cases where the stiffness of the NF is much lower than the one of the rock matrix, the NF acts as a "damper" that prevents crossing. On the same line, high values of initial NF aperture was found to cause excessive leak-off inside the persistent plane and to stop the propagation. The intensity of fractures and fractured volume tend to decrease as the leak-off becomes more important. The same trend was observed for low values of viscosity where the fractured volume and fracture intensity become clearly lower. Finally, regarding the angle

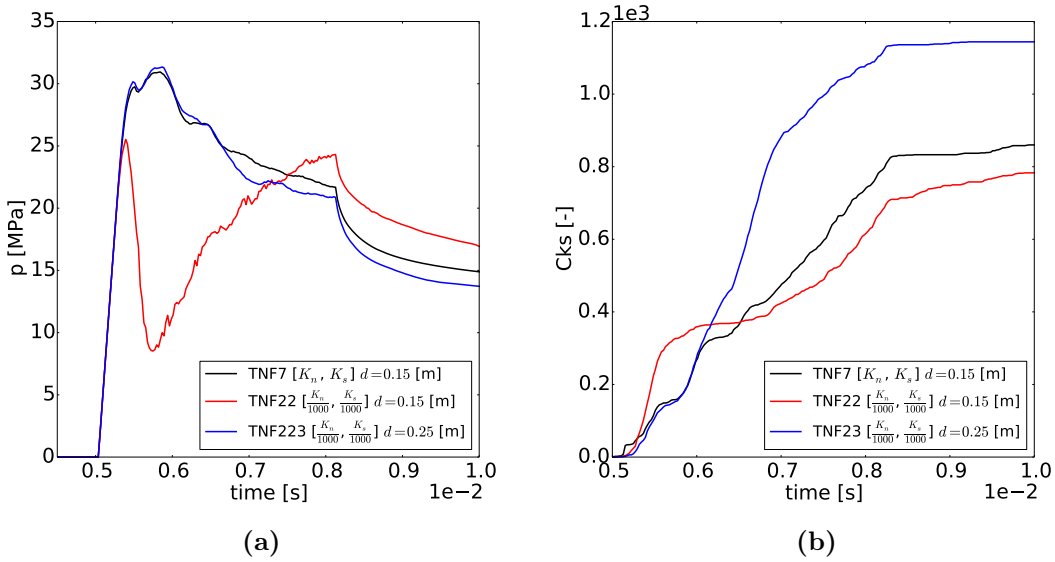

Figure 8.30: Evolution of: (a) Pressure at injection point and (b) Cumulative crack events for the tests [TNF7,TNF22,TNF23].

of approach, high angles (such as 90° and 70°) lead to a "crossing" type of interaction between HF-NF while the HF tends to dilate the lower part of the NF plane and leak-off through it for lower angles. The results are in good agreement with the proposed analysis by (Liu *et al.*, 2015).

Regarding the tests containing non-persistent NF, the effect of stress state on the NF due to either different applied stress field or different NF orientations was studied. Furthermore, the importance of fully 3D analysis of the problem was emphasized as *e.g.*, 2D analysis might be misleading regarding lateral HF propagation which might affect the HF propagation in dense NF networks.

Moreover, several tests were ran in order to estimate the effect of fluid leak-off into the NF on HF growth and the impact on the recorded response. The possible sources of leak-off were investigated by changing the fluid viscosity and the initial NF aperture. From the tests it was shown that, as the conductivity increases, the HF-NF interaction is more prone to cause NF dilation and thus more prone to create new HF from the NF tips. On the other hand, in low leak-off cases, the HF was found to be more prone to cross the NF.

Finally, the impact of NF compliance on HF growth was studied for cases of NF with very low stiffness compared to the intact rock matrix. It was shown that low NF stiffness causes a local stress perturbation that is unfavourable for HF growth. The pressurization by the propagating HF creates a compacted zone along the NF that restrain the fluid to enter into it. Instead, the HF causes a highly fractured zone in front of the NF which causes a high pressure loss and a temporal HF arrest. Re-initiation is most probably going to happen from the NF tips. In some cases bifurcation of the main fracture in a second branch was observed.

In future work, tests for various flow-rates should also be considered as it is believed to be an important control parameter.

Chapter highlights

- Interaction between HF-NF was studied in a way that the numerical tests can be correlated to experiments and *vice-versa*.
- High conductance in persistent NF arrests the HF propagation.
- Low stiffness ratio between the rock matrix and the persistent NF blocks the HF propagation.
- Higher approach angles favour a crossing tendency at the HF-NF intersection point while lower angles favour shear and then dilated tendency on the NF plane.
- While a persistent NF plane is activated in shear, only the part forming large angle with the approaching HF is activated. The other part remains confined due to stress perturbation at the vicinity of the intersection point.
- Higher differential stresses and higher angles favour NF crossing also in the case of non-persistent fractures. For lower values the non-persistent NF is slipping or dilating.
- For the same approach angle of 90°, higher conductance leads to non-persistent NF dilation while low conductance to crossing.
- Low stiffness ratio for non-persistent NF can divert the HF or cause bifurcation of the HF in several branches. The reason is the stress-field perturbation due to presence of the defect.

Conclusions and perspectives

Conclusions

An attempt was made to give more insights on the process of hydraulic fractures propagation in complex environments of naturally fractured rock-mass. To that end, a coupled 3D hydro-mechanical DEM model has been developed to study the propagation of hydraulically driven fractures. The model can reproduce the progressive failure of rocks for various loading conditions and simulate fluid flow in both porous matrix and cracks. The local response of the rock during hydraulic fracture propagation can be assessed, providing critical information about fractures interaction and reorientation, rock deformation, pressure distribution, fractured volume and fracture intensity. Furthermore a DFN plug-in enables the model to take into account single pre-existing fractures or families of discontinuities as explicit fracture sets or stochastic networks.

The formulation of the model and the hydro-mechanical coupling strategy are described extensively. The calibration procedure needed to ensure the relevance of the model's predictions is explained for both the mechanical and the hydraulic scheme. The coupled scheme is verified against analytical and semi-analytical solutions for pressurized penny shaped cracks in impermeable medium. Also, a comparison was made with real data coming from an experiment.

After the model was described and verified, it was applied to a case-study corresponding to a single injection in a lab-scale specimen. During the simulation, the full spatio-temporal evolution of the HF was followed along with the pressure response, fractured volume and fracture intensity. The effect of the flow rate, permeability, fluid compressibility, in-situ stress-state and model resolution on the aforementioned responses was investigated. One of the main findings of this analysis is that that the deviation of the perforation slot's normal from the minimum principal stress direction causes a large decrease of the fractured volume and fracture intensity, low propped volume and creates non planar, percolating HF.

The model was then applied to study multiple injection treatments along a single well-segment. In this test, the effect of multiple HF interaction was studied under different injection slot intervals, well angles and perforation slots orientations. The impact of each parameter on the final fracture volume and fracture intensity was compared. It was found that, due to stress-shadow effects, closely spaced HFs tend to reduce the final stimulated volume but might increase the fracture intensity. Also, it was found that keeping the perforation slots perpendicular to σ_3 in multiple injection treatments while the well is non-favourably oriented (not aligned with σ_3 direction), result in quasi-planar HFs and increased fracture intensity and fractured volume.

Then, as an attempt to study HF propagation in fractured rock masses, a single pre-existing fracture (considered as a NF) was introduced into the specimen. In the first series of tests the NF was persistent. The studied parameters were: the initial aperture, the stiffness ratio between the rock matrix and the fracture and the fluid viscosity. The pressure at the injection point, crack events, cracks activity, fractured volume, fracture intensity, strain, stress field, pressure field and aperture field were recorded. By recording these responses, the model can produce results that are comparable to experiments. From the analysis it turned out that, for a persistent NF, HF propagation can be arrested of the conductance of the NF is high or if its stiffness is low compared to the rock stiffness. Furthermore, it was found that high approach angles favour a

crossing tendency while lower angles favour shear and then dilation of the NF. Finally, it was observed that, when a persistent NF plane is activated in shear, only the segment forming large angle with the approaching HF is activated. The other segment remains confined due to stress re-orientation at the vicinity of the intersection point.

In the second series of tests, a non-persistent fracture was used. The effect of fracture's orientation, differential stress, fluid viscosity, initial aperture aperture and NF to rock matrix stiffness ratio on HF propagation and trajectory along with the delay on the propagation were studied. Specifically, it was found that a low stiffness ratio between the NF and the rock matrix can divert the HF from the initial propagation direction, or cause bifurcation of the HF in several branches. The reason is the stress-field perturbation in the vicinity of the NF.

Perspectives

Towards geomechanics

The setup of a model dealing with progressive failure of rock, multiple fractures interaction, hydro-mechanically processes taking place in both the porous matrix and fracture network and also able to include DFN, opens the way for tackling a large variety of hydro-mechanical problems in the future. Selected topics of ongoing or future work are presented below.

Hydraulic fracturing treatments

Regarding rock stimulation treatments for hydrocarbon or geothermal energy exploitation, comparisons of the model's predictions for field-scale applications with field-data and realistic DFN could bring up important information about the different non-traceable, phenomena that take place during the treatment in the field.

For instance, multi-stage treatments could be handled by the model for parallel and sub-parallel wells through simultaneous and sequential injection including shut-in and flow-back for various pre-existing NF networks. The application not only could help in getting the maximum SRV from the treatment but also reveal the sensitivity of the treatment to the timing of the multi-stage HFs, stress shadow phenomena and pre-existing fractures.

Alternations between formations of different permeability and mechanical properties could also be tested. For example, the effect of the contrast stiffness, toughness and permeability of neighbouring formations and in the interface between them, on HF propagation could be investigated. An example of an ongoing work in this direction is illustrated in Figures III, where an injection is performed in a formation of finite height bounded by two "barrier" formations characterized by much higher toughness. The HF is expected here to propagate along $\sigma_v - \sigma_H$ plane as a circular quasi-planar surface. Then, when the HF meets the barrier formation, due to the higher toughness of the layer, the propagation is blocked in this direction and favoured along the direction of σ_H resulting in an ellipsoidal HF which finally turns into a parallelepiped shape.

On the subject of HF-NF interaction, a more in depth analysis is on the way and, a comparison to large scale experiments and simulations such as (Guglielmi *et al.*, 2015; Rorato *et al.*, 2016; Rutqvist *et al.*, 2015; Tsopela *et al.*, 2016b) has started in collaboration with A.Tsopela (PhD thesis UGA, France).

Regarding the rock behaviour, metamorphic rocks, such as shale for example, exhibit mechanical anisotropy due to thin parallel bedding planes, in the form of transverse isotropy (Bonnelye *et al.*, 2016a,b). The possibility to include transverse isotropy has recently been introduced to the model. In Figure III, the evolution of the Young's modulus and peak-strength of the specimen for varying parallel bedding planes orientation under uniaxial compressive loading as well as the

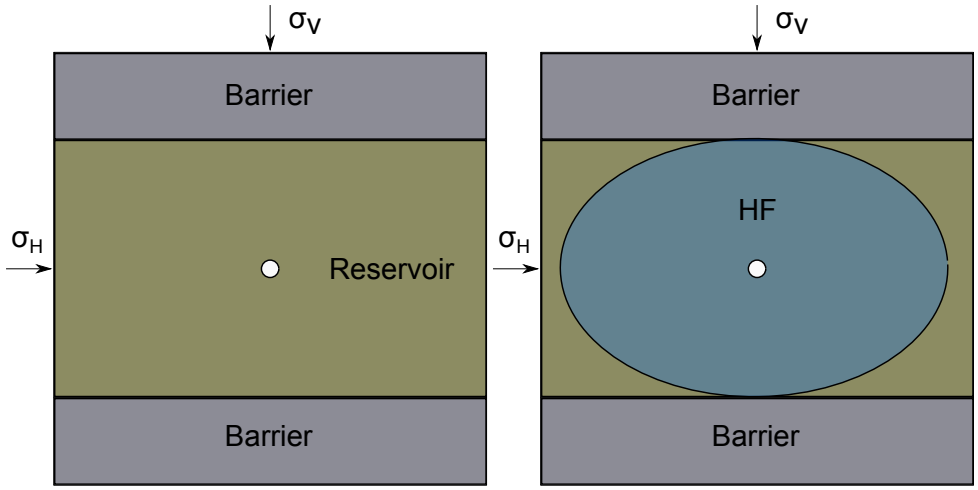

Figure I: Sketch showing the test's configuration and the expected HF pattern caused by the injection and the HF being blocked by the barrier-layers.

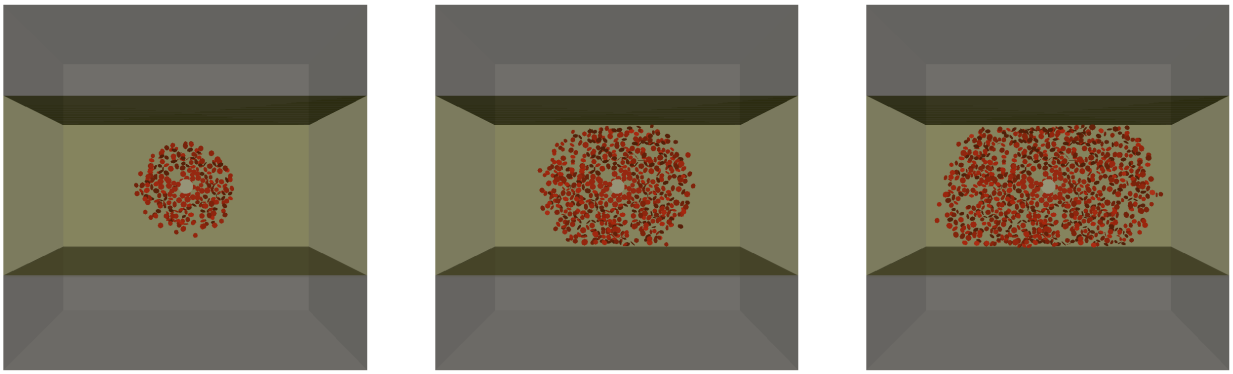

Figure II: Numerical results for the injection in between barrier formations. The red disks represent the cracks in different stages of the injection.

deviatoric strain localization patterns are presented. in a specimen characterized by parallel, thin bedding planes under biaxial loading (plane strain conditions) is shown. The effect of the bedding planes orientation on the shear bands is shown.

Permeability anisotropy could also be implemented, either in a similar way, if needed, or modelled as an emerging property of the elastic properties and strength anisotropy of the rock for a complete HM description of anisotropy.

On the same line, the model, after being verified for flow in a stratified medium (an analytical solution exists *e.g.*, for the so-called "sugar-cube" model), could be used for the calculation of the effective permeability of fractured REVs. More precisely, uncoupled, hydraulic permeability tests can be run on specimens containing a stochastic or deterministic DFN, in order to compute the complete permeability tensor of the medium, similarly to the work done by (Lang *et al.*, 2014). Furthermore, the complete HM model could be used in order to describe the evolution of such an REV in a multi-scale model.

In addition, it has been mentioned throughout the thesis that recording of AEs is one of the basic tools for tracking HF propagation in lab and field tests. A possible correlation of the micro-seismic events from numerical tests to experimental or field data would thus help in the extrapolation and better understanding of the real data. The DEM model used in this study, has been recently enhanced to capture micro-seismicity by computing the energy released from

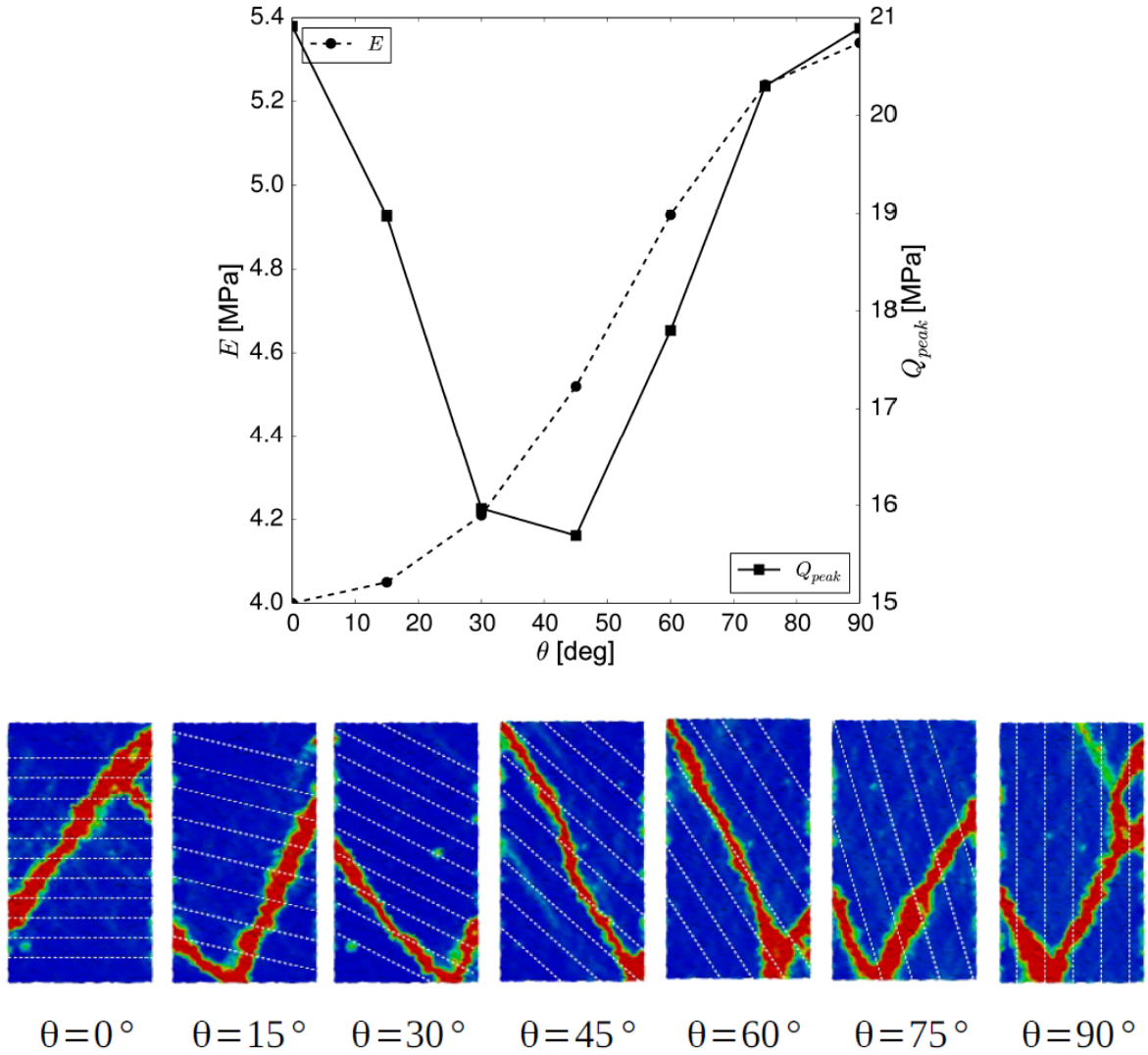

Figure III: Textural anisotropy effect on (Top) Young's modulus E and strength Q_{peak} under triaxial compression and (Bottom) deviatoric strain under biaxial compression, for varying angles of parallel, thin bedding planes. The dashed lines represent the fictitious bedding planes.

the crack events (Raguenel *et al.*, 2015). Thus, including the feature in the coupled PFV-DEM scheme would increase its capabilities by letting it capture better description of HF-NF interaction, NF network activation and induced seismicity, and would permit to make direct comparison with lab tests and field recorded data.

Finally, by carefully accounting for the process zone (for example using a constitutive law with softening) and studying the plastic zones in the vicinity of the HF, the model could be used to study cap-rock integrity, not only for hydrocarbon extraction but also for CO_2 injection and storage, which has recently taken a lot of attention from the scientific community for its crucial impact to the environment (Papanastasiou *et al.*, 2016; Rutqvist, 2012; Selvadurai, 2013).

Shale maturation and mineral decomposition

Apart from hydraulic fracturing treatments, the model has been also applied for the study of NF network genesis from the organic content maturation in shales, in collaboration with Dr. M.G. Teixeira from Federal University of Rio de Janeiro (Brazil) and Prof. F. Renard from Université Grenoble Alpes (France)/University of Oslo (Norway). The numerical tests (Teixeira *et al.*, 2016) were done as a complementary study to explain the creation of a vertical NF network caused by fluid pressurization, considering the fluid migration induced by the maturation of kerogen patches as observed experimentally by (Kobchenko *et al.*, 2011) using Synchrotron X-rays micro-tomography. The outcome of the study can explain the formation of vertical fracture networks in shales during maturation, driving the primary migration of hydrocarbons. Another step forward would be the implementation of a complete thermal coupling in the scheme to deal with the heat-exchange (loss of isothermal conditions) taking place in such environments.

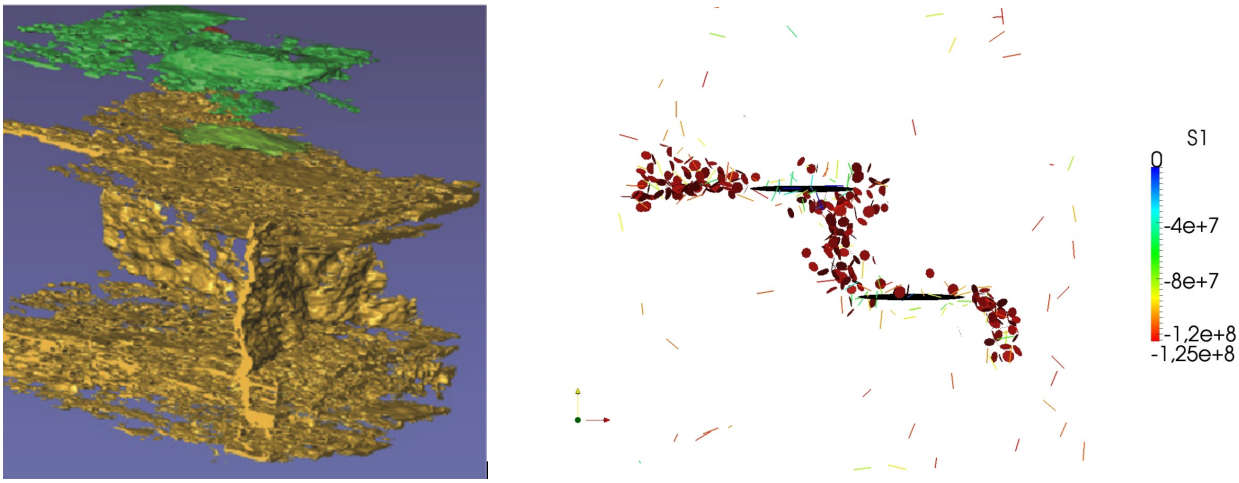

Figure IV: (Left) 3D view of the fracture network with connecting horizontal and vertical cracks and (Right) numerical results for comparison (from Teixeira *et al.*, 2016).

Furthermore, an end-cap model in combination with an erosion law (*e.g.*, Buscarnera and Das, 2015) could be considered in the DEM model to capture: (a) compaction bands, (b) degradation of the formation's mechanical properties (weakening) that might take place during fluid injection in carbonated reservoirs or cap-rocks or during mineral decomposition (Alevizos *et al.*, 2016) and (c) the related fluid/heat release.

Fault activation, episodic tremor and slip

Mineral decomposition can be the cause of deep fluid pressurization/injection that causes episodic tremors and slip (Veveakis *et al.*, 2016). Thus, considering the aforementioned improvements, the code could probably be used to study phenomena such as episodic tremor and slip. A material stability analysis can be performed in scales where micro-HF can take place due to mineral fluid release in fault's principle slip zones or thermal fluid pressurization commonly referred to in literature as a weakening mechanism (Alevizos *et al.*, 2014; Ghabezloo and Sulem, 2009; Platt *et al.*, 2015; Rice, 2006; Rice *et al.*, 2001; Veveakis *et al.*, 2014). In this case, the pore-pressure and temperature can be both triggering factors and the result of the instability at the same time.

Numerical aspects

Although the model has been set up and verified for specific configurations, the complexity of the HF problem leaves space for further refinement and development of the numerical scheme.

Controllability of HF fracture propagation is of primary importance for the validity of the model. As a first step, further verification tests should be considered. More specifically, propagation of penny-shaped crack with leak-off, long term diffusion and in storage - toughness regimes are planned. Additional tests considering transient flow in a single fracture and flow tests in orthogonally stratified medium (sugar-cube model) could be used to verify the flow in DFN and inside the HF.

Also, some further research should be carried on the local propagation criterion. As shown in Subsection 7.1.3, although the macroscopic strength of the medium is DE size independent, the total fracture area seems to be affected by the model's resolution. A parametric study should be done to test if a constitutive law with post-peak softening can tackle this effect. Other, solutions like the application of the J-integral (Rice, 1968) might fit the requirements. Other non-local averaging techniques such as the ones proposed by (Jirásek and Bazant, 1995) could be considered as well.

Moreover, although numerically induced roughness for the NF is treated by the SCL technique, this is not the case for the post-peak behaviour of broken bonds. A series of numerical experiments could be done to study the effect of the local roughness of newly fractured rock and proposing or not a SCL equivalent for this situation.

Regarding HF treatments, at the moment, only Newtonian fluids can be used in the model. More complex rheologies such as power-law fluids could be implemented for the representation of proppant placement. Furthermore, recent advances in YADE code allow for two-phase flow description (Yuan *et al.*, 2015). The feature could also be added to the proposed model for future studies.

Finally, in cases of very dense DFN, a large number of particles might be needed. That would increase the computational cost of the simulations. Different parallelisation schemes might be applicable for optimization.

Bibliography

Abbas, S. and Lecampion, B. (2013), "Initiation and Breakdown of an Axisymmetric Hydraulic Fracture Transverse to a Horizontal Wellbore", in: *Effective and Sustainable Hydraulic Fracturing*, pp. 1–24, DOI: 10.5772/56262 (cit. on pp. 28, 90, 116).

Adachi, J., Siebrits, E., Peirce, A. and Desroches, J. (2007), "Computer simulation of hydraulic fractures", in: *International Journal of Rock Mechanics and Mining Sciences*, Vol. 44, No. 5, pp. 739–757 (cit. on pp. 51, 54).

Adler, P. M. and Thovert, J.-F. (1999), *Fractures and fracture networks*, vol. 15, Springer Science & Business Media (cit. on p. 39).

Administration, U. S. E. I. and Kuuskraa, V. (2011), *World shale gas resources: an initial assessment of 14 regions outside the United States*, US Department of Energy (cit. on p. 24).

Advani, S. H., Lee, T. and Lee, J. (1990), "Three-dimensional modeling of hydraulic fractures in layered media: part I—finite element formulations", in: *Journal of Energy Resources Technology*, Vol. 112, No. 1, pp. 1–9 (cit. on p. 51).

Alain, T. and Vincent, R. (2004), "Hydro-Mechanical Upscaling of a Fractured Rockmass Using a 3D Numerical Approach", in: *Coupled Thermo-Hydro-Mechanical-Chemical Processes in Geo-SystemsFundamentals, Modelling, Experiments and Applications*, ed. by O. Stephanson, vol. 2, Elsevier Geo-Engineering Book Series, Elsevier, pp. 275–280, DOI: http://dx.doi.org/10.1016/S1571-9960(04)80053-3 (cit. on p. 49).

Alevizos, S., Poulet, T. and Veveakis, E. (2014), "Thermo-poro-mechanics of chemically active creeping faults. 1: Theory and steady state considerations", in: *Journal of Geophysical Research: Solid Earth*, Vol. 119, No. 6, pp. 4558–4582 (cit. on p. 139).

Alevizos, S., Poulet, T., Sari, M., Lesueur, M., Regenauer-Lieb, K. and Veveakis, M. (2016), "A framework for fracture network formation in overpressurized impermeable shale: deformability vs diagenesis", in: *Rock Mechanics and Rock Engineering* (cit. on pp. 36, 139).

Argilaga, A., Papachristos, E., Caillerie, D. and Dal Pont, S. (2016), "Homogenization of a cracked saturated porous medium: Theoretical aspects and numerical implementation", in: *International Journal of Solids and Structures*, Vol. 94, pp. 222–237 (cit. on pp. 45, 46).

Arthur, J. D., Bohm, B., Coughlin, B. J. and Layne, M. (2008), "Hydraulic fracturing considerations for natural gas wells of the Fayetteville Shale", in: *ALL Consulting* (cit. on p. 24).

Avseth, P., Flesche, H. and Van Wijngaarden, A.-J. (2003), "AVO classification of lithology and pore fluids constrained by rock physics depth trends", in: *The Leading Edge*, Vol. 22, No. 10, pp. 1004–1011 (cit. on p. 38).

Baghbanan, A. and Jing, L. (2008), "Stress effects on permeability in a fractured rock mass with correlated fracture length and aperture", in: *International Journal of Rock Mechanics and Mining Sciences*, Vol. 45, No. 8, pp. 1320–1334 (cit. on pp. 49, 54).

Bahorich, B., Olson, J. E., Holder, J. *et al.* (2012), "Examining the effect of cemented natural fractures on hydraulic fracture propagation in hydrostone block experiments", in: *SPE Annual Technical Conference and Exhibition*, Society of Petroleum Engineers (cit. on p. 40).

Barenblatt, G. I. (1962), "The mathematical theory of equilibrium cracks in brittle fracture", in: *Advances in applied mechanics*, Vol. 7, pp. 55–129 (cit. on p. 26).

Ben, Y., Xue, J., Miao, Q., Wang, Y., Shi, G.-H. *et al.* (2012), "Simulating hydraulic fracturing with discontinuous deformation analysis", in: *46th US Rock Mechanics/Geomechanics Symposium*, American Rock Mechanics Association (cit. on p. 53).

Blanton, T. L. *et al.* (1982), "An experimental study of interaction between hydraulically induced and pre-existing fractures", in: *SPE unconventional gas recovery symposium*, Society of Petroleum Engineers (cit. on p. 42).

Bonnelye, A., Schubnel, A., David, C., Henry, P., Guglielmi, Y., Gout, C., Fauchille, A.-L. and Dick, P. (2016a), "Elastic wave velocity evolution of shales deformed under uppermost-crustal conditions", in: *Journal of Geophysical Research: Solid Earth* (cit. on p. 136).

Bonnelye, A., Schubnel, A., David, C., Henry, P., Guglielmi, Y., Gout, C., Fauchille, A.-L. and Dick, P. (2016b), "Strength anisotropy of shales deformed under uppermost-crustal conditions", in: *Journal of Geophysical Research: Solid Earth* (cit. on p. 136).

Borst, R. de (2002), "Fracture in quasi-brittle materials: a review of continuum damage-based approaches", in: *Engineering fracture mechanics*, Vol. 69, No. 2, pp. 95–112 (cit. on p. 45).

Bourbiaux, B., Basquet, R., Daniel, J., Hu, L., Jenni, S., Lange, G. and Rasolofosaon, P. (2005), "Fractured reservoirs modelling: a review of the challenges and some recent solutions", in: *First Break*, Vol. 23, No. 9, pp. 33–40 (cit. on p. 38).

Boutt, D. F., Cook, B. K., McPherson, B. J. and Williams, J. (2007), "Direct simulation of fluid-solid mechanics in porous media using the discrete element and lattice-Boltzmann methods", in: *Journal of Geophysical Research: Solid Earth*, Vol. 112, No. B10 (cit. on pp. 49, 50, 54).

Britt, L. (2012), "Fracture stimulation fundamentals", in: *Journal of Natural Gas Science and Engineering*, Vol. 8, pp. 34–51 (cit. on p. 24).

Browning, J., Meredith, P. and Gudmundsson, A. (2016), "Cooling-dominated cracking in thermally stressed volcanic rocks", in: *Geophysical Research Letters*, Vol. 43, No. 16, pp. 8417–8425 (cit. on p. 38).

Bui, Q. (2010), "Initiation of damage with implicit gradient-enhanced damage models", in: *International Journal of Solids and Structures*, Vol. 47, No. 18, pp. 2425–2435 (cit. on p. 46).

Bunger, A. P., Detournay, E. and Garagash, D. I. (2005), "Toughness-dominated hydraulic fracture with leak-off", in: *International journal of fracture*, Vol. 134, No. 2, pp. 175–190 (cit. on p. 51).

Bunger, A. P. and Peirce, A. P. (2013), "Numerical Simulation of Simultaneous Growth of Multiple Interacting Hydraulic Fractures from Horizontal Wells", in: *Shale Energy Engineering 2014@ sTechnical Challenges, Environmental Issues, and Public Policy*, ASCE, pp. 201–210 (cit. on p. 54).

Bunger, A. P. and Peirce, A. P. (2014), "Numerical simulation of simultaneous growth of multiple interacting hydraulic fractures from horizontal wells", in: *Shale Energy Engineering*, pp. 201–210 (cit. on p. 32).

Bunger, A. P., Zhang, X., Jeffrey, R. G. *et al.* (2012), "Parameters affecting the interaction among closely spaced hydraulic fractures", in: *SPE Journal*, Vol. 17, No. 01, pp. 292–306 (cit. on pp. 25, 32).

Burghardt, J., Desroches, J., Lecampion, B., Stanchits, S., Surdi, A., Whitney, N. and Houston, M. (2015), "Laboratory Study of the Effect of Well Orientation, Completion Design, and Rock Fabric on Near-wellbore Hydraulic Fracture Geometry in Shales", in: *15th International Congress of the International Society of Rock Mechanics, Montreal, Quebec, Canada.* ISRM (cit. on pp. 25, 99).

Al-Busaidi, A., Hazzard, J. and Young, R. (2005), "Distinct element modeling of hydraulically fractured Lac du Bonnet granite", in: *Journal of Geophysical Research: Solid Earth (1978–2012)*, Vol. 110, No. B6 (cit. on p. 54).

Buscarnera, G. and Das, A. (2015), "Chemo-mechanics of cemented granular solids subjected to precipitation and dissolution of mineral species", in: *International Journal for Numerical and Analytical Methods in Geomechanics* (cit. on p. 139).

Cannon, N., Schulson, E., Smith, T. and Frost, H. (1990), "Wing cracks and brittle compressive fracture", in: *Acta Metallurgica et Materialia*, Vol. 38, No. 10, pp. 1955–1962, ISSN: 0956-7151, DOI: http://dx.doi.org/10.1016/0956-7151(90)90307-3 (cit. on p. 45).

Carol, I., Jirásek, M. and Bažant, Z. P. (2004), "A framework for microplane models at large strain, with application to hyperelasticity", in: *International Journal of Solids and Structures*, Vol. 41, No. 2, pp. 511–557, ISSN: 0020-7683, DOI: http://dx.doi.org/10.1016/S0020-7683(03)00416-5 (cit. on p. 47).

Catalano, E. (2012), "A pore–scale coupled hydromechanical model for biphasic granular media. Application to granular sediment hydrodynamics", PhD thesis (cit. on p. 61).

Catalano, E., Chareyre, B. and Barthélemy, E. (2014), "Pore-scale modeling of fluid-particles interaction and emerging poromechanical effects", in: *International Journal for Numerical and Analytical Methods in Geomechanics*, Vol. 38, No. 1, pp. 51–71 (cit. on pp. 50, 58, 65, 68).

Chareyre, B., Cortis, A., Catalano, E. and Barthélemy, E. (2012), "Pore-scale modeling of viscous flow and induced forces in dense sphere packings", in: *Transport in porous media*, Vol. 94, No. 2, pp. 595–615 (cit. on pp. 50, 65, 68).

Chau, K. T. and Wang, G. S. (2001), "Condition for the onset of bifurcation in en echelon crack arrays", in: *International Journal for Numerical and Analytical Methods in Geomechanics*, Vol. 25, No. 3, pp. 289–306, ISSN: 1096-9853, DOI: 10.1002/nag.130, URL: http://dx.doi.org/10.1002/nag.130 (cit. on p. 96).

Chen, W., Konietzky, H., Tan, X. and Frühwirt, T. (2016), "Pre-failure damage analysis for brittle rocks under triaxial compression", in: *Computers and Geotechnics*, Vol. 74, pp. 45–55 (cit. on p. 47).

Cho, N., Martin, D. and Sego, D. (2007), "A clumped particle model for rock", in: *International Journal of Rock Mechanics and Mining Sciences*, Vol. 44, No. 7, pp. 997–1010 (cit. on p. 58).

Chuprakov, D., Melchaeva, O. and Prioul, R. (2014), "Injection-sensitive mechanics of hydraulic fracture interaction with discontinuities", in: *Rock Mechanics and Rock Engineering*, Vol. 47, No. 5, pp. 1625–1640 (cit. on p. 42).

Cipolla, C., Wallace, J. *et al.* (2014), "Stimulated Reservoir Volume: A Misapplied Concept?", in: *SPE Hydraulic Fracturing Technology Conference*, Society of Petroleum Engineers (cit. on p. 25).

Comer, J. and Hinch, H. (1987), "Recognizing and quantifying expulsion of oil from the Woodford Formation and age-equivalent rocks in Oklahoma and Arkansas: American Association of Petroleum Geologists Bulletin, v. 71", in: *doi*, Vol. 10, pp. 844–858 (cit. on p. 36).

Couples, G., Lewis, H., Olden, P., Workman, G. and Higgs, N. (2007), "Insights into the faulting process from numerical simulations of rock-layer bending", in: *Geological Society, London, Special Publications*, Vol. 289, No. 1, pp. 161–186 (cit. on p. 37).

Curtis, J. B. (2002), "Fractured shale-gas systems", in: *AAPG bulletin*, Vol. 86, No. 11, pp. 1921–1938 (cit. on p. 40).

D'addetta, G., Kun, F. and Ramm, E. (2002), "On the application of a discrete model to the fracture process of cohesive granular materials", in: *Granular matter*, Vol. 4, No. 2, pp. 77–90 (cit. on p. 46).

Dahi-Taleghani, A., Olson, J. E. *et al.* (2011), "Numerical modeling of multistranded-hydraulic-fracture propagation: accounting for the interaction between induced and natural fractures", in: *SPE journal*, Vol. 16, No. 03, pp. 575–581 (cit. on p. 40).

Damjanac, B. and Cundall, P. (2015), "Application of distinct element methods to simulation of hydraulic fracturing in naturally fractured reservoirs", in: *Computers and Geotechnics* (cit. on pp. 41, 49, 50, 54).

Damjanac, B., Detournay, C. and Cundall, P. A. (2016), "Application of particle and lattice codes to simulation of hydraulic fracturing", in: *Computational Particle Mechanics*, Vol. 3, No. 2, pp. 249–261 (cit. on p. 54).

Damjanac, B., Detournay, C. *et al.* (2013), "Three-Dimensional Numerical Model of Hydraulic Fracturing in Fractured Rock Masses", in: *ISRM International Conference for Effective and Sustainable Hydraulic Fracturing*, International Society for Rock Mechanics (cit. on p. 54).

Davies, R. J., Mathias, S. A., Moss, J., Hustoft, S. and Newport, L. (2012), "Hydraulic fractures: How far can they go?", in: *Marine and petroleum geology*, Vol. 37, No. 1, pp. 1–6 (cit. on p. 24).

Davy, P., Le Goc, R., Darcel, C., Bour, O., De Dreuzy, J.-R. and Munier, R. (2010), "A likely universal model of fracture scaling and its consequence for crustal hydromechanics", in: *Journal of Geophysical Research: Solid Earth*, Vol. 115, No. B10 (cit. on p. 65).

Day-Lewis, A. D. (2008), *Characterization and modeling of in situ stress heterogeneity* (cit. on p. 54).

De Pater, C., Weijers, L., Cleary, M., Quinn, T., Barr, D. and Johnson, D. (1994), "Experimental verification of dimensional analysis for hydraulic fracturing", in: *SPE Production and Facilities (Society of Petroleum Engineers);(United States)*, Vol. 9, No. 4 (cit. on pp. 31, 82).

Deo, M. D., Deo, M., Sorkhabi, R., McLennan, J., Bhide, R., Zhao, N., Sonntag, R. and Evans, J. (2013), "Gas Production Forecasting From Tight Gas Reservoirs: Integrating Natural Fracture Networks and Hydraulic Fractures", in: Vol. Final Report to RPSEA, pp. 07122–44 (cit. on p. 24).

Dershowitz, W. S. (1984), "Rock joint systems", PhD thesis, Massachusetts Institute of Technology (cit. on p. 26).

Desroches, J., Detournay, E., Lenoach, B., Papanastasiou, P., Pearson, J., Thiercelin, M. and Cheng, A. (1994), "The crack tip region in hydraulic fracturing", in: *Proceedings of the Royal Society of London A: Mathematical, Physical and Engineering Sciences*, Vol. 447, No. 1929, pp. 39–48 (cit. on p. 48).

Detournay, E. (1999), "Fluid and solid singularities at the tip of a fluid-driven fracture", in: *IUTAM Symposium on Non-Linear Singularities in Deformation and Flow*, Springer, pp. 27–42 (cit. on p. 48).

Detournay, E. (2004), "Propagation regimes of fluid-driven fractures in impermeable rocks", in: *International Journal of Geomechanics*, Vol. 4, No. 1, pp. 35–45 (cit. on pp. 48, 51).

Detournay, E. (2016), "Mechanics of hydraulic fractures", in: *Annual Review of Fluid Mechanics*, Vol. 48, pp. 311–339 (cit. on p. 29).

Detournay, E. and Cheng, A. H.-D. (1991), "Plane strain analysis of a stationary hydraulic fracture in a poroelastic medium", in: *International Journal of Solids and Structures*, Vol. 27, No. 13, pp. 1645–1662 (cit. on p. 48).

Detournay, E. and Peirce, A. (2014), "On the moving boundary conditions for a hydraulic fracture", in: *International Journal of Engineering Science*, Vol. 84, pp. 147–155 (cit. on p. 30).

Ding, X. and Zhang, L. (2014), "A new contact model to improve the simulated ratio of unconfined compressive strength to tensile strength in bonded particle models", in: *International Journal of Rock Mechanics and Mining Sciences*, Vol. 69, pp. 111–119 (cit. on p. 58).

Dontsov, E. and Peirce, A. (2015), "An enhanced pseudo-3D model for hydraulic fracturing accounting for viscous height growth, non-local elasticity, and lateral toughness", in: *Engineering Fracture Mechanics*, Vol. 142, pp. 116–139 (cit. on p. 51).

Dreuzy, J.-R. de, De Boiry, P., Pichot, G. and Davy, P. (2010), "Use of power averaging for quantifying the influence of structure organization on permeability upscaling in on-lattice networks under mean parallel flow", in: *Water Resources Research*, Vol. 46, No. 8 (cit. on p. 40).

Dreuzy, J.-R., Méheust, Y. and Pichot, G. (2012), "Influence of fracture scale heterogeneity on the flow properties of three-dimensional discrete fracture networks (DFN)", in: *Journal of Geophysical Research: Solid Earth*, Vol. 117, No. B11 (cit. on p. 40).

Duriez, J., Scholtès, L. and Donzé, F.-V. (2016), "Micromechanics of wing crack propagation for different flaw properties", in: *Engineering Fracture Mechanics*, Vol. 153, pp. 378–398 (cit. on pp. 47, 64, 92).

Dyskin, A. V., Germanovich, L. N. and Ustinov, K. B. (1999), "A 3-D model of wing crack growth and interaction", in: *Engineering Fracture Mechanics*, Vol. 63, No. 1, pp. 81–110 (cit. on p. 45).

Economides, M. J., Nolte, K. G., Ahmed, U. and Schlumberger, D. (2000), *Reservoir stimulation*, vol. 18, Wiley Chichester (cit. on pp. 24, 25).

Eshleman, K. N. and Elmore, A. (2013), "Recommended Best Management Practices for Marcellus Shale Gas Development in Maryland", in: *Appalachian Laboratory-University of Maryland Center for Environmental Science*, Vol. 172, (cit. on p. 24).

Exadaktylos, G. and Stavropoulou, M. (2002), "A closed-form elastic solution for stresses and displacements around tunnels", in: *International Journal of Rock Mechanics and Mining Sciences*, Vol. 39, No. 7, pp. 905–916, ISSN: 1365-1609, DOI: `http://dx.doi.org/10.1016/S1365-1609(02)00079-5` (cit. on p. 45).

Exadaktylos, G. (2010), "A new method to solve crack problems based on gradient elasticity", in: *European Journal of Environmental and Civil Engineering*, Vol. 14, No. 8-9, pp. 1081–1090 (cit. on p. 45).

Exadaktylos, G. (2012), "A study of the transient fluid flow around a semi-infinite crack", in: *International Journal of Solids and Structures*, Vol. 49, No. 23, pp. 3323–3334 (cit. on p. 48).

Fairhurst, C. *et al.* (2013), "Fractures and fracturing: hydraulic fracturing in jointed rock", in: *ISRM International Conference for Effective and Sustainable Hydraulic Fracturing*, International Society for Rock Mechanics (cit. on p. 24).

Faivre, M., Paul, B., Golfier, F., Giot, R., Massin, P. and Colombo, D. (2016), "2D coupled HM-XFEM modeling with cohesive zone model and applications to fluid-driven fracture network", in: *Engineering Fracture Mechanics*, Vol. 159, pp. 115–143 (cit. on p. 52).

Fan, J., Dou, L., He, H., Du, T., Zhang, S., Gui, B. and Sun, X. (2012), "Directional hydraulic fracturing to control hard-roof rockburst in coal mines", in: *International Journal of Mining Science and Technology*, Vol. 22, No. 2, pp. 177–181 (cit. on p. 24).

Fan, Z., Jin, Z.-H. and Johnson, S. (2014), "Oil-Gas Transformation Induced Subcritical Crack Propagation and Coalescence in Petroleum Source Rocks", in: *International Journal of Fracture*, Vol. 185, No. 1-2, pp. 187–194 (cit. on p. 36).

Fischer, M., Wright, C., Davidson, B., Goodwin, A., Fielder, E., Buckler, W. and Steinsberger, N. (2002), "Integrating Fracture-Mapping Technologies to Improve Stimulations in the Barnett Shale", in: *Paper SPE 77441 presented at 2002 SPE Annual Technical Conference and Exhibition, San Antonio, Texas, USA*, vol. 29 (cit. on p. 40).

Fjar, E., Holt, R. M., Raaen, A., Risnes, R. and Horsrud, P. (2008), *Petroleum related rock mechanics*, vol. 53, Elsevier (cit. on p. 28).

Fu, P., Johnson, S. M., Hao, Y. and Carrigan, C. R. (2011), "Fully coupled geomechanics and discrete flow network modeling of hydraulic fracturing for geothermal applications", in: *The 36th Stanford geothermal workshop* (cit. on p. 54).

Gale, J. F., Laubach, S. E., Olson, J. E., Eichhubl, P. and Fall, A. (2014), "Natural fractures in shale: A review and new observations", in: *AAPG bulletin*, Vol. 98, No. 11, pp. 2165–2216 (cit. on pp. 36–40).

Gale, J. F., Reed, R. M. and Holder, J. (2007), "Natural fractures in the Barnett Shale and their importance for hydraulic fracture treatments", in: *AAPG bulletin*, Vol. 91, No. 4, pp. 603–622 (cit. on p. 40).

Gale, J. F., Holder, J. *et al.* (2008), "Natural fractures in the Barnett Shale: Constraints on spatial organization and tensile strength with implications for hydraulic fracture treatment in shale-gas reservoirs", in: *The 42nd US Rock Mechanics Symposium (USRMS)*, American Rock Mechanics Association (cit. on p. 37).

Garagash, D. and Detournay, E. (2000), "The tip region of a fluid-driven fracture in an elastic medium", in: *Journal of applied mechanics*, Vol. 67, No. 1, pp. 183–192 (cit. on p. 48).

Gaurav, A., Dao, E. and Mohanty, K. (2012), "Evaluation of ultra-light-weight proppants for shale fracturing", in: *Journal of Petroleum Science and Engineering*, Vol. 92, pp. 82–88 (cit. on p. 24).

Geertsma, J., De Klerk, F. *et al.* (1969), "A rapid method of predicting width and extent of hydraulically induced fractures", in: *Journal of Petroleum Technology*, Vol. 21, No. 12, pp. 1–571 (cit. on p. 50).

Germanovich, L. and Dyskin, A. (2000), "Fracture mechanisms and instability of openings in compression", in: *International Journal of Rock Mechanics and Mining Sciences*, Vol. 37, No. 1, pp. 263–284 (cit. on p. 45).

Ghabezloo, S. and Sulem, J. (2009), "Stress dependent thermal pressurization of a fluid-saturated rock", in: *Rock Mechanics and Rock Engineering*, Vol. 42, No. 1, pp. 1–24 (cit. on p. 139).

Ghani, I., Koehn, D., Toussaint, R. and Passchier, C. W. (2013), "Dynamic development of hydrofracture", in: *Pure and Applied Geophysics*, Vol. 170, No. 11, pp. 1685–1703 (cit. on p. 54).

Grasselli, G., Lisjak, A., Mahabadi, O. K. and Tatone, B. S. (2015), "Influence of pre-existing discontinuities and bedding planes on hydraulic fracturing initiation", in: *European Journal of Environmental and Civil Engineering*, Vol. 19, No. 5, pp. 580–597 (cit. on pp. 24, 54, 55).

Grassl, P., Fahy, C., Gallipoli, D. and Wheeler, S. (2015), "On a 2D hydro-mechanical lattice approach for modelling hydraulic fracture", in: *Journal of the Mechanics and Physics of Solids*, Vol. 75, pp. 104–118, ISSN: 0022-5096, DOI: `http://dx.doi.org/10.1016/j.jmps.2014.11.011` (cit. on p. 55).

Green, A. and Sneddon, I. (1950), "The distribution of stress in the neighbourhood of a flat elliptical crack in an elastic solid", in: *Mathematical Proceedings of the Cambridge Philosophical Society*, vol. 46, 01, Cambridge Univ Press, pp. 159–163 (cit. on p. 50).

Grégoire, D., Lefort, V., Nouailletas, O. and Pijaudier-Cabot, G. (2016), "2D-lattice modelling of crack propagation induced by fluid injection in heterogeneous quasi-brittle materials", in: *Procedia Structural Integrity*, Vol. 2, pp. 2698–2705 (cit. on pp. 49, 50, 54).

Gu, H., Weng, X., Lund, J. B., Mack, M. G., Ganguly, U., Suarez-Rivera, R. *et al.* (2012), "Hydraulic fracture crossing natural fracture at nonorthogonal angles: a criterion and its validation", in: *SPE Production & Operations*, Vol. 27, No. 01, pp. 20–26 (cit. on p. 41).

Guangqing, Z. and Mian, C. (2009), "Complex fracture shapes in hydraulic fracturing with orientated perforations", in: *Petroleum Exploration and Development*, Vol. 36, No. 1, pp. 103–107 (cit. on p. 54).

Guglielmi, Y., Elsworth, D., Cappa, F., Henry, P., Gout, C., Dick, P. and Durand, J. (2015), "In situ observations on the coupling between hydraulic diffusivity and displacements during fault reactivation in shales", in: *Journal of Geophysical Research: Solid Earth*, Vol. 120, No. 11, pp. 7729–7748 (cit. on p. 136).

Guo, J., Zhao, X., Zhu, H., Zhang, X. and Pan, R. (2015), "Numerical simulation of interaction of hydraulic fracture and natural fracture based on the cohesive zone finite element method", in: *Journal of Natural Gas Science and Engineering*, Vol. 25, pp. 180–188 (cit. on p. 41).

GuoXin, Z., Li, X. and Li, H., "Simulation of hydraulic fracture utilizing numerical manifold method", in: *Science China Technological Sciences*, pp. 1–16 (cit. on p. 54).

Harthong, B., Scholtès, L. and Donzé, F.-V. (2012), "Strength characterization of rock masses, using a coupled DEM–DFN model", in: *Geophysical Journal International*, Vol. 191, No. 2, pp. 467–480 (cit. on pp. 47, 64, 65).

Hazzard, J. F., Young, R. P. and Maxwell, S. (2000), "Micromechanical modeling of cracking and failure in brittle rocks", in: *Journal of Geophysical Research: Solid Earth*, Vol. 105, No. B7, pp. 16683–16697 (cit. on p. 46).

Hazzard, J. and Young, R. (2000), "Simulating acoustic emissions in bonded-particle models of rock", in: *International Journal of Rock Mechanics and Mining Sciences*, Vol. 37, No. 5, pp. 867–872 (cit. on pp. 46, 47).

Hossain, M. M. and Rahman, M. (2008), "Numerical simulation of complex fracture growth during tight reservoir stimulation by hydraulic fracturing", in: *Journal of Petroleum Science and Engineering*, Vol. 60, No. 2, pp. 86–104 (cit. on pp. 52, 54).

Inglis, C. (1913), "Stress in a plate due to the presence of sharp corners and cracks", in: *Trans. Roy. Inst. Naval Architects*, Vol. 60, pp. 219–241 (cit. on p. 26).

Irwin, G., Kies, J. and Smith, H. (1958), "Fracture strengths relative to onset and arrest of crack propagation", in: *Proc. ASTM*, vol. 58, pp. 640–657 (cit. on p. 27).

Itasca, C. (1999), "PFC 3D-User manual", in: *Itasca Consulting Group, Minneapolis* (cit. on p. 46).

Itasca, C. (2013), "3DEC Version 5.0, 3 Dimensional Distinct Element Code, User's Manual", in: *Itasca Consulting Group, Minneapolis* (cit. on pp. 46, 50).

Jaber Taheri-Shakib Amir Ghaderi, A. H. (2016), in: DOI: `10.5772/64831` (cit. on p. 120).

Jiang, J. and Younis, R. M. (2015), "Numerical study of complex fracture geometries for unconventional gas reservoirs using a discrete fracture-matrix model", in: *Journal of Natural Gas Science and Engineering*, Vol. 26, pp. 1174–1186 (cit. on p. 40).

Jin, Z.-H., Johnson, S. E. and Fan, Z. (2010), "Subcritical propagation and coalescence of oil-filled cracks: Getting the oil out of low-permeability source rocks", in: *Geophysical Research Letters*, Vol. 37, No. 1 (cit. on p. 36).

Jirásek, M. and Bazant, Z. P. (1995), "Particle model for quasibrittle fracture and application to sea ice", in: *Journal of engineering mechanics*, Vol. 121, No. 9, pp. 1016–1025 (cit. on p. 140).

Kazerani, T. and Zhao, J. (2010), "Micromechanical parameters in bonded particle method for modelling of brittle material failure", in: *International Journal for Numerical and Analytical Methods in Geomechanics*, Vol. 34, No. 18, pp. 1877–1895, ISSN: 1096-9853, DOI: `10.1002/nag.884`, URL: `http://dx.doi.org/10.1002/nag.884` (cit. on p. 47).

Kear, J., White, J., Bunger, A. P., Jeffrey, R., Hessami, M.-A. *et al.* (2013), "Three dimensional forms of closely-spaced hydraulic fractures", in: *ISRM International Conference for Effective and Sustainable Hydraulic Fracturing*, International Society for Rock Mechanics (cit. on pp. 32, 33, 97).

Klimczak, C., Schultz, R. A., Parashar, R. and Reeves, D. M. (2010), "Cubic law with aperture-length correlation: implications for network scale fluid flow", in: *Hydrogeology Journal*, Vol. 18, No. 4, pp. 851–862 (cit. on p. 40).

Kobchenko, M., Hafver, A., Jettestuen, E., Renard, F., Galland, O., Jamtveit, B., Meakin, P. and Dysthe, D. K. (2014), "Evolution of a fracture network in an elastic medium with internal fluid generation and expulsion", in: *Physical Review E*, Vol. 90, No. 5, p. 052801 (cit. on p. 36).

Kobchenko, M., Panahi, H., Renard, F., Dysthe, D. K., Malthe-Sørenssen, A., Mazzini, A., Scheibert, J., Jamtveit, B. and Meakin, P. (2011), "4D imaging of fracturing in organic-rich shales during heating", in: *Journal of Geophysical Research: Solid Earth*, Vol. 116, No. B12 (cit. on pp. 23, 36, 139).

Kovalyshen, Y. and Detournay, E. (2010), "A Reexamination of the Classical PKN Model of Hydraulic Fracture", in: *Transport in Porous Media*, Vol. 81, No. 2, pp. 317–339, ISSN: 1573-1634, DOI: `10.1007/s11242-009-9403-4` (cit. on p. 51).

Kovalyshen, Y. (2010), "Fluid-driven fracture in poroelastic medium", PhD thesis, University of Minnesota (cit. on pp. 30, 48).

Kozicki, J. and Donzé, F. (2008), "A new open-source software developed for numerical simulations using discrete modeling methods", in: *Computer Methods in Applied Mechanics and Engineering*, Vol. 197, No. 49, pp. 4429–4443 (cit. on pp. 46, 58).

Kozicki, J. and Donzé, F. (2009), "Yade-open dem: an open-source software using a discrete element method to simulate granular material", in: *Engineering Computations*, Vol. 26, No. 7, pp. 786–805 (cit. on pp. 46, 58).

Kuhl, E., Ramm, E. and Borst, R. de (2000), "An anisotropic gradient damage model for quasi-brittle materials", in: *Computer Methods in Applied Mechanics and Engineering*, Vol. 183, No. 1, pp. 87–103 (cit. on p. 46).

Lang, P., Paluszny, A. and Zimmerman, R. (2014), "Permeability tensor of three-dimensional fractured porous rock and a comparison to trace map predictions", in: *Journal of Geophysical Research: Solid Earth*, Vol. 119, No. 8, pp. 6288–6307 (cit. on pp. 40, 49, 137).

Latham, J.-P., Xiang, J., Belayneh, M., Nick, H. M., Tsang, C.-F. and Blunt, M. J. (2013), "Modelling stress-dependent permeability in fractured rock including effects of propagating and bending fractures", in: *International Journal of Rock Mechanics and Mining Sciences*, Vol. 57, pp. 100–112 (cit. on p. 49).

Le Goc, R., Dreuzy, J.-R. de and Davy, P. (2010), "Statistical characteristics of flow as indicators of channeling in heterogeneous porous and fractured media", in: *Advances in Water Resources*, Vol. 33, No. 3, pp. 257–269 (cit. on p. 40).

Lecampion, B. and Desroches, J. (2015), "Simultaneous initiation and growth of multiple radial hydraulic fractures from a horizontal wellbore", in: *Journal of the Mechanics and Physics of Solids* (cit. on p. 25).

Leclère, H., Fabbri, O., Daniel, G. and Cappa, F. (2012), "Reactivation of a strike-slip fault by fluid overpressuring in the southwestern French-Italian Alps", in: *Geophysical Journal International*, Vol. 189, No. 1, pp. 29–37 (cit. on p. 23).

Lee, D. S., Herman, J. D., Elsworth, D., Kim, H. T. and Lee, H. S. (2011), "A critical evaluation of unconventional gas recovery from the marcellus shale, northeastern United States", in: *KSCE Journal of Civil Engineering*, Vol. 15, No. 4, pp. 679–687 (cit. on p. 24).

Lei, Q., Latham, J.-P., Xiang, J. and Tsang, C.-F. (2015), "Polyaxial stress-induced variable aperture model for persistent 3D fracture networks", in: *Geomechanics for Energy and the Environment*, Vol. 1, pp. 34–47 (cit. on p. 40).

Liolios, P. A. and Exadaktylos, G. E. (2006), "A solution of steady-state fluid flow in multiply fractured isotropic porous media", in: *International Journal of Solids and Structures*, Vol. 43, No. 13, pp. 3960–3982 (cit. on p. 48).

Lisjak, A., Garitte, B., Grasselli, G., Müller, H. and Vietor, T. (2015), "The excavation of a circular tunnel in a bedded argillaceous rock (Opalinus Clay): short-term rock mass response and FDEM numerical analysis", in: *Tunnelling and Underground Space Technology*, Vol. 45, pp. 227–248 (cit. on p. 47).

Lisjak, A., Grasselli, G. and Vietor, T. (2014), "Continuum–discontinuum analysis of failure mechanisms around unsupported circular excavations in anisotropic clay shales", in: *International Journal of Rock Mechanics and Mining Sciences*, Vol. 65, pp. 96–115 (cit. on p. 47).

Lisjak, A., Kaifosh, P., He, L., Tatone, B., Mahabadi, O. and Grasselli, G. (2017), "A 2D, fully-coupled, hydro-mechanical, FDEM formulation for modelling fracturing processes in discontinuous, porous rock masses", in: *Computers and Geotechnics*, Vol. 81, pp. 1–18 (cit. on pp. 49, 50, 54, 75).

Lisjak, A., Liu, Q., Zhao, Q., Mahabadi, O. and Grasselli, G. (2013), "Numerical simulation of acoustic emission in brittle rocks by two-dimensional finite-discrete element analysis", in: *Geophysical Journal International*, Vol. 195, No. 1, pp. 423–443 (cit. on p. 47).

Lister, J. R. and Kerr, R. C. (1991), "Fluid-mechanical models of crack propagation and their application to magma transport in dykes", in: *Journal of Geophysical Research: Solid Earth*, Vol. 96, No. B6, pp. 10049–10077 (cit. on p. 23).

Liu, Y., Xiu, N., Ding, Y., Wang, X., Lu, Y., Dou, J., Yan, Y. and Liang, T. (2015), "Analysis of multi-factor coupling effect on hydraulic fracture network in shale reservoirs", in: *Natural Gas Industry B*, Vol. 2, No. 2, pp. 162–166 (cit. on pp. 41, 120, 122, 123, 126, 133).

Lo, K. and Kaniaru, K. (1990), "Hydraulic fracture in earth and rock-fill dams", in: *Canadian Geotechnical Journal*, Vol. 27, No. 4, pp. 496–506 (cit. on p. 23).

Maghous, S., Bernaud, D., Fréard, J. and Garnier, D. (2008), "Elastoplastic behavior of jointed rock masses as homogenized media and finite element analysis", in: *International Journal of Rock Mechanics and Mining Sciences*, Vol. 45, No. 8, pp. 1273–1286 (cit. on p. 45).

Mahabadi, O., Lisjak, A., Munjiza, A. and Grasselli, G. (2012), "Y-Geo: new combined finite-discrete element numerical code for geomechanical applications", in: *International Journal of Geomechanics*, Vol. 12, No. 6, pp. 676–688 (cit. on p. 46).

Mahabadi, O., Kaifosh, P., Marschall, P. and Vietor, T. (2014), "Three-dimensional {FDEM} numerical simulation of failure processes observed in Opalinus Clay laboratory samples", in: *Journal of Rock Mechanics and Geotechnical Engineering*, Vol. 6, No. 6, pp. 591–606, ISSN: 1674-7755, DOI: `http://dx.doi.org/10.1016/j.jrmge.2014.10.005` (cit. on p. 47).

Maillot, J., Davy, P., De Dreuzy, J.-R., Le Goc, R. and Darcel, C. (2014), "Comparison between" Poissonian" and" mechanically-oriented" DFN models for predicting flow structure and permeability.", in: *AGU Fall Meeting Abstracts*, vol. 1, p. 0886 (cit. on p. 49).

Mäkel, G. (2007), "The modelling of fractured reservoirs: Constraints and potential for fracture network geometry and hydraulics analysis", in: *Geological Society, London, Special Publications*, Vol. 292, No. 1, pp. 375–403 (cit. on p. 38).

Mas Ivars, D., Pierce, M., Darcel, C., Reyes-Montes, J., Potyondy, D., Young, R. and PA., C. (2011), "The Synthetic Rock Mass Approach for Jointed Rock Mass Modelling", in: *Int J RockMech Min Sci*, Vol. 48, pp. 219–244 (cit. on pp. 47, 63).

Maxwell, S. C. (2011), "What does microseismic tell us about hydraulic fracture deformation", in: *CSEG Recorder*, Vol. 36, No. 8, pp. 31–45 (cit. on p. 25).

Miehe, C. and Mauthe, S. (2016), "Phase field modeling of fracture in multi-physics problems. Part III. Crack driving forces in hydro-poro-elasticity and hydraulic fracturing of fluid-saturated porous media", in: *Computer Methods in Applied Mechanics and Engineering*, Vol. 304, pp. 619–655, ISSN: 0045-7825, DOI: `http://dx.doi.org/10.1016/j.cma.2015.09.021` (cit. on p. 52).

Mikelić, A., Wheeler, M. F. and Wick, T. (2015), "Phase-field modeling of a fluid-driven fracture in a poroelastic medium", in: *Computational Geosciences*, Vol. 19, No. 6, pp. 1171–1195, DOI: `10.1007/s10596-015-9532-5` (cit. on p. 52).

Min, K.-B., Jing, L. and Stephansson, O. (2004a), "Determining the equivalent permeability tensor for fractured rock masses using a stochastic REV approach: method and application to the field data from Sellafield, UK", in: *Hydrogeology Journal*, Vol. 12, No. 5, pp. 497–510 (cit. on p. 49).

Min, K.-B., Rutqvist, J., Tsang, C.-F. and Jing, L. (2004b), "Stress-dependent permeability of fractured rock masses: a numerical study", in: *International Journal of Rock Mechanics and Mining Sciences*, Vol. 41, No. 7, pp. 1191–1210 (cit. on p. 53).

Morita, N., Fuh, G.-F. and Black, A. (1996), "Borehole breakdown pressure with drilling fluids—II. Semi-analytical solution to predict borehole breakdown pressure", in: *International journal of rock mechanics and mining sciences & geomechanics abstracts*, vol. 33, 1, Elsevier, pp. 53–69 (cit. on p. 28).

Muhlhaus, H. .-.-B., Chau, K. T. and Ord, A. (1996), "Bifurcation of crack pattern in arrays of two-dimensional cracks", in: *International Journal of Fracture*, Vol. 77, No. 1, pp. 1–14, ISSN: 1573-2673, DOI: `10.1007/BF00035367`, URL: `http://dx.doi.org/10.1007/BF00035367` (cit. on p. 96).

Murray Jr, G. H. (1968), "Quantitative Fracture Study–Sanish Pool, Mckenzie County, North Dakota", in: *AAPG Bulletin*, Vol. 52, No. 1, pp. 57–65 (cit. on p. 37).

Muskhelishvili, N. (1966), "Some basic problems of the mathematical theory of elasticity", in: *Nauka, Moscow*, Vol. 1, No. 966, p. 2 (cit. on p. 45).

Muskhelishvili, N. I. and Radok, J. R. M. (2008), *Singular integral equations: boundary problems of function theory and their application to mathematical physics*, Courier Corporation (cit. on p. 45).

Nagel, N., Sanchez-Nagel, M., Zhang, F., Garcia, X. and Lee, B. (2013), "Coupled numerical evaluations of the geomechanical interactions between a hydraulic fracture stimulation and a natural fracture system in shale formations", in: *Rock mechanics and rock engineering*, Vol. 46, No. 3, pp. 581–609 (cit. on pp. 25, 54).

Nelson, R. (2001), *Geologic analysis of naturally fractured reservoirs*, Gulf Professional Publishing (cit. on p. 38).

Nguyen, T., Yvonnet, J., Bornert, M. and Chateau, C. (2016), "Initiation and propagation of complex 3D networks of cracks in heterogeneous quasi-brittle materials: Direct comparison between in situ testing-microCT experiments and phase field simulations", in: *Journal of the Mechanics and Physics of Solids* (cit. on p. 46).

Nobakht, M., Clarkson, C. R. and Kaviani, D. (2013), "New type curves for analyzing horizontal well with multiple fractures in shale gas reservoirs", in: *Journal of Natural Gas Science and Engineering*, Vol. 10, pp. 99–112 (cit. on p. 25).

Olson, J. E., Laubach, S. E. and Lander, R. H. (2009), "Natural fracture characterization in tight gas sandstones: Integrating mechanics and diagenesis", in: *AAPG bulletin*, Vol. 93, No. 11, pp. 1535–1549 (cit. on p. 36).

Ostad, M. N., Asghari, O., Emery, X., Azizzadeh, M. and Khoshbakht, F. (2016), "Fracture network modeling using petrophysical data, an approach based on geostatistical concepts", in: *Journal of Natural Gas Science and Engineering*, Vol. 31, pp. 758–768 (cit. on pp. 38, 40).

Ouyang, S., Carey, G. F. and Yew, C. H. (1997), "AN ADAPTIVE FINITE ELEMENT SCHEME FOR HYDRAULIC FRACTURING WITH PROPPANT TRANSPORT", in: *International Journal for Numerical Methods in Fluids*, Vol. 24, No. 7, pp. 645–670, ISSN: 1097-0363, DOI: 10.1002/(SICI)1097-0363(19970415)24:7<645::AID-FLD458>3.0.CO;2-Z (cit. on p. 52).

Özkaya, I. (1988), "A simple analysis of oil-induced fracturing in sedimentary rocks", in: *Marine and Petroleum Geology*, Vol. 5, No. 3, pp. 293–297 (cit. on p. 36).

Papanastasiou, P. (1999), "The effective fracture toughness in hydraulic fracturing", in: *International Journal of Fracture*, Vol. 96, No. 2, pp. 127–147 (cit. on pp. 52, 54).

Papanastasiou, P., Papamichos, E. and Atkinson, C. (2016), "On the risk of hydraulic fracturing in CO2 geological storage", in: *International Journal for Numerical and Analytical Methods in Geomechanics* (cit. on pp. 33, 138).

Paterson, M. S. and Wong, T.-f. (2005), *Experimental rock deformation-the brittle field*, Springer Science & Business Media (cit. on p. 45).

Peirce, A. and Detournay, E. (2008), "An implicit level set method for modeling hydraulically driven fractures", in: *Computer Methods in Applied Mechanics and Engineering*, Vol. 197, No. 33, pp. 2858–2885 (cit. on pp. 48, 51).

Peirce, A., Bunger, A. *et al.* (2015), "Interference Fracturing: Nonuniform Distributions of Perforation Clusters That Promote Simultaneous Growth of Multiple Hydraulic Fractures", in: *SPE Journal*, Vol. 20, No. 02, pp. 384–395 (cit. on p. 32).

Peng, S. and Zhang, J. (2007), "In-situ stress and pore pressure", in: *Engineering Geology for Underground Rocks*, pp. 45–74 (cit. on p. 54).

Perkins, T., Kern, L. *et al.* (1961), "Widths of hydraulic fractures", in: *Journal of Petroleum Technology*, Vol. 13, No. 09, pp. 937–949 (cit. on p. 50).

Platt, J. D., Brantut, N. and Rice, J. R. (2015), "Strain localization driven by thermal decomposition during seismic shear", in: *Journal of Geophysical Research: Solid Earth*, Vol. 120, No. 6, pp. 4405–4433 (cit. on p. 139).

Potyondy, D. (2012), "A flat-jointed bonded particle material for hard-rock", in: *46th U.S. Rock Mechanics/Geomechanics Symposium, 24-27 June, Chicago*, American Rock Mechanics Association (cit. on p. 58).

Potyondy, D. and Cundall, P. (2004), "A bonded-particle model for rock", in: *International journal of rock mechanics and mining sciences*, Vol. 41, No. 8, pp. 1329–1364 (cit. on pp. 46, 47, 58, 61).

Pouya, A. (2012), "Three-dimensional flow in fractured porous media: a potential solution based on singular integral equations", in: *Advances in Water Resources*, Vol. 35, pp. 30–40 (cit. on p. 48).

Pouya, A. (2015), "A finite element method for modeling coupled flow and deformation in porous fractured media", in: *International Journal for Numerical and Analytical Methods in Geomechanics*, Vol. 39, No. 16, pp. 1836–1852 (cit. on p. 52).

Pouya, A. and Ghabezloo, S. (2010), "Flow around a crack in a porous matrix and related problems", in: *Transport in porous media*, Vol. 84, No. 2, pp. 511–532 (cit. on p. 48).

Pouya, A. and Ghoreychi, M. (2001), "Determination of rock mass strength properties by homogenization", in: *International Journal for Numerical and Analytical Methods in Geomechanics*, Vol. 25, No. 13, pp. 1285–1303 (cit. on p. 45).

Raguenel, M., Scholtès, L. and Cupillard, P. (2015), "Extracting acoustic emissions and microseismic activity from a discrete geomechanical model.", in: *35th Gocad Meeting - 2015 RING Meeting*, ASGA (cit. on p. 138).

Ren, F., Ma, G., Fu, G. and Zhang, K. (2015), "Investigation of the permeability anisotropy of 2D fractured rock masses", in: *Engineering Geology*, Vol. 196, pp. 171–182, ISSN: 0013-7952, DOI: `http://dx.doi.org/10.1016/j.enggeo.2015.07.021` (cit. on p. 49).

Riahi, A., Damjanac, B. *et al.* (2013a), "Numerical study of interaction between hydraulic fracture and discrete fracture network", in: *ISRM International Conference for Effective and Sustainable Hydraulic Fracturing*, International Society for Rock Mechanics (cit. on pp. 53, 55).

Riahi, A., Damjanac, B. *et al.* (2013b), "Numerical study of interaction between hydraulic fracture and discrete fracture network", in: *ISRM International Conference for Effective and Sustainable Hydraulic Fracturing*, International Society for Rock Mechanics (cit. on p. 53).

Rice, J. R. (1968), "A path independent integral and the approximate analysis of strain concentration by notches and cracks", in: *Journal of applied mechanics*, Vol. 35, No. 2, pp. 379–386 (cit. on p. 140).

Rice, J. R. (2006), "Heating and weakening of faults during earthquake slip", in: *Journal of Geophysical Research: Solid Earth*, Vol. 111, No. B5 (cit. on p. 139).

Rice, J. R., Lapusta, N. and Ranjith, K. (2001), "Rate and state dependent friction and the stability of sliding between elastically deformable solids", in: *Journal of the Mechanics and Physics of Solids*, Vol. 49, No. 9, pp. 1865–1898 (cit. on p. 139).

Roper, S. and Lister, J. (2005), "Buoyancy-driven crack propagation from an over-pressured source", in: *Journal of Fluid Mechanics*, Vol. 536, pp. 79–98 (cit. on p. 23).

Rorato, R., Donzé, F.-V., Tsopela, A., Pourpak, H. and Onaisi, A. (2016), "Discrete Element Modeling of the Role of In Situ Stress on the Interactions Between Hydraulic and Natural Fractures", in: *New Frontiers in Oil and Gas Exploration*, ed. by C. Jin and G. Cusatis, Cham: Springer International Publishing, pp. 113–136, ISBN: 978-3-319-40124-9, DOI: `10.1007/978-3-319-40124-9_3`, URL: `http://dx.doi.org/10.1007/978-3-319-40124-9_3` (cit. on pp. 25, 136).

Roubin, E., Vallade, A., Benkemoun, N. and Colliat, J.-B. (2015), "Multi-scale failure of heterogeneous materials: A double kinematics enhancement for Embedded Finite Element Method", in: *International Journal of Solids and Structures*, Vol. 52, pp. 180–196 (cit. on p. 46).

Roussel, N. P. and Sharma, M. M. (2011), "Optimizing fracture spacing and sequencing in horizontal-well fracturing", in: *SPE Production & Operations*, Vol. 26, No. 02, pp. 173–184 (cit. on p. 32).

Rubin, A. M. (1995), "Propagation of magma-filled cracks", in: *Annual Review of Earth and Planetary Sciences*, Vol. 23, pp. 287–336 (cit. on p. 23).

Rummel, F. (1987), "{FRACTURE} {MECHANICS} {APPROACH} {TO} {HYDRAULIC} {FRACTURING} {STRESS} {MEASUREMENTS}", in: *Fracture Mechanics of Rock*, ed. by B. K. ATKINSON, London: Academic Press, pp. 217–240, ISBN: 978-0-12-066266-1, DOI: http://dx.doi.org/10.1016/B978-0-12-066266-1.50011-9 (cit. on p. 28).

Rutqvist, J. (2012), "The Geomechanics of CO2 Storage in Deep Sedimentary Formations", in: *Geotechnical and Geological Engineering*, Vol. 30, No. 3, pp. 525–551, DOI: 10.1007/s10706-011-9491-0 (cit. on p. 138).

Rutqvist, J., Rinaldi, A. P., Cappa, F. and Moridis, G. J. (2015), "Modeling of fault activation and seismicity by injection directly into a fault zone associated with hydraulic fracturing of shale-gas reservoirs", in: *Journal of Petroleum Science and Engineering*, Vol. 127, pp. 377–386 (cit. on p. 136).

Rutqvist, J., Tsang, C.-F. and Stephansson, O. (2000), "Uncertainty in the maximum principal stress estimated from hydraulic fracturing measurements due to the presence of the induced fracture", in: *International Journal of Rock Mechanics and Mining Sciences*, Vol. 37, No. 1, pp. 107–120 (cit. on p. 54).

Sahimi, M. (2011), *Flow and transport in porous media and fractured rock: from classical methods to modern approaches*, John Wiley & Sons (cit. on p. 38).

Salimzadeh, S. and Khalili, N. (2015), "A three-phase XFEM model for hydraulic fracturing with cohesive crack propagation", in: *Computers and Geotechnics*, Vol. 69, pp. 82–92 (cit. on p. 52).

Sarris, E. and Papanastasiou, P. (2011), "Modeling of hydraulic fracturing in a poroelastic cohesive formation", in: *International Journal of Geomechanics*, Vol. 12, No. 2, pp. 160–167 (cit. on p. 52).

Sarris, E. and Papanastasiou, P. (2015), "The influence of pumping parameters in fluid-driven fractures in weak porous formations", in: *International Journal for Numerical and Analytical Methods in Geomechanics*, Vol. 39, No. 6, pp. 635–654 (cit. on pp. 30, 32, 53).

Sarris, T. and Paleologos, E. (2004), "Numerical investigation of the anisotropic hydraulic conductivity behavior in heterogeneous porous media", in: *Stochastic Environmental Research and Risk Assessment*, Vol. 18, No. 3, pp. 188–197 (cit. on p. 40).

Savitski, A. and Detournay, E. (2002), "Propagation of a penny-shaped fluid-driven fracture in an impermeable rock: asymptotic solutions", in: *International Journal of Solids and Structures*, Vol. 39, No. 26, pp. 6311–6337 (cit. on pp. 31, 48, 51, 73, 76).

Schmitt, D. R. and Zoback, M. D. (1992), "Diminished pore pressure in low-porosity crystalline rock under tensional failure: Apparent strengthening by dilatancy", in: *Journal of Geophysical Research: Solid Earth*, Vol. 97, No. B1, pp. 273–288 (cit. on p. 52).

Schmitt, D. and Zoback, M. (1993), "Infiltration effects in the tensile rupture of thin walled cylinders of glass and granite: Implications for the hydraulic fracturing breakdown equation", in: *International journal of rock mechanics and mining sciences & geomechanics abstracts*, vol. 30, 3, Elsevier, pp. 289–303 (cit. on p. 52).

Scholtès, L., Chareyre, B., Michallet, H., Catalano, E. and Marzougui, D. (2015), "Modeling wave-induced pore pressure and effective stress in a granular seabed", in: *Continuum Mechanics and Thermodynamics*, Vol. 27, No. 1-2, pp. 305–323 (cit. on pp. 65, 68).

Scholtès, L. and Donzé, F.-V. (2012), "Modelling progressive failure in fractured rock masses using a 3D discrete element method", in: *International Journal of Rock Mechanics and Mining Sciences*, Vol. 52, pp. 18–30 (cit. on pp. 47, 63, 64).

Scholtès, L. and Donzé, F.-V. (2013), "A DEM model for soft and hard rocks: Role of grain interlocking on strength", in: *Journal of the Mechanics and Physics of Solids*, Vol. 61, No. 2, pp. 352–369 (cit. on pp. 47, 58, 59).

Scholtès, L., Donzé, F.-V. and Khanal, M. (2011), "Scale effects on strength of geomaterials, case study: coal", in: *Journal of the Mechanics and Physics of Solids*, Vol. 59, No. 5, pp. 1131–1146 (cit. on pp. 63, 64).

Schrefler, B. A., Secchi, S. and Simoni, L. (2006), "On adaptive refinement techniques in multi-field problems including cohesive fracture", in: *Computer Methods in Applied Mechanics and Engineering*, Vol. 195, No. 4, pp. 444–461 (cit. on p. 52).

Secchi, S. and Schrefler, B. (2012), "A method for 3-D hydraulic fracturing simulation", in: *International journal of fracture*, Vol. 178, No. 1-2, pp. 245–258 (cit. on p. 52).

Segall, P., McKee, E. H., Martel, S. J. and Turrin, B. D. (1990), "Late Cretaceous age of fractures in the Sierra Nevada batholith, California", in: *Geology*, Vol. 18, No. 12, pp. 1248–1251 (cit. on p. 38).

Selvadurai, A. (2013), "Caprock breach: A potential threat to secure geologic sequestration of CO2", in: *Geomechanics in CO Storage Facilities*, pp. 75–94 (cit. on p. 138).

Settgast, R. R., Fu, P., Walsh, S. D., White, J. A., Annavarapu, C. and Ryerson, F. J. (2016), "A fully coupled method for massively parallel simulation of hydraulically driven fractures in 3-dimensions", in: *International Journal for Numerical and Analytical Methods in Geomechanics* (cit. on p. 52).

Shao, J. F. and Rudnicki, J. (2000), "A microcrack-based continuous damage model for brittle geomaterials", in: *Mechanics of Materials*, Vol. 32, No. 10, pp. 607–619 (cit. on p. 46).

Shao, J.-F., Chau, K. and Feng, X. (2006), "Modeling of anisotropic damage and creep deformation in brittle rocks", in: *International Journal of Rock Mechanics and Mining Sciences*, Vol. 43, No. 4, pp. 582–592 (cit. on p. 45).

Sherard, J. L. (1986), "Hydraulic fracturing in embankment dams", in: *Journal of Geotechnical Engineering*, Vol. 112, No. 10, pp. 905–927 (cit. on p. 23).

Shimizu, H., Murata, S. and Ishida, T. (2011), "The distinct element analysis for hydraulic fracturing in hard rock considering fluid viscosity and particle size distribution", in: *International Journal of Rock Mechanics and Mining Sciences*, Vol. 48, No. 5, pp. 712–727, ISSN: 1365-1609, DOI: `http://dx.doi.org/10.1016/j.ijrmms.2011.04.013` (cit. on pp. 54, 55).

Shojaei, A., Taleghani, A. D. and Li, G. (2014), "A continuum damage failure model for hydraulic fracturing of porous rocks", in: *International Journal of Plasticity*, Vol. 59, pp. 199–212 (cit. on p. 52).

Siebrits, E. and Peirce, A. P. (2002), "An efficient multi-layer planar 3D fracture growth algorithm using a fixed mesh approach", in: *International Journal for Numerical Methods in Engineering*, Vol. 53, No. 3, pp. 691–717 (cit. on p. 51).

Smilauer, V., Catalano, E., Chareyre, B., Dorofeenko, S., Duriez, J., Gladky, A., Kozicki, J., Modenese, C., Scholtès, L., Sibille, L., Stransky, J. and Thoeni, K. (2010), "Yade Documentation", in: *http://yade-dem.org/doc/*. Vol. V. Smliauder (ed.) (Cit. on p. 61).

Sneddon, I. (1946), "The distribution of stress in the neighbourhood of a crack in an elastic solid", in: *Proceedings of the Royal Society of London A: Mathematical, Physical and Engineering Sciences*, vol. 187, 1009, The Royal Society, pp. 229–260 (cit. on pp. 50, 51, 72, 74).

Software, R. (2003), "ELFEN, Version 3.7. 0", in: *Rockfield Software Ltd., Technium, Swansea, UK* (cit. on p. 46).

Soliman, M. and Boonen, P. (2000), "Rock mechanics and stimulation aspects of horizontal wells", in: *Journal of Petroleum Science and Engineering*, Vol. 25, No. 3, pp. 187–204 (cit. on p. 25).

Soliman, M., Daal, J. and East, L. (2012), "Fracturing unconventional formations to enhance productivity", in: *Journal of Natural Gas Science and Engineering*, Vol. 8, pp. 52–67 (cit. on p. 25).

Souley, M., Homand, F., Pepa, S. and Hoxha, D. (2001), "Damage-induced permeability changes in granite: a case example at the URL in Canada", in: *International Journal of Rock Mechanics and Mining Sciences*, Vol. 38, No. 2, pp. 297–310 (cit. on p. 49).

Spence, D., Sharp, P. and Turcotte, D. (1987), "Buoyancy-driven crack propagation: a mechanism for magma migration", in: *Journal of Fluid Mechanics*, Vol. 174, pp. 135–153 (cit. on p. 23).

Spencer, C. W. (1987), "Hydrocarbon generation as a mechanism for overpressuring in Rocky Mountain region", in: *AAPG bulletin*, Vol. 71, No. 4, pp. 368–388 (cit. on p. 36).

Stalgorova, E. and Babadagli, T. (2012), "Modeling miscible injection in fractured porous media using random walk simulation", in: *Chemical engineering science*, Vol. 74, pp. 93–104 (cit. on p. 38).

Stanchits, S., Lund, J., Surdi, A., Edelman, E., Whitney, N., Eldredge, R. and Suarez-Rivera, R. (2011), "Hydraulic Fracture Propagation through Preexisting Discontinuity Monitored by Acoustic Emission and Ultrasonic Transmission", in: *AGU Fall Meeting Abstracts* (cit. on pp. 104, 107).

Stanchits, S., Surdi, A., Gathogo, P., Edelman, E. and Suarez-Rivera, R. (2013), "Monitoring the Early Onset of Hydraulic Fracture Initiation by Acoustic Emission and Volumetric Deformation Measurments", in: *ARMA*, Vol. 47, (cit. on pp. 29, 72, 75, 77, 81–83, 104).

Stanchits, S., Burghardt, J. and Surdi, A. (2015), "Hydraulic Fracturing of Heterogeneous Rock Monitored by Acoustic Emission", in: *Rock Mechanics and Rock Engineering*, Vol. 48, No. 6, pp. 2513–2527 (cit. on pp. 29, 104, 106, 107).

Swarbrick, R. E., Osborne, M. J. and Yardley, G. S. (2001), "AAPG Memoir 76, Chapter 1: Comparision of Overpressure Magnitude Resulting from the Main Generating Mechanisms", in: (cit. on p. 36).

Swoboda, G., Shen, X. and Rosas, L. (1998), "Damage model for jointed rock mass and its application to tunnelling", in: *Computers and Geotechnics*, Vol. 22, No. 3, pp. 183–203 (cit. on p. 45).

Swoboda, G. and Yang, Q. (1999), "An energy-based damage model of geomaterials—I. Formulation and numerical results", in: *International journal of solids and structures*, Vol. 36, No. 12, pp. 1719–1734 (cit. on p. 45).

Tang, C., Tham, L., Lee, P., Yang, T. and Li, L. (2002), "Coupled analysis of flow, stress and damage (FSD) in rock failure", in: *International Journal of Rock Mechanics and Mining Sciences*, Vol. 39, No. 4, pp. 477–489 (cit. on p. 49).

Teixeira, M. G., Donzé, F., Renard, F., Panahi, H., Papachristos, E. and Scholtès, L. (2016), "Microfracturing during primary migration in shales", in: *Tectonophysics* (cit. on pp. 37, 139).

Tengattini, A., Das, A., Nguyen, G. D., Viggiani, G., Hall, S. A. and Einav, I. (2014), "A thermomechanical constitutive model for cemented granular materials with quantifiable internal variables. Part I—Theory", in: *Journal of the Mechanics and Physics of Solids*, Vol. 70, pp. 281–296 (cit. on pp. 45, 46).

TOTAL, *TOTAL S.A.* URL: `http://www.total.com` (cit. on p. 24).

Tsai, V. C. and Rice, J. R. (2010), "A model for turbulent hydraulic fracture and application to crack propagation at glacier beds", in: *Journal of Geophysical Research: Earth Surface*, Vol. 115, No. F3 (cit. on p. 23).

Tsang, Y. W. and Witherspoon, P. A. (1981), "Hydromechanical behavior of a deformable rock fracture subject to normal stress", in: *Journal of Geophysical Research: Solid Earth*, Vol. 86, No. B10, pp. 9287–9298, ISSN: 2156-2202, DOI: `10.1029/JB086iB10p09287` (cit. on p. 39).

Tsopela, A., Donzé, F., Guglielmi, Y., Castilla, R. and Gout, C. (2016a), "Hydro-mechanical modeling of hydraulic injection inside a fault zone", in: (cit. on p. 120).

Tsopela, A., Donzé, F., Guglielmi, Y., Castilla, R. and Gout, C. (2016b), "Hydro-mechanical modeling of hydraulic injection inside a fault zone", in: *50th US Rock Mechanics/Geomechanics Symposium. American Rock Mechanics Association* (cit. on p. 136).

Uzoh, C., Han, J., Hu, L., Siripatrachai, N., Osholake, T. and Chen, X. (2010), *Economic optimization analysis of the development process on a field in the Barnett Shale Formation* (cit. on pp. 24, 25).

Van den Eijnden, A., Bésuelle, P., Chambon, R. and Collin, F. (2016), "A FE 2 modelling approach to hydromechanical coupling in cracking-induced localization problems", in: *International Journal of Solids and Structures*, Vol. 97, pp. 475–488 (cit. on pp. 45, 46).

Vermylen, J. P. (2011), *Geomechanical studies of the Barnett shale, Texas, USA*, Doctoral dissertation,Stanford University (cit. on p. 54).

Vernik, L. (1994), "Hydrocarbon-generation-induced microcracking of source rocks", in: *Geophysics*, Vol. 59, No. 4, pp. 555–563 (cit. on p. 36).

Veveakis, E., Poulet, T. and Alevizos, S. (2014), "Thermo-poro-mechanics of chemically active creeping faults: 2. Transient considerations", in: *Journal of Geophysical Research: Solid Earth*, Vol. 119, No. 6, pp. 4583–4605 (cit. on p. 139).

Veveakis, M., Alevizos, S. and Poulet, T. (2016), "Episodic tremor and slip (ETS) as a chaotic multiphysics spring", in: *Physics of the Earth and Planetary Interiors* (cit. on p. 139).

Wang, H., Marongiu-Porcu, M., Economides, M. J. *et al.* (2015), "Poroelastic and poroplastic modeling of hydraulic fracturing in brittle and ductile formations", in: *SPE Production & Operations* (cit. on pp. 52, 53).

Wang, S., Sun, L., Au, A., Yang, T. and Tang, C. (2009), "2D-numerical analysis of hydraulic fracturing in heterogeneous geo-materials", in: *Construction and Building Materials*, Vol. 23, No. 6, pp. 2196–2206 (cit. on p. 54).

Wang, Y. and Mora, P. (2008), "Modeling wing crack extension: implications for the ingredients of discrete element model", in: *Pure and Applied Geophysics*, Vol. 165, No. 3-4, pp. 609–620 (cit. on p. 58).

Warpinski, N. and Teufel, L. (1987), "Influence of geologic discontinuities on hydraulic fracture propagation (includes associated papers 17011 and 17074)", in: *Journal of Petroleum Technology*, Vol. 39, No. 02, pp. 209–220 (cit. on pp. 33, 40, 42, 120).

Weng, X. (2015), "Modeling of complex hydraulic fractures in naturally fractured formation", in: *Journal of Unconventional Oil and Gas Resources*, Vol. 9, pp. 114–135 (cit. on p. 24).

Wheeler, M., Wick, T. and Wollner, W. (2014), "An augmented-Lagrangian method for the phase-field approach for pressurized fractures", in: *Computer Methods in Applied Mechanics and Engineering*, Vol. 271, pp. 69–85 (cit. on p. 54).

Wolfsberg, A. (1997), "Rock Fractures and Fluid Flow: Contemporary Understanding and Applications", in: *Eos, Transactions American Geophysical Union*, Vol. 78, No. 49, pp. 569–573 (cit. on p. 37).

Wong, L. and Einstein, H. (2009), "Systematic evaluation of cracking behavior in specimens containing single flaws under uniaxial compression", in: *International Journal of Rock Mechanics and Mining Sciences*, Vol. 46, No. 2, pp. 239–249, ISSN: 1365-1609, DOI: `http://dx.doi.org/10.1016/j.ijrmms.2008.03.006` (cit. on p. 45).

Yaghoubi, A. and Zoback, M. (2012), "Hydraulic Fracturing Modeling using a Discrete Fracture Network in the Barnett Shale", in: Stanford Stress and Geomechanics Group. American Geophysical Union, Fall Meeting (cit. on p. 53).

Yao, Y., Liu, L. and Keer, L. M. (2015), "Pore pressure cohesive zone modeling of hydraulic fracture in quasi-brittle rocks", in: *Mechanics of Materials*, Vol. 83, pp. 17–29 (cit. on p. 52).

Yew, C. H. and Weng, X. (2014), *Mechanics of hydraulic fracturing*, Gulf Professional Publishing (cit. on pp. 24, 25, 28, 32, 54).

Yoon, J. S., Zang, A. and Stephansson, O. (2014), "Numerical investigation on optimized stimulation of intact and naturally fractured deep geothermal reservoirs using hydro-mechanical coupled discrete particles joints model", in: *Geothermics*, Vol. 52, pp. 165–184 (cit. on pp. 54, 55).

Yuan, C., Chareyre, B. and Darve, F. (2015), "Pore-scale simulations of drainage in granular materials: finite size effects and the representative elementary volume", in: *Advances in Water Resources* (cit. on p. 140).

Yuan, S. and Harrison, J. (2006), "A review of the state of the art in modelling progressive mechanical breakdown and associated fluid flow in intact heterogeneous rocks", in: *International Journal of Rock Mechanics and Mining Sciences*, Vol. 43, No. 7, pp. 1001–1022 (cit. on pp. 45, 49).

Zhang, F., Nagel, N., Lee, B., Sanchez-Nagel, M. *et al.* (2013), "The Influence of Fracture Network Connectivity on Hydraulic Fracture Effectiveness and Microseismicity Generation", in: *47th US Rock Mechanics/Geomechanics Symposium*, American Rock Mechanics Association (cit. on p. 54).

Zhang, H., Zhu, J., Liu, Y., Xu, B. and Wang, X. (2012), "Strength properties of jointed rock masses based on the homogenization method", in: *Acta Mechanica Solida Sinica*, Vol. 25, No. 2, pp. 177–185 (cit. on p. 45).

Zhang, J., Kamenov, A., Zhu, D. and Hill, A. (2015), "Measurement of realistic fracture conductivity in the Barnett shale", in: *Journal of Unconventional Oil and Gas Resources* (cit. on p. 25).

Zhao, D., Swoboda, G. and Laabmayr, F. (2004), "Damage mechanics and its application for the design of an underground theater", in: *Tunnelling and underground space technology*, Vol. 19, No. 6, pp. 567–575 (cit. on p. 46).

Zhao, Q., Lisjak, A., Mahabadi, O., Liu, Q. and Grasselli, G. (2014), "Numerical simulation of hydraulic fracturing and associated microseismicity using finite-discrete element method", in: *Journal of Rock Mechanics and Geotechnical Engineering*, Vol. 6, No. 6, pp. 574–581 (cit. on p. 54).

Zhao, X. and Paul Young, R. (2011), "Numerical modeling of seismicity induced by fluid injection in naturally fractured reservoirs", in: *Geophysics*, Vol. 76, No. 6, WC167–WC180 (cit. on pp. 41, 54, 55).

Zhou, J., Chen, M., Jin, Y. and Zhang, G.-q. (2008), "Analysis of fracture propagation behavior and fracture geometry using a tri-axial fracturing system in naturally fractured reservoirs", in: *International Journal of Rock Mechanics and Mining Sciences*, Vol. 45, No. 7, pp. 1143–1152 (cit. on pp. 33, 40, 41).

Zhou, J., Jin, Y. and Chen, M. (2010), "Experimental investigation of hydraulic fracturing in random naturally fractured blocks", in: *International Journal of Rock Mechanics and Mining Sciences*, Vol. 47, No. 7, pp. 1193–1199 (cit. on pp. 120, 125).

Zhou, L. and Hou, M. Z. (2013), "A new numerical 3D-model for simulation of hydraulic fracturing in consideration of hydro-mechanical coupling effects", in: *International Journal of Rock Mechanics and Mining Sciences*, Vol. 60, pp. 370–380 (cit. on pp. 52, 54).

Zi, G. and Belytschko, T. (2003), "New crack-tip elements for XFEM and applications to cohesive cracks", in: *International Journal for Numerical Methods in Engineering*, Vol. 57, No. 15, pp. 2221–2240 (cit. on p. 52).

Zimmerman, R. W. and Bodvarsson, G. S. (1996), "Hydraulic conductivity of rock fractures", in: *Transport in Porous Media*, Vol. 23, No. 1, pp. 1–30, ISSN: 1573-1634, DOI: `10.1007/BF00145263` (cit. on p. 39).

Zimmerman, R. and Main, I. (2004), "Hydromechanical behavior of fractured rocks", in: *INTERNATIONAL GEOPHYSICS SERIES.* Vol. 89, pp. 363–422 (cit. on pp. 38, 39).

Zimmerman, R., Kumar, S. and Bodvarsson, G. (1991), "Lubrication theory analysis of the permeability of rough-walled fractures", in: *International Journal of Rock Mechanics and Mining Sciences & Geomechanics Abstracts*, vol. 28, 4, Elsevier, pp. 325–331 (cit. on p. 39).

Zoback, M. D. (2010), *Reservoir geomechanics*, Cambridge University Press (cit. on p. 24).

Zoback, M. and Byerlee, J. (1976), "Effect of high-pressure deformation on permeability of Ottawa sand", in: *AAPG Bulletin*, Vol. 60, No. 9, pp. 1531–1542 (cit. on p. 29).

Zoback, M., Rummel, F., Jung, R. and Raleigh, C. (1977), "Laboratory hydraulic fracturing experiments in intact and pre-fractured rock", in: *International Journal of Rock Mechanics and Mining Sciences and Geomechanics Abstracts*, Vol. 14, No. 2, pp. 49–58, ISSN: 0148-9062, DOI: `http://dx.doi.org/10.1016/0148-9062(77)90196-6` (cit. on pp. 28, 90).

Zou, Y., Zhang, S., Ma, X., Zhou, T. and Zeng, B. (2016), "Numerical investigation of hydraulic fracture network propagation in naturally fractured shale formations", in: *Journal of Structural Geology* (cit. on p. 53).